Investigation and Development of Algorithms and Techniques for Microwave Tomography

by

Puyan Mojabi

A Thesis submitted to the Faculty of Graduate Studies of

The University of Manitoba

in partial fulfilment of the requirements of the degree of

Doctor of Philosophy

Department of Electrical and Computer Engineering

University of Manitoba

Winnipeg, Manitoba, Canada

Abstract

This thesis reports on research undertaken in the area of microwave tomography (MWT) where the goal is to find the dielectric profile of an object of interest using microwave measurements collected outside the object. The main focus of this research is on the development of inversion algorithms which solve the electromagnetic inverse scattering problem associated with MWT. These algorithms must deal with two different aspects of the inverse problem: its nonlinearity and ill-posedness. After providing an overview of some of the different possible formulations in terms of a nonlinear optimization problem, details on the use of the Gauss-Newton inversion algorithm which solves this problem are given. Various regularization techniques for the Gauss-Newton inversion algorithm are studied and classified. It is shown that these regularization techniques can be viewed from within a single consistent framework after applying some modifications. Within the framework of the two-dimensional MWT problem, the inversion of transverse magnetic and transverse electric data sets are considered and compared in terms of computational complexity, image quality and convergence rate.

A new solution to the contrast source inversion formulation of the microwave tomography problem for the case where the MWT chamber consists of a circular conductive enclosure is introduced. This solution is based on expressing the unknowns of the problem as truncated eigenfunction expansions corresponding to the Helmholtz operator for a homogeneous background medium with appropriate boundary conditions imposed at the chamber walls.

The MWT problem is also formulated for MWT chambers made of conducting cylinders of arbitrary shapes. A Gauss-Newton inversion algorithm is utilized to invert the data collected in such configurations. It is then shown that collecting microwave scattered-field data inside MWT setups with different boundary conditions can provide a robust set of useful information for the reconstruction of the dielectric profile. To produce good quality reconstructions, the amount of data collected under each boundary condition can be relatively small if the number of different boundary condition configurations is sufficiently high. This leads to a novel MWT setup wherein a rotatable conductive triangular enclosure is used to generate

scattered-field data. Antenna arrays, with as few as only four elements, that are fixed with respect to the object of interest can provide sufficient data to give good reconstructions, if the triangular enclosure is rotated a sufficient number of times.

Preliminary results of using the algorithms presented herein on data collected using two different MWT prototypes currently under development by the University of Manitoba's Electromagnetic Imaging Group are reported. Using the current open-region MWT prototype, an experimental resolution study using the Gauss-Newton inversion method was performed using various cylindrical targets. Results of this resolution study are reported herein and the separation resolution limit of this system is quantified.

Contributions

This thesis reports on contributions made by the author in the area of microwave tomography over a period of several years. As the research was conducted within a larger research group setting, the author's own particular contributions are here listed and briefly described. In addition, a list of publications directly related to these contributions can be found in Appendix A.

- Achieving an understanding of, and clarifying, the nonlinear inverse problem and completing a comparison of state-of-the-art inversion techniques (completed with Colin Gilmore).
- Classification of different regularization techniques for the Gauss-Newton inversion method and showing that all of these regularization techniques can be viewed from within a single consistent framework after applying some modifications.
- Adapting the normalized cumulative periodogram regularization parameter choice method, originally developed for linear inverse problems, for the MWT problem.
- Comparing the two-dimensional transverse magnetic and transverse electric inversions for the open-region configuration and showing that the transverse electric inversion, which utilizes both rectangular components of the electric vector at each receiver position, can result in more accurate reconstruction than the transverse magnetic inversion when utilizing near-field scattering data collected using only a few transmitters and receivers.
- Introducing a new contrast source inversion formulation for microwave tomography inside a circular conductive enclosure which is based on expressing the unknowns as truncated eigenfunction expansions corresponding to the Helmholtz operator in a homogeneous background medium.

- Utilizing the weighted L^2 norm total variation multiplicative regularized Gauss-Newton inversion algorithm, originally developed for low-frequency deep electromagnetic geophysical measurements, for microwave biomedical imaging, and comparing it to other forms of regularized Gauss-Newton inversion algorithms. Based on this algorithm, a pre-scaled multiplicative regularized Gauss-Newton inversion algorithm was introduced.

- Development of a fast and efficient image enhancement technique for the MWT problem.

- Formulation of the microwave tomography problem inside conducting enclosures of arbitrary shapes and performing initial synthetic inversions for such systems (completed with Amer Zakaria and Colin Gilmore), and development of an inversion algorithm to simultaneously invert the microwave data collected in MWT setups with different boundary conditions.

- Proposing a novel microwave tomography setup wherein a rotatable conductive triangular enclosure is used to generate electromagnetic scattering data.

- Testing of a wide-band experimental open-region microwave tomography system (completed with Colin Gilmore, Amer Zakaria, Cam Kaye and Majid Ostadrahimi), and performing a resolution study using this system (completed with Colin Gilmore and Amer Zakaria).

- Preliminary testing of a microwave tomography system with conductive enclosure (completed with Amer Zakaria, Cam Kaye and Colin Gilmore).

As far as the implementation of the algorithms is concerned, all the inversion algorithms and regularization methods were implemented by the author. All of the utilized forward solvers, except the finite element method[1], were implemented by the author.

[1] The utilized finite element method was implemented by Amer Zakaria.

Symbols and Acronyms

Herein, we provide some general remarks as well as a list of commonly used symbols and acronyms.

- **Position vectors**: position vectors are denoted by bold lowercase letters; *e.g.*, $\boldsymbol{p}$, $\boldsymbol{q}$, $\boldsymbol{q}'$, $\boldsymbol{r}$, and $\boldsymbol{r}'$.
- **Functions**: vector-valued functions are denoted by bold uppercase letters such as $\boldsymbol{E}(\boldsymbol{q})$, $\boldsymbol{E}^{\text{inc}}(\boldsymbol{q})$, and $\boldsymbol{E}^{\text{scat}}(\boldsymbol{p})$. Scalar-valued functions are represented by uppercase letters, such as $E_x(\boldsymbol{q})$, lowercase letters, such as $b(\boldsymbol{q})$, or Greek letters, such as $\chi(\boldsymbol{q})$, $\psi(\boldsymbol{q})$; all of which are non-bold letters.
- **Matrices**: matrices are denoted by underlined uppercase bold letters such as $\underline{\boldsymbol{J}}$ and $\underline{\boldsymbol{\Sigma}}$.
- **Vectors**: vectors are denoted by underlined (non-bold) letters such as $\underline{g}$ and $\underline{d}$. Discretized forms of functions will also be represented by vectors. For example, the vector $\underline{\chi}$ represents the discretized form of the function $\boldsymbol{\chi}(\boldsymbol{q})$, or the vector $\underline{E}^{\text{scat}}$ denotes the discrete form of the function $\boldsymbol{E}^{\text{scat}}(\boldsymbol{q})$.
- **Cost-functionals**: the cost-functionals which map L^2 spaces of complex (or real) functions into real numbers are denoted by $\mathcal{C}$, which may come with different superscripts, such as $\mathcal{C}^{\text{LS}}$ and $\mathcal{C}^{\text{MR}}$. The discrete forms of these cost-functionals which map complex (or real) vectors into real numbers are denoted by $\mathcal{F}$ with appropriate superscripts. Thus, $\mathcal{F}^{\text{LS}}$ and $\mathcal{F}^{\text{MR}}$ denote the discrete forms of $\mathcal{C}^{\text{LS}}$ and $\mathcal{C}^{\text{MR}}$ respectively.

  Corresponding to a non-holomorphic cost-functional mapping L^2 spaces of complex functions into real numbers, say $\mathcal{C}(\chi)$, we consider a new cost-functional which is denoted by $\tilde{\mathcal{C}}(\chi, \chi^*)$. The cost-functional $\tilde{\mathcal{C}}(\chi, \chi^*)$, which treats the complex quantity χ and its complex conjugate χ^* as two independent quantities, satisfies $\tilde{\mathcal{C}}(\chi, \chi^*) = \mathcal{C}(\chi)$. We also use this notation in the discrete domain. Thus, corresponding to the cost-functional $\mathcal{F}(\underline{\chi})$, we consider the cost-functional $\tilde{\mathcal{F}}(\underline{\chi}, \underline{\chi}^*)$ which satisfies $\tilde{\mathcal{F}}(\underline{\chi}, \underline{\chi}^*) = \mathcal{F}(\underline{\chi})$.

Symbol	Description
$\hat{x}$, $\hat{y}$, $\hat{z}$	Unit vectors along x, y and z directions.
j	Imaginary unit ($j^2 = -1$).
$\mathcal{D}$	Imaging domain.
$L^2(\mathcal{D})$	L^2 space of functions defined on $\mathcal{D}$.
$\langle\ .\ ,\ .\ \rangle_{\mathcal{D}}$	Inner product defined on $\mathcal{D}$.
$\mathcal{S}$	Measurement domain.
$L^2(\mathcal{S})$	L^2 space of functions defined on $\mathcal{S}$.
$\langle\ .\ ,\ .\ \rangle_{\mathcal{S}}$	Inner product defined on $\mathcal{S}$.
$\boldsymbol{p}$	Position vector in the measurement domain $\mathcal{S}$.
$\boldsymbol{q}$	Position vector in the imaging domain $\mathcal{D}$.
$\bar{\bar{G}}$	Dyadic Green's function of the background medium.
k_b	Wavenumber of the background medium.
λ_b	Wavelength of the background medium.
$\boldsymbol{E}^{\text{inc}}$	Incident electric field (electric field in the absence of the object of interest).
$\boldsymbol{E}$	Total electric field (electric field in the presence of the object of interest).
$\boldsymbol{E}^{\text{scat}}$	Scattered electric field.
$\boldsymbol{E}^{\text{scat}}_{\text{meas}}$	Measured scattered electric field on the measurement domain $\mathcal{S}$.
$(.)^a$	Adjoint operator.
$(.)^*$	Complex conjugate operator.
$(.)^T$	Transposition operator.
$(.)^H$	Hermitian operator (complex conjugate transpose).
$(.)^{-1}$	Inverse operator.
Re	Real part operator.
Im	Imaginary part operator.
∇	Gradient operator.
$\nabla\cdot$	Divergence operator.
$\nabla\times$	Curl operator.
∇^2	Laplacian operator.
χ	Electric contrast of the object of interest.
ϵ_r	Relative complex permittivity of the object of interest.
ϵ_b	Relative complex permittivity of the background medium.

Acronym	Description
MWT	Microwave tomography.
OI	Object of interest (object being imaged).
TE	Transverse electric.
TM	Transverse magnetic.
PEC	Perfect electric conductor.
GNI	Gauss-Newton inversion.
MR-GNI	Multiplicative regularized Gauss-Newton inversion.
CSI	Contrast source inversion.
MR-CSI	Multiplicative regularized contrast source inversion.
BA	Born approximation.
BIM	Born iterative method.
DBIM	Distorted Born iterative method.
MGM	Modified gradient method.
SVD	Singular value decomposition.
TSVD	Truncated singular value decomposition.
CG	Conjugate gradient.
CGLS	Conjugate gradient least squares.
1D	One-dimensional.
2D	Two-dimensional.
3D	Three-dimensional.
NCP	Normalized cumulative periodogram.
GCV	Generalized cross-validation.
MRI	Magnetic resonance imaging.
CT	Computed tomography.
SNR	Signal-to-noise ratio.

Acknowledgments

First and foremost, I would like to thank my academic advisor, Dr. Joe LoVetri, for his direction, support and encouragement during my PhD studies. I would also like to thank colleagues Dr. Colin Gilmore, Amer Zakaria, Ian Jeffrey, Cameron Caye, and Majid Ostadrahimi.

I would also like to express my appreciation for my Ph.D. committee: Dr. Vladimir Okhmatovski, Dr. Kirill Kopotun, and Dr. Aria Abubakar for their efforts in the evaluation and improvement of this work.

Finally, I extend my gratitude to Natural Sciences and Engineering Research Council of Canada, MITACS and Dr. Stephen Pistorius at CancerCare Manitoba for their financial support.

To my parents and Shiva

Contents

List of Figures

1

Introduction

> *For a long time mathematicians felt that ill-posed problems cannot describe real phenomena and objects. However, we shall show in the present book that the class of ill-posed problems includes many classical mathematical problems and, most significantly, that such problems have important applications* (Tikhonov and Arsenin [1]).

This thesis presents research work in the area of microwave tomography. In microwave tomography, which is one form of the electromagnetic inverse scattering problem, the objective is to determine the dielectric profile and/or magnetic profile of the Object of Interest (OI) from microwave measurements collected outside the OI. In this chapter, we first briefly review the concept of inverse problems. The electromagnetic inverse scattering and microwave tomography are described. Finally, the outline of this thesis is presented.

1.1 Inverse problems

Inverse problems deal with determining the internal characteristic(s) of a physical system from the system's output behavior. This is in contrast to *forward problems*, or sometimes called *direct problems*, where one tries to find the output behavior of a physical system given the internal structure thereof. There are several areas of science where inverse problems arise such as electromagnetic scattering, image restoration, computed tomography, remote sensing, acoustics, geophysics, astrometry, *etc*. For example, in x-ray computed tomography, one is interested to find x-ray attenuation coefficients (internal characteristics) within a cross section of the human body (physical system) by scanning the body with narrow x-ray beams and measuring the loss of intensity at detectors placed on the opposite side of the source and outside the body (system's output behavior).

Inverse problems tend to be ill-posed problems in the sense of Hadamard's characterization. In 1923, he introduced three criteria for a problem to be well-posed. Violation of any of these criteria makes the problem ill-posed.

DEFINITION 1.1 Hadamard's three criteria for a well-posed problem.

1. *The solution exists. (Existence)*
2. *The solution is unique. (Uniqueness)*
3. *The solution depends continuously on the given data. (Stability)*

Hadamard thought that ill-posed problems arise when the system under study is not physical or is mathematically modeled in a wrong way. However, nowadays, it is well-known that a correctly-modeled physical problem can be ill-posed. For many practical inverse problems, such as the one considered in this thesis, the existence of a solution is not an issue (given

a reasonable amount of sufficiently accurate measured data) as we usually try to find the internal properties of an *existing* object of interest. The uniqueness and stability then remain as the two main challenges for the solution of inverse problems.

It was in 1963 that Tikhonov introduced his method to treat the ill-posedness of inverse problems. His method, known as Tikhonov regularization, inspired mathematicians to study the theoretical background of inverse problems and develop algorithms to treat their ill-posedness.

1.2 Electromagnetic inverse scattering

In electromagnetic inverse scattering, one tries to infer the location, shape and dielectric (or/and magnetic properties) of the Object of Interest (OI) using electromagnetic wave-field measurements collected outside the OI. There are many applications for the electromagnetic inverse scattering problem, including industrial non-destructive testing [2, 3], geophysical surveys [4, 5], through-wall imaging [6] and medical imaging [7, 8]. The common feature between all these applications is that an electromagnetic source irradiates the OI. The interior characteristic of the OI is then to be found from exterior measurements.

Different applications of the electromagnetic inverse scattering problem are mainly distinguished by the frequency of operation and the data collection procedure. Frequencies utilized for this problem range from 1 Hz to optical frequencies. Data collection can also be performed in different ways. For example, to image the earth's shallow interior three different configurations may be used [9, 10]: (*i*) surface methods, (*ii*) borehole (logging) methods and (*iii*) surface-borehole methods. In surface methods, the transmitters/receivers are moved along the earth's surface and probe downward into the earth. In borehole methods, devices called sondes are moved along a hole that is drilled into the earth. The surface-borehole

methods are hybrid methods which place transmitters/receivers both on the surface and in boreholes.

1.3 Microwave tomography

In this thesis, we consider the microwave frequency range. We therefore refer to the electromagnetic inverse scattering problem within this frequency range as microwave tomography (MWT). In MWT, the OI is successively irradiated by some known incident electromagnetic waves originating from different transmitter positions. Due to the difference between the dielectric/magnetic properties of the OI and those of the known background medium, a scattered electromagnetic field, corresponding to each incident field, will arise which is then measured outside the OI and used to find the shape, location and dielectric/magnetic properties of the OI.

There are many applications for MWT, including industrial non-destructive testing [2, 3], medical imaging [7, 8, 11], and through-wall imaging [6]. The medical imaging applications of MWT is of particular interest as it has been demonstrated that MWT can be useful for breast cancer imaging [8, 12, 13], brain imaging [14], diagnosis of lung cancer, bone imaging [15], and the detection of ischemia in different parts of the body [16]. A general review of different biomedical applications of MWT can be found in [17]. The basic idea behind MWT as a biomedical imaging modality lies in the fact that the dielectric properties of the human body are known to vary significantly between a number of tissue types (*e.g.*, fat, bone, muscle) and more importantly, between healthy and malignant tissues [18] over the microwave frequency range. This highlights MWT's great potential as a cancer diagnostic tool. The potential advantages of MWT for biomedical applications are many, including (*i*) its relatively low cost and portability, (*ii*) its use of safe non-ionizing radiation, and (*iii*) its

ability, without contrast agents, to create quantitative images of living tissue as a way of identifying physiological conditions of those tissues. These allow the possibility of early detection of disease via strategic frequent monitoring of tissue. Probably, the main challenge to make MWT a competitive biomedical imaging modality is its lower resolution compared to Magnetic Resonance Imaging (MRI) and x-ray CT.

The MWT problem is mathematically formulated as a nonlinear ill-posed problem. Research on biomedical microwave tomography that has made use of linearizing assumptions about the wave-propagation within the breast shows that using direct-ray and linear scattering models that ignore higher-order effects, while providing some useful qualitative images, cannot quantitatively reconstruct the bulk-electrical parameters [19, 20, 21, 22]. Thus, accurate quantitative MWT requires the use of the full nonlinear formulation. On the other hand, it is well-known that the MWT problem is ill-posed in the sense of Hadamard [23, 24, 25]. Therefore, the solution to the mathematical problem is not guaranteed to be unique for most measurement configurations and does not depend continuously on the measured data (instability) [26]. The ill-posedness is usually treated by employing different regularization techniques.

In most applications and research works, including this thesis, it is assumed that that the OI and the background medium are non-magnetic. Thus, it is only the dielectric profile of the OI which is to be found.[1] The MWT problem can be formulated in the time domain or the frequency domain. In this thesis, we consider the frequency-domain formulation of the MWT problem.

We also define two terms, namely *reconstruction* and *inversion*. These two terms are used interchangeably within this thesis and have the following meaning: "determination of the

[1] It should be noted that the simultaneous determination of the dielectric and magnetic properties of a magnetic OI has been reported, but only in very few publications [27, 28].

shape, location and dielectric properties of the OI using microwave measurements collected outside the OI."

1.4 Outline of the thesis

Most parts of this thesis consist of a summary of the results published in different journals and conference proceedings. The list of these publications has been provided in Appendix A.

In Chapter 2, we provide the notation that is used in this thesis. The mathematical formulation of the MWT problem based on its integral-equation formulation is also presented using operator notation. Using this mathematical formulation, we define the forward and inverse problems associated with MWT.

In Chapter 3, we cast the MWT problem as an optimization problem wherein an appropriate cost-functional is to be minimized. Within this framework, we briefly study two different classes of optimization methods which are distinguished by their use (or, lack of use) of a forward solver.

In Chapter 4, we present the formulation of the Gauss-Newton inversion algorithm without considering any regularization terms. The formulation is first presented in the continuous domain and then the discretized form thereof is introduced.

Chapter 5 completes Chapter 4 by applying different regularization methods to the Gauss-Newton inversion algorithm. These regularization methods are studied and classified into two main categories. We show that these two regularization strategies can be viewed from a single consistent framework. We also consider incorporation of *a priori* information to regularization terms. This chapter ends with introducing an image enhancement technique

to suppress possible spurious oscillations in the final image obtained from the Gauss-Newton inversion method.

In Chapter 6, we compare the Transverse Magnetic (TM) inversion with the Transverse Electric (TE) inversion both in the near-field and the far-field. This includes a comparison of the computational complexity, image quality and convergence rate.

A new contrast source inversion algorithm which uses eigenfunction expansions of the unknowns is presented in Chapter 7 for the reconstruction of the complex dielectric profile inside a circular conductive enclosure. Orthonormal eigenfunction expansions associated with the Helmholtz operator for a homogeneous medium and Dirichlet boundary conditions are used to effectively discretize all the operators in the cost-functional.

In Chapter 8, we present a novel microwave tomography setup wherein several conductive enclosures of different shapes or a rotatable conductive triangular enclosure are used to generate electromagnetic scattering data. For the rotatable conductive enclosure, the data are collected at each static position of the enclosure using a minimal antenna array having as few as only four co-resident elements. The antenna array remains fixed with respect to the target being imaged and only the boundary of the conductive enclosure is rotated.

Chapter 9 provides an overview of two different microwave tomography prototypes currently under development in our research group. Preliminary inversion results are shown with microwave data collected with 24 co-resident antennas. A resolution study based on the results obtained from our microwave tomography system with plexiglass casing is also presented.

In Chapter 10, we conclude this thesis and provide an outline of future work which one might follow.

2

Problem Statement

Pure mathematics is, in its way, the poetry of logical ideas (Albert Einstein[1]).

In this chapter, we present the mathematical formulation of the MWT problem based on the integral-equation formulation of electromagnetic inverse scattering using operator notation. We will also consider the mathematical formulation of the MWT problem using its differential-equation formulation in Chapter 7. Within this thesis, we consider the tomographic[2] configuration where the Object of Interest (OI) can be considered a two-dimensional (2D) object or the imaging is performed on a 2D slice of a three-dimensional (3D) object.

In the framework of 2D inversion algorithms, we consider two different polarizations for illuminating the OI. In the Transverse Magnetic (TM) polarization, the OI is illuminated with the electric field perpendicular to the transverse plane of the OI which is to be imaged.

[1] Letter to the Editor (in a tribute to Emmy Noether), *The New York Times*, May 5, 1935.
[2] Tomography is derived from the Greek word *tomo* which means “a slice”.

In the 2D Transverse Electric (TE) polarization, the OI is illuminated with the electric field in the transverse plane to be imaged. It should be noted that the TE polarization can be studied using a single magnetic field component perpendicular to the cross section which is to be imaged. However, we do not use the magnetic field formulation for the inversion as it has been shown in [29] that the TE inversion using the electric field formulation is more stable and has better performance than that using the magnetic field formulation.

Although researchers have developed full-vectorial 3D inversion algorithms, *e.g.* [30, 27, 31], the 2D inversion algorithms considered in this thesis are also very important because of their use in existing experimental systems. This is due to the fact that current near-field MWT systems have no, or limited, capability of collecting vectorial field data. For example, in the state-of-the-art MWT system developed at Dartmouth College for breast cancer imaging, the data is collected in seven different planes and a 2D TM inversion algorithm is used to invert the data [12]. The usefulness of this 2D TM assumption for biomedical imaging has been verified in [32]. To the best of the author's knowledge, there is currently no near-field TE MWT system or a near-field 3D MWT system capable of collecting all three components of the field.

In this thesis, we consider the microwave tomography problem in the frequency-domain where time-harmonic fields are used to interrogate the OI. Thus, a time factor of $e^{-j\omega t}$ is implicitly assumed where $j^2 = -1$, and symbols ω and t represent the radial frequency of the utilized field and time respectively.[3]

[3] We will later use 't' as an index to show the number of the active transmitter; see Chapter 3.

2.1 Notation

Consider a bounded imaging domain $\mathcal{D} \subset \mathbb{R}^2$ containing a non-magnetic OI and a measurement domain $\mathcal{S} \subset \mathbb{R}^2$ outside of the object of interest (see figure 2.1). We assume that the $x-y$ plane represents $\mathbb{R}^2$. Let $\boldsymbol{p}$, $\boldsymbol{q}$, $\boldsymbol{r}$, and $\boldsymbol{r}'$ denote position vectors in the $x-y$ plane. Throughout this thesis, we assume $\boldsymbol{p} \in \mathcal{S}$ and $\boldsymbol{q} \in \mathcal{D}$. The position vectors $\boldsymbol{r}$ and $\boldsymbol{r}'$ are chosen to be arbitrary vectors in $\mathbb{R}^2$. The imaging domain $\mathcal{D}$ is immersed in a known non-magnetic homogeneous background medium. Therefore, the relative permittivity and the dyadic Green's function of the background medium are known and denoted by ϵ_b and $\bar{\bar{G}}(\boldsymbol{r}, \boldsymbol{r}')$, respectively. The dyadic Green's function represents the point-source solution for the electromagnetic wave equation in the background medium [33]. Denoting the unit vectors along the x, y, and z directions by $\hat{x}$, $\hat{y}$, and $\hat{z}$ respectively, the dyadic Green's function for the background medium, $\bar{\bar{G}}(\boldsymbol{r}, \boldsymbol{r}')$, is given as [34],

$$\bar{\bar{G}}(\boldsymbol{r}, \boldsymbol{r}') = \begin{cases} (\bar{\bar{I}}_2 - \frac{1}{k_b^2} \nabla_{\boldsymbol{r}} \nabla_{\boldsymbol{r}'}) g(\boldsymbol{r}, \boldsymbol{r}') & \text{TE polarization} \\ g(\boldsymbol{r}, \boldsymbol{r}') \hat{z}\hat{z} & \text{TM polarization} \end{cases} \tag{2.1}$$

The wavenumber of the background medium, k_b, can be written as $k_b^2 = \omega^2 \mu_0 \epsilon_0 \epsilon_b$ where μ_0 and ϵ_0 are the permeability and permittivity of free-space. The dyad $\bar{\bar{I}}_2 = \hat{x}\hat{x} + \hat{y}\hat{y}$ is the 2D identity dyad and $g(\boldsymbol{r}, \boldsymbol{r}')$ is the 2D scalar Green's function for the homogeneous background. The 2D scalar Green's function may be written as $g(\boldsymbol{r}, \boldsymbol{r}') = \frac{j}{4} H_0^1 \left(k_b \left| \boldsymbol{r} - \boldsymbol{r}' \right| \right)$ where $H_0^1 (.)$ denotes the zeroth-order Hankel function of the first kind. The symbol ∇ represents the gradient operator which is taken with respect to the subscript coordinates. In contrast to the TM illumination where $\bar{\bar{G}}(\boldsymbol{r}, \boldsymbol{r}')$ consists of only one component, the dyadic Green's function for the TE case consists of four components; namely, $G_{xx}\hat{x}\hat{x}$, $G_{xy}\hat{x}\hat{y}$, $G_{yx}\hat{y}\hat{x}$, and $G_{yy}\hat{y}\hat{y}$.

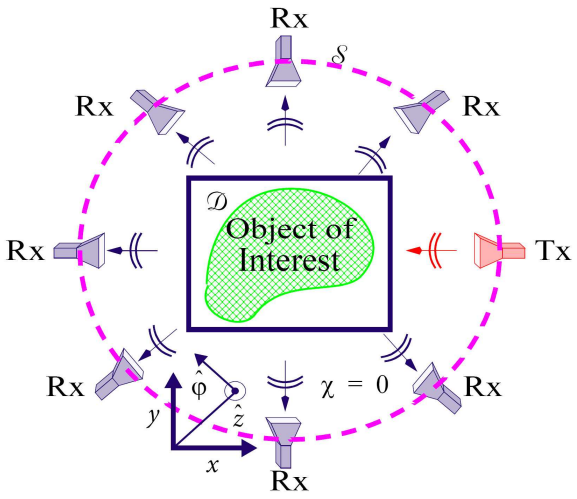

Fig. 2.1: Geometrical model of the microwave tomography problem. Tx and Rx represent the transmitting and receiving antennas respectively. The domain $\mathcal{D}$, which contains the object of interest, is the imaging domain. The domain $\mathcal{S}$, which contains the transmitting and receiving antennas, is the measurement domain and is outside of the object of interest. These two domains are assumed to be in the $x - y$ plane.

To formulate the microwave tomography problem, we define three forms of the electric field: namely the incident, total, and scattered electric field. The incident electric field $\boldsymbol{E}^{\text{inc}}$ is defined as the electric field in the absence of the OI whereas the total electric field $\boldsymbol{E}$ is defined as the electric field in the presence of the OI. The scattered electric field $\boldsymbol{E}^{\text{scat}}$ is then defined as the difference between the total and incident electric fields:

$$\boldsymbol{E}^{\text{scat}} \triangleq \boldsymbol{E} - \boldsymbol{E}^{\text{inc}}. \tag{2.2}$$

The incident electric field can be represented by two rectangular components in the TE case, and only one component in the TM case. That is,

$$\boldsymbol{E}^{\text{inc}} = \begin{cases} E_x^{\text{inc}}\hat{x} + E_y^{\text{inc}}\hat{y} & \text{TE polarization} \\ E_z^{\text{inc}}\hat{z} & \text{TM polarization} \end{cases} \tag{2.3}$$

It should be noted that the 2D assumption means that when the OI is illuminated by TM

waves, the total and scattered electric fields will also only have a $\hat{z}$ component. On the other hand, when the OI is illuminated by TE waves, the total and scattered electric fields will only have $\hat{x}$ and $\hat{y}$ components. As the formulation of the problem within this thesis is based on the electric field (not magnetic field), we will refer to *electric field* as just *field* when there is no ambiguity.

The complex electric contrast function is defined as

$$\chi(\boldsymbol{q}) \triangleq \frac{\epsilon_r(\boldsymbol{q}) - \epsilon_b}{\epsilon_b} \tag{2.4}$$

where $\epsilon_r(\boldsymbol{q})$ is the relative complex permittivity at the point $\boldsymbol{q} \in \mathcal{D}$. In general, these permittivities are complex so as to model lossy materials. The relative complex permittivity of the OI may then be written as

$$\epsilon_r(\boldsymbol{q}) = \epsilon'(\boldsymbol{q}) + j\epsilon''(\boldsymbol{q}) = \epsilon'(\boldsymbol{q}) + j\frac{\sigma(\boldsymbol{q})}{\omega\epsilon_0} \tag{2.5}$$

where $\epsilon'(\boldsymbol{q})$ and $\sigma(\boldsymbol{q})$ represent the (real) relative permittivity and the conductivity of the OI at the angular frequency ω respectively. The unknown to be determined is taken to be either the contrast or the relative complex permittivity of the OI.

2.2 Operator definition

We denote the L^2 space of complex vectorial functions defined on $\mathcal{D}$ by $L^2(\mathcal{D})$ and the L^2 space of complex vectorial functions defined on $\mathcal{S}$ by $L^2(\mathcal{S})$. The norm and inner product on $L^2(\mathcal{D})$ and $L^2(\mathcal{S})$ are defined as

$$\|\boldsymbol{X}\|_{\mathcal{D}} = \langle \boldsymbol{X}, \boldsymbol{X} \rangle_{\mathcal{D}}^{1/2} \text{ and } \langle \boldsymbol{X}_1, \boldsymbol{X}_2 \rangle_{\mathcal{D}} = \int_{\mathcal{D}} \boldsymbol{X}_1(\boldsymbol{q}) \cdot \boldsymbol{X}_2^*(\boldsymbol{q}) d\boldsymbol{q} \tag{2.6}$$

and

$$\|\boldsymbol{Y}\|_{\mathcal{S}} = \langle \boldsymbol{Y}, \boldsymbol{Y} \rangle_{\mathcal{S}}^{1/2} \text{ and } \langle \boldsymbol{Y}_1, \boldsymbol{Y}_2 \rangle_{\mathcal{S}} = \int_{\mathcal{S}} \boldsymbol{Y}_1(\boldsymbol{p}) \cdot \boldsymbol{Y}_2^*(\boldsymbol{p}) d\boldsymbol{p} \tag{2.7}$$

where the superscript $*$ denotes the complex conjugate operator and ' $\cdot$ ' represents the dot-product. The L^2 space of complex scalar functions defined on $\mathcal{D}$ are also denoted by $L^2(\mathcal{D})$ with the norm and inner product defined as

$$\|x\|_{\mathcal{D}} = \langle x, x \rangle_{\mathcal{D}}^{1/2} \text{ and } \langle x_1, x_2 \rangle_{\mathcal{D}} = \int_{\mathcal{D}} x_1(\boldsymbol{q}) x_2^*(\boldsymbol{q}) d\boldsymbol{q}. \tag{2.8}$$

Assuming $\boldsymbol{\Psi} \in L^2(\mathcal{D})$, we define the linear operator $\mathcal{G}_{\mathcal{S}} : L^2(\mathcal{D}) \rightarrow L^2(\mathcal{S})$ as

$$\mathcal{G}_{\mathcal{S}}(\boldsymbol{\Psi}) = k_b^2 \int_{\mathcal{D}} \bar{\bar{G}}(\boldsymbol{p}, \boldsymbol{q}) \cdot \boldsymbol{\Psi}(\boldsymbol{q}) d\boldsymbol{q}, \tag{2.9}$$

and the linear operator $\mathcal{G}_{\mathcal{D}} : L^2(\mathcal{D}) \rightarrow L^2(\mathcal{D})$ as

$$\mathcal{G}_{\mathcal{D}}(\boldsymbol{\Psi}) = k_b^2 \int_{\mathcal{D}} \bar{\bar{G}}(\boldsymbol{q}, \boldsymbol{q}') \cdot \boldsymbol{\Psi}(\boldsymbol{q}') d\boldsymbol{q}'. \tag{2.10}$$

Both integrals, (2.9) and (2.10), are taken over the domain $\mathcal{D}$, but $\mathcal{G}_{\mathcal{S}}(\boldsymbol{\Psi}) \in L^2(\mathcal{S})$ and $\mathcal{G}_{\mathcal{D}}(\boldsymbol{\Psi}) \in L^2(\mathcal{D})$.

Assuming $\boldsymbol{\Phi} \in L^2(\mathcal{D})$ and $\boldsymbol{\Gamma} \in L^2(\mathcal{S})$, the adjoint operators $\mathcal{G}_{\mathcal{S}}^a : L^2(\mathcal{S}) \rightarrow L^2(\mathcal{D})$ and $\mathcal{G}_{\mathcal{D}}^a : L^2(\mathcal{D}) \rightarrow L^2(\mathcal{D})$ (the superscript 'a' denotes the adjoint operator) are defined using the following relations

$$\langle \boldsymbol{\Gamma}, \mathcal{G}_{\mathcal{S}}(\boldsymbol{\Psi}) \rangle_{\mathcal{S}} = \langle \mathcal{G}_{\mathcal{S}}^a(\boldsymbol{\Gamma}), \boldsymbol{\Psi} \rangle_{\mathcal{D}}, \tag{2.11}$$

$$\langle \boldsymbol{\Phi}, \mathcal{G}_{\mathcal{D}}(\boldsymbol{\Psi}) \rangle_{\mathcal{D}} = \langle \mathcal{G}_{\mathcal{D}}^a(\boldsymbol{\Phi}), \boldsymbol{\Psi} \rangle_{\mathcal{D}}. \tag{2.12}$$

Using (2.9), (2.10), (2.11) and (2.12), it is straightforward to show that

$$\mathcal{G}_{\mathcal{S}}^{a}(\mathbf{\Gamma}) = (k_b^2)^* \int_{\mathcal{S}} \bar{\bar{G}}^*(\boldsymbol{q}, \boldsymbol{p}) \cdot \mathbf{\Gamma}(\boldsymbol{p}) d\boldsymbol{p}, \tag{2.13}$$

$$\mathcal{G}_{\mathcal{D}}^{a}(\mathbf{\Phi}) = (k_b^2)^* \int_{\mathcal{D}} \bar{\bar{G}}^*(\boldsymbol{q}, \boldsymbol{q}') \cdot \mathbf{\Phi}(\boldsymbol{q}') d\boldsymbol{q}'. \tag{2.14}$$

We also define the linear operator $\mathcal{G}_{\mathcal{D}}^{\varphi} : L^2(\mathcal{D}) \rightarrow L^2(\mathcal{D})$ as

$$\mathcal{G}_{\mathcal{D}}^{\varphi}(\mathbf{\Psi}) = k_b^2 \int_{\mathcal{D}} \bar{\bar{G}}(\boldsymbol{q}, \boldsymbol{q}') \cdot \mathbf{\Psi}(\boldsymbol{q}') \varphi(\boldsymbol{q}') d\boldsymbol{q}', \tag{2.15}$$

where the scalar function φ is in $L^2(\mathcal{D})$. It is also straightforward to show that $(\mathcal{G}_{\mathcal{D}}^{\varphi})^a = \varphi^* \mathcal{G}_{\mathcal{D}}^{a}$ where $\mathcal{G}_{\mathcal{D}}^{a}$ is given in (2.14).

2.3 Formulation of the problem

In this section, we first present two important equations of the electromagnetic scattering problem, namely the data and domain equations, using the operators defined in Section 2.2. The derivation of these equations can be found in [35]. Based on these two equations, we will define the forward and inverse scattering problems.

2.3.1 Data and domain equations

The scattered electric field on the measurement domain $\mathcal{S}$ due to a contrast function χ and an incident field $\boldsymbol{E}^{\text{inc}}$ can be written as

$$\boldsymbol{E}^{\text{scat}}(\boldsymbol{p}) = \mathcal{G}_{\mathcal{S}}(\chi \boldsymbol{E}). \tag{2.16}$$

This equation is usually referred as the *data equation*. The total electric field, $\boldsymbol{E}$, within the imaging domain $\mathcal{D}$, can be found via

$$\boldsymbol{E}(\boldsymbol{q}) = \boldsymbol{E}^{\text{inc}}(\boldsymbol{q}) + \mathcal{G}_{\mathcal{D}}(\chi \boldsymbol{E}). \tag{2.17}$$

This equation is usually referred as the *domain equation*. Note that the domain equation governs the wave process within the imaging domain $\mathcal{D}$ whereas the data equation gives the scattered field on $\mathcal{S}$ for a given contrast function and total field inside $\mathcal{D}$.

Using the operator defined in (2.15), the domain equation may be re-written as

$$\left(\mathcal{I} - \mathcal{G}_{\mathcal{D}}^{\chi}\right)(\boldsymbol{E}) = \boldsymbol{E}^{\text{inc}}(\boldsymbol{q}) \tag{2.18}$$

where $\mathcal{I}$ denotes the identity operator. Therefore, the total field inside the imaging domain $\mathcal{D}$ can be written as

$$\boldsymbol{E}(\boldsymbol{q}) = \mathcal{E}(\chi) = (\mathcal{I} - \mathcal{G}_{\mathcal{D}}^{\chi})^{-1}(\boldsymbol{E}^{\text{inc}}) \tag{2.19}$$

where $\mathcal{E}$ is a mapping from $L^2(\mathcal{D})$ to $L^2(\mathcal{D})$ and the superscript '-1' denotes the inverse operator.

Using (2.19), equation (2.16) can be re-written as

$$\boldsymbol{E}^{\text{scat}}(\boldsymbol{p}) = \mathcal{E}^{\text{scat}}(\chi) = \mathcal{G}_{\mathcal{S}}\left[\chi\left(\mathcal{I} - \mathcal{G}_{\mathcal{D}}^{\chi}\right)^{-1}\left(\boldsymbol{E}^{\text{inc}}\right)\right]. \tag{2.20}$$

As can be seen from (2.20), $\mathcal{E}^{\text{scat}}$ is a nonlinear mapping from $L^2(\mathcal{D})$ to $L^2(\mathcal{S})$.

Based on these equations, we now briefly explain the forward and inverse scattering problems. Although the focus of this thesis is on the inverse scattering problem, the forward scattering problem is also important as solving the inverse scattering problem requires solving several forward scattering problems either explicitly or implicitly.

2.3.2 Forward scattering problem

In the forward problem, the goal is to find the scattered electric field $\boldsymbol{E}^{\text{scat}}$ on the measurement domain $\mathcal{S}$ for a known contrast function χ, which is immersed in a known background, and a given incident field $\boldsymbol{E}^{\text{inc}}$. This can be achieved by first finding the total field $\boldsymbol{E}$ in the imaging domain $\mathcal{D}$ and then calculating the scattered electric field on $\mathcal{S}$ from (2.16). The electric field $\boldsymbol{E}$ within the imaging domain, for known χ and $\boldsymbol{E}^{\text{inc}}$ functions as well as the known operator $\mathcal{G}_{\mathcal{D}}^{\chi}$, may be found by solving the integral equation given in (2.18). This can be accomplished by minimizing the cost–functional $\mathcal{C}^{\text{FWD}} : L^2(\mathcal{D}) \to \mathbb{R}$ over $\boldsymbol{E}$, where

$$\mathcal{C}^{\text{FWD}}(\boldsymbol{E}) = \frac{1}{\left\|\boldsymbol{E}^{\text{inc}}\right\|_{\mathcal{D}}^2}\left\|\boldsymbol{E}^{\text{inc}} - \left(\mathcal{I} - \mathcal{G}_{\mathcal{D}}^{\chi}\right)(\boldsymbol{E})\right\|_{\mathcal{D}}^2. \tag{2.21}$$

This cost-functional can be minimized using numerical techniques such as the Conjugate Gradient (CG) algorithm where the total field at the m^{th} iteration is updated as

$$\boldsymbol{E}_{m+1} = \boldsymbol{E}_m + \beta_m \boldsymbol{d}_m, \tag{2.22}$$

$\boldsymbol{d}_m$ is the conjugate gradient direction and $\beta_m \in \mathbb{R}$ represents its weight. The CG algorithm may be accelerated by the Fast Fourier Transform (FFT) [36, 37] and the marching-on-in-source-position technique [38]. The closed-form expressions for $\boldsymbol{d}_m$ and β_m as well as a brief description of the utilized marching-on-in-source-position technique can be found in Appendix B.

It should be noted that this formulation of the forward scattering problem is based on the integral equation formulation. The forward scattering problem can also be formulated based on the partial differential equation formulation of the scattering problem. In Chapter 8, we have used a forward solver which is based on the partial differential equation formulation of the forward scattering problem.

2.3.3 Inverse scattering problem

In the inverse scattering problem, the goal is to find the electric contrast $\chi(\boldsymbol{q})$ in the imaging domain $\mathcal{D}$ from the field measurements on the measurement domain $\mathcal{S}$. Denoting the measured scattered field on $\mathcal{S}$ by $\boldsymbol{E}^{\text{scat}}_{\text{meas}}(\boldsymbol{p})$ and noting (2.20), the contrast $\chi(\boldsymbol{q})$ is to be found from

$$\boldsymbol{E}^{\text{scat}}_{\text{meas}}(\boldsymbol{p}) = \mathcal{G}_{\mathcal{S}}\left[\chi\left(\mathcal{I} - \mathcal{G}^{\chi}_{\mathcal{D}}\right)^{-1}\left(\boldsymbol{E}^{\text{inc}}\right)\right]. \tag{2.23}$$

It should be noted that the incident electric field $\boldsymbol{E}^{\text{inc}}$ is assumed to be known (or approximately known). However, the operator $\mathcal{G}^{\chi}_{\mathcal{D}}$ is unknown as the contrast χ is unknown. Different methods for solving (2.23) will be discussed in Chapter 3.

3

Microwave Tomography Algorithms

Can one hear the shape of a drum? (Mark Kac [39])

In MWT, which is an inverse scattering problem, the OI is successively interrogated with a number of known incident fields $\boldsymbol{E}_t^{\text{inc}}$, where $t = 1, \cdots, T_x$. Interaction of the incident field $\boldsymbol{E}_t^{\text{inc}}$ with the OI results in the total field $\boldsymbol{E}_t$. The total and incident electric fields are then measured by some receiver antennas located on $\mathcal{S}$. Thus, the scattered electric field, $\boldsymbol{E}_{\text{meas},t}^{\text{scat}}$, is known at the receiver positions on $\mathcal{S}$. The goal is to find the electric contrast χ in a bounded imaging domain $\mathcal{D}$, which contains the OI, from the measured scattered fields $\boldsymbol{E}_{\text{meas},t}^{\text{scat}}$ on $\mathcal{S}$.

Two approaches based on the formulation of the problem using two different cost-functionals have been successfully used to solve the MWT problem. The first approach, which includes the Gauss-Newton Inversion (GNI) method, uses the conventional cost-functional which is

based on the difference between the measured and predicted scattered data for a particular choice of the material parameters; see for example [40, 41, 42, 30, 43, 12, 4, 44, 45, 46]. The conventional cost-functional is usually augmented by an appropriate regularization term. The second approach, which includes the Modified Gradient Method (MGM) [47] and the Contrast Source Inversion (CSI) method [48], uses the same conventional cost-functional, formulated in terms of the so-called contrast sources, in the case of CSI, added to an error functional involving the domain equation, (2.17), which relates the fields inside the imaging domain to the contrast of the unknown OI. As will be seen, the first approach requires an appropriate solver to solve the forward scattering problem, (2.18), for different incident fields and predicted contrasts. However, the second approach avoids solving the forward scattering problem but requires much more iterations to converge compared to the first approach. These two approaches are now explained.

3.1 The first approach

In this first approach, the MWT problem is formulated as the minimization over χ of the Least-Squares (LS) data misfit cost-functional $\mathcal{C}^{\text{LS}} : L^2(\mathcal{D}) \to \mathbb{R}$,

$$\mathcal{C}^{\text{LS}}(\chi) = \frac{\displaystyle\sum_{t=1}^{T_x} \left\| \boldsymbol{E}_t^{\text{scat}} - \boldsymbol{E}_{\text{meas},t}^{\text{scat}} \right\|_{\mathcal{S}}^2}{\displaystyle\sum_{t=1}^{T_x} \left\| \boldsymbol{E}_{\text{meas},t}^{\text{scat}} \right\|_{\mathcal{S}}^2} = \frac{\displaystyle\sum_{t=1}^{T_x} \left\| \mathcal{E}_t^{\text{scat}}(\chi) - \boldsymbol{E}_{\text{meas},t}^{\text{scat}} \right\|_{\mathcal{S}}^2}{\displaystyle\sum_{t=1}^{T_x} \left\| \boldsymbol{E}_{\text{meas},t}^{\text{scat}} \right\|_{\mathcal{S}}^2} \tag{3.1}$$

where $\boldsymbol{E}_t^{\text{scat}} = \mathcal{E}_t^{\text{scat}}(\chi)$ is the simulated scattered field at the observation points corresponding to the predicted contrast χ and the t^{th} transmitter. The nonlinear operator $\mathcal{E}_t^{\text{scat}} : L^2(\mathcal{D}) \to L^2(\mathcal{S})$ is given in (2.20) where $\boldsymbol{E}^{\text{inc}}$ needs to be replaced by $\boldsymbol{E}_t^{\text{inc}}$. Using (2.20), the above

cost-functional can be re-written as

$$\mathcal{C}^{\mathrm{LS}}(\chi) = \frac{\sum_{t=1}^{T_x} \left\| \mathcal{G}_{\mathcal{S}} \left[\chi \left(\mathcal{I} - \mathcal{G}_{\mathcal{D}}^{\chi} \right)^{-1} \left(\boldsymbol{E}_t^{\mathrm{inc}} \right) \right] - \boldsymbol{E}_{\mathrm{meas},t}^{\mathrm{scat}} \right\|_{\mathcal{S}}^2}{\sum_{t=1}^{T_x} \left\| \boldsymbol{E}_{\mathrm{meas},t}^{\mathrm{scat}} \right\|_{\mathcal{S}}^2}. \tag{3.2}$$

This cost-functional is nonlinear with respect to the unknown contrast χ, and is ill-posed [26]. Thus, an appropriate regularization technique needs to be utilized to handle the ill-posedness of the problem.

3.1.1 Born approximation

When the electric contrast or the size of the OI is small, one may use the well-known Born Approximation (BA) to simplify (3.2). This approximation assumes

$$\left(\mathcal{I} - \mathcal{G}_{\mathcal{D}}^{\chi} \right)^{-1} \approx \mathcal{I}, \tag{3.3}$$

which is equivalent to assuming that the total field inside the imaging domain is equal to the incident field inside the imaging domain. Using this approximation, the nonlinear cost–functional $\mathcal{C}^{\mathrm{LS}}$ is linearized as

$$\mathcal{C}^{\mathrm{LS,BA}}(\chi) = \frac{\sum_{t=1}^{T_x} \left\| \mathcal{G}_{\mathcal{S}}(\chi \boldsymbol{E}_t^{\mathrm{inc}}) - \boldsymbol{E}_{\mathrm{meas},t}^{\mathrm{scat}} \right\|_{\mathcal{S}}^2}{\sum_{t=1}^{T_x} \left\| \boldsymbol{E}_{\mathrm{meas},t}^{\mathrm{scat}} \right\|_{\mathcal{S}}^2}. \tag{3.4}$$

The contrast function χ is then be found by minimizing (3.4) over χ. Although now linear, this remains an ill-posed problem.

Another popular approximation is the Rytov approximation [49]. A significant improvement in the Born approximation can be achieved by employing extended Born approximation whose computational cost is very close to that of the Born approximation [50]. It should be noted that the first iteration of most nonlinear microwave tomography algorithms within the first approach, if started with the zero initial guess, such as the ones presented in Sections 3.1.2 and 3.1.3, results in a predicted contrast which is equivalent to the contrast obtained via Born approximation.

3.1.2 The Born iterative method

The Born Iterative Method (BIM) [51] iteratively updates the contrast χ based on better approximations of the total field inside the imaging domain. At the n^{th} iteration of the BIM, the operator $(\mathcal{I} - \mathcal{G}_{\mathcal{D}}^{\chi})^{-1}$ is approximated as

$$(\mathcal{I} - \mathcal{G}_{\mathcal{D}}^{\chi})^{-1} \approx (\mathcal{I} - \mathcal{G}_{\mathcal{D}}^{\chi_n})^{-1} \tag{3.5}$$

where χ_n is the contrast obtained at the previous iteration of the BIM. The contrast at the n^{th} iteration of the BIM is found by minimizing the cost-functional $\mathcal{C}^{\text{LS,BIM}}(\chi)$:

$$\chi_{n+1} = \arg\min_{\chi} \left\{ \mathcal{C}^{\text{LS,BIM}}(\chi) \right\} = \arg\min_{\chi} \left\{ \frac{\sum_{t=1}^{T_x} \left\| \mathcal{G}_{\mathcal{S}} \left[\chi \left(\mathcal{I} - \mathcal{G}_{\mathcal{D}}^{\chi_n} \right)^{-1} \left(\boldsymbol{E}_t^{\text{inc}} \right) \right] - \boldsymbol{E}_{\text{meas},t}^{\text{scat}} \right\|_{\mathcal{S}}^2}{\sum_{t=1}^{T_x} \left\| \boldsymbol{E}_{\text{meas},t}^{\text{scat}} \right\|_{\mathcal{S}}^2} \right\}. \tag{3.6}$$

Due to the ill-posedness of the problem, the above cost-functional needs to be regularized before minimization. We have studied the regularization of (3.6) in the framework of Tikhonov regularization in conjunction with the Normalized Cumulative Periodogram (NCP) regular-

ization parameter-choice method to determine an appropriate regularization weight [52, 53]. The initial guess of the BIM algorithm is usually chosen to be $\chi_1 = 0$. In this case, the first iteration of the BIM is equivalent to the contrast obtained under the Born approximation. Note that at each iteration of the BIM, a forward solver needs to be called to calculate $(\mathcal{I} - \mathcal{G}_{\mathcal{D}}^{\chi_n})^{-1} \left(\boldsymbol{E}_t^{\text{inc}}\right)$ for different incident fields.

3.1.3 Various Newton-type algorithms

In Newton-type algorithms, the nonlinear cost-functional $\mathcal{C}^{\text{LS}}(\chi)$, which is usually augmented by some regularization terms, is iteratively approximated with a quadratic form at the contrast obtained from the previous iteration. The stationary point of the quadratic model, or some approximation thereof, is then chosen as the next iterate. The contrast at the n^{th} iteration is updated as

$$\chi_{n+1} = \chi_n + \nu_n \Delta\chi_n. \tag{3.7}$$

where $\Delta\chi_n$ is the correction and $\nu_n \in \mathbb{R}^+$ is an appropriate step-length to enforce the reduction of the cost-functional. Some of the utilized Newton-type inversion algorithms include the Newton-Kantorovich (NK) [54], Distorted Born Iterative Method (DBIM) [40, 55], Gauss-Newton Inversion (GNI) [56, 57, 58, 59, 4, 30], quasi-Newton method [42], Levenberg-Marquardt method [46] and the modified Newton method [45]. It can be shown that some of these methods are equivalent if utilizing similar regularization techniques [60, 58].

As for the BIM, it can be shown that these techniques effectively attempt to approximate the operator $(\mathcal{I} - \mathcal{G}_{\mathcal{D}}^{\chi})^{-1}$. Within this class of inversion algorithms, the GNI method and the DBIM have been used in the research presented here. The GNI method will be explained in Chapter 4. The regularization methods in conjunction with the GNI method are studied

in Chapter 5. Our specific implementation of the DBIM, which we refer to as the enhanced DBIM, is outlined in [55], but is not considered herein.

3.1.4 Global optimization techniques

Some global optimization techniques such as genetic algorithms [43] and simulated annealing [61], in conjunction with Tikhonov regularization, have also been used to minimize the nonlinear cost-functional $\mathcal{C}^{\mathrm{LS}}(\chi)$. A thorough overview of different stochastic optimization methods applied to the MWT problem is provided in [62]. The computational complexity of these methods is much more than that of the local optimization techniques. Thus, these methods, in their current state of development, may not be appropriate for this computationally-demanding problem. They are not considered in this thesis.

3.2 The second approach

The first approach formulates the optimization problem in terms of the unknown contrast. However, these methods require the solution to several forward scattering problems., which means applying $(\mathcal{I} - \mathcal{G}_{\mathcal{D}}^{\chi_n})^{-1}$ on the incident fields originating from different transmitters. This step imposes a large computational burden on the algorithm.

In the second approach, the optimization problem is formulated in terms of the unknown contrast and the unknown total fields (or the unknown contrast sources which will be explained below). Noting that the total field inside the imaging domain changes with respect to each transmitter, the number of unknown quantities can become extremely large. However, using this formulation the solution to the forward scattering problem is avoided.

Two different updating schemes within this approach have been suggested. In the first scheme [63], the contrast and the total fields corresponding to each transmitter are updated simultaneously (as one unknown vector in the discrete domain). In the second scheme, *e.g.*, see [47, 48], the contrast and the total fields (or the contrast sources) are treated separately. That is, when optimizing over the total fields (or the contrast sources), the contrast is assumed to be known and when optimizing over the contrast, the total fields (or the contrast sources) are assumed to be known. The Modified Gradient Method (MGM) [47] and the Contrast Source Inversion (CSI) method [48] are the two well-known methods within the second updating scheme. As the CSI method is more computationally efficient than the existing methods within this approach [64], we briefly explain the CSI method for this class of inversion algorithms.

The CSI method formulates the MWT problem in terms of the contrast χ and contrast sources, defined as $\boldsymbol{W}(\boldsymbol{q}) = \chi(\boldsymbol{q})\boldsymbol{E}(\boldsymbol{q})$. Multiplying both sides of (2.17) by the contrast function, we have

$$\boldsymbol{W} = \chi \boldsymbol{E}^{\text{inc}} + \chi \mathcal{G}_{\mathcal{D}}(\boldsymbol{W}). \tag{3.8}$$

The data equation (2.16) is re-written as,

$$\boldsymbol{E}^{\text{scat}} = \mathcal{G}_{\mathcal{S}}(\boldsymbol{W}). \tag{3.9}$$

In the CSI method the cost-functional, $\mathcal{C}^{\text{CSI}} : L^2(\mathcal{D}) \times L^2(\mathcal{D})^{T_x} \rightarrow \mathbb{R}$,

$$\mathcal{C}^{\text{CSI}}(\chi, \boldsymbol{W}_1, \cdots, \boldsymbol{W}_t, \cdots, \boldsymbol{W}_{T_x}) = \frac{\sum_{t=1}^{T_x} \left\| \boldsymbol{E}^{\text{scat}}_{\text{meas},t} - \mathcal{G}_{\mathcal{S}}(\boldsymbol{W}_t) \right\|^2_{\mathcal{S}}}{\sum_{t=1}^{T_x} \left\| \boldsymbol{E}^{\text{scat}}_{\text{meas},t} \right\|^2_{\mathcal{S}}} + \frac{\sum_{t=1}^{T_x} \left\| \chi \boldsymbol{E}^{\text{inc}}_t - \boldsymbol{W}_t + \chi \mathcal{G}_{\mathcal{D}}(\boldsymbol{W}_t) \right\|^2_{\mathcal{D}}}{\sum_{t=1}^{T_x} \left\| \chi \boldsymbol{E}^{\text{inc}}_t \right\|^2_{\mathcal{D}}} \tag{3.10}$$

is minimized via the formation of two interlaced sequences of the unknowns: a sequence of estimates of the contrast $\{\chi_n(\boldsymbol{q})\}$ which is interlaced with a sequence of estimates of the contrast sources $\{\boldsymbol{W}_{t,n}(\boldsymbol{q})\}$. For every step of the CSI method, each sequence is updated via a single step of the CG minimization algorithm while assuming that the other unknown is a constant. We note that the first term of the CSI functional deals with (3.9) in which $\boldsymbol{E}^{\text{scat}}$ is replaced by $\boldsymbol{E}^{\text{scat}}_{\text{meas}}$ whereas the second term incorporates (3.8). The CSI method is usually regularized with the weighted L^2-norm total variation multiplicative regularizer [11]. The inversion method is then referred as the MR-CSI method.

It should be noted that MGM is very similar to the CSI method. In the MGM, the fields and the contrast are updated as opposed to the contrast sources and the contrast in the CSI method. In addition, the Born and the extended Born approximations can also be formulated within the framework of the CSI algorithm [65, 66]. We will consider the CSI formulation of the MWT problem in Chapter 7.

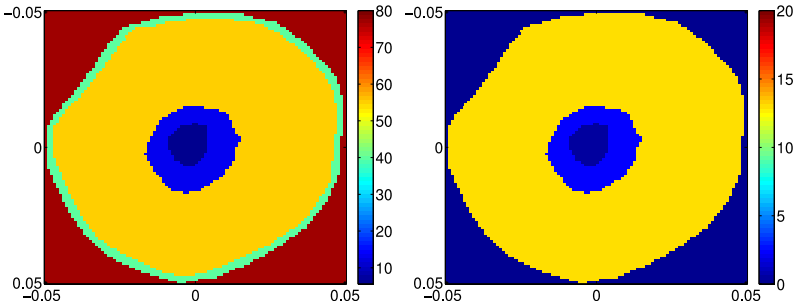

(a) $Re(\epsilon_r)$ True (b) $Im(\epsilon_r)$ True

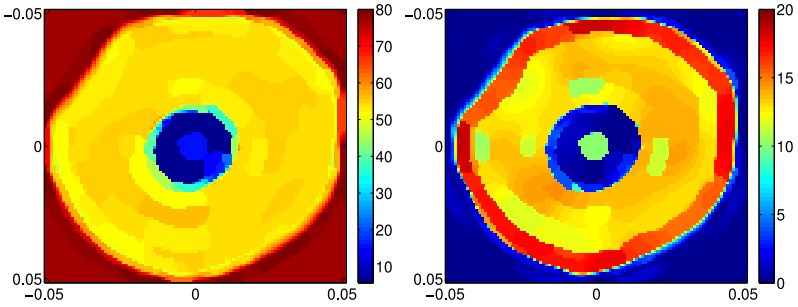

(c) $Re(\epsilon_r)$ MR-CSI (d) $Im(\epsilon_r)$ MR-CSI

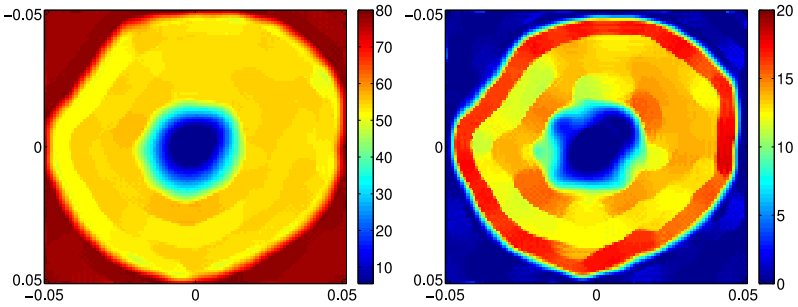

(e) $Re(\epsilon_r)$ Enhanced DBIM (f) $Im(\epsilon_r)$ Enhanced DBIM

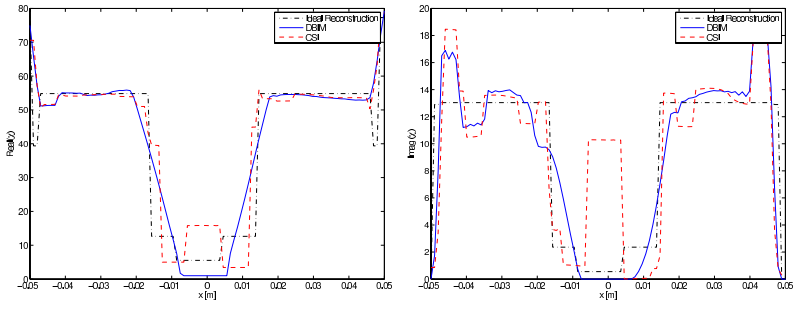

(g) $Re(\epsilon_r)$ Cross Section (h) $Im(\epsilon_r)$ Cross Section

Fig. 3.1: Synthetic leg data set (TM illumination). (a)-(b) The exact relative complex permittivities, (c)-(d) the MR-CSI reconstruction, (e)-(f) the enhanced DBIM reconstruction, and (g)-(h) 2D cross section along $y = 0$ of the ideal (black dash-dot line), MR-CSI (red dashed line) and DBIM (blue solid line). The frequency used was $f = 1.5$ GHz.

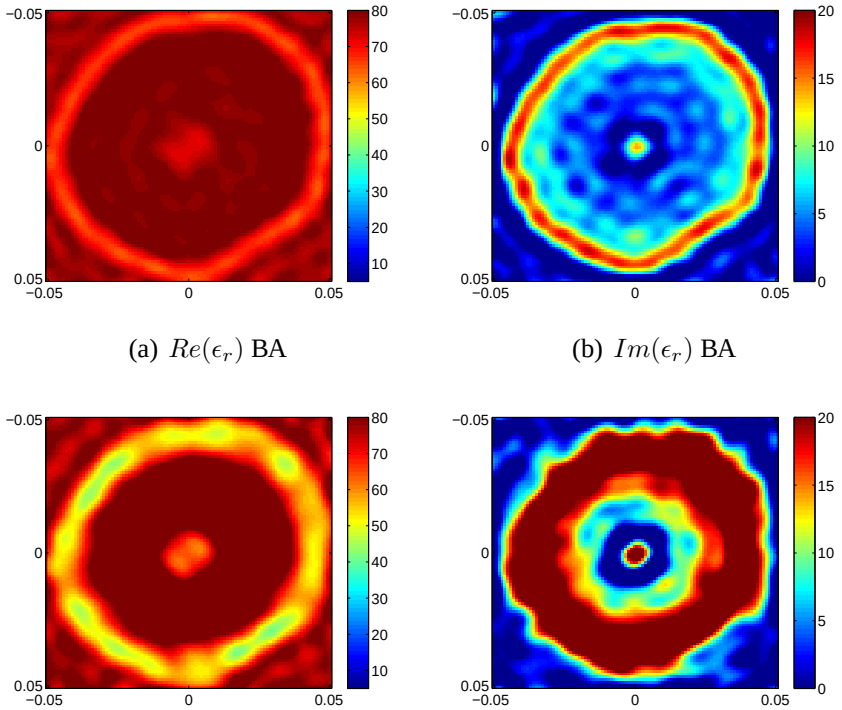

(a) $Re(\epsilon_r)$ BA (b) $Im(\epsilon_r)$ BA

(c) $Re(\epsilon_r)$ BIM (d) $Im(\epsilon_r)$ BIM

Fig. 3.2: Synthetic leg data set (TM illumination). (a)-(b) Born approximation reconstruction, and (c)-(d) the BIM reconstruction. The frequency used was $f = 1.5$ GHz.

3.3 Inversion results

As in the rest of this thesis, we will not consider the Born approximation and the BIM, it is instructive to compare their performances with two state-of-the-art algorithms, namely the MR-CSI method and the enhanced DBIM. The details of the enhanced DBIM are outlined in [55].

While the ultimate test of any inversion algorithm must involve experimentally collected scattering data, it is very useful for comparison purposes to have a synthetic data set where the true contrast is known. Towards this end, we have created a synthetic model of a leg, shown in figure 3.1 (a)-(b). Permittivity values for the model were taken from published

values on human tissue [67]. The model consists of a bone (comprised of a marrow core, $\epsilon_r = 5.5 + j0.55$ surrounded by cortical bone, $\epsilon_r = 12.6 + j2.4$), which is inside of a large mass of muscle ($\epsilon_r = 54.8 + j13.0$), surrounded by skin ($\epsilon_r = 39.4 + j12.9$). Data were generated for the model based on a frequency of 1.5 GHz, with 30 transmitters and 30 receivers evenly spaced on a circle of radius 15 cm. The forward solver utilized a grid of 100×100 cells on a 10 cm $\times$ 10 cm grid. The inversions were performed on a grid of 100×100 cells on a 10.2 cm $\times$ 10.2 cm grid (thus, avoiding the so-called inverse crime [68]). The 'leg' is immersed in a lossless background medium with $\epsilon_b = 77.3$. To every measurement, 3% noise was artificially added using the formula given in [65].

The MR-CSI reconstruction is shown in figure 3.1 (c)-(d), and the enhanced DBIM reconstruction is given in figure 3.1 (e)-(f). A 2D cross section of the $y = 0$ line for all three plots is shown in figure 3.1 (g)-(h). The two reconstructions are remarkably similar, which can be seen particularly clearly in the 2D cross section plots. Neither algorithm accurately resolves the skin, which is not surprising because the skin is approximately 1.5 mm, or $\approx (1/20)$ of the wavelength in the background medium. The only significant differences between the two results are in the marrow core of the bone, where the CSI seems to 'find' an inhomogeneity associated with the marrow bone, while the DBIM reconstruction provides only a smooth region for the whole bone. However, the permittivity value obtained by the CSI method for the marrow bone is not correct, whereas the DBIM reconstruction for the marrow bone is closer the true value. In [55], we have compared the performance of these two methods over a wide range of data sets: noisy synthetic data, free-space far-field data, and near-field water-submerged data. In these cases, the inversion results were remarkably similar.

The inversion of this data set using the Born approximation and the BIM are shown in figure 3.2. As can be seen, these two methods fail to accurately reconstruct the synthetic leg model.

4

The Gauss-Newton Inversion Algorithm

I keep the subject constantly before me and wait till the first dawning open little by little into the full light (Isaac Newton[1]).

As mentioned in Chapter 3, the data misfit cost-functional (3.1) is nonlinear with respect to the contrast χ. To treat the nonlinearity of the problem, iterative techniques are used. In this chapter, we present the mathematical formulation of one of these iterative techniques, namely, the Gauss-Newton Inversion (GNI) method. As for most iterative algorithms for the MWT problem, this inversion algorithm requires that appropriate regularization techniques be used. These will be discussed in Chapter 5.

The GNI method is based on the Newton optimization [69] where the nonlinear cost-functional at the current iteration is approximated with a quadratic form. The stationary

[1] in *Newton Tercentenary Celebrations*, July 15-19, 1946 by The Royal Society of London for the Improvement of Natural Knowledge.

point of the quadratic model is then chosen as the next iterate. In GNI, the cost-functional is the data misfit $\mathcal{C}^{\mathrm{LS}}(\chi)$, (3.1), which is usually augmented by an appropriate regularization term. To describe the general formulation of the GNI method, we denote the cost-functional $\mathcal{C}(\chi) : L^2(\mathcal{D}) \to \mathbb{R}$ to be either the data misfit cost-functional $\mathcal{C}^{\mathrm{LS}}(\chi)$ or a regularized form thereof.

The cost-functional $\mathcal{C}(\chi)$ is not analytic in the complex domain; thus, it is not complex differentiable. To handle this problem, we use Wirtinger calculus [70, 71, 72, 73] where we consider the cost-functional $\tilde{\mathcal{C}}(\chi, \chi^*)$ such that $\tilde{\mathcal{C}}(\chi, \chi^*) = \mathcal{C}(\chi)$ (see Appendix C for more discussion). Therefore, minimizing $\mathcal{C}(\chi)$ will be equivalent to minimizing $\tilde{\mathcal{C}}(\chi, \chi^*)$. According to Wirtinger calculus, $\tilde{\mathcal{C}}(\chi, \chi^*)$ is analytic with respect to χ for fixed χ^* and is analytic with respect to χ^* for fixed χ. Therefore, one can formally define the derivatives of $\tilde{\mathcal{C}}$ with respect to χ and χ^* by treating them as two independent functions. Therefore, at the n^{th} iteration of the GNI algorithm, where the known predicted contrast is χ_n, $\mathcal{C}(\chi_n + \Delta\chi_n)$ may be approximated by the quadratic model

$$\mathcal{C}(\chi_n) + \begin{pmatrix} \frac{\partial \tilde{\mathcal{C}}}{\partial \chi}|_{\chi=\chi_n} \\ \frac{\partial \tilde{\mathcal{C}}}{\partial \chi^*}|_{\chi=\chi_n} \end{pmatrix}^T \begin{pmatrix} \Delta\chi_n \\ \Delta\chi_n^* \end{pmatrix} + \frac{1}{2} \left[\begin{pmatrix} \frac{\partial^2 \tilde{\mathcal{C}}}{\partial \chi \partial \chi}|_{\chi=\chi_n} & \frac{\partial^2 \tilde{\mathcal{C}}}{\partial \chi \partial \chi^*}|_{\chi=\chi_n} \\ \frac{\partial^2 \tilde{\mathcal{C}}}{\partial \chi^* \partial \chi}|_{\chi=\chi_n} & \frac{\partial^2 \tilde{\mathcal{C}}}{\partial \chi^* \partial \chi^*}|_{\chi=\chi_n} \end{pmatrix} \begin{pmatrix} \Delta\chi_n \\ \Delta\chi_n^* \end{pmatrix} \right]^T \begin{pmatrix} \Delta\chi_n \\ \Delta\chi_n^* \end{pmatrix}, \tag{4.1}$$

where the superscript 'T' denotes the transposition operator. The correction $\Delta\chi_n$ is found for the minimum of the quadratic model, (4.1). Thus, the correction satisfies

$$\begin{pmatrix} \frac{\partial^2 \tilde{\mathcal{C}}}{\partial \chi \partial \chi}|_{\chi=\chi_n} & \frac{\partial^2 \tilde{\mathcal{C}}}{\partial \chi \partial \chi^*}|_{\chi=\chi_n} \\ \frac{\partial^2 \tilde{\mathcal{C}}}{\partial \chi^* \partial \chi}|_{\chi=\chi_n} & \frac{\partial^2 \tilde{\mathcal{C}}}{\partial \chi^* \partial \chi^*}|_{\chi=\chi_n} \end{pmatrix} \begin{pmatrix} \Delta\chi_n \\ \Delta\chi_n^* \end{pmatrix} = - \begin{pmatrix} \frac{\partial \tilde{\mathcal{C}}}{\partial \chi}|_{\chi=\chi_n} \\ \frac{\partial \tilde{\mathcal{C}}}{\partial \chi^*}|_{\chi=\chi_n} \end{pmatrix}. \tag{4.2}$$

The contrast is then updated as $\chi_{n+1} = \chi_n + \nu_n \Delta\chi_n$ where the step-length ν_n will be explained in Section 4.3. Note that $\frac{\partial \tilde{\mathcal{C}}}{\partial \chi}|_{\chi=\chi_n}$ and $\frac{\partial \tilde{\mathcal{C}}}{\partial \chi^*}|_{\chi=\chi_n}$, which represent linear mappings

from $L^2(\mathcal{D})$ to $\mathbb{C}$, are the derivatives of $\tilde{\mathcal{C}}(\chi)$ with respect to χ and χ^* at $\chi = \chi_n$. Thus, $\frac{\partial \tilde{\mathcal{C}}}{\partial \chi}|_{\chi=\chi_n}(\Delta\chi_n)$ is the result of operating $\frac{\partial \tilde{\mathcal{C}}}{\partial \chi}|_{\chi=\chi_n} : L^2(\mathcal{D}) \to \mathbb{C}$ on $\Delta\chi_n \in L^2(\mathcal{D})$. The second-order derivatives in (4.1) are linear mappings from $L^2(\mathcal{D})$ to $\mathcal{Z}$ where $\mathcal{Z}$ is the space of all linear operators from $L^2(\mathcal{D})$ to $\mathbb{C}$.

As the cost-functional $\tilde{\mathcal{C}}$ involves the data misfit cost-functional $\mathcal{C}^{\text{LS}}$ which requires the operator $\mathcal{E}^{\text{scat}}$, the derivative operators in (4.2) will all be dependent on the derivatives of $\mathcal{E}^{\text{scat}}$ with respect to the contrast. The approximation within the GNI method is that the derivative operators required in (4.2) are calculated by ignoring the second derivative of $\mathcal{E}^{\text{scat}}$, (2.20), with respect to the contrast; thus, avoiding its computational cost. That is, the scattered field due to the contrast $\chi_n + \Delta\chi_n$ is approximated by the first two terms of the Taylor's expansion [30],

$$\mathcal{E}^{\text{scat}}(\chi_n + \Delta\chi_n) \approx \mathcal{E}^{\text{scat}}(\chi_n) + \frac{\partial \mathcal{E}^{\text{scat}}}{\partial \chi}|_{\chi=\chi_n}(\Delta\chi_n). \tag{4.3}$$

The operator $\frac{\partial \mathcal{E}^{\text{scat}}}{\partial \chi}|_{\chi=\chi_n}$, which is a linear mapping from $L^2(\mathcal{D})$ to $L^2(\mathcal{S})$, is the derivative of $\mathcal{E}^{\text{scat}}$ with respect to χ at $\chi = \chi_n$. Thus, $\frac{\partial \mathcal{E}^{\text{scat}}}{\partial \chi}|_{\chi=\chi_n}(\Delta\chi_n)$ is the result of operating $\frac{\partial \mathcal{E}^{\text{scat}}}{\partial \chi}|_{\chi=\chi_n} : L^2(\mathcal{D}) \to L^2(\mathcal{S})$ on $\Delta\chi_n \in L^2(\mathcal{D})$.

As will be seen in Section 4.1.2, when $\mathcal{C}(\chi)$ is chosen to be $\mathcal{C}^{\text{LS}}(\chi)$, the operators $\frac{\partial^2 \tilde{\mathcal{C}}}{\partial \chi \partial \chi}|_{\chi=\chi_n}$ and $\frac{\partial^2 \tilde{\mathcal{C}}}{\partial \chi^* \partial \chi^*}|_{\chi=\chi_n}$ are ignored under the approximation (4.3). It should be noted that we will also consider optimizing $\mathcal{C}(\chi)$ over χ_R and χ_I in Sections 5.6.2 and D.5.

4.1 Required derivatives for the non-regularized GNI method

We now show the required derivatives for the Gauss-Newton inversion method for the case when $\mathcal{C}(\chi)$ is chosen to be $\mathcal{C}^{\text{LS}}(\chi)$, (3.1). That is, the cost-functional to be minimized is the data misfit cost-functional, without any regularization terms. Similar to the procedure

explained at the beginning of this chapter, we consider the cost-functional $\tilde{\mathcal{C}}^{\text{LS}}(\chi, \chi^*)$ such that $\tilde{\mathcal{C}}^{\text{LS}}(\chi, \chi^*) = \mathcal{C}^{\text{LS}}(\chi)$. Noting that the derivatives of the data misfit cost-functional are dependent on the derivatives of the scattered field operator, $\mathcal{E}^{\text{scat}}$, we first present the first derivative of $\mathcal{E}^{\text{scat}}$ with respect to the contrast. We then briefly explain why calculating the second derivative of $\mathcal{E}^{\text{scat}}$ with respect to the contrast, which is ignored in the GNI method, is computationally expensive. Finally, the required derivatives of the data misfit cost-functional will be given. The derivation of these derivatives can be found in Appendix D.

In Chapter 5, we will consider the GNI method when the data misfit cost-functional is augmented by some appropriate regularization terms.

4.1.1 Derivative of the scattered field with respect to the contrast

Herein, we assume that the t^{th} transmitter is active. As mentioned earlier, the derivative $\frac{\partial \mathcal{E}_t^{\text{scat}}}{\partial \chi}|_{\chi=\chi_n}$ is a linear operator from $L^2(\mathcal{D})$ to $L^2(\mathcal{S})$. This derivative operator, when operating on ψ, can be written as (see Section D.1)

$$\frac{\partial \mathcal{E}_t^{\text{scat}}}{\partial \chi}|_{\chi=\chi_n}(\psi) = k_b^2 \int_{\mathcal{D}} \psi(\boldsymbol{q}) \boldsymbol{E}_t(\boldsymbol{q}; \chi_n) \cdot \bar{\bar{G}}^{\text{inh}}(\boldsymbol{q}, \boldsymbol{p}; \chi_n) d\boldsymbol{q} \tag{4.4}$$

where ψ is an arbitrary function in $L^2(\mathcal{D})$ and $\bar{\bar{G}}^{\text{inh}}(\boldsymbol{q}, \boldsymbol{p}; \chi_n)$ is the Green's function when the background medium is assumed to be χ_n. This Green's function is sometimes referred to as the distorted or inhomogeneous Green's function with respect to the contrast χ_n. The field $\boldsymbol{E}_t(\boldsymbol{q}; \chi_n)$ is the total field inside the imaging domain $\mathcal{D}$ in the presence of χ_n when the t^{th} transmitter is active.

As will be seen, the GNI algorithm also requires the adjoint of $\frac{\partial \mathcal{E}_t^{\text{scat}}}{\partial \chi}|_{\chi=\chi_n}$. Assuming $\boldsymbol{\Gamma}$ is an

arbitrary vector function in $L^2(\mathcal{S})$, the adjoint operator may be written as

$$\left(\frac{\partial \mathcal{E}_t^{\text{scat}}}{\partial \chi}|_{\chi=\chi_n}\right)^a (\mathbf{\Gamma}) = \left(k_b^2\right)^* \left[\boldsymbol{E}_t(\boldsymbol{q};\chi_n)\right]^* \cdot \int_{\mathcal{S}} \left[\bar{\bar{G}}^{\text{inh}}(\boldsymbol{q},\boldsymbol{p};\chi_n)\right]^* \cdot \mathbf{\Gamma}(\boldsymbol{p}) d\boldsymbol{p}. \tag{4.5}$$

Despite the fact that the second derivative of the scattered field with respect to the contrast is neglected in the GNI method, see (4.3), we show the second derivative operator to briefly explain why its calculation is computationally expensive. The second derivative operator $\frac{\partial^2 \mathcal{E}_t^{\text{scat}}}{\partial \chi^2}|_{\chi=\chi_n}$ is a linear mapping from $L^2(\mathcal{D})$ to the space of linear operators which map from $L^2(\mathcal{D})$ to $L^2(\mathcal{S})$. Assuming $\psi \in L^2(\mathcal{D})$ and $\varphi \in L^2(\mathcal{D})$, the second derivative operator may be written as (see Section D.1)

$$\begin{aligned}\left[\frac{\partial^2 \mathcal{E}_t^{\text{scat}}}{\partial \chi^2}|_{\chi=\chi_n}(\varphi)\right](\psi) = k_b^2 \int_{\mathcal{D}} \varphi(\boldsymbol{q}) \Bigg[& \frac{\partial \mathcal{E}_t}{\partial \chi}|_{\chi=\chi_n}(\psi) \cdot \bar{\bar{G}}^{\text{inh}}(\boldsymbol{q},\boldsymbol{p};\chi_n) + \\ & \boldsymbol{E}_t(\boldsymbol{q};\chi_n) \cdot \frac{\partial \bar{\bar{G}}^{\text{inh}}(\boldsymbol{q},\boldsymbol{p};\chi)}{\partial \chi}|_{\chi=\chi_n}(\psi) \Bigg] d\boldsymbol{q}\end{aligned} \tag{4.6}$$

The operator $\mathcal{E}_t$ is given in (2.19) where $\boldsymbol{E}^{\text{inc}}$ needs to be replaced by $\boldsymbol{E}_t^{\text{inc}}$. The calculation of this second derivative is very computationally expensive. To show this, consider $\frac{\partial \mathcal{E}_t}{\partial \chi}|_{\chi=\chi_n}(\psi)$ in the integrand of (4.6). Similar to the derivation of $\frac{\partial \mathcal{E}_t^{\text{scat}}}{\partial \chi}|_{\chi=\chi_n}$, see Appendix D, $\frac{\partial \mathcal{E}_t}{\partial \chi}|_{\chi=\chi_n}(\psi)$ may be derived as

$$\frac{\partial \mathcal{E}_t}{\partial \chi}|_{\chi=\chi_n}(\psi) = k_b^2 \int_{\mathcal{D}} \psi(\boldsymbol{q}') \boldsymbol{E}_t(\boldsymbol{q}';\chi_n) \cdot \bar{\bar{G}}^{\text{inh}}(\boldsymbol{q}',\boldsymbol{q};\chi_n) d\boldsymbol{q}' \tag{4.7}$$

where $\boldsymbol{q}$ and $\boldsymbol{q}'$ are both in the imaging domain $\mathcal{D}$. Therefore, calculating (4.7) requires that the excitation be placed in different $\boldsymbol{q}$, or $\boldsymbol{q}'$, which are both inside the imaging domain. In the discrete form of the problem where the 2D imaging domain is discretized into N pulse basis functions, this results in solving the forward problem N times per GNI iteration.

4.1.2 Required derivatives for the data misfit cost-functional

We show the first and second derivatives of $\tilde{\mathcal{C}}^{\mathrm{LS}}(\chi, \chi^*)$ with respect to χ and χ^* which are required in (4.2). As derived in Appendix D, the first derivatives can be written as

$$\frac{\partial \tilde{\mathcal{C}}^{\mathrm{LS}}}{\partial \chi^*}|_{\chi=\chi_n}(\psi^*) = \left\langle \eta_{\mathcal{S}} \sum_{t=1}^{T_x} \left[\frac{\partial \mathcal{E}_t^{\mathrm{scat}}}{\partial \chi}|_{\chi=\chi_n} \right]^a (\mathcal{E}_t^{\mathrm{scat}}(\chi_n) - \boldsymbol{E}_{\mathrm{meas},t}^{\mathrm{scat}}), \psi \right\rangle_{\mathcal{D}}, \tag{4.8}$$

and

$$\frac{\partial \tilde{\mathcal{C}}^{\mathrm{LS}}}{\partial \chi}|_{\chi=\chi_n}(\psi) = \left[\frac{\partial \tilde{\mathcal{C}}^{\mathrm{LS}}}{\partial \chi^*}|_{\chi=\chi_n}(\psi^*) \right]^*. \tag{4.9}$$

The normalization factor $\eta_{\mathcal{S}}$ is given as

$$\eta_{\mathcal{S}} = \left[\sum_{t=1}^{T_x} \left\| \boldsymbol{E}_{\mathrm{meas},t}^{\mathrm{scat}} \right\|_{\mathcal{S}}^2 \right]^{-1}. \tag{4.10}$$

The second derivatives are derived as as,

$$\left[\frac{\partial^2 \tilde{\mathcal{C}}^{\mathrm{LS}}}{\partial \chi^* \partial \chi}|_{\chi=\chi_n}(\varphi) \right](\psi^*) = \left\langle \eta_{\mathcal{S}} \sum_{t=1}^{T_x} \left[\frac{\partial \mathcal{E}_t^{\mathrm{scat}}}{\partial \chi}|_{\chi=\chi_n} \right]^a \left[\frac{\partial \mathcal{E}_t^{\mathrm{scat}}}{\partial \chi}|_{\chi=\chi_n} \right](\varphi), \psi \right\rangle_{\mathcal{D}}, \tag{4.11}$$

$$\left[\frac{\partial^2 \tilde{\mathcal{C}}^{\mathrm{LS}}}{\partial \chi \partial \chi}|_{\chi=\chi_n}(\varphi) \right](\psi) = \left\langle \eta_{\mathcal{S}} \sum_{t=1}^{T_x} \left\{ \left[\frac{\partial^2 \mathcal{E}_t^{\mathrm{scat}}}{\partial \chi^2}|_{\chi=\chi_n}(\varphi) \right]^a \left(\mathcal{E}_t^{\mathrm{scat}}(\chi_n) - \boldsymbol{E}_{\mathrm{meas},t}^{\mathrm{scat}} \right) \right\}^*, \psi^* \right\rangle_{\mathcal{D}}, \tag{4.12}$$

$$\left[\frac{\partial^2 \tilde{\mathcal{C}}^{\mathrm{LS}}}{\partial \chi \partial \chi^*}|_{\chi=\chi_n}(\varphi^*) \right](\psi) = \left\{ \left[\frac{\partial^2 \tilde{\mathcal{C}}^{\mathrm{LS}}}{\partial \chi^* \partial \chi}|_{\chi=\chi_n}(\varphi) \right](\psi^*) \right\}^*, \tag{4.13}$$

and

$$\left[\frac{\partial^2 \tilde{\mathcal{C}}^{\mathrm{LS}}}{\partial \chi^* \partial \chi^*}|_{\chi=\chi_n}(\varphi^*) \right](\psi^*) = \left\{ \left[\frac{\partial^2 \tilde{\mathcal{C}}^{\mathrm{LS}}}{\partial \chi \partial \chi}|_{\chi=\chi_n}(\varphi) \right](\psi) \right\}^*. \tag{4.14}$$

Utilizing (4.8) and (4.9), the second term of (4.1), when $\mathcal{C}(\chi) = \mathcal{C}^{\text{LS}}(\chi)$, will be

$$\text{Re}\left\langle 2\eta_{\mathcal{S}} \sum_{t=1}^{T_x} \left[\frac{\partial \mathcal{E}_t^{\text{scat}}}{\partial \chi}|_{\chi=\chi_n} \right]^a \left(\mathcal{E}_t^{\text{scat}}(\chi_n) - \boldsymbol{E}_{\text{meas},t}^{\text{scat}} \right), \Delta\chi_n \right\rangle_{\mathcal{D}}. \tag{4.15}$$

Also, utilizing (4.11), (4.12), (4.13), and (4.14), the third term of (4.1), when $\mathcal{C}(\chi) = \mathcal{C}^{\text{LS}}(\chi)$, will be

$$\begin{aligned} &\text{Re}\left\langle 2\eta_{\mathcal{S}} \sum_{t=1}^{T_x} \left[\frac{\partial \mathcal{E}_t^{\text{scat}}}{\partial \chi}|_{\chi=\chi_n} \right]^a \left[\frac{\partial \mathcal{E}_t^{\text{scat}}}{\partial \chi}|_{\chi=\chi_n} \right] (\Delta\chi_n), \Delta\chi_n \right\rangle_{\mathcal{D}} + \\ &\text{Re}\left\langle 2\eta_{\mathcal{S}} \sum_{t=1}^{T_x} \left[\frac{\partial^2 \mathcal{E}_t^{\text{scat}}}{\partial \chi^2}|_{\chi=\chi_n}(\Delta\chi_n) \right]^a \left(\mathcal{E}_t^{\text{scat}}(\chi_n) - \boldsymbol{E}_{\text{meas},t}^{\text{scat}} \right), \Delta\chi_n^* \right\rangle_{\mathcal{D}}. \end{aligned} \tag{4.16}$$

As can be seen both (4.15) and (4.16) are real numbers. This is consistent with the fact that $\mathcal{C}^{\text{LS}}$ is a mapping from $L^2(\mathcal{D})$ to $\mathbb{R}$.

4.2 Finding the correction in the non-regularized GNI method

Herein, we assume that the cost-functional to be minimized is the data misfit cost-functional $\mathcal{C}^{\text{LS}}$ (without any regularization terms). Noting that the second derivative of the scattered field will be avoided in the Gauss-Newton inversion method, see (4.3), the derivatives $\frac{\partial^2 \tilde{\mathcal{C}}^{\text{LS}}}{\partial \chi \partial \chi}$, (4.12), and $\frac{\partial^2 \tilde{\mathcal{C}}^{\text{LS}}}{\partial \chi^* \partial \chi^*}$, (4.14), are ignored. Ignoring these derivatives and noting (4.2), it is straightforward to see that $\Delta\chi_n$ can be found by satisfying

$$\frac{\partial^2 \tilde{\mathcal{C}}^{\text{LS}}}{\partial \chi^* \partial \chi}|_{\chi=\chi_n} (\Delta\chi_n) = -\frac{\partial \tilde{\mathcal{C}}^{\text{LS}}}{\partial \chi^*}|_{\chi=\chi_n}. \tag{4.17}$$

As can be seen both the left-hand and right-hand sides of (4.17) represent linear operators which map $L^2(\mathcal{D})$ to $\mathbb{C}$. This means that for an arbitrary $\psi \in L^2(\mathcal{D})$, the correction must

satisfy

$$\left[\frac{\partial^2\tilde{\mathcal{C}}^{\text{LS}}}{\partial\chi^*\partial\chi}|_{\chi=\chi_n}(\Delta\chi_n)\right](\psi^*) = -\left[\frac{\partial\tilde{\mathcal{C}}^{\text{LS}}}{\partial\chi^*}|_{\chi=\chi_n}\right](\psi^*). \tag{4.18}$$

Using (4.8) and (4.11), equation (4.18) may be written as

$$\begin{aligned}\left\langle \eta_{\mathcal{S}}\sum_{t=1}^{T_x}\left[\frac{\partial\mathcal{E}_t^{\text{scat}}}{\partial\chi}|_{\chi=\chi_n}\right]^a\left[\frac{\partial\mathcal{E}_t^{\text{scat}}}{\partial\chi}|_{\chi=\chi_n}\right](\Delta\chi_n),\psi\right\rangle_{\mathcal{D}} = \\ \left\langle -\eta_{\mathcal{S}}\sum_{t=1}^{T_x}\left[\frac{\partial\mathcal{E}_t^{\text{scat}}}{\partial\chi}|_{\chi=\chi_n}\right]^a(\mathcal{E}_t^{\text{scat}}(\chi_n)-\boldsymbol{E}_{\text{meas},t}^{\text{scat}}),\psi\right\rangle_{\mathcal{D}}.\end{aligned} \tag{4.19}$$

Therefore, the correction $\Delta\chi_n$ can be found from

$$\sum_{t=1}^{T_x}\left[\frac{\partial\mathcal{E}_t^{\text{scat}}}{\partial\chi}|_{\chi=\chi_n}\right]^a\left[\frac{\partial\mathcal{E}_t^{\text{scat}}}{\partial\chi}|_{\chi=\chi_n}\right](\Delta\chi_n) = -\sum_{t=1}^{T_x}\left[\frac{\partial\mathcal{E}_t^{\text{scat}}}{\partial\chi}|_{\chi=\chi_n}\right]^a(\mathcal{E}_t^{\text{scat}}(\chi_n)-\boldsymbol{E}_{\text{meas},t}^{\text{scat}}). \tag{4.20}$$

It should be noted that for the case where $\mathcal{C}(\chi)$ is an augmented form of $\mathcal{C}^{\text{LS}}(\chi)$ by an appropriate regularization term, the regularization term will also contribute in finding the correction. This will be explained in the Chapter 5.

4.3 Step-length

Having found the correction $\Delta\chi_n$, the contrast is updated as

$$\chi_{n+1} = \chi_n + \nu_n\Delta\chi_n \tag{4.21}$$

where ν_n is an appropriate step-length chosen to enforce the reduction of the cost-functional. We note that $\Delta\chi_n$ is a descent direction for the quadratic form of the cost-functional; not necessarily for the cost-functional itself. In fact, if the quadratic model is not a good approximation to the cost-functional, the correction may lead to an increase in the cost-functional.

That's why some form of line search algorithm is required to enforce the reduction of the cost-functional at each iteration. Formally, ν_n can be found from the following minimization

$$\nu_n = \arg\min_{\nu} \{\mathcal{C}(\chi_n + \nu\Delta\chi_n)\} . \tag{4.22}$$

This minimization can be done using different nonlinear optimization routines. However, due to the fact that these techniques require several cost-functional evaluation and noting that evaluating the cost-functional is very expensive[2], such optimization techniques will be very computationally expensive. Therefore, we adopt a line search algorithm described in [4, 45]. In this line search algorithm, we start with the full step, *i.e.* $\nu_n = 1$, and check whether it satisfies,

$$\mathcal{C}(\chi_n + \nu_n\Delta\chi_n) \leq \mathcal{C}(\chi_n) + \beta\nu_n\delta\mathcal{C}_n \tag{4.23}$$

where β is a small positive number[3] and $\delta\mathcal{C}_n$ is the decrease rate of $\mathcal{C}(\chi)$ at χ_n in the direction of $\Delta\chi_n$. If ν_n satisfies (4.23), we choose it as an appropriate step-length; otherwise we reduce the step-size along $\Delta\chi_n$ until we find a ν_n which satisfies (4.23). In this procedure, the function $g(\nu) \triangleq \mathcal{C}(\chi_n + \nu\Delta\chi_n)$ is approximated by a quadratic expression in terms of ν and a new candidate for the step-length is then found by minimizing this quadratic form. As in [4], the minimum possible value for ν is set to 0.1. If the step-length becomes less than 0.1, we choose $\nu = 0.1$ and terminate the line-search algorithm. The details of this algorithm can be found in [45].

[2] Note that evaluating the cost-functional for each guess of the step-length requires calling the forward solver T_x times to calculate $\mathcal{E}_t^{\text{scat}}(\chi_n + \nu_n\Delta\chi_n)$ for $t = 1, \cdots, T_x$.

[3] In our implementation, it is set to be 10^{-4}.

4.4 Termination criteria for the GNI method

The inversion algorithm terminates if one of the following three conditions is satisfied: *(i)* the cost-functional $\mathcal{C}(\chi)$ is less than a prescribed error, *(ii)* the difference between two successive $\mathcal{C}(\chi)$ becomes less than a prescribed value, or *(iii)* the total number of iterations exceeds a prescribed maximum.

4.5 Discretization

Due to the fact that the number of measurements, *i.e.*, the data obtained with an actual MWT system, is limited and that the inversion algorithm needs to be implemented using a computer, we discretize the problem. The discretization is, in fact, a projection from the continuous domain to a finite dimensional discrete domain.

We discretize the imaging domain $\mathcal{D}$ into N cells using 2D pulse basis functions. Thus, the contrast function is represented by the complex vector $\underline{\chi} \in \mathbb{C}^N$. We also assume that the number of measured data is M. Thus, the measured scattered data on the discrete measurement domain $\mathcal{S}$ is denoted by the complex vector $\underline{E}^{\text{scat}}_{\text{meas}} \in \mathbb{C}^M$. The vector $\underline{E}^{\text{scat}}_{\text{meas}}$ is the stacked version of the measured scattered fields for each transmitter. That is,

$$\underline{E}^{\text{scat}}_{\text{meas}} = \begin{pmatrix} \underline{E}^{\text{scat}}_{\text{meas},1} \\ \vdots \\ \underline{E}^{\text{scat}}_{\text{meas},t} \\ \vdots \\ \underline{E}^{\text{scat}}_{\text{meas},T_x} \end{pmatrix}_{M\times 1} \tag{4.24}$$

Assuming that the t^{th} transmitter is active, the simulated scattered field corresponding to the predicted contrast at the n^{th} iteration of the GNI algorithm, $\underline{\chi}_n$, is denoted by $\underline{E}^{\text{scat}}_{t,n}$ which is the discretized form of $\mathcal{E}^{\text{scat}}_t(\chi_n)$. The vector $\underline{E}^{\text{scat}}_n \in \mathbb{C}^M$ is then formed by stacking $\underline{E}^{\text{scat}}_{t,n}$. That is,

$$\underline{E}^{\text{scat}}_n = \begin{pmatrix} \underline{E}^{\text{scat}}_{1,n} \\ \vdots \\ \underline{E}^{\text{scat}}_{t,n} \\ \vdots \\ \underline{E}^{\text{scat}}_{T_x,n} \end{pmatrix}_{M\times 1} \tag{4.25}$$

Assuming that the t^{th} transmitter is active, we define the matrix $\underline{\boldsymbol{J}}_{t,n}$ at the n^{th} iteration of the GNI algorithm which contains the derivative of the scattered field vector $\underline{E}^{\text{scat}}$ with respect to $\underline{\chi}$ evaluated at $\underline{\chi} = \underline{\chi}_n$. That is, $\underline{\boldsymbol{J}}_{t,n}$ represents the discrete form of $\frac{\partial \mathcal{E}^{\text{scat}}_t}{\partial \chi}|_{\chi=\chi_n}$. The matrix $\underline{\boldsymbol{J}}_n \in \mathbb{C}^{M\times N}$ is then formed by stacking $\underline{\boldsymbol{J}}_{t,n}$ matrices ($t = 1, \cdots, T_x$). We will refer to $\underline{\boldsymbol{J}}_n$ as the Jacobian matrix. Each row of the Jacobian matrix corresponds to a particular receiver location, say, $\boldsymbol{p}$ and a particular polarization along some direction, say, $\hat{\tau}$ and a particular transmitter, say, the t^{th} transmitter. That is, one row for each individual datum of the collected data. The ordering of the rows will obviously depend on the ordering of this data, but the i^{th} element in such a row will correspond to the derivative of this scattered field with respect to $[\underline{\chi}]_i$, the i^{th} element of the vector $\underline{\chi}$. From (4.4), this element may be found by

$$k_b^2 \int_{\mathcal{D}} \Pi^i(\boldsymbol{q}) \boldsymbol{E}_t(\boldsymbol{q};\chi_n) \cdot \bar{\bar{G}}^{\text{inh}}(\boldsymbol{q},\boldsymbol{p};\chi_n) \cdot \hat{\tau} d\boldsymbol{q}. \tag{4.26}$$

where $\Pi^i(\boldsymbol{q})$ is the 2D pulse function which is equal 1 at the i^{th} voxel of the imaging domain and 0 otherwise. For our cases, the polarization direction $\hat{\tau}$ is considered to be either $\hat{x}$ or $\hat{y}$ in the TE case and $\hat{z}$ in the TM case.

That being said, the discrete form of (4.20), may be written as

$$\underline{\boldsymbol{J}}_n^H \underline{\boldsymbol{J}}_n \Delta\underline{\chi}_n = \underline{\boldsymbol{J}}_n^H \underline{d}_n \tag{4.27}$$

where the superscript 'H' denotes the Hermitian operator (complex conjugate transpose). The vector $\underline{d}_n \in \mathbb{C}^M$ is the discrepancy between the measured data and the simulated data corresponding to $\underline{\chi}_n$; *i.e.*,

$$\underline{d}_n = -\left(\underline{E}_n^{\text{scat}} - \underline{E}_{\text{meas}}^{\text{scat}}\right). \tag{4.28}$$

It should also be noted that the solution to (4.27) can be considered as the solution to the minimization,

$$\Delta\underline{\chi}_n = \arg\min_{\Delta\underline{\chi}} \left\| \underline{\boldsymbol{J}}_n \Delta\underline{\chi} - \underline{d}_n \right\|^2. \tag{4.29}$$

The discretized form of the cost-functional $\mathcal{C}^{\text{LS}}$ will be denoted by $\mathcal{F}^{\text{LS}}$. Thus,

$$\mathcal{F}^{\text{LS}}(\underline{\chi}_n) = \frac{\left\| \underline{E}_n^{\text{scat}} - \underline{E}_{\text{meas}}^{\text{scat}} \right\|^2}{\left\| \underline{E}_{\text{meas}}^{\text{scat}} \right\|^2} \tag{4.30}$$

where $\|.\|$ denotes the L^2-norm on $\mathbb{C}^M$.

In this thesis, we show inversion results from experimental data sets as well as synthetic data sets. To all synthetic data sets, unless otherwise stated, 3% noise was artificially added using the formula [65]

$$\underline{E}_{\text{meas},t}^{\text{scat}} = \underline{E}_t^{\text{scat,fwd}} + max\left[\forall_t\, \underline{E}_t^{\text{scat,fwd}}\right] \frac{\eta}{\sqrt{2}} (\underline{\vartheta}_1 + j\underline{\vartheta}_2) \tag{4.31}$$

where $\underline{E}_t^{\text{scat,fwd}}$ is the scattered field on the measurement domain obtained by the utilized forward solver, $\underline{\vartheta}_1$ and $\underline{\vartheta}_2$ are two real vectors whose elements are uniformly distributed zero-mean random numbers between -1 and 1, and $\eta = 0.03$. The noisy data $\underline{E}_{\text{meas},t}^{\text{scat}}$ is then

used to test inversion algorithms against synthetic data sets. To avoid inverse crime [68], the discretization used in the utilized inversion algorithms to invert $\underline{E}^{\text{scat}}_{\text{meas},t}$ is chosen to be different than the discretization used in the forward solver to generate $\underline{E}^{\text{scat,fwd}}_{t}$.

Finally, we note that there are different ways to discretize the problem. Mostly, in this thesis, we use 2D pulse functions to discretize the contrast function. Discretization may also be achieved using other methods, such as the eigenfunctions for the problem, see Chapter 7, and triangular meshes [12].

5

Regularization

> *Nonlinear ill-posed problems constitute a much broader area [compared to linear ill-posed problems], and their numerical treatment is often specialized to the particular application.* (Per Christian Hansen [74])

In this chapter, we present different methods to treat the ill-posedness of the microwave tomography problem in the framework of the Gauss-Newton inversion method. These methods are referred to as regularization methods and they need to be utilized to stabilize the solution by adding constraints to the data misfit cost-functional that thereby reduce the influence of errors and noise. The art of regularization lies in two areas: (*i*) applying the right kind of regularization which may depend on the computational resources and the available *a priori* information, and (*ii*) applying the right amount (weight) of regularization which depends on the noise level in the collected data. In the microwave tomography problem, where the nonlinearity is treated by iterative techniques such as the Gauss-Newton inversion method,

the regularization weight at each iteration may also depend on how far the predicted solution at the current iterate is from the expected solution.

In the first part of this chapter, we classify different regularization methods for the GNI method into two strategies. These two strategies may be distinguished by the type of the cost-functional to be minimized. In the first strategy, the cost-functional to be minimized is the data misfit functional $\mathcal{C}^{\mathrm{LS}}$, (3.1), which is ill-posed [40, 75, 41, 12, 54, 46, 44]. Due to this ill-posedness, we need to regularize (4.2) at each iteration of the GNI method. In the second strategy, the cost-functional $\mathcal{C}^{\mathrm{LS}}$ is first regularized and the GNI method is then applied to the regularized cost-functional [38, 30, 4, 76, 45]. Therefore, equation (4.2) does not need to be regularized throughout different GNI iterations. In each regularization method that is discussed the regularization weight is either explicitly chosen or is implicit to the method. The basic idea behind the appropriate regularization weight for the GNI method is that the regularization weight should be large in early GNI iterations where the predicted solution is far from the true solution and should gradually decrease as the algorithm gets closer to the true solution. We refer to this idea as *adaptive* regularization [77, 27]. Throughout this chapter, we denote the *positive* parameter α as the regularization parameter which (partially) governs the regularization weight.

In the second part of this chapter, we consider incorporation of *a priori* information to regularization terms. This chapter ends with introducing an image enhancement technique to suppress possible spurious oscillations in the final image obtained from the Gauss-Newton inversion method. We now start the first part of this chapter by explaining the two regularization strategies, mentioned above, in more details.

5.1 The first strategy

This strategy chooses the data misfit $\mathcal{C}^{\mathrm{LS}}$, (3.1), as the cost-functional to be minimized. Therefore, in the discrete domain, satisfying (4.2) will be equivalent to the minimization (4.29). It is well-known that the matrix $\underline{\underline{\boldsymbol{J}}}_n$ is an ill-conditioned matrix, making (4.29) a discrete linear ill-posed problem which needs to be regularized.[1] There are two published general approaches for regularizing (4.29) in the electromagnetic inverse scattering case: penalty and projection methods.

5.1.1 Penalty methods

Tikhonov regularization [1] is probably the most popular penalty method where the regularized solution of (4.29) is found from the minimization [40, 75, 41, 46, 54]

$$\Delta\underline{\chi}_n = \arg\min_{\Delta\underline{\chi}} \left\{ \left\| \underline{\underline{\boldsymbol{J}}}_n \Delta\underline{\chi} - \underline{d}_n \right\|^2 + \alpha_n \Omega(\Delta\underline{\chi}) \right\}. \tag{5.1}$$

The regularization term $\Omega(\Delta\underline{\chi})$ is usually chosen to be in the form of an L^2-norm, making (5.1) a least squares minimization. Herein, we assume $\Omega(\Delta\underline{\chi}) = \left\| \underline{\underline{\boldsymbol{R}}} \Delta\underline{\chi} \right\|^2$ where $\underline{\underline{\boldsymbol{R}}}$ is an appropriate matrix whose nullspace intersects trivially with that of $\underline{\underline{\boldsymbol{J}}}_n$; thus, ensuring a unique solution for (5.1). In this case, (5.1) can be written as a damped least squares minimization

$$\Delta\underline{\chi}_n = \arg\min_{\Delta\underline{\chi}} \left\| \begin{pmatrix} \underline{\underline{\boldsymbol{J}}}_n \\ \sqrt{\alpha_n}\underline{\underline{\boldsymbol{R}}} \end{pmatrix} \Delta\underline{\chi} - \begin{pmatrix} \underline{d}_n \\ \underline{0} \end{pmatrix} \right\|^2 \tag{5.2}$$

[1] We note that the minimization (4.29) is the result of the discretization of a Fredholm integral equation of the first kind. It is well-known that the discretized form of a Fredholm integral equation of the first kind results in a discrete ill-posed problem [23].

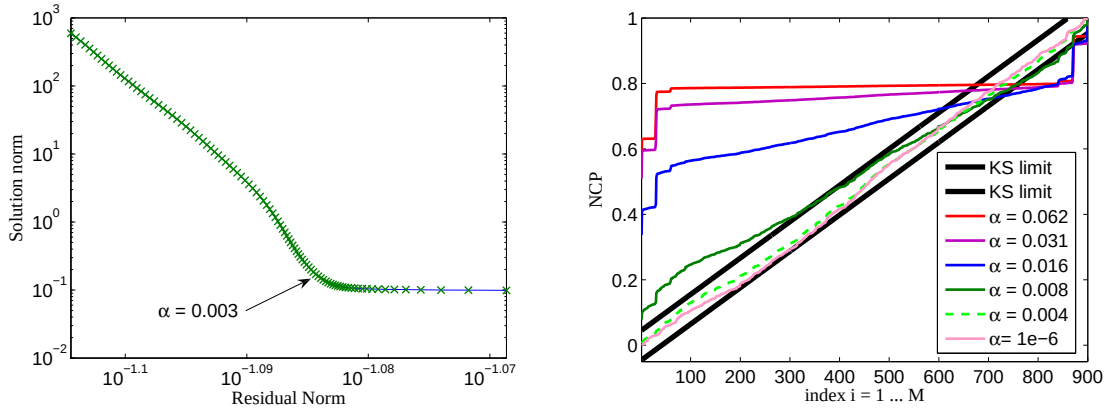

(a) *L*-curve (b) NCP

Fig. 5.1: (a) The *L*-curve and (b) the NCP plot.

where $\underline{0}$ is the zero vector of appropriate size. The minimization (5.2) is equivalent to

$$(\underline{\boldsymbol{J}}_n^H \underline{\boldsymbol{J}}_n + \alpha_n \underline{\boldsymbol{R}}^H \underline{\boldsymbol{R}}) \Delta \underline{\chi}_n = \underline{\boldsymbol{J}}_n^H \underline{d}_n. \tag{5.3}$$

In this case, the weight of the regularization is determined by the positive parameter α_n which needs to be chosen at each GNI iteration. This weight is usually determined using either one of the standard regularization parameter-choice methods [23] or an *ad hoc* technique [75, 41, 46, 54]. The standard regularization parameter-choice methods, such as the *L*-curve [78, 79], the Generalized Cross-Validation (GCV) [80], [54, 46], and the Normalized Cumulative Periodogram (NCP) [81, 82, 53, 52] methods, can be very computationally expensive and may also fail in choosing an appropriate regularization weight. For example, the GCV functional may become very flat so that locating its minimum, which corresponds to an appropriate regularization parameter, will be numerically difficult [78].

To show one example of how these standard regularization parameter-choice methods choose an appropriate regularization parameter α_n, we have shown the *L*-curve and NCP at one iteration of a MWT problem, described in [52], in figure 5.1. To construct the *L*-curve, see

figure 5.1 (a), we have solved (5.3) for 100 different α when $\underline{\boldsymbol{R}}$ is chosen to be the identity matrix $\underline{\boldsymbol{I}}$. Thus, the discrete *L*-curve consists of 100 points. The vertical axis in figure 5.1 (a) is the solution norm, $\left\|\Delta\underline{\chi}_n\right\|$, for different choices of α_n, whereas the horizontal axis is the residual norm, $\left\|\underline{\boldsymbol{J}}_n\Delta\underline{\chi}_n - \underline{d}_n\right\|$, for different choices of α_n. If the value of α_n is chosen to be too large, the residual norm will be large while having a small solution norm. This results in an over-regularized solution. On the other hand, if the value of α is chosen to be too small, the solution norm will be large while having the residual norm small. This results in an under-regularized solution. To balance these two norms, it is suggested by Hansen [83] that one chooses the regularization parameter which corresponds to the corner of this curve.

We have also shown the NCP parameter-choice method for the same problem in figure 5.1 (b). The main idea behind the NCP method is to choose the largest α_n that makes $\underline{\boldsymbol{J}}_n\Delta\underline{\chi}_n - \underline{d}_n$, look like white noise. This can be done by starting with a large α_n for which the residual vector, $\underline{\boldsymbol{J}}_n\Delta\underline{\chi}_n - \underline{d}_n$, does not look like white noise. According to the NCP parameter-choice method, if this α_n is chosen as the regularization parameter, the solution will be an over-regularized solution. We then reduce α until the first instance where we have a residual vector that looks like white noise. Here, "looks like white noise" is defined using the Kolmogorov-Smirnov (KS) limits. The metric that is used to see if the residual "looks" like white noise is that the NCP of $\underline{\boldsymbol{J}}_n\Delta\underline{\chi}_n - \underline{d}_n$ fits between the KS limits which are bounds around a straight line. The largest α_n for which the NCP fits between the KS limits is considered to be an appropriate regularization parameter. At this point, if we decrease α_n further, the NCP will be still between the KS limits. However, the solution is more likely to be unstable (under-regularized solution).

Regarding the use of standard regularization parameter-choice methods such as the *L*-curve, NCP and GCV methods within the first regularization strategy, it should be noted that these methods have been developed for linear inverse problems where the discrete Picard condition

[84] is satisfied for the underlying unperturbed problem [23], [83]. We have provided a mathematical discussion of why standard regularization parameter-choice methods may fail for the microwave tomography problem in [53] (in the framework of the NCP parameter-choice method). However, they may not be appropriate for nonlinear inverse scattering problems, especially when the initial guess to the GNI algorithm is very far from the true solution [46].

The *ad hoc* techniques are usually faster but are dependent on the noise level of the measured data. Therefore, they may need to be modified for different microwave tomography systems. However, it is easier to incorporate adaptive regularization using *ad hoc* techniques as compared to the standard regularization parameter-choice methods. For example, in [41], the regularization parameter α_n is chosen to be proportional to $\|\underline{d}_n\|^2$. That is, the regularization weight decreases during the GNI iterations; thus providing the adaptive regularization.

We note that the penalty term $\Omega(\Delta_{\underline{\chi}_n})$ can have other forms such as the L^1-norm total variation or maximum entropy [45]. It should also be mentioned that this type of regularization, when $\underline{\underline{\boldsymbol{R}}}$ is chosen to be the identity matrix $\underline{\underline{\boldsymbol{I}}}$, may be viewed as the Levenberg-Marquardt approach [46, 85, 69] where the matrix $\underline{\boldsymbol{J}}_n^H \underline{\boldsymbol{J}}_n$ is augmented by $\alpha_n \underline{\underline{\boldsymbol{I}}}$.

5.1.2 Projection methods

Projection methods attempt to regularize (4.29) by projecting it onto a subspace having a basis that can be used to represent the solution $\Delta_{\underline{\chi}_n}$ with sufficient accuracy while maintaining the stability. The projection may be achieved by Krylov subspace methods such as the Conjugate Gradient Least Squares (CGLS) or Least Squares with QR factorization (LSQR) methods [86, 74], [12], [87]: at the k^{th} iteration of the Krylov subspace methods, the solution

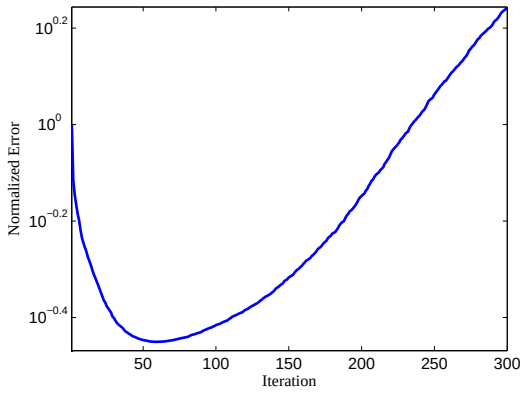

Fig. 5.2: The semi-convergence behavior of the CGLS scheme applied to an ill-posed problem. The vertical axis shows the normalized error between the true solution and the reconstructed solution. The horizontal axis shows the number of CGLS iterations (from 1 to 300).

is restricted to lie in

$$\Delta \underline{\chi}_n^{(k)} \in \mathcal{K}_k(\underline{\boldsymbol{J}}_n^H \underline{\boldsymbol{J}}_n, \underline{\boldsymbol{J}}_n^H \underline{d}_n) \tag{5.4}$$

where $\mathcal{K}_k$ is the k-dimensional Krylov subspace defined by $\underline{\boldsymbol{J}}_n$ and $\underline{d}_n$. The Krylov subspace algorithms, when applied to an ill-posed system of equations, exhibit a *semi-convergence* behavior [88, 74]. That is, they improve the solution at their early iterations, where the solution space is restricted to a Krylov subspace of small dimension, however, they start deteriorating the solution by inverting the noise in later iterations. Therefore, the stopping iteration k plays the role of the regularization parameter: the fewer the iterations, the stronger the regularization. To demonstrate this semi-convergence behavior, we have shown the performance of the CGLS algorithm applied to a standard linear ill-posed problem, known as the Satellite problem [89] developed at the US Air Force Phillips Laboratory, in figure 5.2. The vertical axis shows the normalized error between the reconstructed solution and the true solution. The horizontal axis shows the number of CGLS iterations (from 1 to 300). As can be seen, the normalized error between the reconstructed solution and the true solution decreases at early CGLS iterations. After iteration 54, which would be the ideal stopping iteration, the normalized error starts increasing. It should be noted that this plot cannot be used to find the

stopping iteration in reality. This is due to the fact that the true solution, based on which the plot shown in figure 5.2 is made, is to be found and thus, is not available. The stopping iteration is usually determined using either standard regularization parameter-choice methods such as the *L*-curve method [90] or by some *ad hoc* techniques [12, 87].

As in penalty methods, adaptive regularization is difficult to incorporate in the standard regularization parameter-choice methods whereas they can be easily incorporated into the *ad hoc* techniques. For example in [12, 57], an *ad hoc* technique has been used to determine the regularization weight in the CGLS scheme where the stopping iteration is chosen to be small in early GNI iterations and then increases in later GNI iterations. Considering that the smaller the stopping iteration, the stronger the regularization, this *ad hoc* technique is an attempt at adaptive regularization for the GNI method.

The projection can also be achieved by the Truncated Singular Value Decomposition (TSVD) where the unknown $\Delta\underline{\chi}_n$ is projected onto the subspace spanned by the first few right singular vectors of the matrix $\underline{\boldsymbol{J}}_n$ [91, 74, 92]. Writing the Singular Value Decomposition (SVD) of the matrix $\underline{\boldsymbol{J}}_n$ as $\underline{\boldsymbol{J}}_n = \underline{\boldsymbol{U}}\,\underline{\boldsymbol{S}}\,\underline{\boldsymbol{V}}^H$, the regularized solution of (4.29) using the TSVD method can be written as

$$\Delta\underline{\chi}_n = \sum_{i=1}^{k} \frac{\underline{u}_i^H \underline{d}_n}{s_i} \underline{v}_i \tag{5.5}$$

where the left singular vector $\underline{u}_i$ and the right singular vector $\underline{v}_i$ are the i^{th} column of the orthonormal matrices $\underline{\boldsymbol{U}}$ and $\underline{\boldsymbol{V}}$, respectively. The singular value s_i is the i^{th} diagonal element of the matrix $\underline{\boldsymbol{S}}$. In (5.5), the integer k, which determines the dimension of the subspace spanned by the right singular vectors $\underline{v}_i$, is the regularization parameter: the smaller the k, the stronger the regularization. It should be mentioned that in (5.5), we have assumed that the singular values s_i are ordered in a non-increasing sequence; *i.e.*, $s_i \geq s_{i+1} \geq 0$. Similar to Krylov subspace regularization methods, the regularization parameter k may be determined from standard regularization parameter-choice methods or *ad hoc* techniques.

5.2 The second strategy

In the second strategy, the nonlinear ill-posed cost-functional $\mathcal{C}^{\mathrm{LS}}$, (3.1), is first regularized and then the GNI method is applied to the regularized cost-functional. Therefore, equation (4.2) does not need to be regularized throughout the GNI iterations. At least, three different methods for regularizing the cost-functional $\mathcal{C}^{\mathrm{LS}}$ for the GNI method have been reported in the literature. These are additive, multiplicative, and additive-multiplicative regularization.

5.2.1 Additive regularization

In this case, $\mathcal{C}^{\mathrm{LS}}$ is regularized by an additive term (see for example, [76, 38]):

$$\mathcal{C}(\chi) = \mathcal{C}^{\mathrm{LS}}(\chi) + \alpha \mathcal{C}^{\mathrm{AR}}(\chi) \tag{5.6}$$

where $\mathcal{C}^{\mathrm{AR}}$ is an appropriate additive regularizer. The regularizer $\mathcal{C}^{\mathrm{AR}}$ is usually chosen to be the L^2-norm total variation of the contrast which is written as

$$\mathcal{C}^{\mathrm{AR}}(\chi) = \frac{1}{A} \int_{\mathcal{D}} |\nabla \chi(\boldsymbol{q})|^2 \, d\boldsymbol{q} \tag{5.7}$$

where A is the area (or volume, in the case of three-dimensional imaging) of $\mathcal{D}$ and ∇ denotes the spatial gradient operator. To handle the fact that the cost-functional $\mathcal{C}^{\mathrm{AR}}(\chi)$ is not holomorphic in χ, we use the Wirtinger calculus as before. Thus, we consider the cost-functional $\tilde{\mathcal{C}}^{\mathrm{AR}}(\chi, \chi^*)$ which satisfies $\tilde{\mathcal{C}}^{\mathrm{AR}}(\chi, \chi^*) = \mathcal{C}^{\mathrm{AR}}(\chi)$ (see Chapter 4 and Appendix C for more discussion). The cost-functional $\tilde{\mathcal{C}}^{\mathrm{AR}}(\chi, \chi^*)$ is holomorphic in χ for fixed χ^* and holomorphic in χ^* for fixed χ. Thus, the following formal derivative operators can be derived

for this regularizer (see Section D.3 for the proof)

$$\frac{\partial\tilde{\mathcal{C}}^{\mathcal{AR}}}{\partial\chi^*}|_{\chi=\chi_n}(\psi^*)=\left\{\frac{\partial\tilde{\mathcal{C}}^{\text{AR}}}{\partial\chi}|_{\chi=\chi_n}(\psi)\right\}^*=\left\langle-\frac{1}{A}\nabla^2\chi_n,\psi\right\rangle_{\mathcal{D}}, \tag{5.8}$$

$$\left[\frac{\partial^2\tilde{\mathcal{C}}^{\mathcal{AR}}}{\partial\chi^*\partial\chi}|_{\chi=\chi_n}(\varphi)\right](\psi^*)=\left\{\left[\frac{\partial^2\tilde{\mathcal{C}}^{\mathcal{AR}}}{\partial\chi\partial\chi^*}|_{\chi=\chi_n}(\varphi^*)\right](\psi)\right\}^*=\left\langle-\frac{1}{A}\nabla^2\varphi,\psi\right\rangle_{\mathcal{D}}, \tag{5.9}$$

and

$$\left[\frac{\partial^2\tilde{\mathcal{C}}^{\text{AR}}}{\partial\chi\partial\chi}|_{\chi=\chi_n}(\varphi)\right](\psi)=\left\{\left[\frac{\partial^2\tilde{\mathcal{C}}^{\text{AR}}}{\partial\chi^*\partial\chi^*}|_{\chi=\chi_n}(\varphi^*)\right](\psi^*)\right\}^*=0. \tag{5.10}$$

where ∇^2 denotes the Laplacian operator and ψ and φ are two arbitrary functions in $L^2(\mathcal{D})$.

Noting (4.2), and considering (5.10) as well as utilizing the GNI approximation (which results in ignoring $\frac{\partial^2\tilde{\mathcal{C}}^{\text{LS}}}{\partial\chi\partial\chi}$ and $\frac{\partial^2\tilde{\mathcal{C}}^{\text{LS}}}{\partial\chi^*\partial\chi^*}$), the correction $\Delta\chi_n$ may be found by satisfying

$$\left[\frac{\partial^2\tilde{\mathcal{C}}^{\text{LS}}}{\partial\chi^*\partial\chi}|_{\chi=\chi_n}+\alpha\frac{\partial^2\tilde{\mathcal{C}}^{\text{AR}}}{\partial\chi^*\partial\chi}|_{\chi=\chi_n}\right](\Delta\chi_n)=-\frac{\partial\tilde{\mathcal{C}}^{\text{LS}}}{\partial\chi^*}|_{\chi=\chi_n}-\alpha\frac{\partial\tilde{\mathcal{C}}^{\text{AR}}}{\partial\chi^*}|_{\chi=\chi_n}. \tag{5.11}$$

Utilizing (5.8), (5.9), (4.8), and (4.11), the above equation results in the following equation

$$\begin{aligned}\eta_{\mathcal{S}}\sum_{t=1}^{T_x}\left[\left[\frac{\partial\mathcal{E}_t^{\text{scat}}}{\partial\chi}|_{\chi=\chi_n}\right]^a\left[\frac{\partial\mathcal{E}_t^{\text{scat}}}{\partial\chi}|_{\chi=\chi_n}\right]-\frac{\alpha}{A}\nabla^2\right](\Delta\chi_n)=\\ -\eta_{\mathcal{S}}\sum_{t=1}^{T_x}\left[\frac{\partial\mathcal{E}_t^{\text{scat}}}{\partial\chi}|_{\chi=\chi_n}\right]^a(\mathcal{E}_t^{\text{scat}}(\chi_n)-\boldsymbol{E}_{\text{meas},t}^{\text{scat}})+\frac{\alpha}{A}\nabla^2\chi_n.\end{aligned} \tag{5.12}$$

Thus, using this specific regularizer, the correction vector in the discrete domain at the n^{th} iteration is found by solving

$$(\underline{\boldsymbol{J}}_n^H\underline{\boldsymbol{J}}_n-\gamma\underline{\boldsymbol{\Sigma}})\Delta\underline{\chi}_n=\underline{\boldsymbol{J}}_n^H\underline{d}_n+\gamma\underline{\boldsymbol{\Sigma}}\underline{\chi}_n \tag{5.13}$$

where the matrix $\boldsymbol{\Sigma}$ is the discrete representation of the $\frac{1}{A}\nabla^2$ operator. The positive param-

eter γ is equal to $\alpha/\eta_{\mathcal{S}}$. In this case, the regularization weight remains constant throughout different GNI iterations, as both the matrix $\underline{\underline{\boldsymbol{\Sigma}}}$ and its coefficient γ remain constant throughout different GNI iterations. Therefore, this regularization type will not provide adaptive regularization unless the user changes the regularization weight manually. In this case, the parameter α is usually chosen via *ad hoc* techniques [76, 38]. It should also be mentioned that this regularization method favors smooth solutions due to the presence of the matrix $\underline{\underline{\boldsymbol{\Sigma}}}$ in (5.13) which provides Laplacian regularization. We also note that the matrix $\underline{\underline{\boldsymbol{\Sigma}}}$ is implemented by assuming that its argument vanishes on the boundary of the imaging domain; *i.e.*, utilizing Dirichlet conditions [93] (see (D.43) and its related discussion). Under this zero boundary condition, the matrix $\boldsymbol{\Sigma}$ has no nullspace [94, pg. 102]; thus providing a unique solution for (5.13).

5.2.2 Multiplicative regularization

In this case, the cost-functional $\mathcal{C}^{\text{LS}}$ is regularized with a multiplicative term. That is, at the n^{th} iteration of the GNI algorithm, we minimize ([4, 56, 45])

$$\mathcal{C}_n(\chi) = \mathcal{C}^{\text{LS}}(\chi)\mathcal{C}_n^{\text{MR}}(\chi). \tag{5.14}$$

Here, we consider the multiplicative regularizer $\mathcal{C}_n^{\text{MR}}$ as the weighted L^2-norm total variation of the unknown contrast, defined as [4, 56]

$$\mathcal{C}_n^{\text{MR}}(\chi) = \int_{\mathcal{D}} b_n^2(\boldsymbol{q})(|\nabla\chi(\boldsymbol{q})|^2 + \alpha_n^2)d\boldsymbol{q} \tag{5.15}$$

where

$$b_n(\boldsymbol{q}) \triangleq A^{-\frac{1}{2}}(|\nabla\chi_n(\boldsymbol{q})|^2 + \alpha_n^2)^{-\frac{1}{2}}. \tag{5.16}$$

The choice of the positive parameter α_n^2 is explained below. For the regularizer (5.15), it can be shown that (see Section D.3)

$$\frac{\partial \tilde{\mathcal{C}}_n^{\mathrm{MR}}}{\partial \chi^*}|_{\chi=\chi_n}(\psi^*) = \left\{ \frac{\partial \tilde{\mathcal{C}}_n^{\mathrm{MR}}}{\partial \chi}|_{\chi=\chi_n}(\psi) \right\}^* = \left\langle -\nabla \cdot (b_n^2 \nabla \chi_n), \psi \right\rangle_{\mathcal{D}}, \tag{5.17}$$

$$\left[\frac{\partial^2 \tilde{\mathcal{C}}_n^{\mathrm{MR}}}{\partial \chi^* \partial \chi}|_{\chi=\chi_n}(\varphi) \right](\psi^*) = \left\{ \left[\frac{\partial^2 \tilde{\mathcal{C}}_n^{\mathrm{MR}}}{\partial \chi \partial \chi^*}|_{\chi=\chi_n}(\varphi^*) \right](\psi) \right\}^* = \left\langle -\nabla \cdot (b_n^2 \nabla \varphi), \psi \right\rangle_{\mathcal{D}}, \tag{5.18}$$

$$\left[\frac{\partial^2 \tilde{\mathcal{C}}_n^{\mathrm{MR}}}{\partial \chi \partial \chi}(\varphi) \right](\psi) = \left\{ \left[\frac{\partial^2 \tilde{\mathcal{C}}_n^{\mathrm{MR}}}{\partial \chi^* \partial \chi^*}(\varphi^*) \right](\psi^*) \right\}^* = 0, \tag{5.19}$$

where '$\nabla\cdot$' represents the divergence operator and $\tilde{\mathcal{C}}_n^{\mathrm{MR}}(\chi, \chi^*) = \mathcal{C}_n^{\mathrm{MR}}(\chi)$. Using this multiplicative regularizer, the correction in the discrete domain can then be found by solving

$$(\underline{\boldsymbol{J}}_n^H \underline{\boldsymbol{J}}_n - \beta_n \underline{\boldsymbol{\mathcal{L}}}_n) \Delta \underline{\chi}_n = \underline{\boldsymbol{J}}_n^H \underline{d}_n + \beta_n \underline{\boldsymbol{\mathcal{L}}}_n \underline{\chi}_n \tag{5.20}$$

where $\underline{\boldsymbol{\mathcal{L}}}_n$ represents the discrete form of the $\nabla \cdot (b_n^2 \nabla)$ operator and $\beta_n = \|\underline{d}_n\|^2$. The positive parameter α_n^2 is chosen to be $\mathcal{F}^{\mathrm{LS}}(\underline{\chi}_n)/\Delta A$ where ΔA is the area of a single cell in the discretized domain $\mathcal{D}$.[2] The operator $\underline{\boldsymbol{\mathcal{L}}}_n$, which changes throughout the GNI iterations, provides an edge-preserving regularization. That is, if one specific region of the reconstructed χ_n is homogeneous, the weight b_n^2 will be almost constant for that region. Therefore, the operator $\underline{\boldsymbol{\mathcal{L}}}_n$ will be approximately equal to $b_n^2 \nabla^2$ which favors smooth solutions. On the other hand, if there is a discontinuity (edge) at some region of χ_n, the corresponding b_n^2 for that region will be small. Thus, the discontinuity will not be smoothed out and will be preserved. The regularization operator $\underline{\boldsymbol{\mathcal{L}}}_n$ may be considered as a weighted Laplacian regularizer. A detailed explanation about weighted Laplacian regularizers can be found in [95]. It has been shown in [96, Section 3.5] and [97] that the nullspace of $\underline{\boldsymbol{\mathcal{L}}}_n$ is spanned by a constant vec-

[2] Note that $\mathcal{F}^{\mathrm{LS}}(\underline{\chi}_n)$ is the discrete form of $\mathcal{C}^{\mathrm{LS}}(\chi_n)$; see (4.30).

tor. Noting that the nullspace of $\underline{\boldsymbol{J}}_n^H \underline{\boldsymbol{J}}_n$ contains high-frequent components [23, 82], the nullspace of $\underline{\boldsymbol{\mathcal{L}}}_n$ and $\underline{\boldsymbol{J}}_n^H \underline{\boldsymbol{J}}_n$ intersect trivially; thus, ensuring a unique solution for (5.20).

This multiplicative regularization *automatically* determines the regularization weight which is governed by the discrepancy between the measured data and the simulated data corresponding to $\underline{\chi}_n$. As can be seen from (5.20), the weight of the operator $\underline{\boldsymbol{\mathcal{L}}}_n$ depends on $\|\underline{d}_n\|^2$ which provides adaptive regularization. That is, if the predicted solution is far from the true solution, the regularization weight is high. When the predicted solution gets closer to the true solution, the L^2-norm of the discrepancy $\underline{d}_n$ decreases; thus decreasing the regularization weight. In addition to the weighted L^2-norm total variation form, the multiplicative regularization term may be used in the forms of the standard L^2-norm [45] and the L^2-norm total variation (not weighted) [4]. As opposed to the weighted L^2-norm total variation multiplicative regularizer, see (5.15), these two forms of the multiplicative regularizer do not have the edge-preserving characteristic and will not be discussed in this thesis.

Throughout this thesis, we will refer to the GNI algorithm with the weighted L^2-norm total variation Multiplicative Regularizer (MR) as the MR-GNI method.

5.2.3 Additive-multiplicative regularization

In this case, we regularize $\mathcal{C}^{\text{LS}}$, (3.1), as [30, 59]

$$\mathcal{C}(\chi) = \mathcal{C}^{\text{LS}}(\chi) \left[1 + \alpha \mathcal{C}^{\text{AR}}(\chi)\right]. \tag{5.21}$$

Choosing $\mathcal{C}^{\text{AR}}$ as in (5.7), the correction in the discrete domain can be found by solving

$$(\underline{\boldsymbol{J}}_n^H \underline{\boldsymbol{J}}_n - \lambda_n \underline{\boldsymbol{\Sigma}}) \Delta \underline{\chi}_n = \underline{\boldsymbol{J}}_n^H \underline{d}_n + \lambda_n \underline{\boldsymbol{\Sigma}} \underline{\chi}_n \tag{5.22}$$

where[3]

$$\lambda_n = \frac{\alpha \left\| \underline{d}_n \right\|^2}{1 + \alpha \mathcal{F}^{\mathcal{AR}}(\underline{\chi}_n)}. \tag{5.23}$$

This regularization favors smooth solution due to the presence of the matrix $\underline{\boldsymbol{\Sigma}}$ in (5.22). Unlike the additive regularization, see (5.13), the weight of the regularization is not constant but changes throughout the GNI iterations. As can be seen from (5.22), the regularization weight governed by the positive parameter λ_n decreases when the algorithm gets closer to the true solution. However, the user is still required to set the positive parameter α at the beginning of the GNI algorithm. The algorithm then provides adaptive regularization based on the given α. It should be pointed out that this regularization can be viewed as a multiplicative regularization where the regularizer is $1+\alpha\mathcal{C}^{\text{AR}}(\chi)$ or as an additive regularization where the regularizer is $\mathcal{C}^{\text{LS}}(\chi)\mathcal{C}^{\text{AR}}(\chi)$. As explained in Section 5.2.1, the nullspace of $\underline{\boldsymbol{J}}_n^H \underline{\boldsymbol{J}}_n - \lambda_n \underline{\boldsymbol{\Sigma}}$ is trivial; thus, ensuring a unique solution for (5.22).

5.3 Consistent framework and discussion

Considering that the contrast $\chi(\boldsymbol{q})$ is zero on the boundary of $\mathcal{D}$, it can be shown that the operators $\underline{\boldsymbol{\Sigma}}$ and $\underline{\boldsymbol{\mathcal{L}}}_n$ are self-adjoint and negative definite (see Appendix E for the proof). Therefore, the operators $\underline{\boldsymbol{\Sigma}}$ and $\underline{\boldsymbol{\mathcal{L}}}_n$ can be represented by $-\underline{\boldsymbol{A}}^H \underline{\boldsymbol{A}}$ and $-\underline{\boldsymbol{B}}_n^H \underline{\boldsymbol{B}}_n$ respectively (for example, using Cholesky decomposition [98, Section 4.2]). Using this notation, the correction vector $\Delta\underline{\chi}_n$ in (5.13), (5.20), and (5.22) can be written, respectively, as

$$(\underline{\boldsymbol{J}}_n^H \underline{\boldsymbol{J}}_n + \gamma \underline{\boldsymbol{A}}^H \underline{\boldsymbol{A}}) \Delta\underline{\chi}_n = \underline{\boldsymbol{J}}_n^H \underline{d}_n - \gamma \underline{\boldsymbol{A}}^H \underline{\boldsymbol{A}} \underline{\chi}_n, \tag{5.24}$$

$$(\underline{\boldsymbol{J}}_n^H \underline{\boldsymbol{J}}_n + \beta_n \underline{\boldsymbol{B}}_n^H \underline{\boldsymbol{B}}_n) \Delta\underline{\chi}_n = \underline{\boldsymbol{J}}_n^H \underline{d}_n - \beta_n \underline{\boldsymbol{B}}_n^H \underline{\boldsymbol{B}}_n \underline{\chi}_n, \tag{5.25}$$

[3] As mentioned in Section 'Symbols and Acronyms', $\mathcal{F}^{\mathcal{AR}}(\underline{\chi}_n)$ represents the discrete form of $\mathcal{C}^{\mathcal{AR}}(\chi_n)$.

$$(\underline{\boldsymbol{J}}_n^H \underline{\boldsymbol{J}}_n + \lambda_n \underline{\boldsymbol{A}}^H \underline{\boldsymbol{A}}) \Delta \underline{\chi}_n = \underline{\boldsymbol{J}}_n^H \underline{d}_n - \lambda_n \underline{\boldsymbol{A}}^H \underline{\boldsymbol{A}} \underline{\chi}_n. \tag{5.26}$$

Now, if we consider the penalty term $\Omega(\Delta\underline{\chi})$ in (5.1) as $\left\| \underline{\boldsymbol{R}}(\Delta\underline{\chi} + \underline{\chi}_n) \right\|^2$, the correction corresponding to (5.1) can be written as

$$\Delta \underline{\chi}_n = \arg\min_{\Delta\underline{\chi}} \left\| \begin{pmatrix} \underline{\boldsymbol{J}}_n \\ \sqrt{\alpha_n}\underline{\boldsymbol{R}} \end{pmatrix} \Delta\underline{\chi} - \begin{pmatrix} \underline{d}_n \\ -\sqrt{\alpha_n}\underline{\boldsymbol{R}}\underline{\chi}_n \end{pmatrix} \right\|^2 \tag{5.27}$$

which is equivalent to solving

$$(\underline{\boldsymbol{J}}_n^H \underline{\boldsymbol{J}}_n + \alpha_n \underline{\boldsymbol{R}}^H \underline{\boldsymbol{R}}) \Delta \underline{\chi}_n = \underline{\boldsymbol{J}}_n^H \underline{d}_n - \alpha_n \underline{\boldsymbol{R}}^H \underline{\boldsymbol{R}} \underline{\chi}_n. \tag{5.28}$$

It can be easily seen that by choosing $\underline{\boldsymbol{R}}$ equal to $\underline{\boldsymbol{A}}$, and α_n equal to either γ or λ_n, the penalty method applied to (4.29) is equivalent to the additive or additive-multiplicative regularization applied to the data misfit $\mathcal{C}^{\text{LS}}$. Also, by varying $\underline{\boldsymbol{R}}$ throughout the GNI iterations and choosing it to be $\underline{\boldsymbol{B}}_n$ at the n^{th} GNI iteration and setting α_n equal to β_n, the penalty method applied to (4.29) will be equivalent to the multiplicative regularization applied to $\mathcal{C}^{\text{LS}}$.

It can be shown that Krylov subspace regularization provides similar results to TSVD regularization [94, pg. 50], [74, pg. 146] due to the similarity between the Krylov subspace basis and the SVD basis. It can also be shown that the effect of TSVD regularization is very similar to that of Tikhonov regularization when $\Omega(\Delta\underline{\chi}) = \left\|\Delta\underline{\chi}\right\|^2$ [94, pg. 13], [23], [83]. Therefore, assuming appropriate regularization weight, Krylov subspace regularization and the TSVD regularization methods applied to (4.29) produce results which closely follow the

Tikhonov solution

$$\Delta\underline{\chi}_n = \arg\min_{\Delta\underline{\chi}} \left\{ \left\| \underline{\boldsymbol{J}}_n \Delta\underline{\chi} - \underline{d}_n \right\|^2 + \alpha_n \left\| \Delta\underline{\chi} \right\|^2 \right\}. \tag{5.29}$$

Now, assuming $\Omega(\Delta\underline{\chi})$ in (5.1) to be $\left\| \underline{\boldsymbol{R}}(\Delta\underline{\chi} + \underline{\chi}_n) \right\|^2$ and substituting $\underline{y} = \underline{\boldsymbol{R}}(\Delta\underline{\chi} + \underline{\chi}_n)$, the Tikhonov functional in (5.1) can be written as

$$\underline{y}_n = \arg\min_{\underline{y}} \left\{ \left\| \underline{\tilde{\boldsymbol{J}}}_n \underline{y} - \underline{\tilde{d}}_n \right\|^2 + \alpha_n \left\| \underline{y} \right\|^2 \right\} \tag{5.30}$$

where $\underline{\tilde{\boldsymbol{J}}}_n = \underline{\boldsymbol{J}}_n \underline{\boldsymbol{R}}^{-1}$ and $\underline{\tilde{d}}_n = \underline{d}_n + \underline{\boldsymbol{J}}_n \underline{\chi}_n$. Note that, here, we have implicitly assumed that the inverse of the regularization matrix $\underline{\boldsymbol{R}}$ exists, which is not always true. Having found $\underline{y}_n$ from (5.30), the correction $\Delta\underline{\chi}_n$ can be found by solving the well-posed system of equations

$$\underline{\boldsymbol{R}} \Delta\underline{\chi}_n = \underline{y}_n - \underline{\boldsymbol{R}} \underline{\chi}_n. \tag{5.31}$$

Using the aforementioned similarity between the Tikhonov regularization and Krylov subspace regularization as well as the TSVD regularization, the regularized solution $\underline{y}_n$ obtained from (5.30) will be similar to the regularized solution obtained by applying Krylov subspace regularization or the TSVD method to

$$\underline{\tilde{\boldsymbol{J}}}_n \underline{y}_n = \underline{\tilde{d}}_n. \tag{5.32}$$

Therefore, if we apply Krylov subspace regularization or the TSVD method to (5.32) to obtain $\underline{y}_n$, and then find $\Delta\underline{\chi}_n$ from (5.31), the resulting $\Delta\underline{\chi}_n$ will be similar to the Tikhonov solution when $\Omega(\Delta\underline{\chi}_n)$ is chosen to be $\left\| \underline{\boldsymbol{R}}(\Delta\underline{\chi}_n + \underline{\chi}_n) \right\|^2$ which satisfies (5.28). Therefore, the TSVD and Krylov subspace regularization methods can be viewed in the same form as (5.24), (5.25), (5.26) and (5.28) by applying them to (5.32) rather than (4.29).

It should be noted that these regularization methods, if modified as explained above, can all be applied from this framework and they will result in the same $\Delta\underline{\chi}_n$ for the appropriate choice of the regularization operator and its weight. However, their application will differ in some important aspects such as the computational complexity. For example, although Krylov subspace regularization and TSVD methods, applied to (4.29), will result in similar solutions, the computational complexity of Krylov subspace regularization is significantly less than that of the TSVD method. A more detailed computational complexity analysis of the regularization techniques considered here are described next in Section 5.4.

Among the regularization methods considered here, the additive-multiplicative and multiplicative regularization methods *automatically* adjust the regularization weight and provide adaptive regularization throughout the GNI iterations. As opposed to other regularization methods considered herein, the multiplicative regularization *automatically* changes the regularization operator, $\underline{\boldsymbol{\mathcal{L}}}_n$, during the GNI iterations. This will result in an edge-preserving regularization if the multiplicative regularizer is chosen as the weighted L^2-norm total variation of the unknown contrast.

5.4 Computational complexity analysis

To compare the computational complexity of the regularization techniques considered in this chapter, we utilize the conventions introduced in Section 4.5. Thus, $\underline{\boldsymbol{J}}_n \in \mathbb{C}^{M\times N}$ and the calculation of both $\underline{\boldsymbol{J}}_n\underline{r}$ ($\underline{r} \in \mathbb{C}^N$) and $\underline{\boldsymbol{J}}_n^H\underline{s}$ ($\underline{s} \in \mathbb{C}^M$) requires MN operations. The computational complexity of the CGLS and LSQR methods, as two Krylov subspace regularization schemes, is $2k \times (MN)$ when applied to (4.29) (k is the dimension of the projection). Note that the CGLS and LSQR methods require two matrix-vector multiplications in each iteration. As k is usually chosen to be a very small integer, this regularization technique can be

computationally attractive. The TSVD approach is computationally expensive as finding the SVD of the matrix $\underline{\boldsymbol{J}}_n$ in (4.29) requires $\mathcal{O}(MN^2)$ operations if $M \geq N$ or $\mathcal{O}(M^2N)$ when $M \leq N$ [90]. This can make the TSVD algorithm impractical for large-scale problems. It should also be noted that the TSVD method requires the explicit form of the matrix $\underline{\boldsymbol{J}}_n$ for performing the SVD. However, the other regularization methods discussed herein only require the definition of the matrix $\underline{\boldsymbol{J}}_n$ as a 'black-box' operator which implements two matrix vector multiplications: (*i*) $\underline{\boldsymbol{J}}_n \underline{r}$ and (*ii*) $\underline{\boldsymbol{J}}_n^H \underline{s}$. This can be very important in large-scale problems when the calculation of the explicit form of the Jacobian matrix is not feasible.

Comparing (5.3), (5.13), (5.20) and (5.22), it can be concluded that the computational complexity of the penalty methods and the methods which belong to the second strategy is very close. The main difference between these methods lies in the computational cost of multiplying $\underline{\boldsymbol{R}}^H \underline{\boldsymbol{R}}$, $\underline{\boldsymbol{\Sigma}}$ and $\underline{\boldsymbol{\mathcal{L}}}_n$ by an arbitrary vector of the proper size. Specifically, the matrix $\underline{\boldsymbol{\Sigma}}$ is a symmetric Block Toeplitz with Toeplitz Blocks [94, pg. 100] and its matrix-vector multiplication can be accelerated by the Fast Fourier Transform (FFT). Therefore, the computational complexity of $\underline{\boldsymbol{\Sigma}} \Delta \underline{\chi}_n$ can be ignored compared to that of $\underline{\boldsymbol{J}}_n^H \underline{\boldsymbol{J}} \Delta \underline{\chi}_n$. Using this approximation, the computational cost for finding the correction from (5.13) and (5.22) is about $2P \times (2MN)$ operations where P is the number of Conjugate Gradient (CG) iterations required for convergence (assuming that the CG method is used for solving (5.13) and (5.22)). Note that each iteration of the CG algorithm requires two matrix-vector multiplications and we have assumed that $\underline{\boldsymbol{J}}_n$ is only available as a 'black-box' operator. Therefore, it can be easily seen that the computational complexity of the Krylov subspace regularization applied to (4.29) is much less than that of the penalty methods as well as the methods of the second strategy due to the fact that usually $k \ll P$. However, it should be noted that the computational complexity of the Krylov subspace regularization techniques will increase drastically when applied to (5.32) as the operation of the matrices $\underline{\tilde{\boldsymbol{J}}}_n$ and $\underline{\tilde{\boldsymbol{J}}}_n^H$ on arbitrary vectors of correct size is expensive due to the presence of $\underline{\boldsymbol{R}}^{-1}$ in the definition of the matrix

$\underline{\tilde{\boldsymbol{J}}}_n$. If the methods of the first strategy utilize a standard regularization parameter-choice method, such as the *L*-curve algorithm or the GCV method, the computational cost of these algorithms needs to be considered in the overall computational cost of the regularization technique.

5.5 Comparison between different inversion results

Different regularization methods in conjunction with the Gauss-Newton inversion method for electromagnetic inverse scattering problems were studied and classified into two categories. It was shown that all of these regularization methods can be viewed from within a single consistent framework after applying some modifications. This framework helps to clarify the function of these regularization and may lead to future advances. Although, these regularization methods, after applying the modifications explained in Section (5.3), can result in the same reconstruction, it is instructive to compare their performance in their standard forms; *i.e.*, without applying any modifications to them. In this section, we compare the performance of the GNI algorithm using different regularization techniques against two experimental data sets; one assuming the TM polarization and the other assuming the TE polarization.

5.5.1 UPC Barcelona experimental data set

The Universitat Politècnica de Catalunya (UPC) Barcelona data set was collected using a near-field 2.33 GHz microwave scanner system which consists of 64 water-immersed antennas equispaced on a 12.5 cm-radius circular array [99]. In their system, for each case of using one of the 64 antennas as a sole transmitter, field data is collected using only the 33 antennas positioned in front of the transmitting antenna. The measured data is then cali-

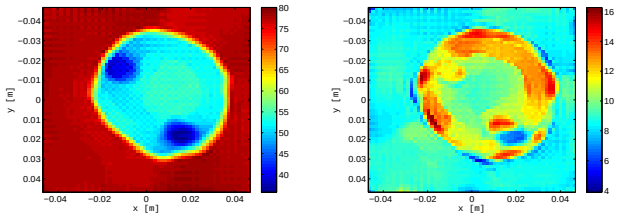

(a) $Re(\epsilon_r)$ (b) $Im(\epsilon_r)$

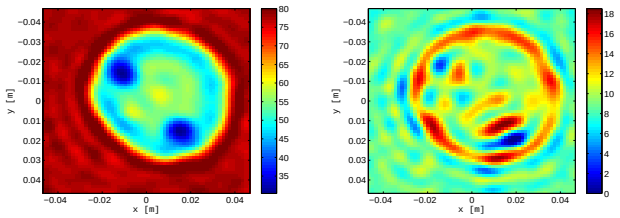

(c) $Re(\epsilon_r)$ (d) $Im(\epsilon_r)$

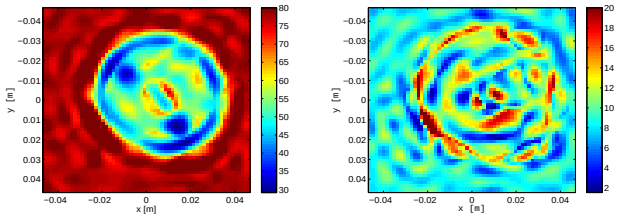

(e) $Re(\epsilon_r)$ (f) $Im(\epsilon_r)$

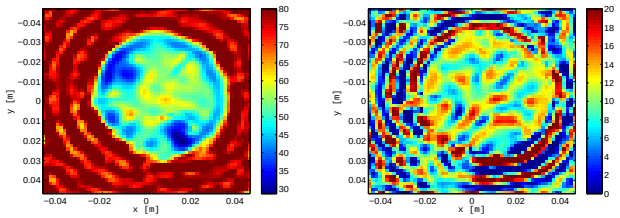

(g) $Re(\epsilon_r)$ (h) $Im(\epsilon_r)$

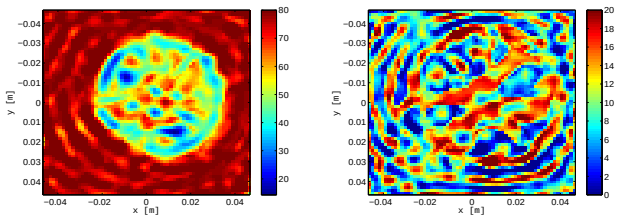

(i) $Re(\epsilon_r)$ (j) $Im(\epsilon_r)$

Fig. 5.3: UPC experimental data set: reconstructed relative complex permittivity of a real human forearm (BRAGREG data set) using (a)-(b): MR-GNI, (c)-(d): GNI with the additive-multiplicative L^2-norm total variation regularizer, (e)-(f): GNI with the additive L^2-norm total variation regularizer, (g)-(h): GNI with the identity Tikhonov regularizer, and (i)-(j): GNI with Krylov subspace regularization

brated such that a line source perpendicular to the imaging domain can be used to model the incident field inside $\mathcal{D}$ (2D-TM assumption). The data collection tank is filled with a background solution of water, having relative permittivity $\epsilon_b = 77.3 + j8.66$ at 2.33 GHz. In this thesis, we consider two targets from this data set; namely, BRAGREG and FANCENT. In this section, we invert the BRAGREG data set (data file: BRAGREG.ASC) which is collected from a real human forearm. The inversion results are constrained to lie within the region defined by $0 \leq \text{Re}(\epsilon_r) \leq 80$ and $0 \leq \text{Im}(\epsilon_r) \leq 20$, as in [11]. We consider the imaging domain $\mathcal{D}$ to be a 0.094 m $\times 0.094$ m square discretized into 60×60 pulse basis functions and start the MR-GNI algorithm, explained in Section 5.2.2, with $\chi = 0$. The reconstruction of this target using the MR-GNI method after 13 iterations is shown in figure 5.3 (a)-(b). The overall structure of the forearm can be seen in the images of the real and imaginary parts of the complex permittivity. The MR-GNI inversion is very similar to the MR-CSI reconstruction of this target [11]. The expected relative permittivities are approximately $54 + j11$ for muscle and $12 + j2.5$ for bones at $f = 2.33$ GHz according to [100]. Similar to the MR-CSI reconstruction of this target [11], the complex permittivity of the muscle is reconstructed well. However, the reconstructed real and imaginary parts of the bone complex permittivity are higher than their expected values due to the low dynamic range of the collected data [101, 11] as well as the use of the 2D-TM approximation for what is really a 3D problem. It should be noted that the contribution to the measured scattered field arising from within the bones is very small due to the high reflection coefficient at the bone–muscle boundary. The reconstruction of this target using GNI in conjunction with some other regularization techniques namely additive-multiplicative L^2-norm total variation (Section 5.2.3), additive L^2-norm total variation (Section 5.2.1), Tikhonov with $\underline{\boldsymbol{R}} = \underline{\boldsymbol{I}}$ (Section 5.1.1), and Krylov subspace (Section 5.1.2) regularizers, is shown in figure 5.3 (c)-(j). Comparing the GNI reconstructions of this target using different regularization methods, the edge-preserving characteristic of the utilized weighted L^2-norm total variation multiplicative regularizer can

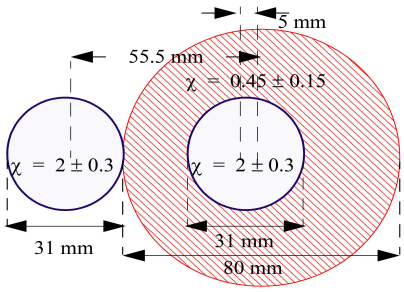

Fig. 5.4: *FoamTwinDiel* target from Institut Fresnel second experimental data set.

clearly be seen.

5.5.2 Institut Fresnel second experimental data set

For the second Institut Fresnel experimental data set [102], the transmitting and receiving antennas are both wide-band ridged horn antennas and are located on a circle of radius 1.67 m. This data set is collected from four different targets; namely, *FoamDielInt*, *FoamDielExt*, *FoamTwinDiel*, and *FoamMetExt*. These targets are all long circular cylinders and have no variations in the longitudinal direction. Both TE and TM polarizations are measured for each target and the background medium is free space. The *FoamDielInt* and *FoamDielExt* data sets are collected using 8 transmitters and 241 receivers per transmitter. The *FoamTwinDiel* and *FoamMetExt* data sets are collected using 18 transmitters and 241 receivers per transmitter. The *FoamDielInt*, *FoamDielExt*, and *FoamTwinDiel* data sets are collected for 9 frequencies from 2 GHz to 10 GHz, in 1 GHz step. The *FoamMetExt* data set is collected for 17 frequencies from 2 GHz to 18 GHz, in 1 GHz step. The measured data is then calibrated such that the horn transmitting and receiving antennas can be approximated by magnetic line sources in the TE case and electric line sources in the TM case [103]. In this thesis, we consider the inversion from all of these data sets. In this section, we consider the *FoamTwinDiel* target shown in figure 5.4 from which a TE data set has been collected (data

file: FoamDielExtTE.exp). The frequency of operation is chosen to be $f = 6$ GHz. The inversion of this data set using the GNI method using different regularization methods is shown in figure 5.5. Similar to the inversion of the human forearm data set, the reconstruction using the MR-GNI method outperforms the other reconstruction results.

5.6 Incorporating a priori information into the regularizer

Sometimes, there may be *a priori* information about the OI which can be incorporated into the inversion algorithm. One way to incorporate *a priori* information into the inversion algorithm is to include it in the regularizer. In this section, we consider two types of *a priori* information about the OI. In the first case, the goal is to find the shape and location of an OI which consists of some homogeneous objects with known permittivities. This problem is sometimes referred as shape and location reconstruction. The second case deals with *a priori* information about the average expected ratio between the real and imaginary parts of the OI's contrast.

5.6.1 Shape and location reconstruction

For binary location and shape reconstruction, where one is interested to find the shape and location of a homogeneous target with a known contrast χ^h, Crocco and Isernia [104] introduced an additive regularizer for the CSI algorithm which pushes each pixel in the imaging domain to have a contrast equal to either zero or χ^h. It should be noted that χ^h is not a function but a constant, $\chi^h \in \mathbb{C}$. Allowing the inversion algorithm to converge to a zero contrast is important as part of the imaging domain which is not occupied by the OI has the contrast of zero; *i.e.*, $\chi(\boldsymbol{q} \in \mathcal{D} - \text{OI}) = 0$. The weight of this additive regularizer was chosen using an *ad hoc* algorithm which does not provide an adaptive regularization [104]. Based on this

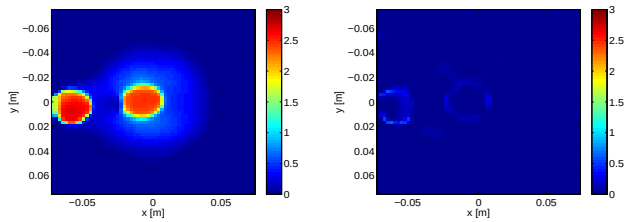

(a) $Re(\chi)$ (b) $Im(\chi)$

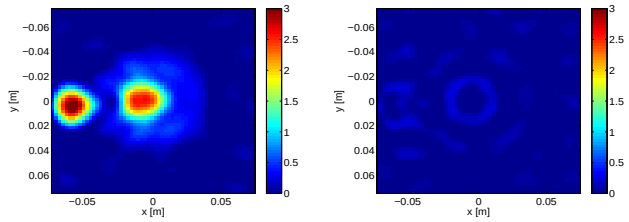

(c) $Re(\chi)$ (d) $Im(\chi)$

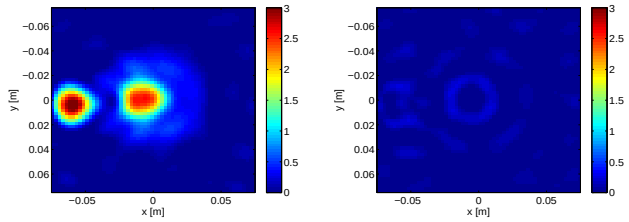

(e) $Re(\chi)$ (f) $Im(\chi)$

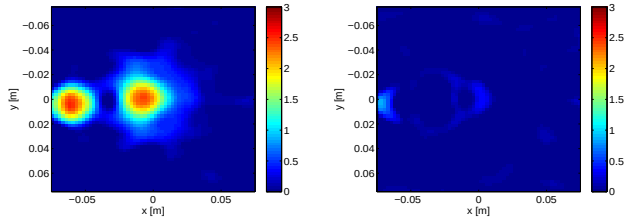

(g) $Re(\chi)$ (h) $Im(\chi)$

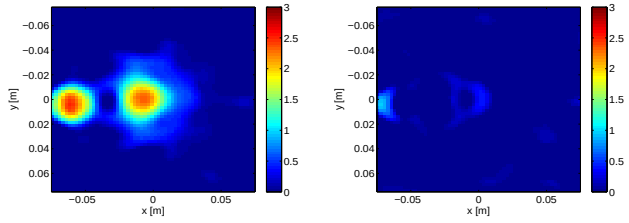

(i) $Re(\chi)$ (j) $Im(\chi)$

Fig. 5.5: Institut Fresnel experimental TE data set (*FoamTwinDiel* target): reconstructed contrast at the frequency of 6 GHz using (a)-(b): MR-GNI, (c)-(d): GNI with the additive-multiplicative L^2-norm total variation regularizer, (e)-(f): GNI with the additive L^2-norm total variation regularizer, (g)-(h): GNI with the identity Tikhonov regularizer, and (i)-(j): GNI with Krylov subspace regularization

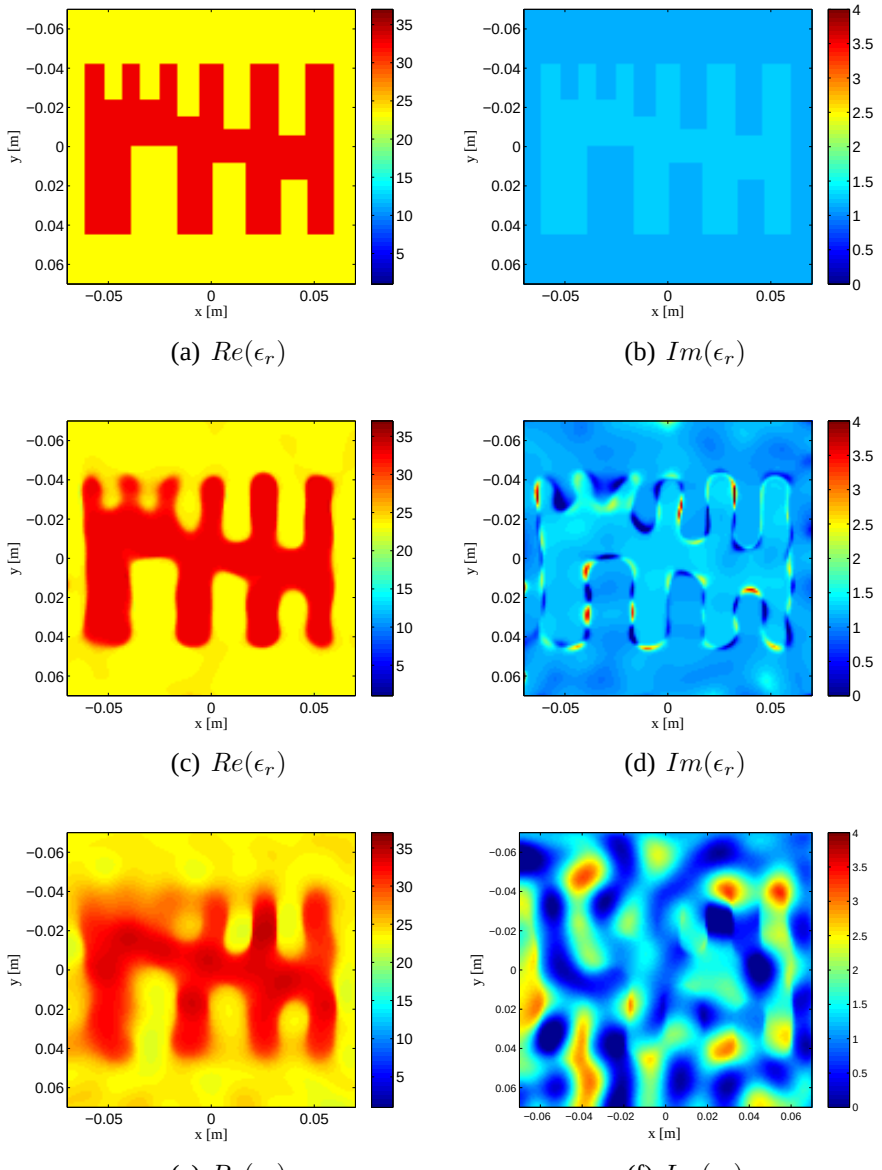

(a) $Re(\epsilon_r)$ (b) $Im(\epsilon_r)$

(c) $Re(\epsilon_r)$ (d) $Im(\epsilon_r)$

(e) $Re(\epsilon_r)$ (f) $Im(\epsilon_r)$

Fig. 5.6: Synthetic *E*-target data set (I) with TM illumination: (collected at $f = 1.5$ GHz) (a)-(b) true object, (c)-(d) shape and location reconstruction by assuming $\chi_1^h = 0$ and $\chi_2^h = 0.40 - j0.013$, and (e)-(f) the MR-GNI reconstruction (without shape and location reconstruction).

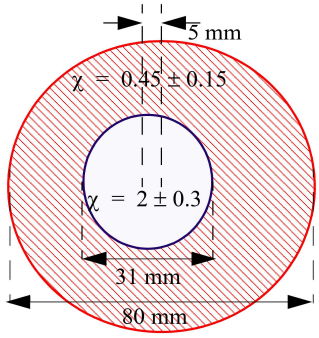

(a) *FoamDielInt* target

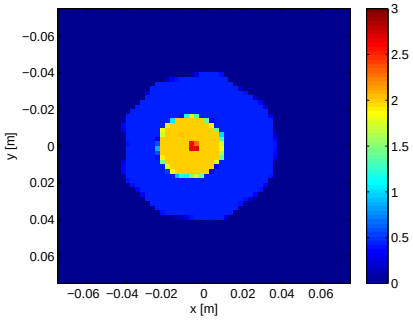

(b) $Re(\chi)$

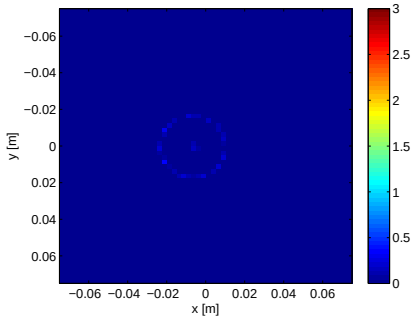

(c) $Im(\chi)$

Fig. 5.7: Institut Fresnel experimental TE data set ($f = 6$ GHz): (a) *FoamDielInt* target, (b)-(c) shape and location reconstruction of the *FoamDielInt* target (assuming $\chi_1^h = 0$, $\chi_2^h = 0.45$, and $\chi_3^h = 2$).

algorithm, Abubakar and van den Berg [105] introduced a multiplicative regularizer which can provide an adaptive regularization in the framework of the CSI algorithm. They also extended their algorithm for the case when there are several homogeneous targets inside the imaging domain. That is, it is more than a binary inversion algorithm which is only capable of reconstructing the shape and location of one homogeneous target. Based on [105], we introduce a GNI algorithm for shape and location reconstruction. As will be seen below, the proposed GNI algorithm is capable of incorporating *a priori* information about several homogeneous targets inside $\mathcal{D}$.

In the GNI method for shape and location reconstruction, the cost-functional to be mini-

mized at the n^{th} iteration of the algorithm is

$$\mathcal{C}_n(\chi) = \mathcal{C}^{\text{LS}}(\chi)\mathcal{C}_n^{\text{MR,hom}}(\chi). \tag{5.33}$$

The multiplicative regularizer $\mathcal{C}_n^{\text{MR,hom}}$ is given as

$$\mathcal{C}_n^{\text{MR,hom}}(\chi) = \frac{1}{A}\int_{\mathcal{D}} \prod_{l=1}^{L} \frac{\left|\chi(\boldsymbol{q}) - \chi_l^h\right|^2 + \alpha_n^2}{\left|\chi_n(\boldsymbol{q}) - \chi_l^h\right|^2 + \alpha_n^2} d\boldsymbol{q} \tag{5.34}$$

where $\chi_l^h \in \mathbb{C}$ is the l^{th} known homogeneous contrast in the imaging domain. The positive parameter α_n^2 is chosen to be $\mathcal{C}^{\text{LS}}(\chi_n)$. The required derivatives for this regularizer to be used in the framework of the GNI method can be written as (see Section D.4 for the derivations)

$$\frac{\partial \tilde{\mathcal{C}}_n^{\text{MR,hom}}}{\partial \chi^*}(\psi^*) = \left\{ \frac{\partial \tilde{\mathcal{C}}_n^{\text{MR,hom}}}{\partial \chi}(\psi) \right\}^* = \left\langle \frac{1}{A}\sum_{l=1}^{L} \xi_{l,n}^2 \left(\chi_n - \chi_l^h\right), \psi \right\rangle_{\mathcal{D}}, \tag{5.35}$$

$$\left[\frac{\partial^2 \tilde{\mathcal{C}}_n^{\text{MR,hom}}}{\partial \chi^* \partial \chi}|_{\chi=\chi_n}(\varphi)\right](\psi^*) = \left\{ \left[\frac{\partial^2 \tilde{\mathcal{C}}_n^{\text{MR,hom}}}{\partial \chi \partial \chi^*}|_{\chi=\chi_n}(\varphi^*)\right](\psi) \right\}^* = \left\langle \frac{1}{A}\sum_{l=1}^{L} \xi_{l,n}^2 \varphi, \psi \right\rangle_{\mathcal{D}}, \tag{5.36}$$

and,

$$\left[\frac{\partial^2 \tilde{\mathcal{C}}_n^{\text{MR,hom}}}{\partial \chi \partial \chi}|_{\chi=\chi_n}(\varphi)\right](\psi) = \left\{ \left[\frac{\partial^2 \tilde{\mathcal{C}}_n^{\text{MR,hom}}}{\partial \chi^* \partial \chi^*}|_{\chi=\chi_n}(\varphi^*)\right](\psi^*) \right\}^* = 0, \tag{5.37}$$

where $\tilde{\mathcal{C}}_n^{\text{MR,hom}}(\chi, \chi^*) = \mathcal{C}_n^{\text{MR,hom}}(\chi)$ and

$$\xi_{l,n}(\boldsymbol{q}) \triangleq \left(\left|\chi_n(\boldsymbol{q}) - \chi_l^h\right|^2 + \alpha_n^2\right)^{-\frac{1}{2}}. \tag{5.38}$$

Thus, the correction in the discrete domain can be found by satisfying

$$(\underline{\boldsymbol{J}}_n^H \underline{\boldsymbol{J}}_n + \beta_n \sum_{l=1}^{L} \underline{\boldsymbol{D}}_{l,n}) \Delta \underline{\chi}_n = \underline{\boldsymbol{J}}_n^H \underline{d}_n - \beta_n \sum_{l=1}^{L} \underline{\boldsymbol{D}}_{l,n}(\underline{\chi}_n - \chi_l^h \underline{e}) \tag{5.39}$$

where $\underline{e} \in \mathbb{C}^N$ is a vector of all ones. The matrix $\underline{\underline{\boldsymbol{D}}}_{l,n} \in \mathbb{C}^{N\times N}$ is a diagonal matrix whose diagonal elements are given as

$$\underline{\underline{\boldsymbol{D}}}_{l,n} = \text{diag}\left(\frac{1}{A}\underline{\xi}^2_{l,n}\right), \tag{5.40}$$

where $\underline{\xi}^2_{l,n} \in \mathbb{C}^N$ is the discretized form of $\xi^2_{l,n}(\boldsymbol{q})$. The regularization weight β_n is also $\|\underline{d}_n\|^2$.

Using this GNI algorithm, we show two different inversions; one with the TM polarization and the other with the TE polarization. For the first example, we consider a synthetic data set which we refer to as the synthetic *E*-target data set (I). The target, shown in figure 5.6 (a)-(b), has the same geometry as the target used in [106] for a resolution test study. The relative complex permittivity of the target is $32.7 + j1.28$ and that of the background medium is $23.4 + j1.13$. At the frequency of 1.5 GHz, the OI is illuminated by 16 transmitters, which are electric line sources (TM illumination) and equally spaced on a circle of radius 0.1 m. The scattered field data is collected at 16 receivers per transmitter. We then add 3% noise to this synthetically collected data set (according to (4.31)). The inversion is then performed on a different grid and using another discretization compared to the ones used to collect the synthetic data set (to avoid the inverse crime). For the inversion algorithm, we utilize two different values for χ^h; namely $\chi^h_1 = 0$ and $\chi^h_2 = 0.40 - j0.013$. We note that χ^h_2 is the contrast corresponding to the relative complex perimittivity of the OI. Using these two values for χ^h, the shape and location inversion of this target is shown in figure 5.6 (c)-(d) which shows an accurate reconstruction of the target's shape and location. We have also shown the MR-GNI reconstruction of this target, which is a *blind* inversion of this data set, in figure 5.6 (e)-(f).

The first example is the inversion of the *FoamDielInt* target from the Institut Fresnel second TE experimental data set explained in Section 5.5.2. The target, shown in figure 5.7 (a),

consists of two cylinders with contrasts of $\chi = 0.45 \pm 0.15$ and 2 ± 0.3. Thus, the inversion algorithm utilizes three different values for χ^h; namely, $\chi_1^h = 0$, $\chi_2^h = 0.45$, and $\chi_3^h = 2$. Using these three different χ^h, the GNI algorithm converged in 8 iterations and the inversion results are shown in figure 5.7 (b)-(c). As can be seen, the algorithm accurately reconstructs the shape and location of the two homogeneous objects.

5.6.2 Pre-scaled Gauss-Newton inversion algorithm

In some applications such as biomedical imaging, the magnitude of the real and imaginary parts of the expected contrast can be considerably out of balance [107]. Usually, it is the real part of the contrast which is much larger than the imaginary part of the contrast. Therefore, the inversion algorithm will inadvertently favor the reconstruction of the real part over that of the imaginary part. This usually results in an oscillatory reconstruction in the reconstructed imaginary part of the contrast. To enhance the imaginary-part reconstruction for these cases, Meaney *et. al.* have suggested a pre-scaled Gauss-Newton inversion algorithm based on Tikhonov regularization which balances the reconstruction of the real and imaginary parts of the contrast by introducing a variable for the scaled real part of the contrast and optimizing with respect to this scaled real part and the imaginary part of the contrast.

Inspired by the work of Meaney *et. al.* [107], we present a pre-scaled multiplicative regularized Gauss-Newton inversion method. We accomplish this by introducing the cost-functional

$$\mathcal{C}(\chi_R, \chi_I) = \mathcal{C}^{\text{LS}}(\chi_R, \chi_I)\mathcal{C}^{\text{MR,scaled}}(\chi_R, \chi_I). \tag{5.41}$$

Note that $\mathcal{C}^{\text{LS}}(\chi_R, \chi_I)$ is just $\mathcal{C}^{\text{LS}}(\chi)$ when $\chi = \chi_R + j\chi_I$. The multiplicative regularizer

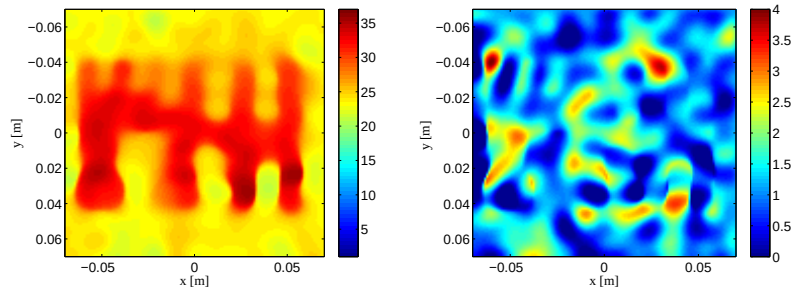

(a) $Re(\epsilon_r)$ (b) $Im(\epsilon_r)$

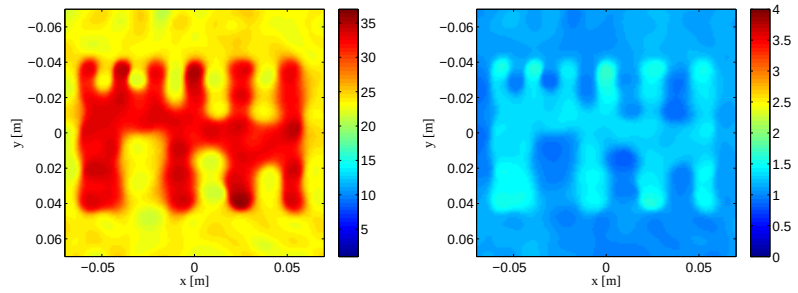

(c) $Re(\epsilon_r)$ (d) $Im(\epsilon_r)$

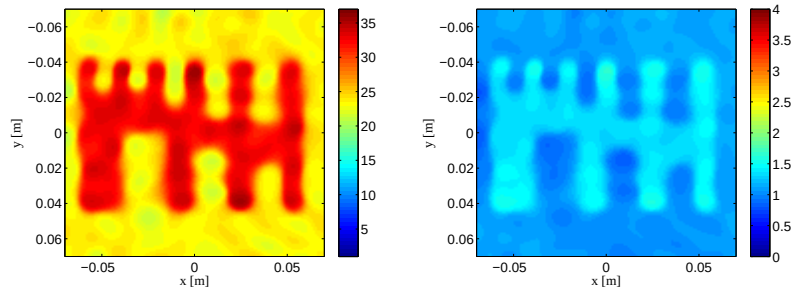

(e) $Re(\epsilon_r)$ (f) $Im(\epsilon_r)$

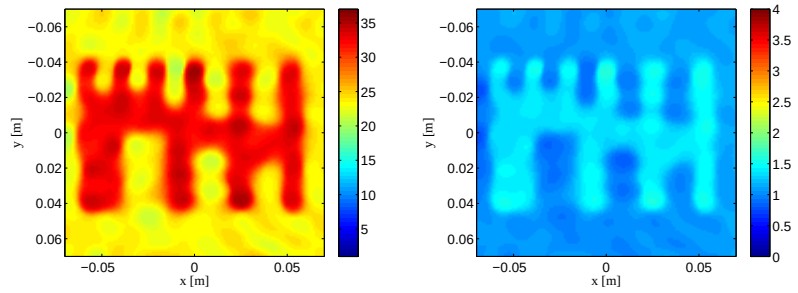

(g) $Re(\epsilon_r)$ (h) $Im(\epsilon_r)$

Fig. 5.8: Inversion of the synthetic *E*-target data set II with TM illumination (collected at $f = 2$ GHz) using (a)-(b) MR-GNI, (c)-(d) pre-scaled MR-GNI with $Q = 20$, (e)-(f) pre-scaled MR-GNI with $Q = 40$, and (g)-(h) pre-scaled MR-GNI with $Q = 60$.

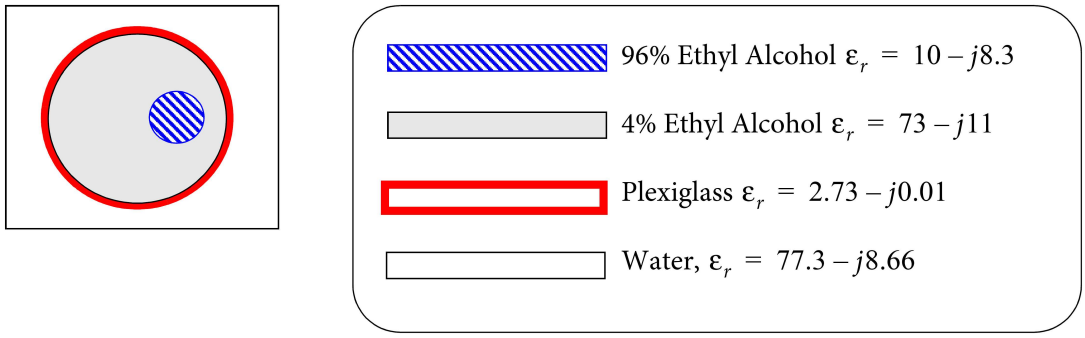

Fig. 5.9: The schematic of the FANCENT phantom from UPC Barcelona experimental data set.

$\mathcal{C}^{\text{MR,scaled}}(\chi_R, \chi_I)$ at the n^{th} iteration of the algorithm is given as

$$\mathcal{C}_n^{\text{MR,scaled}}(\chi_R, \chi_I) = \frac{1}{A}\int_{\mathcal{D}} \frac{|\nabla\chi_R|^2 + Q^2\,|\nabla\chi_I|^2 + \alpha_n^2}{|\nabla\chi_{R,n}|^2 + Q^2\,|\nabla\chi_{I,n}|^2 + \alpha_n^2} d\boldsymbol{q} \tag{5.42}$$

where $\chi_{R,n}$ and $\chi_{I,n}$ are the real and imaginary parts of the known predicted contrast at the n^{th} iteration of the GNI algorithm. The positive parameter α_n^2 is chosen in the same way presented in Section 5.2.2. The positive real parameter $Q \in \mathbb{R}^+$ is selected based on the average expected ratio between the real part and imaginary part of the OI's expected contrast. As can be seen, the weight of $|\nabla\chi_I|$ is chosen to be Q times more than that of $|\nabla\chi_R|$. When Q is chosen to be 1, $\mathcal{C}_n^{\text{MR,scaled}}$ will be the same as $\mathcal{C}_n^{\text{MR}}$ given in (5.15).

As in the procedure explained in Chapter 4, which was to find $\Delta\chi$ and $\Delta\chi^*$, the correction $\Delta\chi_{R,n}$ and $\Delta\chi_{I,n}$ may be found by satisfying

$$\begin{pmatrix} \frac{\partial^2\mathcal{C}}{\partial\chi_R\partial\chi_R}|_{\chi=\chi_n} & \frac{\partial^2\mathcal{C}}{\partial\chi_R\partial\chi_I}|_{\chi=\chi_n} \\ \frac{\partial^2\mathcal{C}}{\partial\chi_I\partial\chi_R}|_{\chi=\chi_n} & \frac{\partial^2\mathcal{C}}{\partial\chi_I\partial\chi_I}|_{\chi=\chi_n} \end{pmatrix} \begin{pmatrix} \Delta\chi_{R,n} \\ \Delta\chi_{I,n} \end{pmatrix} = - \begin{pmatrix} \frac{\partial\mathcal{C}}{\partial\chi_R}|_{\chi=\chi_n} \\ \frac{\partial\mathcal{C}}{\partial\chi_I}|_{\chi=\chi_n} \end{pmatrix} \tag{5.43}$$

where $\chi_n = \chi_{R,n} + j\chi_{I,n}$. Similar to the work of Meaney *et. al.* [107] which introduces a dummy variable to balance the average magnitude of the real and imaginary parts of the contrast when solving for $\Delta\chi_{R,n}$ and $\Delta\chi_{I,n}$, we introduce the variable $\chi_R^{\text{scaled}} = \chi_R/Q$; thus,

balancing the average magnitude of χ_R^{scaled} and χ_I. We, therefore, optimize over χ_R^{scaled} and χ_I. In other words, instead of satisfying (5.43), we satisfy

$$\begin{pmatrix} Q^2 \frac{\partial^2 \mathcal{C}}{\partial \chi_R \partial \chi_R}|_{\chi=\chi_n} & Q \frac{\partial^2 \mathcal{C}}{\partial \chi_R \partial \chi_I}|_{\chi=\chi_n} \\ Q \frac{\partial^2 \mathcal{C}}{\partial \chi_I \partial \chi_R}|_{\chi=\chi_n} & \frac{\partial^2 \mathcal{C}}{\partial \chi_I \partial \chi_I}|_{\chi=\chi_n} \end{pmatrix} \begin{pmatrix} \Delta\chi_{R,n}^{\text{scaled}} \\ \Delta\chi_{I,n} \end{pmatrix} = - \begin{pmatrix} Q \frac{\partial \mathcal{C}}{\partial \chi_R}|_{\chi=\chi_n} \\ \frac{\partial \mathcal{C}}{\partial \chi_I}|_{\chi=\chi_n} \end{pmatrix}. \tag{5.44}$$

After finding $\Delta\chi_{R,n}^{\text{scaled}}$, and $\Delta\chi_{I,n}$ from the above equation, the real and imaginary parts of the contrast is updated in the form of $\chi_{R,n+1} = \chi_{R,n} + \alpha_n \Delta\chi_{R,n}$ and $\chi_{I,n+1} = \chi_{I,n} + \alpha_n \Delta\chi_{I,n}$ where α_n is an appropriate step-length and $\Delta\chi_{R,n} = Q\Delta\chi_{R,n}^{\text{scaled}}$.

The derivative operators required for solving (5.44) are derived in Section D.5. Noting that the operator $\frac{\partial^2 \mathcal{E}_i^{\text{scat}}}{\partial \chi^2}$ is neglected in the GNI method, the discrete form of (5.44) will be

$$\begin{pmatrix} Q^2 \text{Re}\left(\underline{\boldsymbol{J}}_n^H \underline{\boldsymbol{J}}_n\right) - \beta_n Q^2 \underline{\boldsymbol{\mathcal{L}}}_n^{\text{scaled}} & -Q\text{Im}\left(\underline{\boldsymbol{J}}_n^H \underline{\boldsymbol{J}}_n\right) \\ Q\text{Im}\left(\underline{\boldsymbol{J}}_n^H \underline{\boldsymbol{J}}_n\right) & \text{Re}\left(\underline{\boldsymbol{J}}_n^H \underline{\boldsymbol{J}}_n\right) - Q^2 \beta_n \underline{\boldsymbol{\mathcal{L}}}_n^{\text{scaled}} \end{pmatrix} \begin{pmatrix} \Delta\underline{\chi}_{R,n}^{\text{scaled}} \\ \Delta\underline{\chi}_{I,n} \end{pmatrix} = \begin{pmatrix} Q\text{Re}\left(\underline{\boldsymbol{J}}_n^H \underline{d}_n\right) + Q\beta_n \underline{\boldsymbol{\mathcal{L}}}_n^{\text{scaled}} \underline{\chi}_{R,n} \\ \text{Im}\left(\underline{\boldsymbol{J}}_n^H \underline{d}_n\right) + Q^2 \beta_n \underline{\boldsymbol{\mathcal{L}}}_n^{\text{scaled}} \underline{\chi}_{I,n} \end{pmatrix}, \tag{5.45}$$

where $\beta_n^2 = \|\underline{d}_n\|^2$. The operator $\underline{\boldsymbol{\mathcal{L}}}_n^{\text{scaled}}$ is the discrete form of the operator $\nabla \cdot \left[(b_n^{\text{scaled}})^2 \nabla\right]$ where

$$b_n^{\text{scaled}}(\boldsymbol{q}) \triangleq A^{-\frac{1}{2}} (|\nabla\chi_{R,n}(\boldsymbol{q})|^2 + Q^2 |\nabla\chi_{I,n}(\boldsymbol{q})|^2 + \alpha_n^2)^{-\frac{1}{2}}. \tag{5.46}$$

We note that when $Q = 1$, solving (5.45) is equivalent to solving (5.20), the problem formulated in terms of $\Delta\chi$ and $\Delta\chi^*$. This can be easily seen by multiplying the second row of (5.45) by j and adding that to the first row of (5.45), and is a verification that optimizing over χ_R and χ_I is equivalent of that over χ and χ^*.

Using the proposed pre-scaled MR-GNI, we show the inversion of two different data sets.

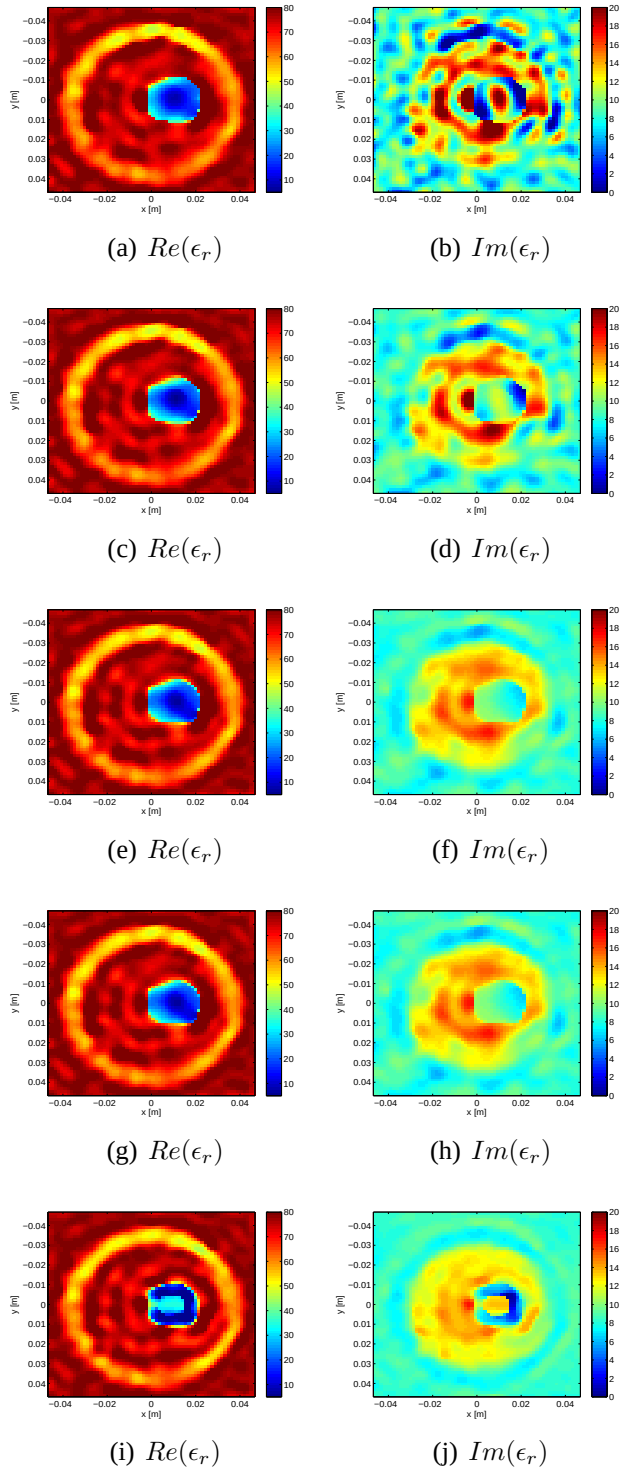

(a) $Re(\epsilon_r)$ (b) $Im(\epsilon_r)$

(c) $Re(\epsilon_r)$ (d) $Im(\epsilon_r)$

(e) $Re(\epsilon_r)$ (f) $Im(\epsilon_r)$

(g) $Re(\epsilon_r)$ (h) $Im(\epsilon_r)$

(i) $Re(\epsilon_r)$ (j) $Im(\epsilon_r)$

Fig. 5.10: Reconstructed relative complex permittivity of the FANCENT phantom from UPC Barcelona experimental data set (TM illumination) using (a)-(b) MR-GNI, (c)-(d) pre-scaled MR-GNI with $Q = 2$, (e)-(f) pre-scaled MR-GNI with $Q = 5$, (g)-(h) pre-scaled MR-GNI with $Q = 10$, and (i)-(j) pre-scaled MR-GNI with $Q = 20$.

The first one is the synthetic data set collected from the *E*-target at $f = 2$ GHz using the same procedure explained in Section 5.6.1. We refer to this data set as the synthetic *E*-target data set (II). The inversion of this data set using the MR-GNI, which is explained in Section 5.2.2 and is equivalent to the proposed pre-scaled MR-GNI method with $Q = 1$, is shown in figure 5.8 (a)-(b). As can be seen, the imaginary-part reconstruction is very oscillatory. We now use the pre-scaled MR-GNI method with three different values of Q; namely $Q = 20$, $Q = 40$, and $Q = 60$. As can be seen in figure 5.8 (c)-(h), all of these three pre-scaled inversions are successful in reconstructing the imaginary part of the contrast. We note that the true ratio between the real and imaginary parts of the OI's contrast is about 40 (see Section 5.6.1).

As another example, we consider the FANCENT phantom from the UPC Barcelona experimental data set which is calibrated for the TM polarization. The UPC MWT system was explained in Section 5.5.1. The FANCENT phantom is shown in figure 5.9. The inversion results are constrained to lie within the region defined by $0 \leq \text{Re}(\epsilon_r) \leq 80$ and $0 \leq \text{Im}(\epsilon_r) \leq 20$, as in [11]. The MR-GNI inversion of this data set is shown in figure 5.10 (a)-(b). Although the real-part reconstruction is satisfactory, the imaginary-part reconstruction is very oscillatory. We now use the pre-scaled MR-GNI method with four different values for Q. As can be seen, having Q equal to 2, 5, and 10 improves the imaginary-part reconstruction compared to the MR-GNI reconstruction. However, increasing Q to 20 starts deteriorating the reconstruction. We note that the ratio between the real and imaginary parts of the contrast is about 9.5 in 96% ethyl alcohol and 1.7 in 4% ethyl alcohol.

5.7 An image enhancement algorithm

After the GNI method converges to a final solution (image), say $\hat{\chi}$, this final reconstruction can still be enhanced using a post-processing image enhancement algorithm. Although this topic is not related to the regularization of the data misfit cost-functional, it is presented in this chapter as it is based on the weighted L^2-norm total variation multiplicative regularization. Inspired by the work of Abubakar *et. al.* on a deblurring algorithm for linear inverse problems [108], we enhance the final reconstruction of the GNI method by the weighted L^2-norm total variation multiplicative regularizer. We accomplish this by first approximating the nonlinear operator $\mathcal{E}_t^{\text{scat}}$, (2.20), with the linear operator $\mathcal{K}_t$ defined as

$$\mathcal{K}_t(\chi) = \mathcal{G}_{\mathcal{S}}\left[\chi\left(\mathcal{I} - \mathcal{G}_{\mathcal{D}}^{\hat{\chi}}\right)^{-1}\left(\boldsymbol{E}_t^{\text{inc}}\right)\right] = \mathcal{G}_{\mathcal{S}}\left[\chi\mathcal{E}_t(\hat{\chi})\right] = \mathcal{G}_{\mathcal{S}}\left(\chi\boldsymbol{E}_t^{\hat{\chi}}\right) \tag{5.47}$$

where $\boldsymbol{E}_t^{\hat{\chi}} = \mathcal{E}_t(\hat{\chi})$ is the known total field inside $\mathcal{D}$ due to the known contrast $\hat{\chi}$ when the t^{th} transmitter is active. We then construct the linear cost-functional $\mathcal{C}^{\text{Lin}}$ as

$$\mathcal{C}^{\text{Lin}}(\chi) = \eta_{\mathcal{S}}\sum_{t=1}^{T_x}\left\|\mathcal{K}_t(\chi) - \boldsymbol{E}_{\text{meas},t}^{\text{scat}}\right\|_{\mathcal{S}}^2 \tag{5.48}$$

This cost-functional is then regularized as

$$\mathcal{C}(\chi) = \mathcal{C}^{\text{lin}}(\chi)\mathcal{C}^{\text{R}}(\chi). \tag{5.49}$$

This multiplicatively regularized cost-functional $\mathcal{C}(\chi)$ is minimized using the Conjugate Gradient (CG) method over the contrast χ where the initial guess to the CG algorithm is the final reconstruction from the GNI method; *i.e.*, $\hat{\chi}$. At the m^{th} iteration of the CG method,

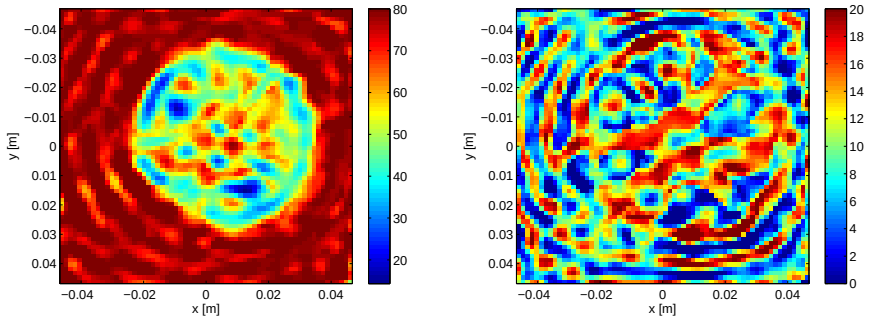

(a) $Re(\epsilon_r)$ (b) $Im(\epsilon_r)$

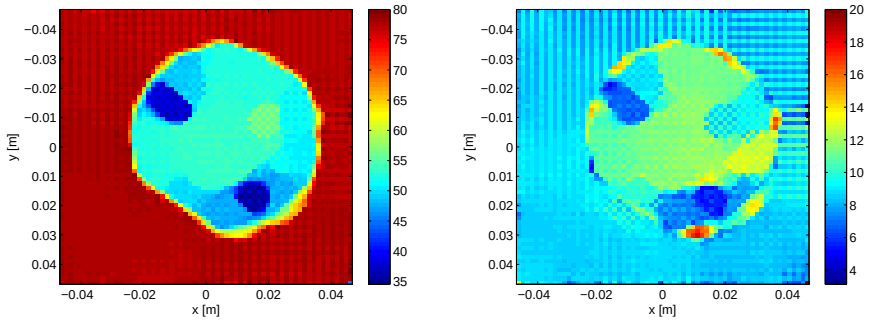

(c) $Re(\epsilon_r)$ (d) $Im(\epsilon_r)$

Fig. 5.11: Real human forearm: (a)-(b) reconstruction using the GNI-CGLS method and (c)-(d) its corresponding enhanced reconstruction.

where χ_m is known, the multiplicative regularizer is given by

$$\mathcal{C}_m^{\mathrm{R}}(\chi) = \frac{1}{A}\int_{\mathcal{D}} \frac{|\nabla\chi(\boldsymbol{q})|^2 + \delta_{m+1}^2}{|\nabla\chi_m(\boldsymbol{q})|^2 + \delta_m^2} d\boldsymbol{q} \tag{5.50}$$

To ensure the convexity of the cost-functional (5.49), the positive parameter δ_{m+1}^2 is chosen to be [108],

$$\delta_{m+1}^2 = \frac{1}{2}\frac{\|b_m \nabla\chi_m\|_{\mathcal{D}}^2}{\|b_m\|_{\mathcal{D}}^2} \tag{5.51}$$

where $b_m \triangleq A^{-\frac{1}{2}}(|\nabla\chi_m|^2 + \delta_m^2)^{-\frac{1}{2}}$.

In the discrete domain, the contrast vector is updated as

$$\underline{\chi}_{m+1} = \begin{cases} \hat{\underline{\chi}} & m = 0 \\ \underline{\chi}_m + \alpha_m \underline{v}_m & m \geq 1 \end{cases} \tag{5.52}$$

where $\underline{v}_m$ is the CG direction at the m^{th} iteration of the image enhancement algorithm and α_m is a real number (step-length). The CG direction $\underline{v}_m$ can be found from [109]

$$\underline{v}_m = \begin{cases} \underline{g}_1 & m = 1 \\ \underline{g}_m + \frac{\left\|\underline{g}_m\right\|^2}{\left\|\underline{g}_{m-1}\right\|^2} \underline{v}_{m-1} & m \geq 2 \end{cases} \tag{5.53}$$

where $\underline{g}_m$ (gradient) is the maximum rate of change in the cost-functional, (5.49), at the m^{th} iteration. It is well-known that it is the derivative with respect to $\underline{\chi}^*$ which defines the maximum rate of change [71]. In the continuous domain, this derivative may be found as

$$\frac{\partial \tilde{\mathcal{C}}}{\partial \chi^*}|_{\chi=\chi_m}(\psi^*) = \left\langle \eta_{\mathcal{S}} \mathcal{C}_m^{\text{R}}(\chi_m) \sum_{t=1}^{T_x} \mathcal{K}_t^a \left(\mathcal{K}_t(\chi_m) - \boldsymbol{E}_{\text{meas},t}^{\text{scat}} \right) - \mathcal{C}^{\text{lin}}(\chi_m) \mathcal{L}_m \chi_m, \psi \right\rangle_{\mathcal{D}} \tag{5.54}$$

where $\mathcal{L}_m \chi_m = \nabla \cdot (b_m^2 \nabla \chi_m)$ and $\tilde{\mathcal{C}}(\chi, \chi^*) = \mathcal{C}(\chi)$. Thus, in the discrete domain, the gradient $\underline{g}_m$ will be

$$\underline{g}_m = \eta_{\mathcal{S}} \mathcal{F}_m^{\text{R}}(\underline{\chi}_m) \underline{\boldsymbol{K}}^H (\underline{\boldsymbol{K}}\, \underline{\chi}_m - \underline{E}_{\text{meas}}^{\text{scat}}) - \mathcal{F}^{\text{lin}}(\underline{\chi}_m) \underline{\boldsymbol{\mathcal{L}}}_m \underline{\chi}_m \tag{5.55}$$

where $\underline{\boldsymbol{K}} \in \mathbb{C}^{M \times N}$ is the matrix which represents the discrete forms of $\mathcal{K}_t$ operators and $\underline{\boldsymbol{\mathcal{L}}}_m$ is the discrete form of $\mathcal{L}_m$. The cost-functionals $\mathcal{F}_m^{\text{R}}(\underline{\chi}_m)$ and $\mathcal{F}^{\text{lin}}(\underline{\chi}_m)$ are also the discrete forms of $\mathcal{C}_m^{\text{R}}(\chi_m)$ and $\mathcal{C}^{\text{lin}}(\chi_m)$ respectively. The closed-form expression for the step-length α_m can be found in [108]. As in [108], the enhancement procedure terminates when the normalized difference between two successive enhanced contrasts becomes less

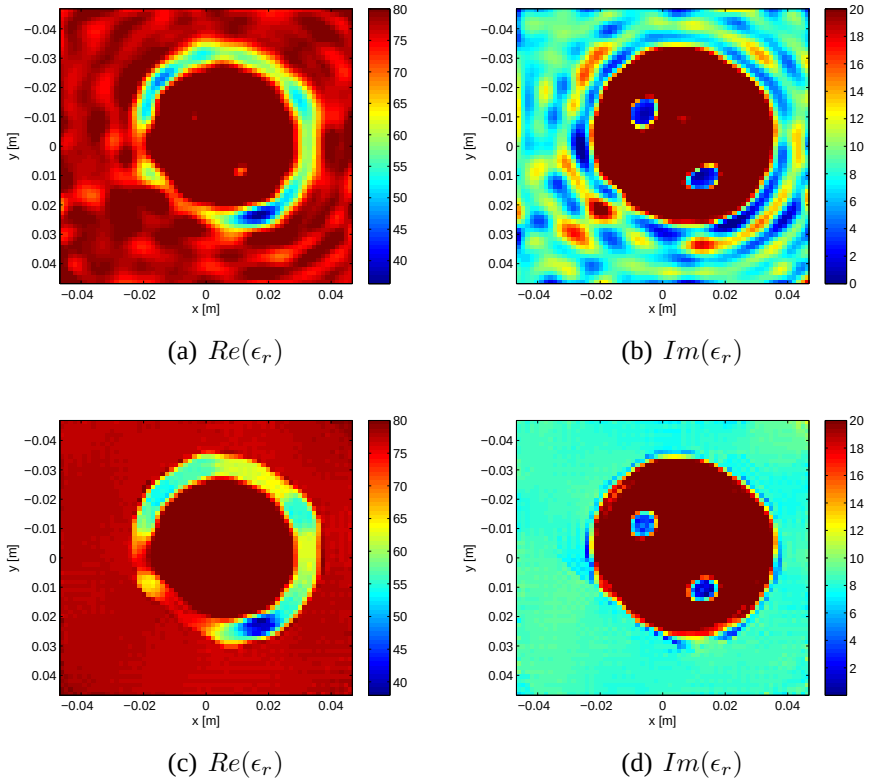

(a) $Re(\epsilon_r)$ (b) $Im(\epsilon_r)$

(c) $Re(\epsilon_r)$ (d) $Im(\epsilon_r)$

Fig. 5.12: (a)-(b) Reconstruction of the human forearm at the 5^{th} iteration of the GNI-CGLS method and (c)-(d) its corresponding enhanced reconstruction.

than a prescribed tolerance:

$$\frac{\|\chi_{m+1} - \chi_m\|^2_{\mathcal{D}}}{\|\chi_{m+1}\|^2_{\mathcal{D}}} < \text{tol}. \tag{5.56}$$

In our implementation, the prescribed tolerance, tol, is set to be 10^{-6}.

To show the performance of this enhancement algorithm, we consider two different experimental data sets; one with the TM polarization and the other one with the TE polarization. In both cases, we start the inversion algorithm with $\chi = 0$. For the inversion algorithm, we utilize the GNI algorithm equipped with the CGLS regularization technique. We refer to this algorithm, which is explained in Section 5.1.2, as the GNI-CGLS method. The stopping iteration of the CGLS regularization scheme is chosen using the *ad hoc* two-step procedure outlined in [12]. The GNI-CGLS and the enhancement algorithms were run as Matlab

scripts on quad-core 2.66 GHz machine. The utilized forward solver in the GNI method is a Method of Moments (MoM) solver which utilizes the CG method accelerated by the Fast Fourier Transform (FFT) [37] and the marching-on-in-source-position technique [38].

We apply the GNI-CGLS algorithm to the real human forearm data set which was described in Section 5.5.1. The GNI-CGLS algorithm converged after 24 iterations and the data misfit $\mathcal{C}^{\text{LS}}$ at the last iteration was 4.7%. The inversion result using the GNI-CGLS algorithm is shown in figure 5.11 (a)-(b)[4] where the reconstruction results are very oscillatory. The enhancement algorithm was then applied to this reconstruction which took 312 CG iterations applied to (5.49). The computation times were 31 minutes for the GNI-CGLS method and 4 minutes for the enhancement algorithm.

The enhanced reconstruction, shown in figure 5.11 (c)-(d), shows the overall structure of the arm as well as the positions of the two bones clearly. It can easily be seen that the utilized enhancement suppresses the spurious oscillations in the original reconstruction and also preserves the edges of the two bones. The reconstructed permittivity for the muscle tissue is close to the expected value; however, the reconstructed permittivity of the bones is higher than the expected value.

The data misfit $\mathcal{C}^{\text{LS}}$ for the enhanced reconstructed contrast is 5.2% which is slightly larger than the data misfit corresponding to the GNI-CGLS reconstructed contrast. This may seem surprising at first, but it is well-known that if inversion algorithms converge to where the data misfit is below the noise level, then the convergence is probably to the wrong local minimum. That is, a smaller data misfit cost-functional $\mathcal{C}^{\text{LS}}$ does not necessarily mean a better reconstruction as the data misfit should not become smaller than the noise level of the calibrated measured data (Morozov discrepancy principle [110]). Due to several sources of error in the calibrated measured data such as modeling the horn antennas by line sources,

[4] This is the same reconstruction as the one shown in figure 5.3 (i)-(j).

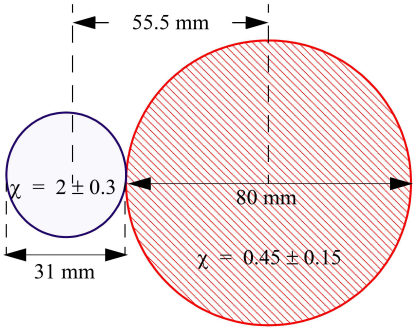

(a) *FoamDielExtTE* target

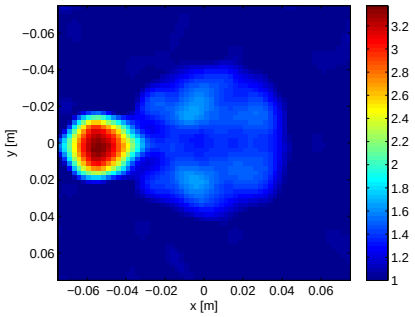

(b) $Re(\epsilon_r)$

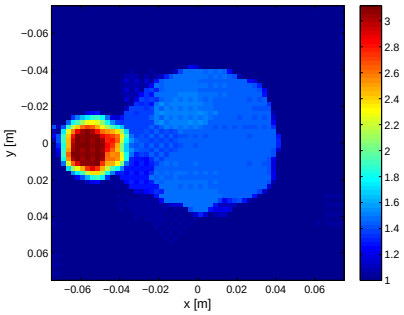

(c) $Re(\epsilon_r)$

Fig. 5.13: (a) *FoamDielExt* target (b) TE inversion of the *FoamDielExt* (real part) using the GNI-CGLS method, and (b) its corresponding enhanced reconstruction.

possible temperature shifts and the actual measurement noise, it is not easy, if not impossible, to find the noise level of the calibrated measured data.

To show the performance of the enhancement algorithm when the GNI-CGLS algorithm is not completely converged, we consider the reconstructed contrast at the 5^{th} iteration of the GNI-CGLS algorithm whose corresponding $\mathcal{C}^{\text{LS}}$ is 20%. The reconstructed contrast at this iteration has been shown in figure 5.12 (a)-(b). We took this contrast to be $\hat{\chi}$ in (5.47) and constructed its corresponding matrix $\boldsymbol{K}$. The enhancement algorithm was then performed which took 105 CG iterations. The enhanced contrast corresponding to this choice of $\hat{\chi}$ is shown in figure 5.12 (c)-(d). It can be seen that the MR enhancement also successfully improves this contrast which is not the final converged solution of the GNI-CGLS method.

Finally, we consider the *FoamDielExt* target, shown in figure 5.13 (a), from the Institut Fresnel second TE experimental data set. This data set was described in Section 5.5.2. The GNI-CGLS inversion of this multiple-frequency TE data set converged after 24 iterations where the real part of the reconstructed permittivity is shown in figure 5.13 (b). We have used a frequency-hopping technique as outline in [111] to utilize the scattering data collected at 9 different frequencies. With the frequency-hopping technique, the data from each frequency are inverted independently, and the solution from the lower frequency is used as the initial guess for the next higher frequency. Within this thesis, we refer to this form of inverting multiple frequency data as the multiple-frequency reconstruction[5]. The imaginary part of the reconstructed permittivity (not shown here) is very small indicating a lossless object. The data misfit $\mathcal{C}^{\text{LS}}$ for the final reconstruction at 10 GHz is 4.3%. The enhancement of this reconstruction, which took 74 CG iterations applied to (5.49), is shown in figure 5.13 (c). The computation times were 2 hours and 57 minutes for the GNI-CGLS algorithm and 4 minutes for the enhancement. The data misfit for the enhanced rconstruction at 10 GHz is 4.1%. For this target, both reconstructions are very good due to having a high signal to noise ratio in the measured data as well as utilizing multiple-frequency data in the inversion.

In Section 8.2, we also show the performance of this enhancement when $\hat{\chi}$ is the final reconstruction from the MR-GNI algorithm. As will be seen there, the enhancement algorithm still improves the final reconstruction of the MR-GNI method.

[5] Another form of inverting multiple frequency data is to invert the data from all frequencies simultaneously [112].

6

TM Versus TE Inversion

I remember my first look at the great treatise of Maxwell's when I was a young man... I saw that it was great, greater and greatest, with prodigious possibilities in its power... I was determined to master the book and set to work. I was very ignorant. I had no knowledge of mathematical analysis (having learned only school algebra and trigonometry which I had largely forgotten) and thus my work was laid out for me. It took me several years before I could understand as much as I possibly could. Then I set Maxwell aside and followed my own course. And I progressed much more quickly... It will be understood that I preach the gospel according to my interpretation of Maxwell. (Oliver Heaviside [113])

Several 2D Transverse Magnetic (TM) inversion algorithms have been tested against experimental data whereas only a few 2D Transverse Electric (TE) inversion methods have been investigated experimentally. The 2D TM problem can be formulated as a scalar problem for a single electric field component. This is not the case for 2D TE problems where two electric field components in the transverse plane need to be taken into account in the formulation and this results in a more complex (*i.e.*, vectorial) formulation compared to the

TM case. It should be noted that TE problems can also be formulated as scalar problems for a single magnetic field component. However, for the TE inversion, it has been shown in [29] that inverting the integral equation for the two electric field components is more stable and has better performance than inverting the integral equation of the single magnetic field component.

From a physical perspective, the TE-polarized case includes polarization charges at dielectric discontinuities, which are difficult to model numerically [114]. On the other hand, TE-polarized data may contain more useful information about the object of interest as it is based on two different components of the electric field as opposed to one in the TM-polarized case. Note that these two polarizations are physically uncoupled: they provide independent information about the object being imaged. This fact can be used to improve the reconstruction in tomographic configurations by either simultaneously inverting TE and TM data [115] or using a cascaded TE-TM algorithm [116, 117].

There are only a few reports on the inversion of TE experimental data (using any method). In the special edition of the journal *Inverse Problems* dedicated to inversions of the first Fresnel data set [118], only two papers dealt with the single TE case data that was provided: the first one [119] was concerned with determining the shape of the conducting u-shaped scatterer and the second one [103] used the MR-CSI method to reconstruct the dielectric contrast of this scatterer. In the second special edition of *Inverse Problems* dedicated to the second Fresnel data set [102, 120], which includes TE and TM data for four targets, only two contributions addressed the TE-polarized data: the first one [112] applied the MR-CSI method to reconstruct the constitutive parameters of all the targets in the data set and in the second contribution [121], a TM inversion algorithm based on the Diagonal Tensor Approximation and the Contrast Source Inversion method (DTA-CSI) was applied to invert the TE-polarized data. This last contribution uses a *calibration* of the TE data in a way that,

according to the authors, allows the use of the scalar TM inversion algorithm. In addition, a 2D TE bi-conjugate gradient inversion method is used in [117] to reconstruct buried objects from experimental TE scattering data. In [122] an iterative multi-scaling approach was applied to the single u-shaped metal target case from the first Fresnel data set, in both TE and TM illuminations. Most recently, a TE stochastic inversion algorithm which utilizes *a priori* information about the object of interest has been used to reconstruct the second Fresnel data set [123].

In this chapter, the GNI method is applied to the complete second TE Fresnel experimental data set which are combinations of lossless dielectric and metallic cylinders. As the Fresnel data contains only far-field scattering data, we also show the performance of the TE inversion against near-field synthetic scattering data. These TE inversions are compared with the TM inversions of the same targets. The motivation for moving to the near-field is that it is postulated that the independent information available in the near-field TE data may results in better images compared to the near-field TM case. This does not hold in the far-field, because in the far-field assuming $\boldsymbol{E} = E_{\varphi}\hat{\varphi}$, where $\boldsymbol{E}$ denotes the electric field and $\hat{\varphi}$ is the unit vector in the φ direction (figure 2.1), is a good approximation for the TE case. We note that the scalar component E_{φ} is simple to measure. In the near-field such an approximation is not valid and therefore two orthogonal field components need to be measured independently. This is difficult in practice and is one reason why 2D TE near-field microwave tomography systems have not been constructed. It should be noted that the two orthogonal electric field components of TE near-field configurations can be extracted by measuring the single magnetic field component and then taking the derivative thereof. To compute an accurate derivative, magnetic field measurements must be performed in close proximities, which can cause difficulties in microwave tomography systems with co-resident antenna arrays (*e.g.*, coupling between the co-resident antennas [124]). However, in TE far-field configurations, one can measure the single magnetic field component and then use a

plane-wave approximation in order to extract the electric field from the magnetic field.

The main contribution of this chapter is to provide a quantitative comparison of TE and TM inversions of synthetic and experimental data sets for various cases including near-field and far-field imaging. This includes a comparison of computational complexity, image quality and convergence rate. The result of the TE versus TM investigation presented in this chapter may be useful for justifying the added cost of TE tomography systems.

6.1 Theoretical computational complexity analysis

Before presenting inversion results, a description of the per-iteration computational complexity of the utilized TE and TM GNI algorithms is now given. We consider the GNI method with the additive-multiplicative regularization as explained in Section 5.2.3. The following conventions are used: the total number of receiver positions is denoted by R_x, and the number of receiver positions per transmitter by R. The number of CG iterations required for the TE and TM forward solvers are denoted by F_{TE} and F_{TM}, respectively. The number of CG iterations to find the Gauss-Newton correction in the TE and TM cases are denoted by P_{TE} and P_{TM}, respectively.

6.1.1 Jacobian matrix

As mentioned in Section 4.5, each row of the Jacobian matrix $\underline{\boldsymbol{J}}_n$ corresponds to the derivatives of the scattered field over the pixels of the imaging domain for a particular receiver located at, say, $\boldsymbol{p}$ and a particular polarization along some direction, say, $\hat{\tau}$ and a particular transmitter, say, the t^{th} transmitter as given in (4.26).

Finding the distorted dyadic Green's function for the R_x different receiver positions requires calling the forward solver $2R_x$ times in the TE case and R_x times in the TM case. This is due to the fact that two different polarizations should be considered in the TE illumination while only one polarization is needed for the TM illumination. The computational cost of finding $\boldsymbol{E}_t(\boldsymbol{q};\chi_n)$ for different transmitter locations is T_x calls of the forward solver for both TE and TM cases as the TE-polarized data is calibrated (or synthetically created) using an infinite magnetic line source directed in $\hat{z}$ direction.

In our implementation, the elements of the matrix $\underline{\boldsymbol{J}}_n$, as given in (4.26), are not found explicitly because we only need to do the right matrix-vector multiplication using $\underline{\boldsymbol{J}}_n$ and $\underline{\boldsymbol{J}}_n^H$, see for example (5.22). Therefore, the integration and the dot-product $\boldsymbol{E}_t \cdot \bar{\bar{G}}^{\text{inh}}$, required in (4.26), is computed when $\underline{\boldsymbol{J}}_n$ (or $\underline{\boldsymbol{J}}_n^H$) operate on a vector and will be considered in the computational complexity of finding the correction.

6.1.2 The correction

Solving $\Delta_{\underline{\chi}_n}$ in (5.22) using CG requires multiplying $\underline{\boldsymbol{J}}_n^H \underline{\boldsymbol{J}}_n$ by a vector and this requires approximately $8RT_xN$ multiplications in the TE case and $2RT_xN$ multiplications in the TM case. This can be explained as follows: in the TE case, the multiplication of the Jacobian matrix $\underline{\boldsymbol{J}}_n$ with a vector $\underline{r} \in \mathbb{C}^{N\times 1}$ can be written as,

$$\underline{\boldsymbol{J}}_n \, \underline{r} = \begin{pmatrix} \underline{\boldsymbol{G}}^{\text{inh}}_{xx,n}(\underline{E}_{x,n} \odot \underline{r}) + \underline{\boldsymbol{G}}^{\text{inh}}_{yx,n}(\underline{E}_{y,n} \odot \underline{r}) \\ \underline{\boldsymbol{G}}^{\text{inh}}_{xy,n}(\underline{E}_{x,n} \odot \underline{r}) + \underline{\boldsymbol{G}}^{\text{inh}}_{yy,n}(\underline{E}_{y,n} \odot \underline{r}) \end{pmatrix}, \tag{6.1}$$

and in the TM case as

$$\underline{\boldsymbol{J}}_n \, \underline{r} = \underline{\boldsymbol{G}}^{\text{inh}}_{zz,n}(\underline{E}_{z,n} \odot \underline{r}), \tag{6.2}$$

where $\underline{\underline{\boldsymbol{G}}}^{\text{inh}}_{\varsigma\eta,n}$ represents the matrix form of the $\hat{\varsigma}\hat{\eta}$-component of the distorted dyadic Green's function and $\underline{E}_{\varsigma,n}$ denotes the vector form of the $\hat{\varsigma}$-component of the total field within the imaging domain. Both $\underline{\underline{\boldsymbol{G}}}^{\text{inh}}_{\varsigma\eta,n}$ and $\underline{E}_{\varsigma,n}$ correspond to the predicted contrast $\underline{\chi}_n$. The operation $\odot$ denotes the elementwise product (Hadamard product) of two conforming vectors. Using (6.1) and (6.2), it can be concluded that the matrix-vector multiplication $\underline{\underline{\boldsymbol{J}}}_n\, \underline{r}$ requires approximately $4RT_xN$ operations in the TE case and R_xT_xN operations in the TM case. The same conclusion can be drawn for multiplying the matrix $\underline{\underline{\boldsymbol{J}}}_n^H$ by an arbitrary vector of the correct size. Therefore, the computational cost of calculating $\underline{\underline{\boldsymbol{J}}}_n^H \underline{\underline{\boldsymbol{J}}}_n \Delta\underline{\chi}_n$, as required in (5.22), is about $8RT_xN$ in the TE case and $2RT_xN$ in the TM case.

The matrix $\underline{\underline{\boldsymbol{\Sigma}}}$ for a rectangular imaging domain is a symmetric Block Toeplitz matrix with Toeplitz Blocks [94, pg. 100], so its multiplication with a vector can be accelerated using the FFT; thus, the computational cost of $\underline{\underline{\boldsymbol{\Sigma}}}\Delta\underline{\chi}_n$ is neglected compared to that of $\underline{\underline{\boldsymbol{J}}}_n^H \underline{\underline{\boldsymbol{J}}}_n \Delta\underline{\chi}_n$. Therefore, the computational cost for finding the Gauss–Newton correction is about $2P_{\text{TE}} \times (8RT_xN)$ for the TE case and $2P_{\text{TM}} \times (2RT_xN)$ for the TM case. Note that each iteration of the CG algorithm requires two matrix-vector multiplications. Assuming $P_{\text{TE}} \approx P_{\text{TM}}$, the computational complexity of finding the correction in the TE case is almost four times more than that in the TM case.

6.1.3 The forward solver

In both the TE and TM polarization solutions, we employ a CG-FFT forward solver as explained in [59]. The discretization procedure used in the TE forward solver has been described in Appendix F. A comparison between the computational complexity of the TE CG-FFT and TM CG-FFT forward solvers is provided in [59]. As discussed in [59], it can be shown that the per-iteration computational complexity of the TE CG-FFT algorithm, utilized in the forward solver, is approximately twice that of the TM case.

6.1.4 Line search

The computational cost of the utilized line search algorithm is approximately equal to that of evaluating $\mathcal{F}(\underline{\chi}_n + \nu_n \Delta\underline{\chi}_n)$ for the known background Green's function and this is equal to calling the forward solver T_x times for both TE and TM cases. We note that $\mathcal{F}(\underline{\chi})$ is the discrete form of $\mathcal{C}(\chi)$ given in (5.21) in the case of additive-multiplicative regularization. As mentioned earlier, if the full step satisfies the condition (4.23), we choose it as an appropriate step-length. From our experience with the regularized cost-functional (5.21) (as well as (5.14)), the full step mostly satisfies the condition (4.23); therefore, very few calls to this line search algorithm are made in the cases that we have run. This can be explained as follows. In the Gauss-Newton optimization, the correction $\Delta\underline{\chi}_n$ may lead to an increase in the cost-functional if (*i*) $\underline{\boldsymbol{J}}_n^H \underline{\boldsymbol{J}}_n - \lambda_n \underline{\boldsymbol{\Sigma}}$, see (5.22), is not positive-definite, or (*ii*) the quadratic model of the nonlinear regularized cost-functional $\mathcal{F}(\underline{\chi})$ at $\underline{\chi}_n$ is not a *good* approximation to $\mathcal{F}(\underline{\chi})$ [42]. As pointed out in Section 5.3, the matrix $\underline{\boldsymbol{J}}_n^H \underline{\boldsymbol{J}}_n - \lambda_n \underline{\boldsymbol{\Sigma}}$ is positive definite. Moreover, due to the use of adaptive regularization, the regularization weight λ_n is maximum at early GNI iterations where the predicted contrast can be very far from the true solution. Thus, at early GNI iterations, the quadratic model of $\mathcal{F}(\underline{\chi})$ is dominated by that of the regularizer. Noting that the regularizer is an L^2-norm, the quadratic model of the regularized cost-functional has a good chance to be a good approximation of $\mathcal{F}(\underline{\chi})$ at early GNI iterations. As the algorithm gets closer to the true solution, the regularization weight λ_n is lessened. Thus, the quadratic model of the regularized cost-functional is dominated by that of the data misfit functional. Due to the fact that the predicted contrast is close to the true solution, the quadratic model of the regularized cost-functional has a good chance to be a good approximation of $\mathcal{F}(\underline{\chi})$. Therefore, the use of adaptive regularization will usually make the quadratic model of the regularized cost-functional be a good approximation to $\mathcal{F}(\underline{\chi})$.

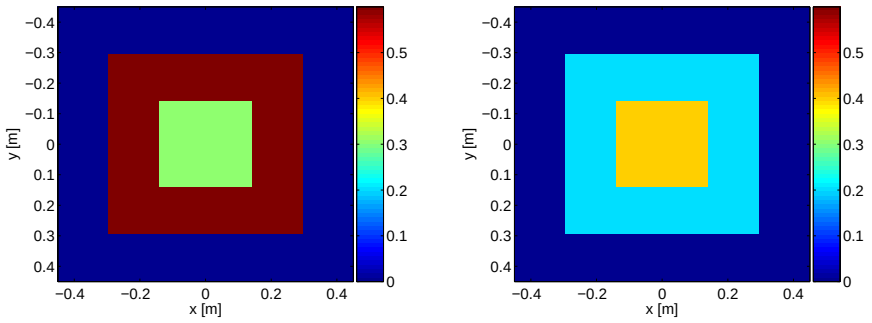

(a) $Re(\chi)$ (b) $Im(\chi)$

Fig. 6.1: The exact contrast of the scatterer for the synthetic test case (concentric squares)

6.2 Inversion results

The inversion results from both synthetic and experimental data are now shown. To be able to compare the TE inversion with the TM inversion, we introduce an image error cost–functional defined as,

$$\mathcal{M}(\underline{\chi}) = \frac{\left\|\underline{\chi} - \underline{\chi}^{\text{true}}\right\|^2}{\left\|\underline{\chi}^{\text{true}}\right\|^2} \tag{6.3}$$

where $\underline{\chi}$ is the final reconstruction, $\underline{\chi}^{\text{true}}$ is the true contrast and $\|.\|$ denotes the L^2-norm on $\mathbb{C}^N$. For the experimental data, $\underline{\chi}^{\text{true}}$ is created according to the geometrical configurations and the average permittivity of the object being imaged. For the synthetic data, as the data is generated on a different grid than the one used in the GNI algorithm (to avoid an inverse crime), the image error cost–functional (6.3) is calculated by interpolating onto a finer and finer mesh until the calculated norm converges. For the synthetic data sets, all parameters of the forward solver are kept the same for the TE and TM polarizations. We have also added 3% RMS additive white noise to the synthetic data set using the formula (4.31).

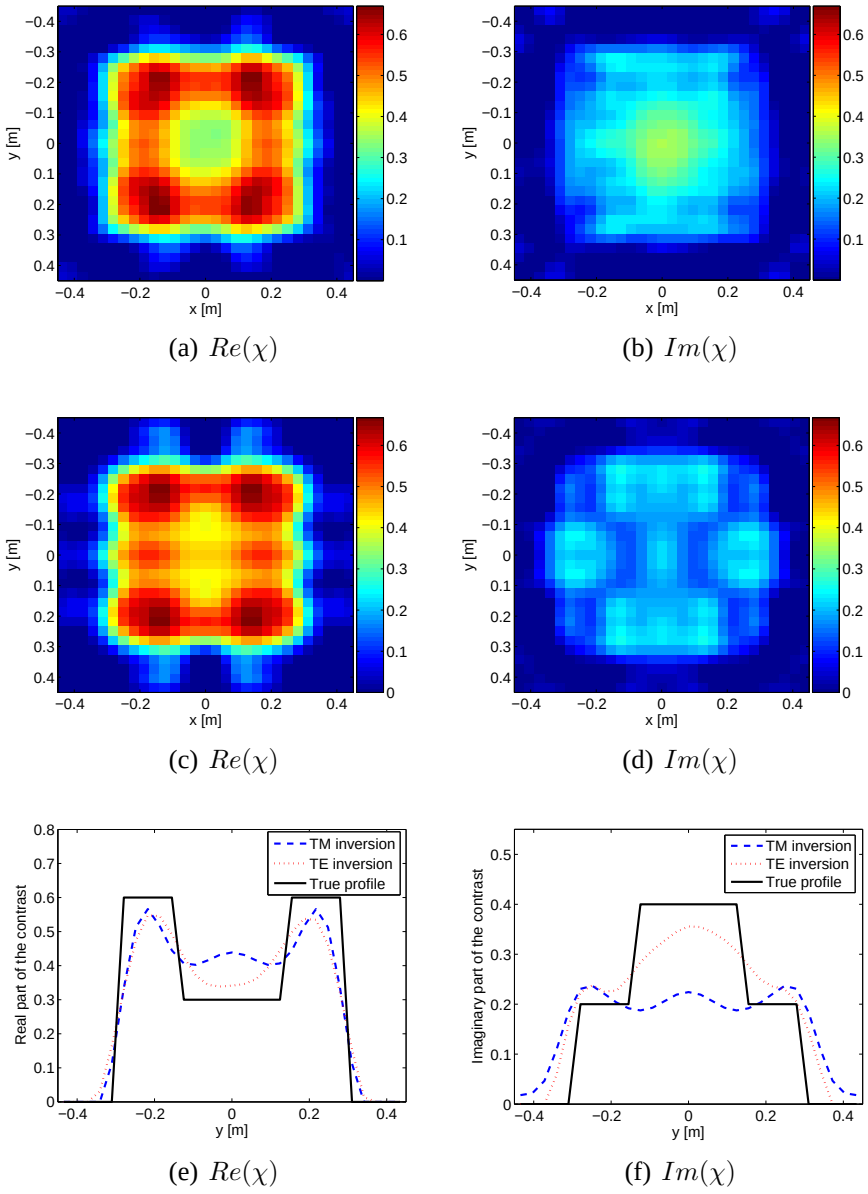

(a) $Re(\chi)$ (b) $Im(\chi)$

(c) $Re(\chi)$ (d) $Im(\chi)$

(e) $Re(\chi)$ (f) $Im(\chi)$

Fig. 6.2: Inversion of the concentric squares synthetic data set using the GNI method with additive-multiplicative regularization (the first scenario: $T_x = 10$ and $R = R_x = 10$) (a)-(b) TE case, (c)-(d) TM case, and (e)-(f) cross-section at $x = 0$.

6.2.1 Synthetic data: concentric squares

We consider a similar test case which has been used in [48, 125, 29]. The scatterer consists of two concentric squares with an inner square having dimension of $\lambda_b \times \lambda_b$ (λ_b is the wavelength in the background medium) with a contrast of $0.3 + j0.4$. The inner square is surrounded by an exterior square having sides of $2\lambda_b$ and contrast $\chi = 0.6 + j0.2$. The exact contrast profile is shown in figure 6.1. The frequency of operation is chosen to be 1 GHz and free space is assumed for the background medium. The imaging domain $\mathcal{D}$ consists of a square having sides of $3\lambda_b$. We consider three different scenarios for collecting the data. In the first scenario, we choose 10 transmitters and 10 receivers ($R_x = R = 10$) on the measurement circle $\mathcal{S}$ and in the second scenario, we choose 30 transmitters and 30 receivers ($R_x = R = 30$) on $\mathcal{S}$. Therefore, the length of the vector $\underline{E}^{\text{meas}}$ in the second scenario is 9 times that of $\underline{E}^{\text{meas}}$ in the first scenario. In these two scenarios, the transmitters and receivers are placed evenly on the measurement circle $\mathcal{S}$ of radius $2.33\lambda_b = 70$ cm. In the third scenario, we choose 10 transmitters and 10 receivers ($R_x = R = 10$) evenly placed on the measurement circle $\mathcal{S}$ of radius $10\lambda_b = 300$ cm. The forward data is then generated on a grid of 30×30 for both TE and TM polarizations. The transmitters for the TE and TM cases are the magnetic line source and electric line source respectively. For the TE case, E_x and E_y components are collected at the receiver positions whereas in the TM case, the E_z component is collected. We will note that the synthetically collected data in the first and second scenarios may be considered as the near-field data whereas the collected data in the third scenario is at far-field.

For the first scenario, the TE and TM inversions are shown in figure 6.2. As can be seen, both TE and TM inversions provide good reconstructions for the real part of the contrast profile. However, the TM inversion is not successful in reconstructing the imaginary part of the contrast: the inner square is unresolved in the imaginary part of the TM inversion.

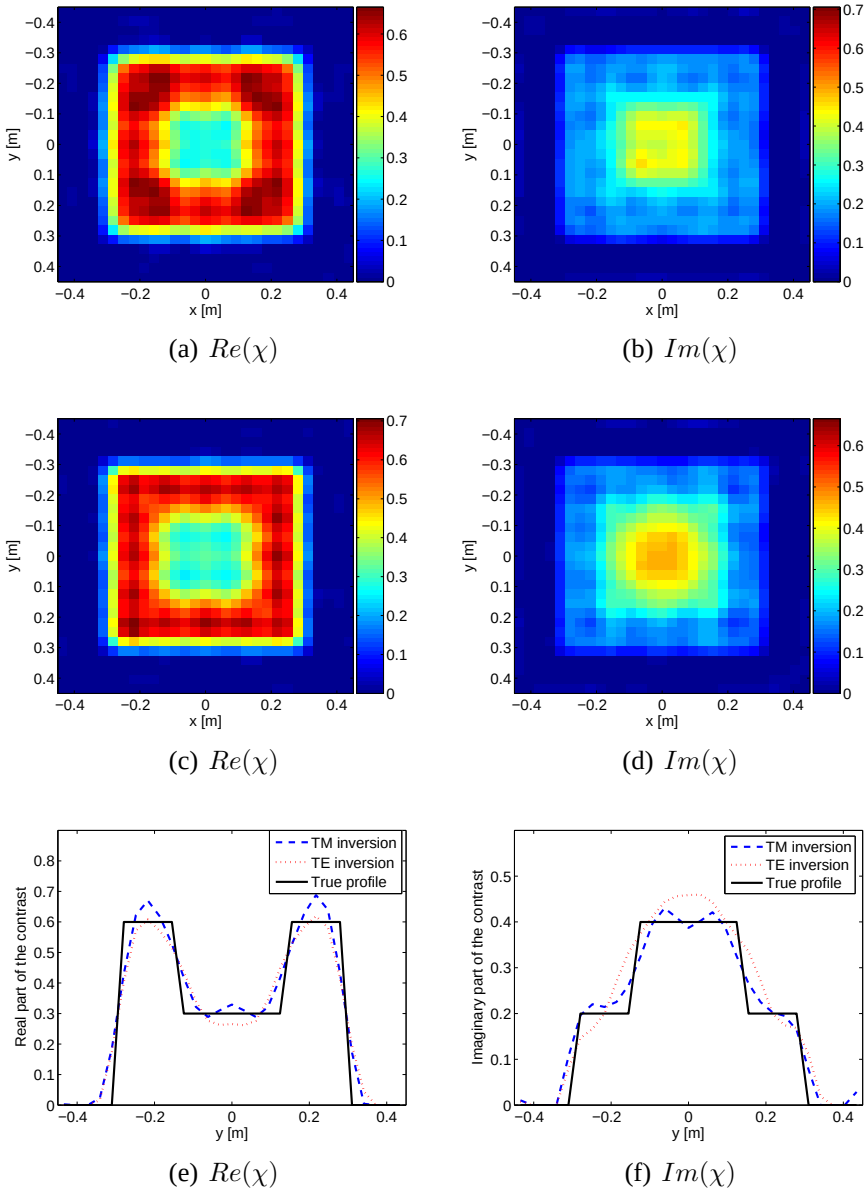

(a) $Re(\chi)$ (b) $Im(\chi)$

(c) $Re(\chi)$ (d) $Im(\chi)$

(e) $Re(\chi)$ (f) $Im(\chi)$

Fig. 6.3: Inversion of the concentric squares synthetic data set using the GNI method with additive-multiplicative regularization (the second scenario: $T_x = 30$ and $R = R_x = 30$) (a)-(b) TE case, (c)-(d) TM case, and (e)-(f) cross-section at $x = 0$.

It should be noted that when the number of transmitters/receivers was decreased to 8, the TE inversion also failed (not shown here) in reconstructing this target. The TE and TM inversions for the second scenario are shown in figure 6.3. In this case, both TE and TM inversions are successful in reconstructing the real and imaginary parts of the contrast. For the third scenario which utilizes the same number of transmitters and receivers as in the first scenario but located in far-field, the TE and TM inversions are shown in figure 6.4. In this case, the TE and TM inversions are very similar. The number of GNI iterations utilized to reconstruct this target and the value of $\mathcal{M}(\underline{\chi})$ in these three different scenarios are given in Table 6.1 and Table 6.2.

That the TE inversion outperforms the TM inversion in the first scenario is probably due to the fact that the TE near-field data contains more information than the TM near-field data (the length of the vector $\underline{E}^{\text{scat}}_{\text{meas}}$ in the TE case is twice that in the TM case). Noting that the measurement circle $\mathcal{S}$ is in the near-field for this test case, it is expected that $\underline{E}^{\text{scat}}_{\text{meas},x}$ and $\underline{E}^{\text{scat}}_{\text{meas},y}$ provide non-redundant information. However, when the number of transmitters and receivers increases in the second scenario, the TM scattering data provides sufficient information to reconstruct the object with a reasonable accuracy while the TE inversion also provides a good reconstruction in this case. Comparing the inversion results for the first and third scenarios, we speculate that the TE far-field data does not provide extra information compared to the TM far-field data.

6.2.2 Synthetic E-target data set (III)

Next, we consider the E-target with the same geometry as described in Section 5.6.1. However, we choose the relative complex permittivity of the target to be $70 + j17$ and that of the background medium to be $77.5 + j20$. At a frequency of 0.9 GHz, the OI is illuminated by 16 transmitters, which are magnetic line sources (in the TE case) and electric line sources (in

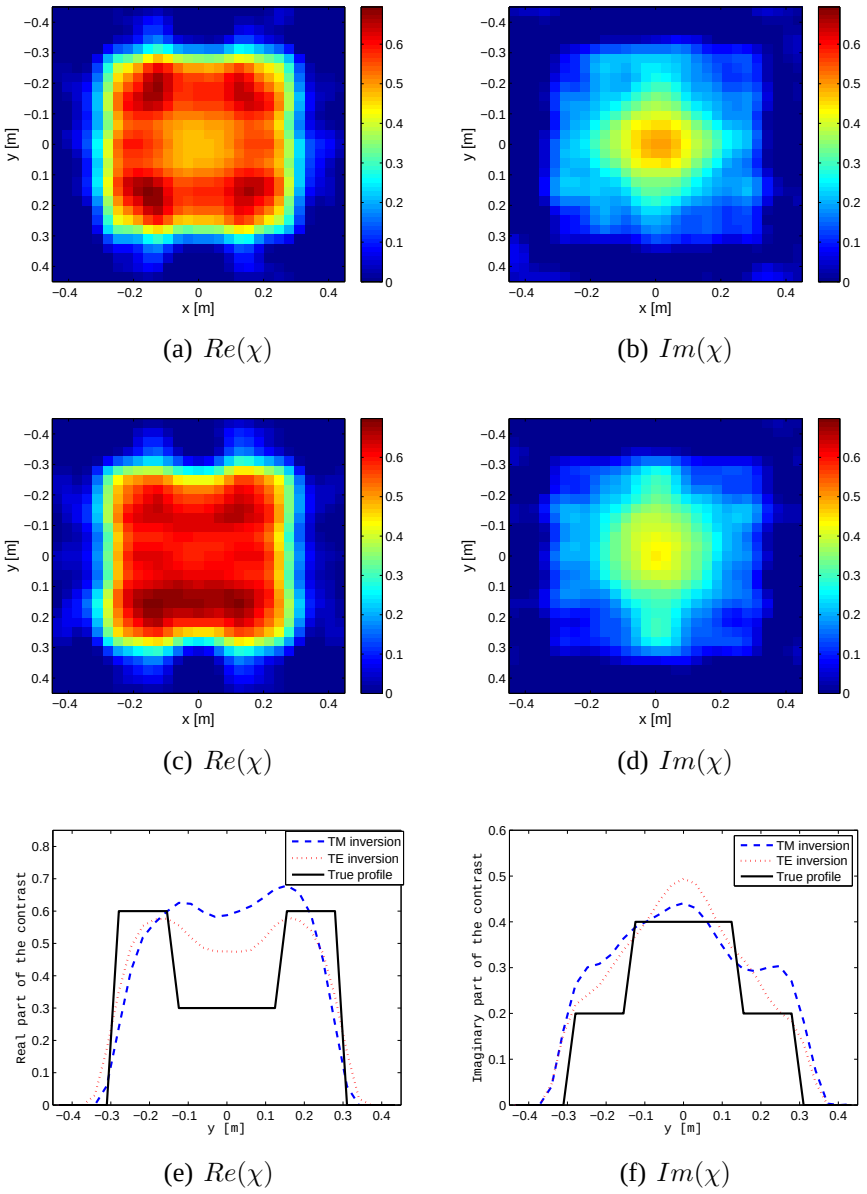

(a) $Re(\chi)$ (b) $Im(\chi)$

(c) $Re(\chi)$ (d) $Im(\chi)$

(e) $Re(\chi)$ (f) $Im(\chi)$

Fig. 6.4: Inversion of the concentric squares synthetic data set using the GNI method with additive-multiplicative regularization (the third scenario: $T_x = 10$ and $R = R_x = 10$ and the transmitters/receivers are located in far-field) (a)-(b) TE case, (c)-(d) TM case, and (e)-(f) cross-section at $x = 0$.

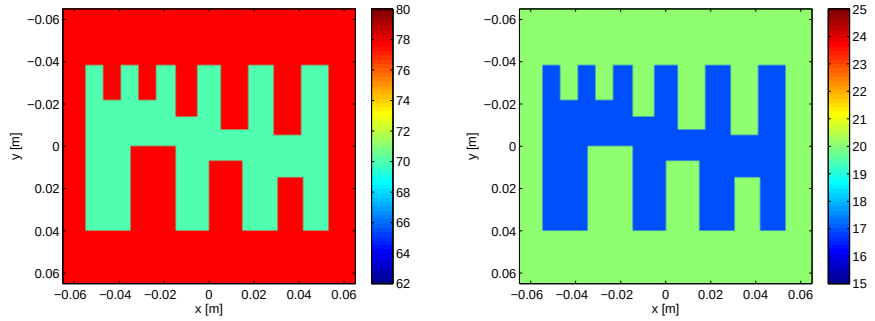

(a) $Re(\epsilon_r)$ (b) $Im(\epsilon_r)$

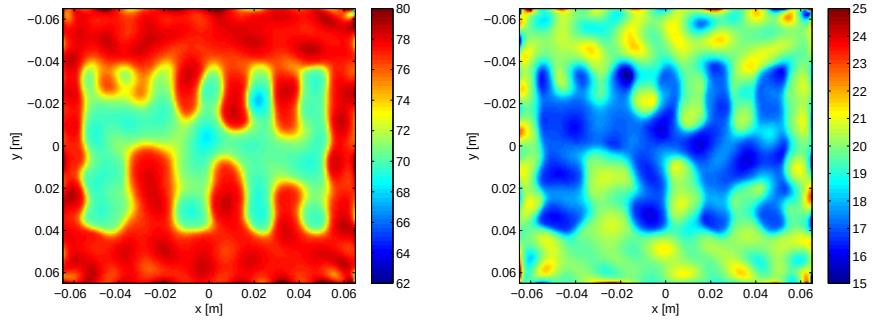

(c) $Re(\epsilon_r)$ (d) $Im(\epsilon_r)$

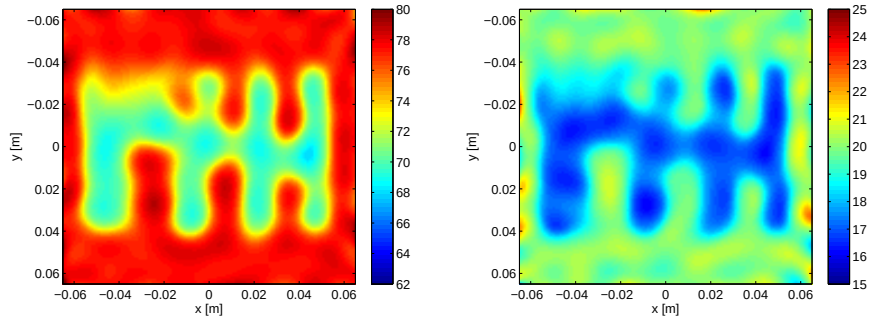

(e) $Re(\epsilon_r)$ (f) $Im(\epsilon_r)$

Fig. 6.5: Synthetic E-target data set (III) (collected at $f = 0.9$ GHz) (a)-(b) true profile, (c)-(d) TE inversion, and (e)-(f) TM inversion.

the TM case) and equally spaced on a circle of radius 0.1 m. The scattered field data along both x and y directions in the TE case and along z direction in the TM case is collected at 16 receivers per transmitter. We then add 3% noise to this synthetically collected data set according to [65]. We refer to this data set as synthetic *E*-target data set (III). We note that both the geometry of the target and the relative complex permittivities of and the background medium and target as well as the frequency of operation are the same as thosed used in [106] for a resolution test study. The TE and TM data sets are collected using 16 transmitters and 16 receivers. The inversion of this data set using the Binary GNI algorithm[1], explained in Section 5.6.1, is shown in figure 6.5. As can be seen, the TE inversion outperforms the TM inversion in reconstructing this complicated target. The number of GNI iterations utilized to reconstruct this target and the value of $\mathcal{M}(\underline{\chi})$ in both polarizations are given in Table 6.1 and Table 6.2.

6.2.3 Experimental data: the second Fresnel data set

The second Fresnel data set was explained in Section 5.5.2. We have shown the multiple-frequency inversion for all Fresnel targets in both TE and TM polarizations in [59]. For the multiple-frequency reconstruction, we have used the GNI method in conjunction with the frequency-hopping technique presented in [111]. The number of GNI iterations required for the convergence and the value of $\mathcal{M}(\underline{\chi})$ for all Fresnel targets in both polarizations are given in Tables 6.1 and 6.2. Table 6.1 shows a faster convergence for the TE inversion of the Fresnel targets. The value of the image error cost–functional shows a relatively similar reconstructions for the TE and TM inversions.

In this section, we only show the inversion of two Fresnel targets: *FoamDielExt* and *FoamMetExt*. The *FoamDielExt* target is shown in figure 5.13(a). The inversion of the data set

[1] We have utilized two different values for χ^h (see (5.34)); namely $\chi_1^h = 0$ and $\chi_2^h = -0.1 - j0.013$.

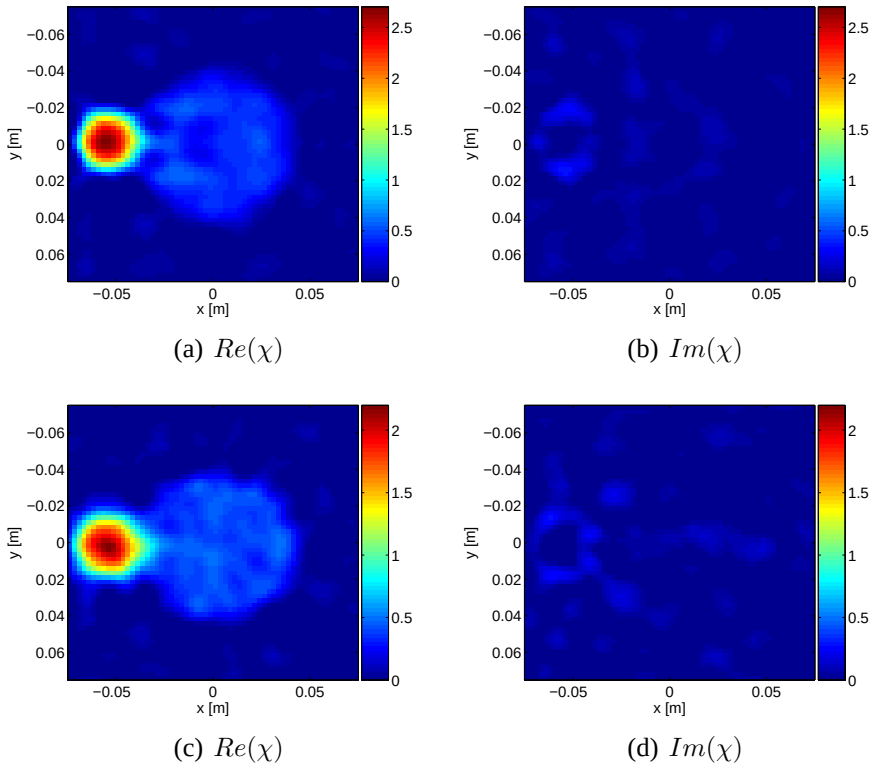

(a) $Re(\chi)$ (b) $Im(\chi)$

(c) $Re(\chi)$ (d) $Im(\chi)$

Fig. 6.6: *FoamDielExt* reconstruction (a)-(b) TE case (c)-(d) TM case

collected from this target in both polarizations is shown in figure 6.6. As can be seen, the reconstructed imaginary parts of both TE and TM inversions are small which indicates that the target is lossless. The *FoamMetExt* target is shown in 6.7. For this target, which consists of a metallic cylinder and a lossless dielectric cylinder, we have limited the maximum value of the imaginary part to be 4 at $f = 2$ GHz as otherwise the imaginary part of the metal cylinder will become too high (on the order of 200), making the convergence of the forward solver difficult. Therefore, if the imaginary part of the contrast of this target becomes more than four, it is set to four. The inversion of the data set collected from this target is shown in figure 6.8. As can be seen, the shape of the dielectric cylinder is reconstructed well in the TE case whereas its shape in the proximity of the metallic cylinder is not reconstructed in the TM case. Also, for both polarizations the reconstructed real part of the metallic cylinder is close to zero whereas the imaginary part is indicated to be an object of high loss.

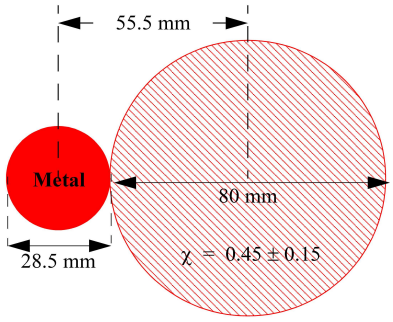

Fig. 6.7: The *FoamMetExt* target.

We have also investigated the single-frequency inversion of the experimental Fresnel data for both polarizations at $f = 6$ GHz [59]. For example for the *FoamTwinDiel* target, shown in figure 5.4. The TE inversion algorithm converged after 7 iterations for the TE case and 25 iterations for the TM case. The data misfit $\mathcal{F}^{\text{LS}}$ for the first iteration was 0.3803 for the TE case and 0.3809 for the TM case. However, in the final reconstruction, the data misfit reduced to 0.0285 for the TE case and 0.0266 for the TM case. The data misfit for different iterations of the inversion algorithm, *i.e.*, the GNI method with the additive-multiplicative regularization, for both TE and TM inversions is shown in figure 6.9(a). To check the sensitivity of this convergence rate for another regularization method, we have also shown the convergence of the GNI method with the Krylov subspace (CGLS) regularization method in figure 6.9(b). In addition, to check the sensitivity of the convergence rate to the line search algorithm described in Section 4.3, we have also used another line search technique. This line search algorithm uses the Matlab function *fminsearch* which is based on the simplex method [126]. As opposed to the line search algorithm presented in Section 4.3, this method does not require the derivative of the cost-functional. The convergence of the GNI method with the CGLS regularization technique equipped with this line search algorithm applied to FoamTwinDiel data set at $f = 6$ GHz is shown in figure 6.9(c).

As far as the computational complexity of the TE and TM inversions is concerned, the

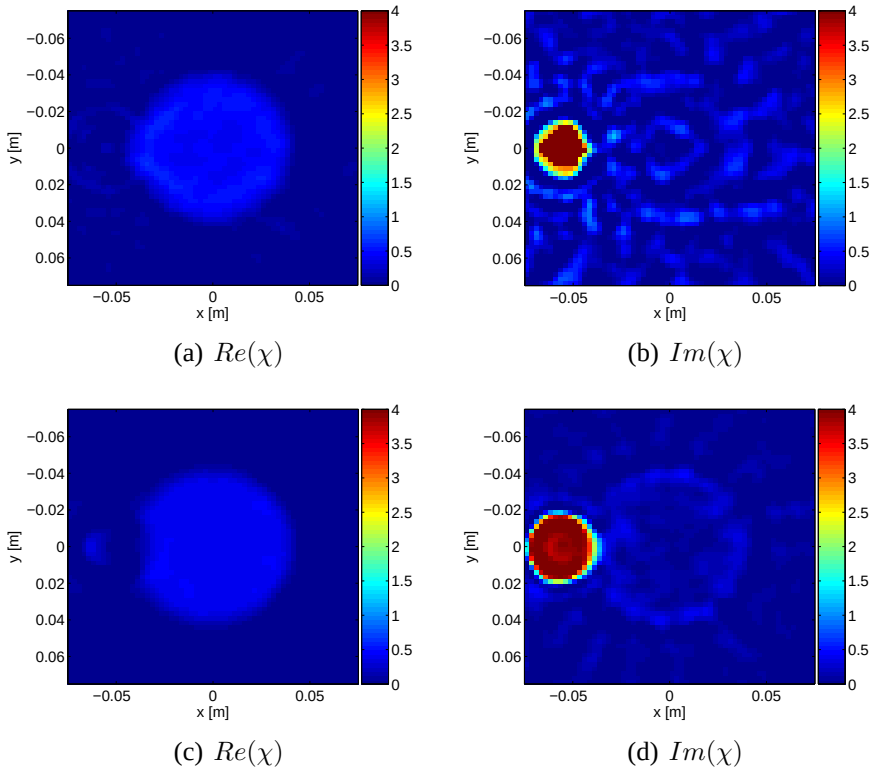

(a) $Re(\chi)$ (b) $Im(\chi)$

(c) $Re(\chi)$ (d) $Im(\chi)$

Fig. 6.8: *FoamMetExt* reconstruction (a)-(b) TE case (c)-(d) TM case

inversion codes have been written in object-oriented Matlab and all the computations are performed on a computer with a quad-core 2.66 GHz Intel processor and 2 GB of RAM. As an example, we consider the *FoamDielInt* target where $T = 8$, $R_x = 360$, $R = 241$ and $N = 3600$. In the first GNI iteration at $f = 2$ GHz we have $F_{\text{TE}} = 12$ and $P_{\text{TE}} = 50$ for the TE case whereas in the TM case, $F_{\text{TM}} = 9$ and $P_{\text{TM}} = 48$. Finding the Gauss-Newton correction took about 320 sec for the TE case and 79 sec for the TM case. That is, finding the correction in the TE case is about 4 times more expensive than that in the TM case which matches the expected theoretical ratio. Also, for each transmitter, the forward solver took about 0.99 sec in the TE case and 0.31 sec in the TM case showing that the per-iteration computational complexity of the TE forward solver is about 2.4 times more than that of the TM case which is very close to the approximate theoretical ratio. Also, in the inversion of the *FoamDielInt* target, the line search algorithm was called once for each frequency in both

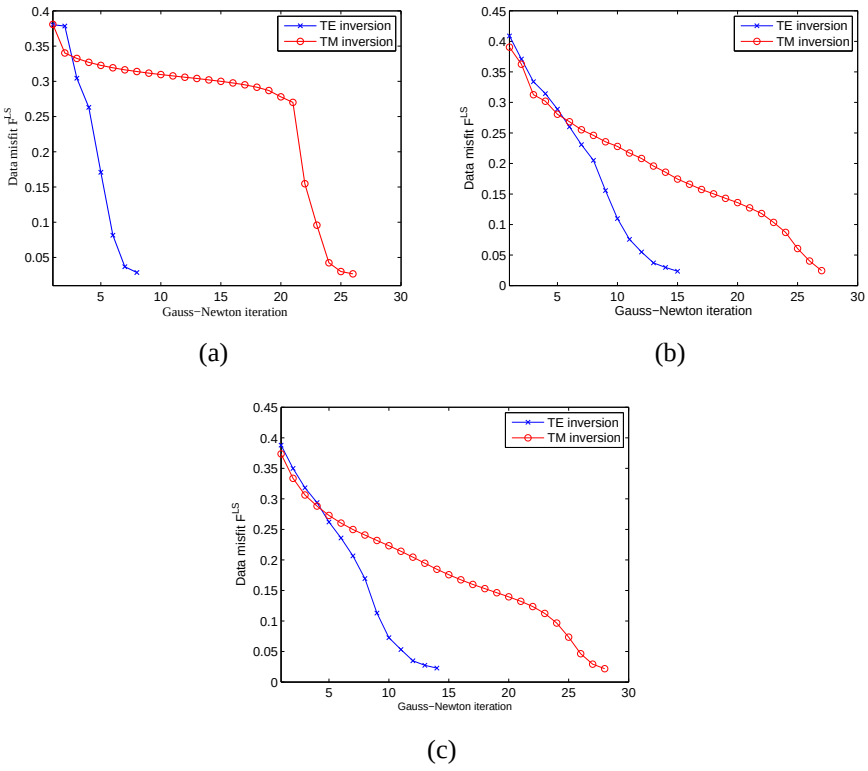

Fig. 6.9: The data misfit $\mathcal{F}^{\mathrm{LS}}$ for the single-frequency inversion of the *FoamTwinDiel* target at $f = 6$ GHz: (a) GNI with additive-multiplicative regularization equipped with the line search algorithm explained in Section 4.3, (b) GNI with CGLS regularization equipped with the line search algorithm explained in Section 4.3, and (c) GNI with CGLS regularization equipped with the simplex line-search method.

polarizations.

The computational cost can be significantly alleviated by using the marching-on-in-source-position technique [38], [30] which essentially reduces F_{TE} and F_{TM}. For example, in the first GNI iteration for the *FoamDielInt* target at $f = 2$ GHz, it took about 691 sec for the TE case and 114 sec for the TM case to find the inhomogeneous Green's function without using the marching-on-in-source-position technique. However, the update procedure took just 295 sec for the TE case and 53 sec for the TM case when this technique was used.

It is important to note that for experimental tomographic systems where the receiver posi-

tions are the same as transmitter positions, which is the case for most practical microwave imaging systems currently in existence, computational savings can be made in updating the Green's function of the inhomogeneous background using the already updated total field corresponding to each transmitter.

6.3 Discussion and summary of results

For all Fresnel targets, the TE and TM inversions are very similar. This is probably due to the fact that the measured data is collected in the far-field where only one scalar field component is required to represent the electric field vector: $E_{\varphi}^{\text{meas}}$ in the TE case and E_{z}^{meas} in the TM case. Thus, in the far-field, splitting $E_{\varphi}^{\text{meas}}$ into E_{x}^{meas} and E_{y}^{meas} does not provide more information than the TM case. In the first scenario of the synthetic test case, where $T_x = 10$ and $R_x = R = 10$ and the collected data is in the near-field, the TE inversion provides more accurate reconstruction compared to the TM inversion. This is likely due to the fact that E_{x}^{meas} and E_{y}^{meas} provide non-redundant information for the TE inversion whereas the TM inversion only utilizes the E_{z}^{meas} field. However, when the number of transmitters and receivers increases to 30 for the same test case, the TE and TM inversions provide similar results which verifies the fact that the TM inversion lacked enough information compared to the TE case when $T_x = R_x = R = 10$. Keeping the number of transmitters and receivers as in the first scenario but placing them in the far-field (the third scenario), the TE and TM inversions result in a similar reconstruction. This is consistent with the similar performance of TE and TM inversions of Fresnel data set. In addition for the synthetic *E*-target data set (III), where $T_x = 16$ and $R_x = R = 16$, the binary TE near-field inversion outperformed the binary TM near-field inversion.

In all cases considered in this chapter, the TE inversion requires the same or a fewer number

Tab. 6.1: Number of GNI iterations required for the convergence (multiple-frequency inversion)

Target	**TE case**	**TM case**
Concentric squares (1st scenario)	6	6
Concentric squares (2nd scenario)	8	8
Concentric squares (3rd scenario)	5	6
E-target	4	4
FoamDielInt	14	21
FoamDielExt	15	27
FoamTwinDiel	19	36
FoamMetExt	19	25
FoamTwinDiel ($f = 6$ GHz)	7	25

of iterations than the TM inversion to converge. The same observation has been reported in [122] where the TE Iterative Multi-Scaling Approach (IMSA) converged faster than the TM IMSA when the signal to noise ratio of the collected data was low. Also, in [127], it has been theoretically speculated that the TE inversion has a lower degree of nonlinearity compared to the TM case which may result in a faster convergence in the TE case. In addition, the actual computational cost of the TE and TM inversions were very close to the approximate theoretical ones presented in Section 6.1.

To verify these results using another regularization technique, we have also inverted these data sets using the CGLS regularization scheme. The conclusion from the inversion results obtained from the GNI-CGLS method is consistent with that obtained from the GNI method with the additive-multiplicative regularizer. We have also used another line search algorithm which is a derivative-free method which resulted in a similar convergence compared to the derivative-based line search method.

Considering all this numerical data, we speculate that the ultimate performance and convergence of the GNI algorithm applied to these data sets are highly dependent on the information content of the field, irrespective of the regularization and line search strategies. Thus,

Tab. 6.2: Image error cost–functional $\mathcal{M}(\underline{\chi})$

Target	**TE case**	**TM case**
Concentric squares (1st scenario)	0.10	0.15
Concentric squares (2nd scenario)	0.06	0.05
Concentric squares (3rd scenario)	0.14	0.16
E-target	0.13	0.18
FoamDielInt	0.13	0.14
FoamDielExt	0.16	0.18
FoamTwinDiel	0.20	0.18
FoamMetExt	0.23	0.29
FoamTwinDiel ($f = 6$ GHz)	0.22	0.20

the TE inversion, which utilizes both rectangular components of the electric vector at each receiver position, may result in more accurate reconstruction than the TM inversion when utilizing near-field scattering data collected using only a few transmitters and receivers.

7

Eigenfunction Contrast Source Inversion

> *Wir müssen wissen. Wir werden wissen.* Translation: *We must know. We will know.* (David Hilbert [128][1], who was the first to use the German word 'eigen' to address eigenvalues and eigenvectors).

In most MWT systems that have been developed for biomedical applications the OI and the antennas are contained within an enclosed chamber made from a dielectric material such as plexiglass [129, 76, 130, 131, 132]. The chamber is used to contain a matching fluid to improve the coupling of the microwave energy into the OI. Most of the MWT algorithms used to invert data from these systems assume that the matching fluid extends to infinity, not to the boundary of the casing. This approximation is adequate when the losses of the matching medium are sufficiently large that little or no energy that reaches the boundary of the chamber makes it back to the antennas. To make such an approximation work, the

[1] Hilbert addressed the Society of German Scientists and Physicians by this quote in the fall of 1930. This quote can also be read on his tombstone.

antennas need to be placed close to the OI and away from the boundary, or they need to be directive antennas that direct the main energy towards the OI (*e.g.*, an open-ended waveguide approach).

Recently, researchers have considered the MWT problem when the chamber surrounding the antennas and the OI is made of metallic material (*e.g.*, we use a stainless steel chamber). Various potential advantages to using a conductive chamber with a *lossless* (or a low-loss) matching medium include advantages related to the inversion algorithms which must be used for these systems as well as to practical data collection advantages such as better Signal-to-Noise Ratios (SNR) [133, 134, 135]. The latter is particularly important as it has been suggested in [106, 136] that the true resolution limit for MWT is governed by the achievable SNR of the measurements and not the wavelength. To invert the microwave measurements collected inside a metallic enclosure, researchers have implemented different algorithms which take the metallic casing into account. In [137], a calibration technique was proposed which when applied to the measured data collected inside a circular metallic enclosure allows it to be used by standard inversion algorithms that assume an unbounded matching medium. The proposed calibration technique is based on the reciprocity of the fields inside a circular metallic enclosure and those in an open-space system. It is currently unclear whether such a calibration procedure removes information from the data. In [42], a quasi-Newton inversion algorithm in conjunction with an embedding technique has been used to take into account the circular metallic enclosure. An integral equation formulation of the MR-CSI method was used in [134] that uses the Green's function of the metallic cavity. An inversion algorithm, based on CG minimization in conjunction with the Finite Element Method (FEM) forward solver was used in [138]. A Gauss-Newton inversion algorithm with a FEM forward solver to calculate the Jacobian matrix was used in [135] to invert the data collected in conducting cylinders of arbitrary shapes (which will be explained in the next chapter). To the best of our knowledge, all of these inversion algorithms have been applied

only to synthetically collected data.

More recently, an inversion algorithm, based on the CG algorithm and a Zernike polynomial representation of the unknown dielectric properties of the OI, was tested against experimentally collected data from the MWT system currently under development at the Institut Fresnel [139]. This system operates at 434 MHz and is enclosed by a circular metallic casing of radius 27.6 cm. In addition, the role of different design parameters in MWT systems with electrically conducting enclosures has been studied in [133] through the singular value expansion of the integral operator mapping the contrast sources inside the OI to the measurement domain outside the OI.

In this chapter, we introduce a new method of solving the Contrast Source Inversion (CSI) formulation of the electromagnetic inverse problem using the spectral decomposition of the appropriate boundary value problem applicable to the conductive enclosure MWT setup. From a mathematical perspective, one immediate advantage of using a conductive enclosure setup is that the associated boundary value problem for the electric field is well approximated by the Helmholtz operator in a finite domain which is terminated by Perfect Electric Conductor (PEC) boundary conditions (*i.e.*, homogeneous Dirichlet boundary conditions). This boundary value problem has a discrete set of eigenvalues, *i.e.*, a discrete spectrum, with a complete set of eigenfunctions that is usually used to expand the electromagnetic field within the domain. Thus, the Helmholtz operator applied to the field represented as an eigenfunction expansion can be replaced by a corresponding eigenfunction expansion where the corresponding eigenvalue replaces the operator operating on each eigenfunction in the expansion. Similarly, the inverse Helmholtz operator for such a boundary value problem has the same eigenfunctions but with eigenvalues that are the reciprocal of those for the forward operator. In the CSI functional defined for the electromagnetic inverse problem the inverse Helmholtz operator is applied to the so-called contrast sources, defined to be the product

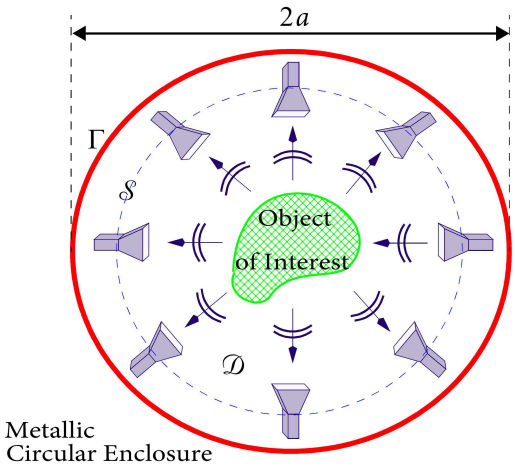

Fig. 7.1: Microwave tomography system enclosed by a circular PEC enclosure Γ (red circle) of radius a. The cross section of the enclosure, which is the imaging domain, is denoted by $\mathcal{D}$. The measurement domain (blue dotted circle), which is outside the object of interest, is denoted by $\mathcal{S}$.

of the total field and the contrast [48, 11, 112, 103]. Taking advantage of the well-known spectral decomposition of the Helmholtz operator within a circular boundary supporting homogeneous Dirichlet boundary conditions, we herein introduce the appropriate eigenfunction expansions for the unknowns in the CSI method, the contrast and the contrast sources. This effectively discretizes all the operators in the CSI functional with the result that the optimization problem becomes one of minimizing the CSI functional over the coefficients of these eigenfunction expansions. One unique result of using the eigenfunction expansion for the unknowns is that the imaging domain becomes the whole interior domain of the conductive enclosure. This is in contrast to the traditional form of the CSI algorithm where the unknown contrast is discretized into pulse basis functions.

7.1 Formulation

We consider a PEC enclosure with boundary denoted as Γ of circular cross-section having radius a. The interior volume of the enclosure is denoted by $\mathcal{D}$ which will also denote the imaging domain. The formulation is given for 2D fields; thus, we assume that the domain $\mathcal{D}$ is located in the $x-y$ plane. Inside the enclosure, which will contain the OI, we assume a known homogeneous background medium having a, possibly complex, relative permittivity ϵ_b. The geometrical model of the microwave tomography system is shown in figure 7.1. We also consider the position vector $\boldsymbol{r}$ which is in $\mathcal{D}$.

In this chapter, we assume a 2D TM model where the electric field is represented by the single longitudinal component $\boldsymbol{E} = E\hat{z}$. Thus, in this chapter, we refer to the electric field by its scalar component E. The physics of the problem can be modeled using various forms of the Helmholtz equation for E. To aid in the formulation we define the Helmholtz differential operator in a homogeneous background medium, $\mathcal{H}_b : L^2(\mathcal{D}) \rightarrow L^2(\mathcal{D})$, as

$$\mathcal{H}_b(\zeta) \triangleq \nabla^2\zeta(\boldsymbol{r}) + k_b^2\zeta(\boldsymbol{r}) \tag{7.1}$$

where ∇^2 denotes the Laplacian operator with respect to the coordinate $\boldsymbol{r}$.

In the MWT problem considered herein, the OI is successively illuminated by known incident fields E_t^{inc}, ($t = 1, 2, \cdots, T_x$). Each incident field is produced by a source function S_t, and the field itself satisfies the inhomogeneous Helmholtz equation

$$\mathcal{H}_b(E_t^{\text{inc}}) = -S_t(\boldsymbol{r}), \tag{7.2}$$

with Dirichlet boundary condition

$$E_t^{\text{inc}}(\boldsymbol{r} \in \Gamma) = 0. \tag{7.3}$$

When the OI is present, this same source produces the total field E_t. The scattered field will then be $E_t^{\text{scat}} \triangleq E_t - E_t^{\text{inc}}$. It is easily shown that the scattered field satisfies the same Helmholtz differential equation but with the source function replaced by $k_b^2 \chi(\boldsymbol{r}) E_t(\boldsymbol{r})$. That is, the scattered field satisfies

$$\mathcal{H}_b(E_t^{\text{scat}}) = -k_b^2 \chi(\boldsymbol{r}) E_t(\boldsymbol{r}), \tag{7.4}$$

with the same homogeneous boundary condition,

$$E_t^{\text{scat}}(\boldsymbol{r} \in \Gamma) = 0. \tag{7.5}$$

The inverse problem is defined as that of finding the electric contrast $\chi(\boldsymbol{r})$ from measurement data, which consists of the scattered field on the measurement domain $\mathcal{S}$, located outside the OI. The scattered field data is obtained from appropriately calibrated measurements of the total and incident fields at the same location. In this chapter, we consider the CSI method to solve the inverse scattering problem. We now give a brief overview of the Contrast Source Inversion (CSI) formulation as applied to the enclosed region inverse problem. As mentioned in Section 3.2, the CSI method [48, 11, 112, 103] casts the MWT problem as an optimization problem over the contrast χ and a new variable called the contrast source w_t, defined as $w_t(\boldsymbol{r}) \triangleq \chi(\boldsymbol{r}) E_t(\boldsymbol{r})$. These variables are solved for iteratively by minimizing the specially formulated CSI functional using the CG method. The CSI functional is formulated via the inverse operator corresponding to the problem formulation previously described.

That is, from (7.4), the scattered field corresponding to the t^{th} transmitter may be written as

$$E_t^{\text{scat}}(\boldsymbol{r}) = \mathcal{H}_b^{-1}(-k_b^2 w_t), \tag{7.6}$$

where $\mathcal{H}_b^{-1}$ denotes the inverse of the Helmholtz operator $\mathcal{H}_b$ and includes the boundary condition $E_t^{\text{scat}}(\boldsymbol{r} \in \Gamma) = 0$.

At the n^{th} iteration of the CSI method, the cost–functional $\mathcal{C}_n : L^2(\mathcal{D}) \times L^2(\mathcal{D})^{T_x} \rightarrow \mathbb{R}$ is given by [140]

$$\begin{aligned}\mathcal{C}_n(\chi, w_t) &= \mathcal{C}_{\mathcal{S}}(w_t) + \mathcal{C}_{\mathcal{D},n}(\chi, w_t) = \\ &\frac{\sum_t \left\| E_{\text{meas},t}^{\text{scat}} - \mathcal{M}_{\mathcal{S},t}\mathcal{H}_b^{-1}(-k_b^2 w_t) \right\|_{\mathcal{S}}^2}{\sum_t \left\| E_{\text{meas},t}^{\text{scat}} \right\|_{\mathcal{S}}^2} + \frac{\sum_t \left\| \chi E_t^{\text{inc}} - w_t + \chi\mathcal{H}_b^{-1}(-k_b^2 w_t) \right\|_{\mathcal{D}}^2}{\sum_t \left\| \chi_{n-1} E_t^{\text{inc}} \right\|_{\mathcal{D}}^2}\end{aligned} \tag{7.7}$$

where $E_{\text{meas},t}^{\text{scat}}$ denotes the measured scattered field and $\mathcal{M}_{\mathcal{S},t}$ represents the characteristic operator which selects the measurement points on $\mathcal{S}$; both corresponding to the t^{th} transmitter. Note that information gathered from different transmitters is incorporated into the functional by summing over the transmitters. The second term of the cost-functional $\mathcal{C}_n$, *i.e.* $\mathcal{C}_{\mathcal{D},n}$, may be regarded as the Maxwell regularizer [27] which is introduced to handle the ill-posedness of the problem.

The cost-functional $\mathcal{C}_n(\chi, w_t)$ is iteratively minimized via the formation of two interlaced sequences: a sequence of contrast estimates $\{\chi_n\}$ computed in an interlaced fashion with a sequence of contrast source estimates $\{w_{t,n}\}$. That is, at each iteration, each unknown is updated using a single step of the CG algorithm while assuming that the other unknown is constant. Note that the CSI functional is quite general, but a form of the inverse operator $\mathcal{H}_b^{-1}$ which is amenable to mathematical manipulation (*e.g.*, the derivative of functional is required for the implementation of the CG optimization), and which lends itself to efficient and accurate computation is required. There are many ways to formulate this operator which

meets these requirements. Integral equation methods and the inverse of finite-difference discretization have been used (see, for example, [48, 112, 103] for integral equation formulations in unbounded domains, [140] for a novel use of the inverse of a finite-difference discretization, and [134] for an integral equation formulation applicable to the PEC-enclosed problem).

7.2 Eigenfunction contrast source inversion

The inverse operator $\mathcal{H}_b^{-1}$ for the PEC-enclosed-region problem can be expressed using the eigenfunction expansion of the boundary-value problem that has been defined. Using polar coordinates $\boldsymbol{r}(\rho, \theta)$, the orthonormal eigenfunctions of $\mathcal{H}_b$ which satisfy the homogeneous Dirichlet boundary condition on Γ ($\rho = a$) may be written as

$$\psi_{mp}(\boldsymbol{r}) = \frac{1}{\sqrt{N_{mp}}} J_m(\frac{x_{mp}\rho}{a}) \cos(m\theta), \tag{7.8}$$

$$\varphi_{mp}(\boldsymbol{r}) = \frac{1}{\sqrt{N_{mp}}} J_m(\frac{x_{mp}\rho}{a}) \sin(m\theta), \tag{7.9}$$

where x_{mp} represents the p^{th} zero ($p \in \mathbb{N}$) of the m^{th}-order Bessel function of the first kind, J_m where $m \in \mathbb{N} \cup \{0\}$. The normalization constants N_{mp} can be easily calculated as

$$N_{mp} = \begin{cases} \pi a^2 J_{m+1}^2(x_{mp}) & m = 0 \\ \frac{\pi a^2}{2} J_{m+1}^2(x_{mp}) & \text{otherwise} \end{cases} \tag{7.10}$$

The eigenvalues, each of multiplicity two, corresponding to ψ_{mp} and φ_{mp} are

$$\lambda_{mp} = k_b^2 - (\frac{x_{mp}}{a})^2. \tag{7.11}$$

The completeness of the eigenfunctions allows us to express both the contrast, $\chi(\boldsymbol{r})$, and the contrast source functions, $w_t(\boldsymbol{r})$, inside the bounded domain $\mathcal{D}$ as eigenfunction expansions:

$$\chi(\boldsymbol{r}) = \sum_{m,p} \gamma_{mp}\psi_{mp}(\boldsymbol{r}) + \mu_{mp}\varphi_{mp}(\boldsymbol{r}) \tag{7.12}$$

and

$$w_t(\boldsymbol{r}) = \sum_{m,p} \alpha_{mp,t}\psi_{mp}(\boldsymbol{r}) + \beta_{mp,t}\varphi_{m,p}(\boldsymbol{r}) \tag{7.13}$$

where γ_{mp}, μ_{mp}, $\alpha_{mp,t}$ and $\beta_{mp,t}$ are the unknown coefficients to be determined. Note that a double summation is required for these eigenfunction expansions, as compared to the single summation used in the Singular Value Expansion (SVE) given by [133] and the Zernike expansion used by [139].

A useful property of the eigenfunctions ψ_{mp} and φ_{mp} for the operator $\mathcal{H}_b$ is that they are also the eigenfunctions of the inverse operator $\mathcal{H}_b^{-1}$, but the corresponding eigenvalues for the eigenfunctions of $\mathcal{H}_b^{-1}$ are λ_{mp}^{-1}. Using this property along with (7.13), allows us to express (7.6) as

$$E_t^{\text{scat}}(\boldsymbol{r}) = \mathcal{H}_b^{-1}(-k_b^2 w_t) = -k_b^2 \sum_{m,p} \lambda_{mp}^{-1} \left[\alpha_{mp,t}\psi_{mp}(\boldsymbol{r}) + \beta_{mp,t}\varphi_{mp}(\boldsymbol{r})\right], \tag{7.14}$$

and the scattered field on the measurement domain as

$$\begin{aligned} E_t^{\text{scat}}(\boldsymbol{r} \in \mathcal{S}) &= \mathcal{M}_{\mathcal{S},t}\mathcal{H}_b^{-1}(-k_b^2 w_t) \\ &= -k_b^2 \sum_{m,p} \lambda_{mp}^{-1} \left[\alpha_{mp,t}\mathcal{M}_{\mathcal{S},t}\psi_{mp}(\boldsymbol{r}) + \beta_{mp,t}\mathcal{M}_{\mathcal{S},t}\varphi_{mp}(\boldsymbol{r})\right]. \end{aligned} \tag{7.15}$$

The incident field at $\boldsymbol{r}$ is now assumed to be that of a line source located at $\boldsymbol{r}_t$ and can

therefore be written as

$$E_t^{\text{inc}}(\boldsymbol{r}) = E^{\text{inc}}(\boldsymbol{r};\boldsymbol{r}_t) = \mathcal{H}_b^{-1}[-\frac{1}{\rho}\delta(\rho-\rho_t)\delta(\theta-\theta_t)] \tag{7.16}$$

where δ represents the Dirac delta function. Using an eigenfunction expansion for the Dirac delta function, the incident field may be written as an eigenfunction expansion with known coefficients:

$$E_t^{\text{inc}}(\boldsymbol{r}) = -\sum_{m,p} \lambda_{mp}^{-1}\left[\psi_{mp}(\boldsymbol{r})\psi_{mp}(\boldsymbol{r}_t) + \varphi_{mp}(\boldsymbol{r})\varphi_{mp}(\boldsymbol{r}_t)\right]. \tag{7.17}$$

It should be noted that (7.17) is not a convergent series when $\boldsymbol{r} = \boldsymbol{r}_t$ [141], which reflects the singularity at the source point.

In the above analysis, we have implicitly assumed that $\lambda_{mp} \neq 0$. This assumption is always valid when the background medium is lossy. However, λ_{mp} may become zero for lossless backgrounds. This case has been discussed in [133] and a procedure to treat this problem has been proposed.

7.3 Discretizing the CSI functional using the eigenfunction expansions

We now introduce truncated eigenfunction expansions for the contrast, contrast sources, and incident fields into the CSI functional by assuming $m = 0, \cdots, M-1$ and $p = 1, \cdots, P$ for each of the expansions. The measured data corresponding to the t^{th} transmitter is denoted as the vector $\underline{E}^{\text{scat}}_{\text{meas},t} \in \mathbb{C}^R$, where R is the number of receivers, chosen to be constant for each transmitter. The unknown vector $\underline{a}_t \in \mathbb{C}^{2MP}$ contains the coefficients $\alpha_{mp,t}$ and $\beta_{mp,t}$ and the unknown vector $\underline{b} \in \mathbb{C}^{2MP}$ contains γ_{mp} and μ_{mp}. In order to evaluate the norms involved in the Maxwell regularizer term $\mathcal{C}_{\mathcal{D},n}$ we choose to discretize the domain $\mathcal{D}$ in a

uniform rectangular grid. The number of discretized points within $\mathcal{D}$ is denoted by Q. With this notation, matrices $\underline{\boldsymbol{Z}}_t \in \mathbb{C}^{R\times 2MP}$ and $\underline{\boldsymbol{F}} \in \mathbb{C}^{Q\times 2MP}$ are introduced in such a way that $\underline{\boldsymbol{Z}}_t\underline{a}_t$ and $\underline{\boldsymbol{F}}\,\underline{a}_t$ represent the discrete representation of $\mathcal{M}_{\mathcal{S},t}\mathcal{H}_b^{-1}(-k_b^2 w_t)$, (7.15), and $\mathcal{H}_b^{-1}(-k_b^2 w_t)$, (7.14), respectively.

It should be noted that it is only in this chapter where we use M to imply the orders of Bessel functions used in the expansions. In other chapters, we use M as the number of measured data.

We also consider the matrix $\underline{\boldsymbol{B}} \in \mathbb{R}^{Q\times 2MP}$ such that $\underline{\boldsymbol{B}}\,\underline{b}$ represents the discrete form of the contrast function χ, given in (7.12). The vector $\underline{u}_t^{\text{inc}} \in \mathbb{C}^Q$ includes the incident field corresponding to the t^{th} transmitter, E_t^{inc}, at the Q discrete points inside $\mathcal{D}$. To avoid the singularity of the incident field at the transmitting antenna location, the Q discretization points are chosen so as to not be collocated with the transmitter locations.

Using these discretized operators and vectors, the cost-functional $\mathcal{C}_n(\chi, w_t)$, (7.7), can be rewritten as

$$\mathcal{F}_n(\underline{b},\underline{a}_t) = \mathcal{F}_{\mathcal{S}}(\underline{a}_t) + \mathcal{F}_{\mathcal{D},n}(\underline{b},\underline{a}_t) = \eta_{\mathcal{S}} \sum_t \left\| \underline{E}^{\text{scat}}_{\text{meas},t} - \underline{\boldsymbol{Z}}_t\underline{a}_t \right\|^2 + \eta_{\mathcal{D},n} \sum_t \left\| \underline{u}_t^{\text{inc}} \odot (\underline{\boldsymbol{B}}\,\underline{b}) - \underline{\boldsymbol{B}}\,\underline{a}_t + (\underline{\boldsymbol{B}}\,\underline{b}) \odot (\underline{\boldsymbol{F}}\,\underline{a}_t) \right\|^2 \tag{7.18}$$

The weights $\eta_{\mathcal{S}}$ and $\eta_{\mathcal{D},n}$ are given by

$$\eta_{\mathcal{S}} = \Big(\sum_t \left\| \underline{E}^{\text{scat}}_{\text{meas},t} \right\|^2\Big)^{-1}, \tag{7.19}$$

and

$$\eta_{\mathcal{D},n} = \Big(\sum_t \left\| \underline{u}_t^{\text{inc}} \odot (\underline{\boldsymbol{B}}\,\underline{b}_{n-1}) \right\|^2\Big)^{-1}, \tag{7.20}$$

where $\odot$ denotes the Hadamard, *i.e.* elementwise, product of two vectors of the same size.

The cost-functional $\mathcal{F}_n(\underline{b}, \underline{a}_t)$ is then minimized iteratively over $\underline{b}$ and $\underline{a}_t$. Each iteration of the inversion algorithm consists of two parts: (*i*) updating $\underline{a}_t$ by minimizing $\mathcal{F}_n(\underline{b}, \underline{a}_t)$ assuming $\underline{b} = \underline{b}_{n-1}$, and (*ii*) updating $\underline{b}$ by minimizing $\mathcal{F}_n(\underline{b}, \underline{a}_t)$ assuming $\underline{a}_t = \underline{a}_{t,n}$.

It should be noted that choosing the number of eigenfunctions in the expansion, $M \times P$, can be considered a form of projection-based regularization [58], see Section 5.1.2, where the unknown functions are projected into the subspace spanned by the chosen eigenfunctions. But, as compared to projection-based regularization methods which have been utilized in the framework of the Gauss-Newton inversion method, *e.g.*, Truncated Singular Value Decomposition (TSVD) and Krylov subspace regularization methods (see Section 5.1.2 and references therein), the stability of the eigenfunction CSI method is not very sensitive to the choice of M and P which defines the subspace dimension. This is probably due to the presence of the Maxwell regularizer in the CSI functional which provides another level of regularization. In fact, the overall regularization associated with the eigenfunction CSI method can be considered a hybrid regularization [90, 88] where a Tikhonov-based regularization (*i.e.*, the Maxwell regularizer) and a projection-based regularization (*i.e.*, truncating the number of eigenfunctions) are utilized together.

As discussed in Appendix C, the cost-functional $\mathcal{F}_{\mathcal{S}}$ is not holomorphic in $\underline{a}_t$ and the cost-functional $\mathcal{F}_{\mathcal{D}}$ is not holomorphic in $\underline{a}_t$ and $\underline{b}$. To handle this problem, we use the Wirtinger calculus where we consider the cost-functionals $\tilde{\mathcal{F}}_{\mathcal{S}}(\underline{a}_t, \underline{a}_t^*)$ and $\tilde{\mathcal{F}}_{\mathcal{D}}(\underline{b}, \underline{b}^*, \underline{a}_t, \underline{a}_t^*)$. These two cost-functionals satisfy $\tilde{\mathcal{F}}_{\mathcal{S}}(\underline{a}_t, \underline{a}_t^*) = \mathcal{F}(\underline{a}_t)$ and $\tilde{\mathcal{F}}_{\mathcal{D}}(\underline{b}, \underline{b}^*, \underline{a}_t, \underline{a}_t^*) = \mathcal{F}_{\mathcal{D}}(\underline{b}, \underline{a}_t)$. The cost-functional $\tilde{\mathcal{F}}_{\mathcal{S}}$ is holomorphic in $\underline{a}_t$ for fixed $\underline{a}_t^*$ and vice versa. The cost-functional $\tilde{\mathcal{F}}_{\mathcal{D}}$ is holomorphic in $\underline{b}$ for fixed $\underline{b}^*$ (and vice versa), and is holomorphic in $\underline{a}_t$ for fixed $\underline{a}_t^*$ (and vice versa).

7.4 Updating procedure

We now show how $\underline{a}_t$ and $\underline{b}$ are updated in the proposed CSI method.

7.4.1 Updating $\underline{a}_t$

Assuming that $\underline{a}_t$ and $\underline{b}$ at the $(n-1)^{th}$ iteration of the algorithm, *i.e.* $\underline{a}_{t,n-1}$ and $\underline{b}_{n-1}$, are known, we update $\underline{a}_t$ as

$$\underline{a}_{t,n} = \underline{a}_{t,n-1} + \varsigma_n \underline{v}_{t,n} \tag{7.21}$$

where $\varsigma_n \in \mathbb{R}$ is the step size. The empirically modified Polak-Ribière CG direction $\underline{v}_{t,n}$ is given by [64]

$$\underline{v}_{t,n} = \begin{cases} 0 & n = 0 \\ \underline{g}_{t,n} + \frac{\mathrm{Re}\left\{\sum_t \underline{g}_{t,n}^H (\underline{g}_{t,n} - \underline{g}_{t,n-1})\right\}}{\sum_t \underline{g}_{t,n-1}^H \underline{g}_{t,n-1}} \underline{v}_{t,n-1} & \text{otherwise} \end{cases} \tag{7.22}$$

where $\underline{g}_{t,n}$ is the direction of the maximum rate of change in $\mathcal{F}_n(\underline{b}, \underline{a}_t)$ with respect to $\underline{a}_t$ evaluated at $\underline{a}_{t,n-1}$ and the superscript H denotes the Hermitian operator. As shown in [71], it is the derivative with respect to $\underline{a}_t^*$ which determines the direction of the maximum rate of change of $\mathcal{F}_n(\underline{b}, \underline{a}_t)$. Therefore,

$$\underline{g}_{t,n} = \frac{\partial \tilde{\mathcal{F}}_{\mathcal{S}}}{\partial \underline{a}_t^*}\Big|_{\underline{a}_{t,n-1}} + \frac{\partial \tilde{\mathcal{F}}_{\mathcal{D},n}}{\partial \underline{a}_t^*}\Big|_{\underline{b}_{n-1}, \underline{a}_{t,n-1}} \tag{7.23}$$

The derivative $\partial \tilde{\mathcal{F}}_{\mathcal{S}} / \partial \underline{a}_t^*|_{\underline{a}_{t,n-1}}$ is given by

$$\frac{\partial \tilde{\mathcal{F}}_{\mathcal{S}}}{\partial \underline{a}_t^*}\Big|_{\underline{a}_{t,n-1}} = -\eta_{\mathcal{S}} \underline{\boldsymbol{Z}}_t^H (\underline{E}_{\text{meas},t}^{\text{scat}} - \underline{\boldsymbol{Z}}_t \, \underline{a}_{t,n-1}). \tag{7.24}$$

The derivative $\partial\tilde{\mathcal{F}}_{\mathcal{D},n}/\partial\underline{a}_t^*|_{\underline{b}_{n-1},\underline{a}_{t,n-1}}$ can be written as

$$\frac{\partial\tilde{\mathcal{F}}_{\mathcal{D},n}}{\partial\underline{a}_t^*}|_{\underline{b}_{n-1},\underline{a}_{t,n-1}} = -\eta_{\mathcal{D},n}\underline{\boldsymbol{B}}^H\underline{d}_{t,n-1} + \eta_{\mathcal{D},n}\underline{\boldsymbol{F}}^H((\underline{\boldsymbol{B}}\,\underline{b}_{n-1})^* \odot \underline{d}_{t,n-1}) \tag{7.25}$$

where

$$\underline{d}_{t,n-1} = \underline{u}_t^{\text{inc}} \odot (\underline{\boldsymbol{B}}\,\underline{b}_{n-1}) - \underline{\boldsymbol{B}}\,\underline{a}_{t,n-1} + (\underline{\boldsymbol{B}}\,\underline{b}_{n-1}) \odot (\underline{\boldsymbol{F}}\,\underline{a}_{t,n-1}). \tag{7.26}$$

The step-length ς_n is found by the minimization

$$\varsigma_n = \arg\min_{\varsigma}\left\{\mathcal{F}_{\mathcal{S}}(\underline{a}_{t,n-1} + \varsigma\underline{v}_{t,n-1}) + \mathcal{F}_{\mathcal{D},n}(\underline{b}_{n-1}, \underline{a}_{t,n-1} + \varsigma\underline{v}_{t,n-1})\right\} \tag{7.27}$$

which results in

$$\varsigma_n = -\frac{\text{Re}\left\{\sum_t \underline{g}_{t,n}^H\underline{v}_{t,n}\right\}}{\eta_{\mathcal{S}}\sum_t\left\|\underline{\boldsymbol{Z}}_t\underline{v}_{t,n}\right\|^2 + \eta_{\mathcal{D},n}\sum_t\left\|-\underline{\boldsymbol{B}}\,\underline{v}_{t,n} + (\underline{\boldsymbol{B}}\,\underline{b}_{n-1}) \odot (\underline{\boldsymbol{F}}\,\underline{v}_{t,n})\right\|^2}. \tag{7.28}$$

7.4.2 Updating $\underline{b}$

Assuming $\underline{a}_{t,n}$ is known, we minimize $\mathcal{F}_n(\underline{b}, \underline{a}_t)$ with respect to $\underline{b}$. Noting that $\mathcal{F}_{\mathcal{S}}(\underline{a}_t)$ does not depend on $\underline{b}$, the vector $\underline{b}$ at the n^{th} iteration of the CSI algorithm may be found as

$$\begin{aligned}\underline{\boldsymbol{B}}\,\underline{b}_n &= \arg\min_{\underline{\boldsymbol{B}}\,\underline{b}}\mathcal{F}_{\mathcal{D},n}(\underline{b}, \underline{a}_{t,n}) \\ &= \arg\min_{\underline{\boldsymbol{B}}\,\underline{b}}\eta_{\mathcal{D},n}\left\{\left\|(\underline{\boldsymbol{B}}\,\underline{b}) \odot (\underline{u}_t^{\text{inc}} + \underline{\boldsymbol{F}}\,\underline{a}_{t,n}) - \underline{\boldsymbol{B}}\,\underline{a}_{t,n}\right\|^2\right\}.\end{aligned} \tag{7.29}$$

The vector $\underline{\boldsymbol{B}}\,\underline{b}_n$ can then be obtained as

$$\underline{\boldsymbol{B}}\,\underline{b}_n = [\sum_t \underline{u}_{t,n}^* \odot (\underline{\boldsymbol{B}}\,\underline{a}_{t,n})] \oslash [\sum_t \underline{u}_{t,n}^* \odot u_{t,n}] \tag{7.30}$$

where $\underline{u}_{t,n} = \underline{u}_t^{\text{inc}} + \underline{\boldsymbol{F}}\,\underline{a}_{t,n}$ and $\oslash$ represents the elementwise division (Hadamard division) between two vectors of the same size. It should be noted that finding $\underline{b}_n$ from $\underline{\boldsymbol{B}}\,\underline{b}_n$ is not necessary as updating $\underline{a}_t$ requires $\underline{\boldsymbol{B}}\,\underline{b}$, not $\underline{b}$.

7.4.3 Initial guess for $\underline{a}_t$

The CSI algorithm requires an initial guess for $\underline{a}_t$ and $\underline{b}$ at the beginning of the algorithm. One method might be to assume a zero initial guess for $\underline{a}_t$ as well as $\underline{b}$ and then update $\underline{a}_t$ using the steepest-descent algorithm (which is traditionally the first step of any conjugate gradient algorithm). If this route is followed then a choice would need to be made on the normalization term $\eta_{\mathcal{D},n}$ which is undefined at the first step for this choice of initial guess. One approach might be to use prior information on the value of the contrast to provide a non-zero $\underline{\boldsymbol{B}}\,\underline{b}$. Alternatively, one could ignore the Maxwell regularizer, by assuming $\eta_{\mathcal{D},n} = 0$, and minimize the data-error functional, $\mathcal{F}_{\mathcal{S}}(\underline{a}_t)$, on its own, using perhaps, a single step in the steepest descent direction.

The method that we choose allows some flexibility in that this data-error functional minimization is approached using Krylov subspace regularization. Explicitly, the initial guess for $\underline{a}_t$ may be found by

$$\underline{a}_{t,0} = \arg\min_{\underline{a}_t} \left\{ \left\| \underline{E}^{\text{scat}}_{\text{meas},t} - \boldsymbol{Z}\underline{a}_t \right\|^2 \right\} \tag{7.31}$$

subject to a Krylov subspace regularization technique, *e.g.* the Conjugate Gradient Least Squares (CGLS) method [86]. These iterative algorithms, when applied to an ill-posed system of equations like (7.31), exhibit a *semi-convergence* behavior [88]. That is, they improve the solution at their early iterations, where the solution space is restricted to a Krylov subspace of small dimension. However, they start deteriorating the solution by inverting the

noise – in our case, the noise in $\underline{E}^{\text{scat}}_{\text{meas},t}$ – in later iterations. An appropriately regularized solution can therefore be obtained by early termination of the utilized Krylov subspace algorithm when the dimension of the subspace is large enough to produce a good regularized solution and small enough to suppress the effect of noise. Therefore, the iteration at which the algorithm is stopped plays the role of the regularization parameter for this type of regularization: the fewer the iterations, the stronger the regularization.

To find $\underline{a}_{t,0}$, we utilize the CGLS algorithm as the Krylov subspace regularization and choose the maximum possible regularization weight of this regularization. That is, only one iteration of the CGLS algorithm is applied to the least squares problem $\underline{\boldsymbol{Z}}_t \underline{a}_t = \underline{E}^{\text{scat}}_{\text{meas},t}$. The initial guess to the CGLS method is considered to be the zero vector of appropriate size. Therefore, the regularized solution $\underline{a}_{t,0}$ will be $\underline{a}_{t,0} = \xi_t \underline{h}_t$ where $\underline{h}_t$ is the CG direction at the first iteration of the CGLS algorithm (that is, the steepest descent direction) applied to $\underline{\boldsymbol{Z}}_t \underline{a}_t = \underline{E}^{\text{scat}}_{\text{meas},t}$ and ξ_t is the CGLS step size. Finding $\underline{h}_t$ and ξ_t, the regularized solution $\underline{a}_{t,0}$ can be written as

$$\underline{a}_{t,0} = \frac{\left\| \underline{\boldsymbol{Z}}_t^H \underline{E}^{\text{scat}}_{\text{meas},t} \right\|^2}{\left\| \underline{\boldsymbol{Z}}_t \underline{\boldsymbol{Z}}_t^H \underline{E}^{\text{scat}}_{\text{meas},t} \right\|^2} \underline{\boldsymbol{Z}}_t^H \underline{E}^{\text{scat}}_{\text{meas},t}. \tag{7.32}$$

We note that (7.32) is equivalent with the backpropagation solution, given in [48, 11]. The formulation as a Krylov subspace regularized minimization of the data-error functional gives us the option of performing more than the first steepest-descent step. Unfortunately, finding the optimum stopping iteration in these methods is difficult and, because we rely on the Maxwell regularizer, we have found that there is no need to use more than the first few steps of the Krylov-based method to obtain the initial value of $\underline{a}_t$. In fact, in all the results presented herein, only the first step is used, because no advantage was gained in using more than the first step. Having found $\underline{a}_{t,0}$, the vector $\underline{\boldsymbol{B}}\, \underline{b}_0$ can be found from (7.30).

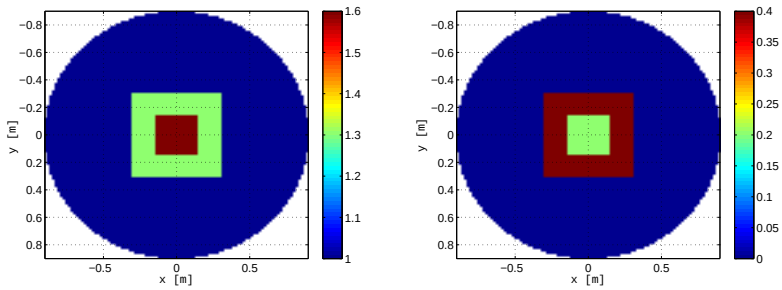

(a) Exact $Re(\epsilon_r)$ (b) Exact $Im(\epsilon_r)$

Fig. 7.2: Exact relative permittivity for the concentric squares data set.

7.5 Inversion results

In this section, we show inversion results for two synthetic data sets. All synthetic data sets have been created with a frequency-domain Finite Element Method (FEM) forward solver. To all synthetic data sets, 3% noise was added using the formula (4.31). The noisy data $\underline{E}^{\text{scat}}_{\text{meas},t}$ is then used to test the inversion algorithm against three synthetic data sets. To show the robustness of the inversion algorithm with respect to the noise level η, see (4.31), we also show inversion results of the second data set when η is chosen to be 0.15 and 0.25.

We avoid frequencies associated with the zero eigenvalue since at such frequencies the inverse operator $\mathcal{H}_b^{-1}$ does not exist. That is, no resonant frequencies have been chosen. In addition, all examples are run with no prior information and the only constraint imposed on the contrast is that the corresponding relative permittivity should be physical (*i.e.*, the real part of the relative permittivity is kept greater than one, and the imaginary part is kept non-negative). In all inversions considered herein, unless otherwise stated, we assume $M = P = 30$. Utilizing $M = P = 30$, *i.e.*, projecting the unknown contrast into 900 eigenfunctions, provides stable solutions for the data sets considered herein. Increasing the number of eigenfunctions to $M = P = 40$ and $M = P = 50$ results in very similar reconstructions compared to the results obtained using $M = P = 30$. However, the inversion results start to deteriorate when

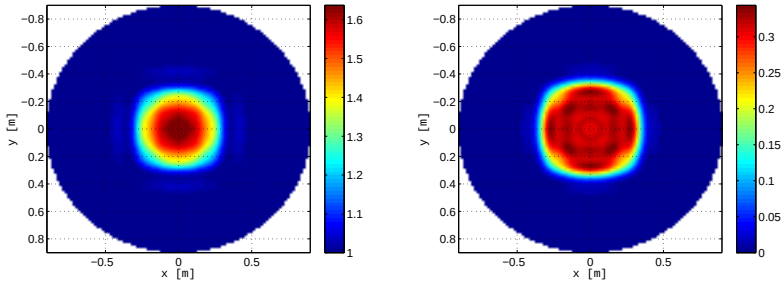

(a) Recons. $Re(\epsilon_r)$ $(M = P = 10)$ (b) Recons. $Im(\epsilon_r)$ $(M = P = 10)$

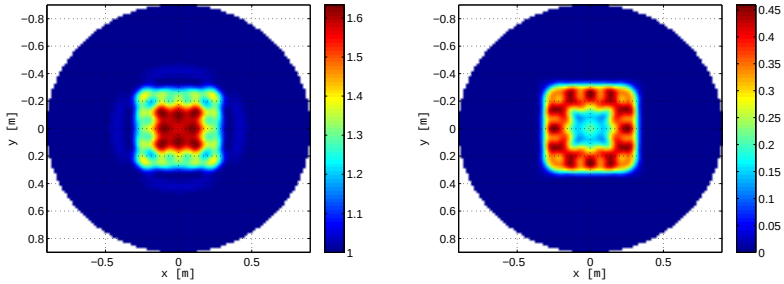

(c) Recons. $Re(\epsilon_r)$ $(M = P = 20)$ (d) Recons. $Im(\epsilon_r)$ $(M = P = 20)$

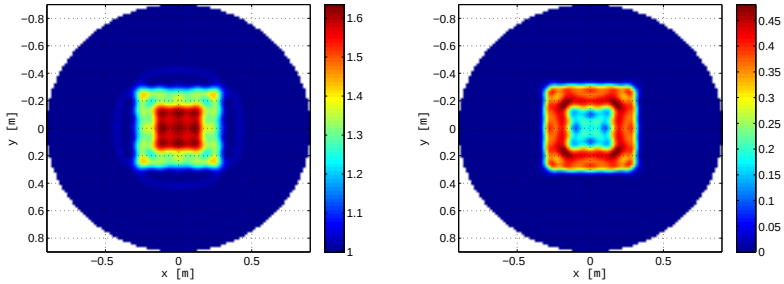

(e) Recons. $Re(\epsilon_r)$ $(M = P = 30)$ (f) Recons. $Im(\epsilon_r)$ $(M = P = 30)$

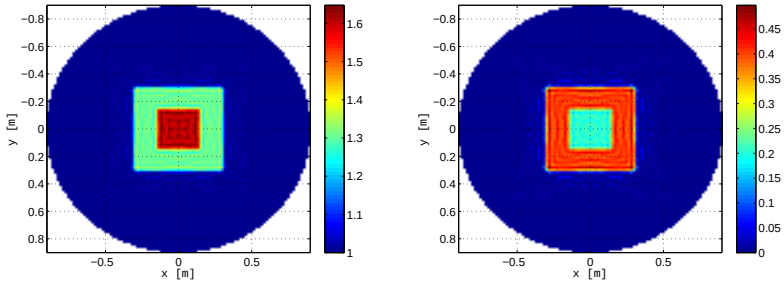

(g) Direct Expan. $Re(\epsilon_r)$ (h) Direct Expan. $Im(\epsilon_r)$

Fig. 7.3: Concentric squares data set (a)-(b) eigenfunction CSI reconstruction when $M = P = 10$, (c)-(d) eigenfunction CSI reconstruction when $M = P = 20$, (e)-(f) eigenfunction CSI reconstruction when $M = P = 30$, and (g)-(h) direct eigenfunction expansion of the exact dielectric profile of the object of interest ($M = P = 30$).

M and P are chosen to be more than 50. For the first data set, we show the performance of the eigenfunction CSI method using five different sets of values for M and P.

In all synthetic data sets considered herein, we show the *direct* eigenfunction expansion for the exact dielectric profile of the OI (for $M = P = 30$) which is obtained from the expansion (7.12) with coefficients computed by taking the inner product of the exact contrast with the expansion. We call this direct expansion the theoretical limit for the method given the chosen number of eigenfunction terms. We also define the error between the direct expansion and the reconstructed expansion as

$$EE = \frac{\left\|\epsilon_{MP} - \epsilon_{MP}^{d}\right\|}{\left\|\epsilon_{MP}^{d}\right\|} \tag{7.33}$$

where ϵ_{MP} and ϵ_{MP}^{d} are the reconstructed and direct eigenfunction expansions of the relative permittivity respectively. This *eigenfunction error*, EE, is most easily computed using Parseval's theorem.

For the targets considered in this chapter, we also show the inversion results from the scattering data collected in an open-region background using the integral-equation based CSI method [48]. We refer to this algorithm as the IE-CSI method. In all of these open-region reconstructions, we have used the same transmitters and receivers as used in the eigenfunction CSI method. We have also used $\eta = 0.03$, see (4.31), to generate noisy scattering data for the open-region cases.

7.5.1 Synthetic data set I: concentric squares

For the first numerical example, we consider the OI to be two concentric squares. This target has been used in other publications such as [48, 125, 29, 134]. The inner square

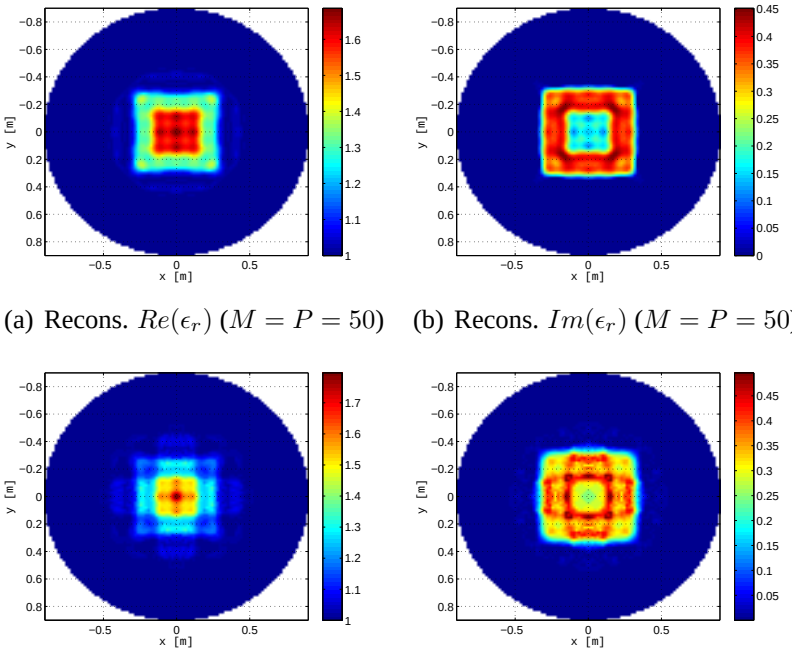

(a) Recons. $Re(\epsilon_r)$ ($M = P = 50$) (b) Recons. $Im(\epsilon_r)$ ($M = P = 50$)

(c) Recons. $Re(\epsilon_r)$ ($M = P = 70$) (d) Recons. $Im(\epsilon_r)$ ($M = P = 70$)

Fig. 7.4: Concentric squares data set: (a)-(b) eigenfunction CSI reconstruction when $M = P = 50$, and (c)-(d) eigenfunction CSI reconstruction when $M = P = 70$.

has dimension of $\lambda_b \times \lambda_b$ (λ_b is the wavelength in the background medium) with a relative permittivity of $1.6 + j0.2$. The inner square is surrounded by an exterior square having sides of $2\lambda_b$ and relative permittivity of $1.3 + j0.4$. The OI is surrounded by a circular PEC cylinder of radius $3\lambda_b$. The exact permittivity profile is shown in figure 7.2. The frequency of operation is chosen to be 1 GHz and the relative permittivity of the background medium is assumed to be $\epsilon_b = 1$; thus $\lambda_b = 0.3$ m. The OI is illuminated by 30 transmitters evenly spaced on a circle of radius $2.33\lambda_b$. The data is then collected using 40 transmitters evenly spaced on a circle of radius $2.17\lambda_b$.

The inversion algorithm is tested against this data set in five different cases distinguished by the number of eigenfunctions used: (*i*) 100 ($M = P = 10$), (*ii*) 400 ($M = P = 20$), (*iii*) 900 ($M = P = 30$), (*iv*) 2500 ($M = P = 50$), and (*v*) 4900 ($M = P = 70$). The inversion result for the first case is shown in figure 7.3(a)-(b) where it can be seen that the two

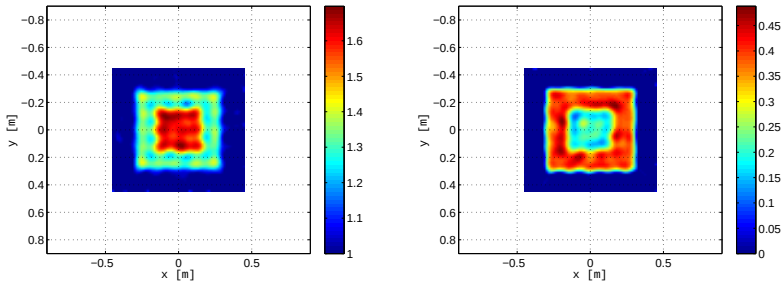

(a) Recons. $Re(\epsilon_r)$ (b) Recons. $Im(\epsilon_r)$

Fig. 7.5: Concentric squares data set: open-region IE-CSI reconstruction. The imaging domain is a 0.9 m $\times$ 0.9 m square.

concentric squares are not resolved. Increasing the number of eigenfunctions in the second case to 400, the algorithm does a good job of resolving the two squares and reconstructs their complex relative permittivities as shown in figures 7.3(c)-(d). In the third case, shown in figure 7.3(e)-(f), the edges of the squares are sharper compared to the second case. The direct eigenfunction expansion for the exact dielectric profile of the OI (for $M = P = 30$) is shown in figure 7.3(g)-(h) where the corresponding EE is 0.03. Increasing the number of eigenfunctions in the fourth case to 2500, the reconstruction result, see figure 7.4(a)-(b), remained similar to the $M = P = 30$ case. However, the inversion results start to deteriorate when M and P are chosen to be more than 50. In figure 7.4(c)-(d), we have shown the inversion result for the fifth case ($M = P = 70$) where the inversion algorithm cannot produce an acceptable reconstruction for the OI. The computational time of the eigenfunction CSI method for the $M = P = 30$ case was 1.36 seconds per CSI iteration (23 minutes in total) on a 2.66 GHz machine. The open-region reconstruction of this target using the IE-CSI method is shown in figure 7.5.

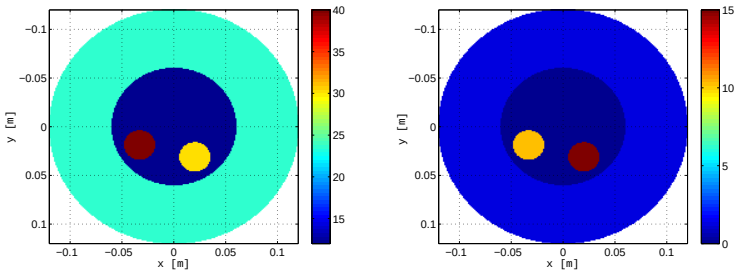

(a) Exact $Re(\epsilon_r)$ (b) Exact $Im(\epsilon_r)$

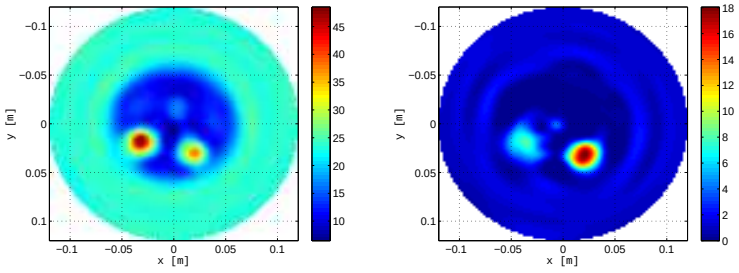

(c) Recons. $Re(\epsilon_r)$ (d) Recons. $Im(\epsilon_r)$

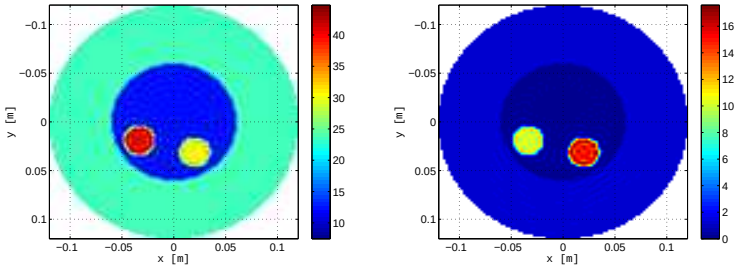

(e) Direct Expan. $Re(\epsilon_r)$ (f) Direct Expan. $Im(\epsilon_r)$

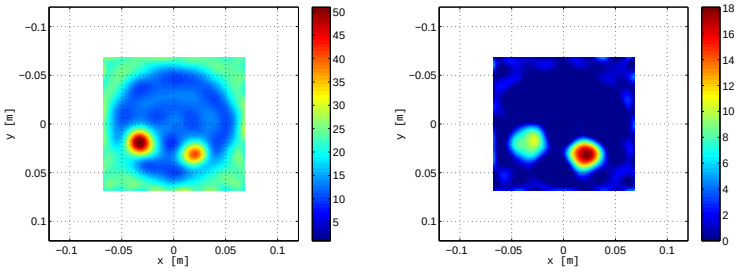

(g) open-region Recons. $Re(\epsilon_r)$ (h) open-region Recons. $Im(\epsilon_r)$

Fig. 7.6: Synthetic data set II (a)-(b) exact relative permittivity of the object of interest (c)-(d) eigenfunction CSI reconstruction, (e)-(f) direct eigenfunction expansion of the exact dielectric profile of the object of interest ($M = P = 30$), and (g)-(h) open-region reconstruction of the object of interest using the IE-CSI method. For the eigenfunction CSI method, the imaging domain is the whole interior of the metallic enclosure whereas for the open-region IE-CSI method, it is a 0.136 m $\times$ 0.136 m square.

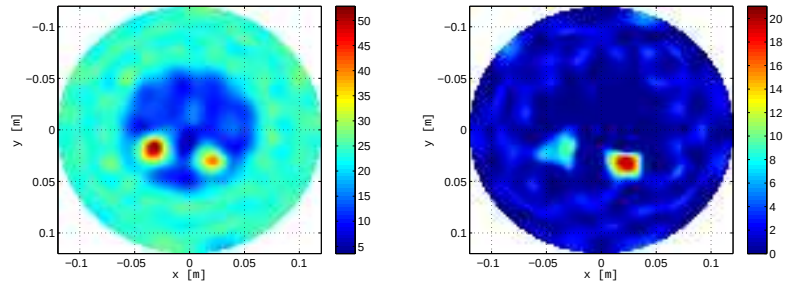

(a) Recons. $Re(\epsilon_r)$ (b) Recons. $Im(\epsilon_r)$

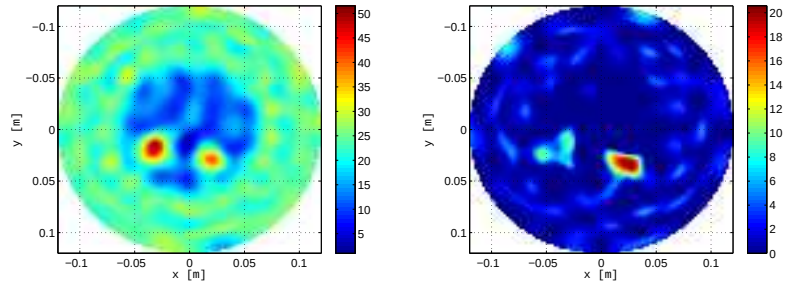

(c) Recons. $Re(\epsilon_r)$ (d) Recons. $Im(\epsilon_r)$

Fig. 7.7: Eigenfunction CSI reconstruction of the synthetic data set II with (a)-(b) 15% noise ($\eta = 0.15$), and (c)-(d) 25% noise ($\eta = 0.25$).

7.5.2 Synthetic data set II: circular targets with lossy background

We consider an OI which consists of three circular regions. Two of these circular regions have the same radius of 0.015 m and their relative complex permittivities are $40 + j10$ and $30 + j15$. These two circular regions are surrounded by another circular region with radius of 0.06 m and relative permittivity of 12. The OI is immersed in a lossy background and enclosed by a circular PEC enclosure of radius 0.12 m. The object of interest is successively irradiated by 32 transmitters evenly spaced on a circle of radius 0.1 m. The data is collected using 32 receivers per transmitter where the receiver locations are the same as the transmitter locations. The frequency of operation is chosen to be 1 GHz at which the complex permittivity of the background medium is $23.4 + j1.13$. The OI is shown in figure 7.6(a)-(b) and the reconstructed permittivity using eigenfunction contrast source inversion method is

shown in figure 7.6(c)-(d). The direct eigenfunction expansion for the exact dielectric profile of the OI (for $M = P = 30$) is shown in figure 7.6(e)-(f) where the corresponding EE is 0.11. The computational time for this target was 1.90 seconds (21 minutes in total) on a 2.66 GHz machine. The open-region reconstruction for this target is shown in figure 7.6(g)-(h). To show the robustness of the eigenfunction CSI algorithm with respect to the noise level, the inversion results of this target when the noise level is 15% and 25% are shown in figure 7.7(a)-(b) and figure 7.7(c)-(d) respectively.

8

A Novel Microwave Tomography System

The theory I propose may therefore be called a theory of the Electromagnetic Field, because it has to do with the space in the neighborhood of the electric or magnetic bodies, and it may be called a Dynamical Theory, because it assumes that in that space there is matter in motion, by which the observed electromagnetic phenomena are produced. (James Clerk Maxwell [142][1]).

Contributions to microwave tomography have been made in all aspects of the technology, especially the development of improved inverse algorithms; *e.g.*, [12, 11, 30, 40, 56]. During the past two decades, the actual physical setup used to collect the required electromagnetic scattering data has not undergone much innovation, other than the diverse antenna or transducer systems that have been reported; *e.g.*, [129, 85, 99, 143, 131, 130, 144, 145]. Obtaining good images from MWT requires the accurate collection of a substantial amount of electromagnetic scattering data, which, for efficiency, is best performed using a relatively

[1] The original set of Maxwell's equations, which utilizes the concept of displacement current, first appeared in this paper.

large number of co-resident antennas. In the systems described in [129, 145] the number of elements in the arrays range from 16 to 24 where small monopoles or Vivaldi antennas have been used. The large arrays facilitate gathering bistatic scattering data at many angles without mechanically repositioning the antennas. The antenna elements themselves are typically not taken fully into account in the electromagnetic system model of the associated nonlinear optimization problem, although this is an important consideration in achieving good images (*cf.* the antenna compensation schemes in [124]). Including the antennas in the system model is a way of reducing the modeling error that exists between the numerical system model and the actual system from which data is collected. Modeling error also occurs when assuming a homogeneous unbounded domain for the system model because Boundary Conditions (BCs) for a dielectric discontinuity are actually required to properly account for the finite extent of the matching-fluid region.

Both the antenna and the BC modeling errors can be reduced by the use of a lossy matching-fluid of sufficiently high loss such that electromagnetic energy returning from the boundary or any passive antenna to any receiving antenna is not appreciable. Although this may reduce the modeling errors, the net effect of using a lossy matching fluid in MWT systems may be to reduce the accuracy of the complex permittivity profile reconstructions because the addition of any loss reduces the dynamic range and achievable signal-to-noise ratio (SNR) of the system. To achieve as much accuracy and resolution as possible from an MWT system it is important to not rely on matching fluid loss to diminish both types of modeling errors (loss should only be used to reduce the contrast so as to allow more energy to penetrate the target). Thus, unless a complex system model is to be used—one which accurately models the co-resident antennas as well as the boundaries of the system—the only way to reduce modeling error is to either (*i*) incorporate specialized calibration techniques for the measured data, or (*ii*) construct MWT systems that retain the capacity to provide large amounts of independent scattered field data but can be modeled accurately and efficiently.

The purpose of this chapter is to propose a novel MWT system within a rotatable conductive enclosure that uses a minimal antenna array which is *fixed* with respect to the target being imaged. Scattered-field data is obtained by taking bistatic measurements between each pair of elements of the fixed array at several different static positions of the rotatable enclosure. The inverse problem is formulated for the transverse magnetic (TM) 2D case and the enclosure is chosen to have a triangular shape. Although it is not easily shown with numerical experiments using synthetic data, the practical implementation of this system should reduce both types of modeling error: the BCs at the conductive-enclosure boundary are easily modeled and the antenna modeling error will be minimized because, as will be shown, small arrays with as few as four elements can be used.

The shape of the enclosure is chosen to be triangular because it is the polygon that allows the greatest number of fixed-angle step-rotations before producing a redundant configuration. We note that recently, Wadbro and Berggren have considered MWT in a rotating metallic hexagonal-shaped container where the object of interest is illuminated by waveguides connected to each side of the metallic container [146]. The container, along with the waveguides, can then be rotated to collect more scattering data and the topology optimization techniques were used to invert the data [146]. At each rotation such a system produces the identical incident field with respect to the boundary of the enclosure because the sources (*i.e.*, the waveguides) remain fixed with respect to the boundary. In the system described here, each rotation of the boundary produces a different incident field with respect to the boundary.

From a theoretical perspective, the first question to answer is: *Can MWT systems with different BCs provide non-redundant scattering information about the OI?* This question will be answered in Section 8.1. The proposed system is then explained in Section 8.2.

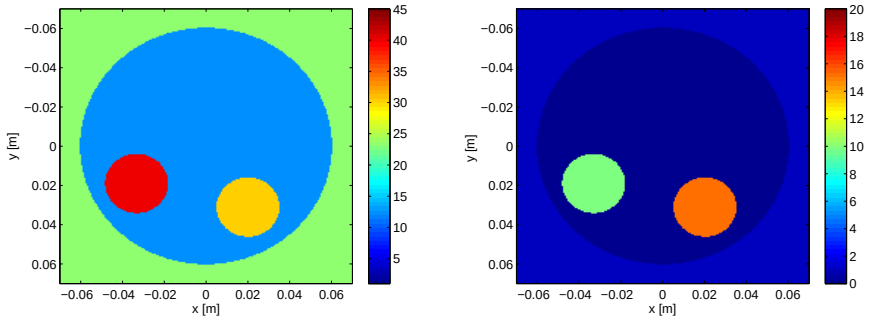

(a) $Re(\epsilon_r)$ (b) $Im(\epsilon_r)$

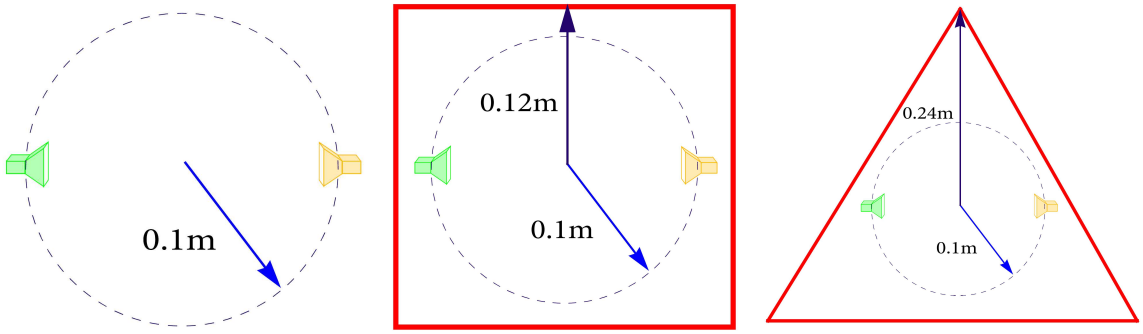

(c) Open-region case (d) Square PEC-enclosed-region case (e) Triangular PEC-enclosed-region case

Fig. 8.1: Synthetic data set: (a)-(b) exact relative permittivity, (c) configuration for the open-region case, (d) configuration for the square PEC-enclosed-region case (The red square is the PEC enclosure), and (e) configuration for the triangular PEC-enclosed-region case (The red equilateral triangle is the PEC enclosure).

8.1 Different BCs for MWT

As mentioned earlier, in most MWT systems currently in existence [129, 76, 130, 131, 144, 145], the OI and the antennas are contained within an enclosed chamber, usually made from a dielectric material such as plexiglass. The dielectric chamber is usually filled with a lossy matching fluid. Most MWT algorithms used to invert data from these systems assume that the matching fluid extends to infinity, not to the boundary of the dielectric casing. That is, they assume that the scattering data is collected in a homogeneous embedding. In other words, the BC for the problem will be the Sommerfeld radiation condition. We will refer to

the scattering data collected in such systems as the open-region scattering data.

More recently, researchers have considered MWT in a metallic casing where the OI and the antennas are enclosed by a circular metallic enclosure [133, 134, 147, 42, 138, 139, 148]. We have also considered microwave tomography inside conducting cylinders of arbitrary shapes [135]. The use of conducting enclosures imposes a zero boundary condition for the total field which can be easily modeled within the utilized inversion algorithm. We will refer to the scattering data collected in such systems as the PEC-enclosed-region scattering data. In this section, we show inversion results from the open-region and PEC-enclosed-region scattering data. For the PEC-enclosed-region scattering data, we consider PEC enclosures of different shapes. The utilized inversion algorithm is the MR-GNI, which has been explained in Section 5.2.2. As mentioned in Chapter 4, calculation of the Jacobian matrix and the simulated scattered field require repeated forward solver calls. For the open-region case, we utilize the method of moments (MoM) with the conjugate gradient algorithm accelerated by the fast Fourier transform (CG-FFT). The CG-FFT forward solver is also accelerated by employing the marching-on-in-source-position technique. Motivated by the desire to model arbitrary PEC boundaries with both straight and curved edges, we utilize a finite element method (FEM) based on triangular elements for the PEC-enclosed embedding. The FEM provides an accurate and fast forward solver, and in fact, is easier to implement with a PEC boundary than with absorbing boundary conditions, which are required for a homogeneous embedding. As the FEM mesh is based on triangles, and the inverse solver based on rectangular pulse-basis functions, we interpolate as required between the two meshes with a bi-linear interpolation algorithm [135].

We consider the target described in Section 7.5.2, and take three different configurations for collecting the scattering data; namely, open-region, square PEC-enclosed-region, and equilateral triangular PEC-enclosed-region. In all these three cases, the transmitters and

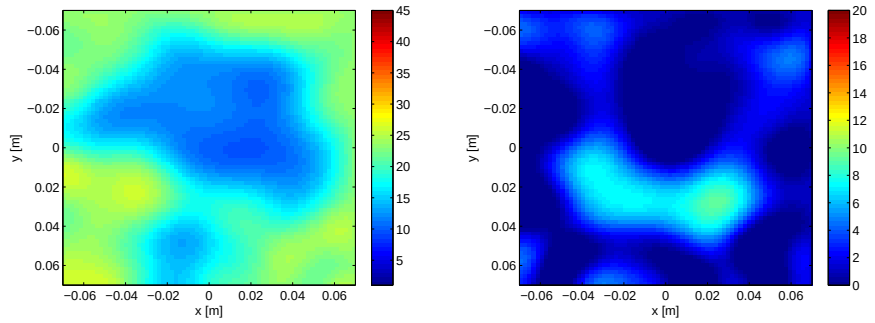

(a) $Re(\epsilon_r)$ (b) $Im(\epsilon_r)$

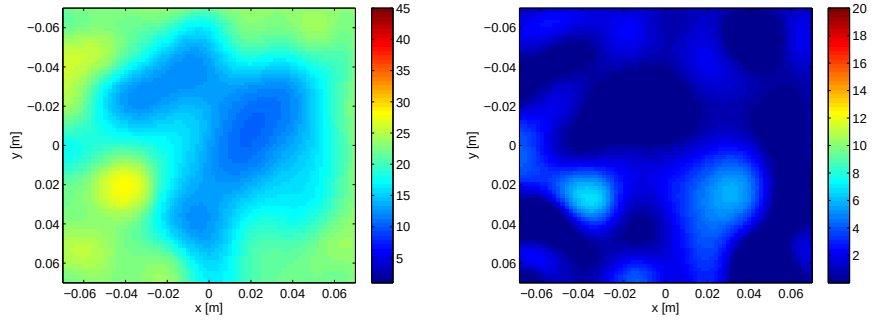

(c) $Re(\epsilon_r)$ (d) $Im(\epsilon_r)$

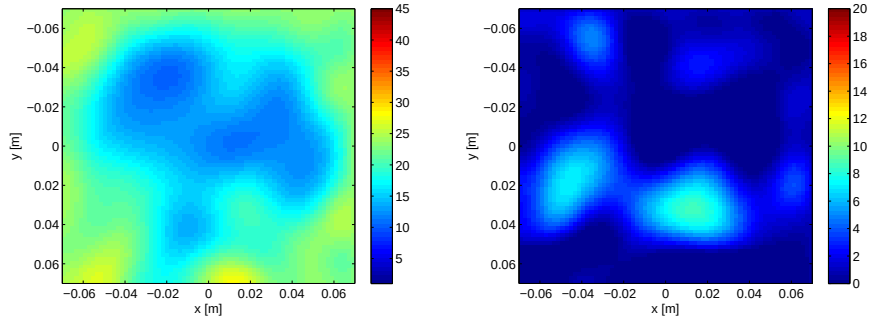

(e) $Re(\epsilon_r)$ (f) $Im(\epsilon_r)$

Fig. 8.2: 1st scenario: 7 transmitters and 7 receivers (a)-(b) inversion of the scattering data collected in the open-region embedding, (c)-(d) inversion of the scattering data collected in the square PEC-enclosed embedding, and (e)-(f) inversion of the scattering data collected inside the equilateral PEC-enclosed embedding.

receivers are evenly spaced on a circle of radius 0.1 m and the frequency of operation is 1 GHz. The target and these three configurations are shown in figure 8.1.

Two different scenarios are used to collect the scattering data. In the first scenario, we utilize 7 transmitters and 7 receivers for collecting the scattering data on the measurement circle. To all these synthetic data sets, 3% noise was added using the formula (4.31). The inversion results for these three cases are shown in figure 8.2. As can be seen, all these three inversions result in similar poor reconstructions.

That these reconstructions are very similar gives rise to the following question: *do these three scattering data sets, which are collected under different BCs, provide similar information about the OI?* To answer this question, we have developed an inversion algorithm to simultaneously invert the scattering data collected in different configurations. For example, for the case where there are two sets of scattering data, one collected in an open-region configuration and the other one in a PEC-enclosed-region configuration, we construct the following cost-functional,

$$\mathcal{C}_n(\chi) = \frac{1}{2}\left[\mathcal{C}^{\text{LS}}_{\text{open}}(\chi) + \mathcal{C}^{\text{LS}}_{\text{pec}}(\chi)\right]\mathcal{C}^{\text{MR}}_n(\chi) \tag{8.1}$$

This cost-functional is minimized using the GNI method. The subscript n denotes the n^{th} iteration of the GNI method, and $\mathcal{C}^{\text{LS}}_{\text{open}}$ and $\mathcal{C}^{\text{LS}}_{\text{pec}}$ represent the data misfit cost-functional, see (3.1), for the open-region and PEC-enclosed-region cases respectively. The regularizer $\mathcal{C}^{\text{MR}}_n$ is given in (5.15) and the steering parameter δ^2_n, in the discrete domain, is given as

$$\delta^2_n = \frac{1}{2}\frac{\mathcal{F}^{\text{LS}}_{\text{open}}(\underline{\chi}_n) + \mathcal{F}^{\text{LS}}_{\text{pec}}(\underline{\chi}_n)}{\Delta A}. \tag{8.2}$$

where $\underline{\chi}_n$ is the known contrast vector at the n^{th} iteration of the algorithm. Recall that $\mathcal{F}^{\text{LS}}_{\text{open}}(\underline{\chi}_n)$ and $\mathcal{F}^{\text{LS}}_{\text{pec}}(\underline{\chi}_n)$ are the discrete forms of $\mathcal{C}^{\text{LS}}_{\text{open}}(\chi_n)$ and $\mathcal{C}^{\text{LS}}_{\text{pec}}(\chi_n)$. The contrast is then

updated in the form of $\underline{\chi}_{n+1} = \underline{\chi}_n + \nu_n \Delta\underline{\chi}_n$ where ν_n is the step-length and the correction $\Delta\underline{\chi}_n$ is found by solving

$$\left(\underline{\boldsymbol{A}}_n^H \underline{\boldsymbol{A}}_n - \beta_n \underline{\boldsymbol{\mathcal{L}}}_n\right) \Delta\underline{\chi}_n = \underline{\boldsymbol{A}}_n^H \underline{d}_n^{\text{open,pec}} + \beta_n \underline{\boldsymbol{\mathcal{L}}}_n \underline{\chi}_n. \tag{8.3}$$

The complex matrix $\underline{\boldsymbol{A}}_n$ is constructed as

$$\underline{\boldsymbol{A}}_n = \begin{pmatrix} \sqrt{\eta_{\mathcal{S},\text{open}}}\, \underline{\boldsymbol{J}}_{\text{open},n} \\ \sqrt{\eta_{\mathcal{S},\text{pec}}}\, \underline{\boldsymbol{J}}_{\text{pec},n} \end{pmatrix} \tag{8.4}$$

where $\underline{\boldsymbol{J}}_{\text{open},n}$ and $\underline{\boldsymbol{J}}_{\text{pec},n}$ are the Jacobian matrices for the open-region and PEC-enclosed-region cases at the n^{th} iteration of the algorithm respectively. The normalization factors for the open-region and PEC-enclosed-region scattering data, $\eta_{\mathcal{S},\text{open}}$ and $\eta_{\mathcal{S},\text{pec}}$, are also given in (4.10). The vector $\underline{d}_n^{\text{open,pec}}$ is given as

$$\underline{d}_n = \begin{pmatrix} \underline{d}_{\text{open},n} \\ \underline{d}_{\text{pec},n} \end{pmatrix} = \begin{pmatrix} \underline{E}^{\text{scat}}_{\text{open},n} - \underline{E}^{\text{scat}}_{\text{meas,open}} \\ \underline{E}^{\text{scat}}_{\text{pec},n} - \underline{E}^{\text{scat}}_{\text{meas,pec}} \end{pmatrix} \tag{8.5}$$

where $\underline{E}^{\text{scat}}_{\text{open},n}$ and $\underline{E}^{\text{scat}}_{\text{pec},n}$ are the complex vectors containing the simulated scattered field at the observation points corresponding to the predicted contrast $\underline{\chi}_n$ for the open-region and PEC-enclosed-region cases. The complex vectors $\underline{E}^{\text{scat}}_{\text{meas,open}}$ and $\underline{E}^{\text{scat}}_{\text{meas,pec}}$ represent the measured data for the open-region and PEC-enclosed-region cases. The discrete regularization operator $\underline{\boldsymbol{\mathcal{L}}}_n$ has been described in Section 5.2.2. The weight of this regularization, *i.e.*, β_n, will be

$$\beta_n = \mathcal{F}^{\text{LS}}_{\text{open}}(\underline{\chi}_n) + \mathcal{F}^{\text{LS}}_{\text{pec}}(\underline{\chi}_n). \tag{8.6}$$

Using this inversion algorithm, we simultaneously invert the three data sets described above (where 7 transmitters/receivers are used). In figure 8.3, we show the simultaneous inver-

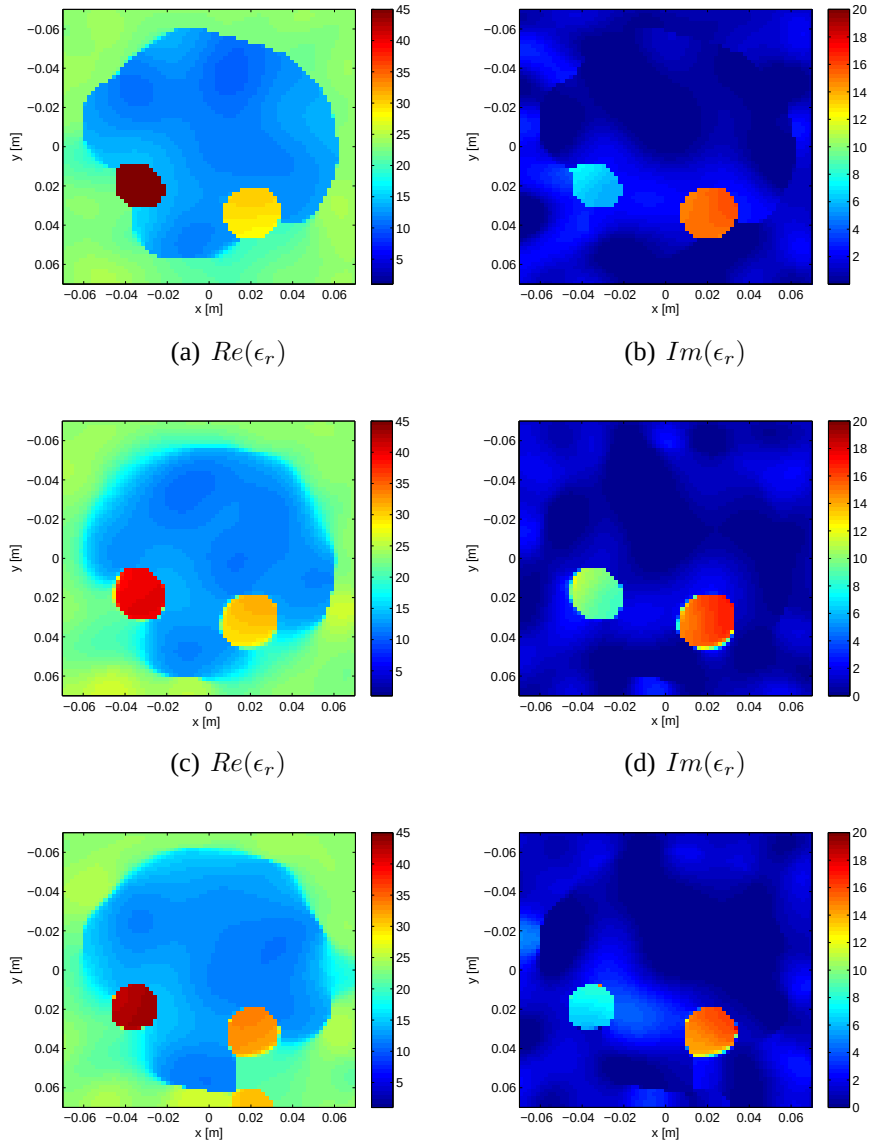

(a) $Re(\epsilon_r)$ (b) $Im(\epsilon_r)$

(c) $Re(\epsilon_r)$ (d) $Im(\epsilon_r)$

(e) $Re(\epsilon_r)$ (f) $Im(\epsilon_r)$

Fig. 8.3: 1st scenario: 7 transmitters and 7 receivers; simultaneous inversion of (a)-(b) scattering data collected in the open-region and square PEC-enclosed region configurations, (c)-(d) scattering data collected in the open-region and triangular PEC-enclosed region configurations, and (e)-(f) scattering data collected in the square PEC-enclosed region and triangular PEC-enclosed region configurations.

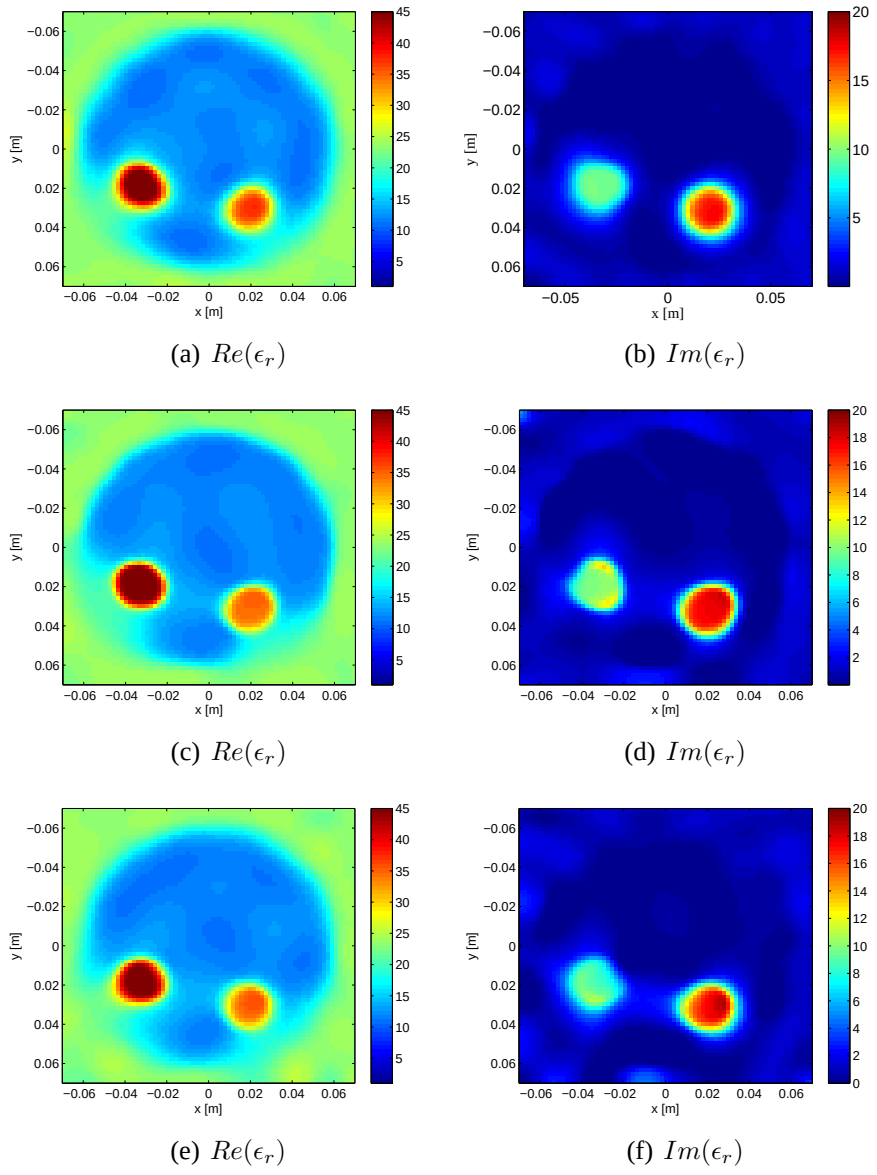

(a) $Re(\epsilon_r)$ (b) $Im(\epsilon_r)$

(c) $Re(\epsilon_r)$ (d) $Im(\epsilon_r)$

(e) $Re(\epsilon_r)$ (f) $Im(\epsilon_r)$

Fig. 8.4: 2nd scenario: 16 transmitters and 16 receivers (a)-(b) inversion of the scattering data collected in the open-region embedding, (c)-(d) inversion of the scattering data collected in the square PEC-enclosed embedding, and (e)-(f) inversion of the scattering data collected in the triangular PEC-enclosed embedding.

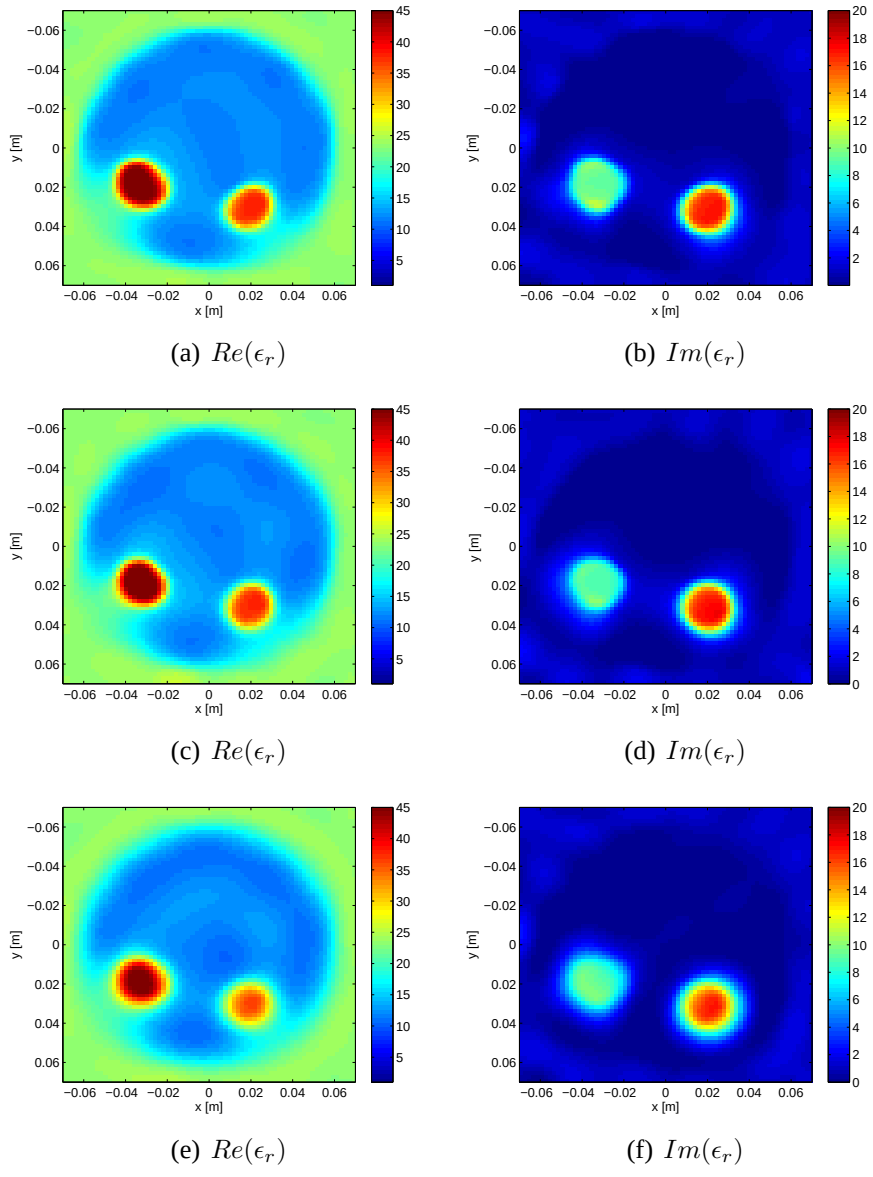

(a) $Re(\epsilon_r)$ (b) $Im(\epsilon_r)$

(c) $Re(\epsilon_r)$ (d) $Im(\epsilon_r)$

(e) $Re(\epsilon_r)$ (f) $Im(\epsilon_r)$

Fig. 8.5: 2nd scenario: 16 transmitters and 16 receivers; simultaneous inversion of (a)-(b) scattering data collected in the open-region and square PEC-enclosed region configurations, (c)-(d) scattering data collected in the open-region and triangular PEC-enclosed region configurations, and (e)-(f) scattering data collected in the square PEC-enclosed and triangular PEC-enclosed region configurations.

sion of (*i*) open-region and square PEC-enclosed-region scattering data, (*ii*) open-region and triangular PEC-enclosed-region scattering data, and (*iii*) square PEC-enclosed-region and triangular PEC-enclosed-region scattering data. As can be seen, the simultaneous inversion results are very close to the true profile. Comparing figure 8.3 and figure 8.2, it can be easily seen that the simultaneous inversion has resulted in a more accurate reconstruction compared to the separate inversions of each data set. That being said, and noting that these data sets are distinguished by their corresponding BCs, it can be concluded that these three BCs have provided non-redundant information about the OI.

We now consider the second scenario for collecting the scattering data in these three configurations, where we increase the number of transmitters/receivers to 16. Again, 3% noise is added to each data set. The inversion of each data set is shown in figure 8.4. The simultaneous inversion of these data sets are shown in figure 8.5. In this scenario, the separate inversion of each data set and the simultaneous inversions result in similar reconstruction.

From these two scenarios and other similar inversion results (not shown here), it can be concluded that MWT systems with different BCs, at least when utilizing very few transmitters and receivers, provides non-redundant information for the reconstruction. We note that the necessary condition to obtain non-redundant information is to use a lossless or low-loss background medium to not suppress the reflection from the PEC enclosure.

8.2 MWT system using a rotatable conductive enclosure

Based on the idea that collecting scattering data using few transceivers and under different BCs yields different usable information, we now consider a rotatable equilateral triangular metallic casing, Γ, which encloses the OI and a few transceivers, see figure 8.6. The OI is located in the bounded imaging domain $\mathcal{D} \subset \mathbb{R}^2$. The transceivers are located on the

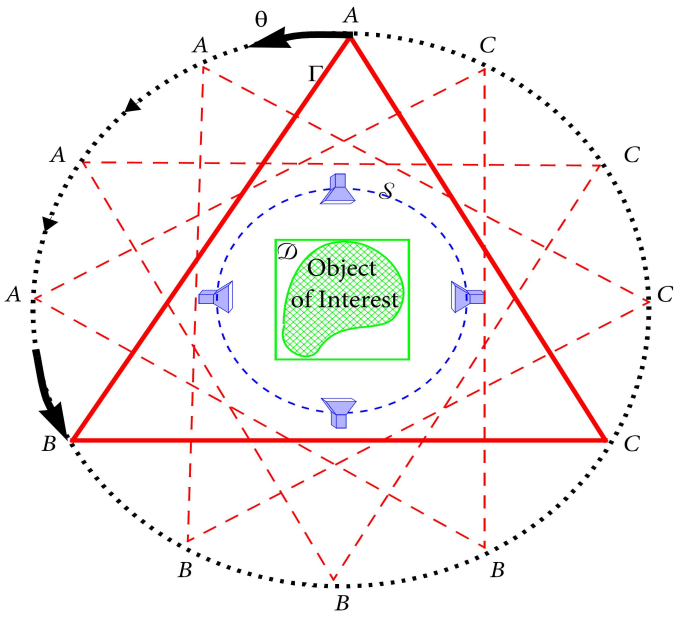

Fig. 8.6: The geometrical configuration of the MWT problem with a rotatable conductive triangular enclosure. The red equilateral triangle, $\triangle ABC$, represents the metallic casing, which encloses the imaging domain $\mathcal{D}$ and the measurement domain $\mathcal{S}$. The dotted black circle is the circumscribing circle of the triangle. The triangular enclosure can rotate on within a circumscribing circle for θ degrees where $\theta \in [0^\circ, 120^\circ)$.

measurement domain $\mathcal{S} \subset \mathbb{R}^2$, which is outside the OI. We assume that the metallic casing is a PEC and is filled with a lossless or low-loss matching fluid with a known relative complex permittivity of ϵ_b. To obtain more scattering data by changing the BCs of the MWT system, the enclosure Γ is rotated at angles $\theta_l \in [0^\circ, 120^\circ)$, $l = 1, \cdots, L$, with respect to the fixed $\mathcal{D}$ and fixed $\mathcal{S}$ as depicted in figure 8.6. At the l^{th} configuration of the enclosure Γ, the OI is successively illuminated by some incident electric field, $\boldsymbol{E}^{\text{inc}}_{l,t}$ where t denotes the transmitter index ($t = 1, \cdots, T_x$). Interaction of the incident field with the OI results in the total field $\boldsymbol{E}_{l,t}$. Note that the field obtained depends not only on the transmitter location, but also on the orientation of the enclosure. The total and incident electric fields are then measured by the receiver antennas located on $\mathcal{S}$. Thus, the scattered field at the observation points, contaminated by measurement noise, is known and denoted by $\boldsymbol{E}^{\text{scat}}_{\text{meas},l,t}$.

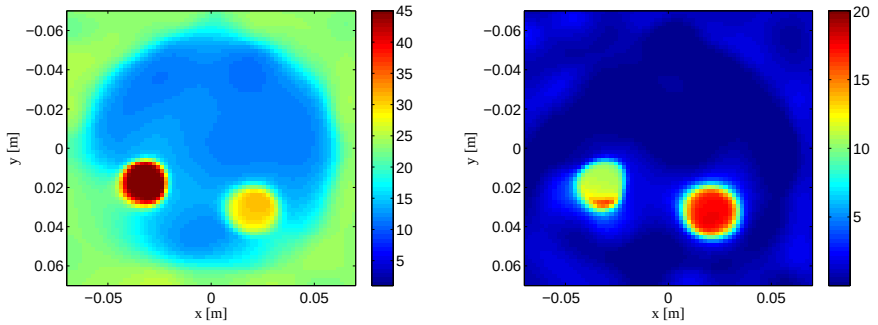

(a) $Re(\epsilon_r)$ (b) $Im(\epsilon_r)$

Fig. 8.7: Synthetic data set ($f = 1$ GHz). (a)-(b) Reconstructed relative complex permittivity when the scattering data is collected inside the rotatable triangular conductive enclosure using 4 transmitters and 4 receivers and 12 rotations of the enclosure.

The MWT problem may then be formulated as the minimization over χ of the following nonlinear least-squares data misfit cost-functional

$$\mathcal{C}^{\text{ROT}}(\chi) = \frac{1}{L}\sum_{l=1}^{L}\mathcal{C}_l^{\text{LS}}(\chi) = \frac{1}{L}\sum_{l=1}^{L}\eta_{\mathcal{S},l}\sum_{t=1}^{T_x}\left\|\boldsymbol{E}_{l,t}^{\text{scat}} - \boldsymbol{E}_{\text{meas},l,t}^{\text{scat}}\right\|_{\mathcal{S}}^2 \tag{8.7}$$

where $\boldsymbol{E}_{l,t}^{\text{scat}}$ is the simulated scattered field on $\mathcal{S}$ due to a predicted contrast χ when the t^{th} transmitter is active at the l^{th} configuration of the triangular enclosure. That is, $\boldsymbol{E}_{l,t}^{\text{scat}}(\boldsymbol{p}) = \mathcal{E}_{l,t}^{\text{scat}}(\chi)$. The operator $\mathcal{E}_{l,t}^{\text{scat}}$ is given in (2.20) where the incident field needs to be replaced with the incident field when the t^{th} transmitter is active at the l^{th} configuration of the triangular enclosure; *i.e.*, $\boldsymbol{E}_{l,t}^{\text{inc}}$. The normalization factor is given by

$$\eta_{\mathcal{S},l} = \left(\sum_{t=1}^{T_x}\left\|\boldsymbol{E}_{\text{meas},l,t}^{\text{scat}}\right\|_{\mathcal{S}}^2\right)^{-1}. \tag{8.8}$$

We regularize (8.7) by the weighted L^2-norm total variation multiplicative regularizer, $\mathcal{C}^{\text{MR}}(\chi)$, given in (5.15). Thus, at the n^{th} iteration of the inversion algorithm, we minimize the regu-

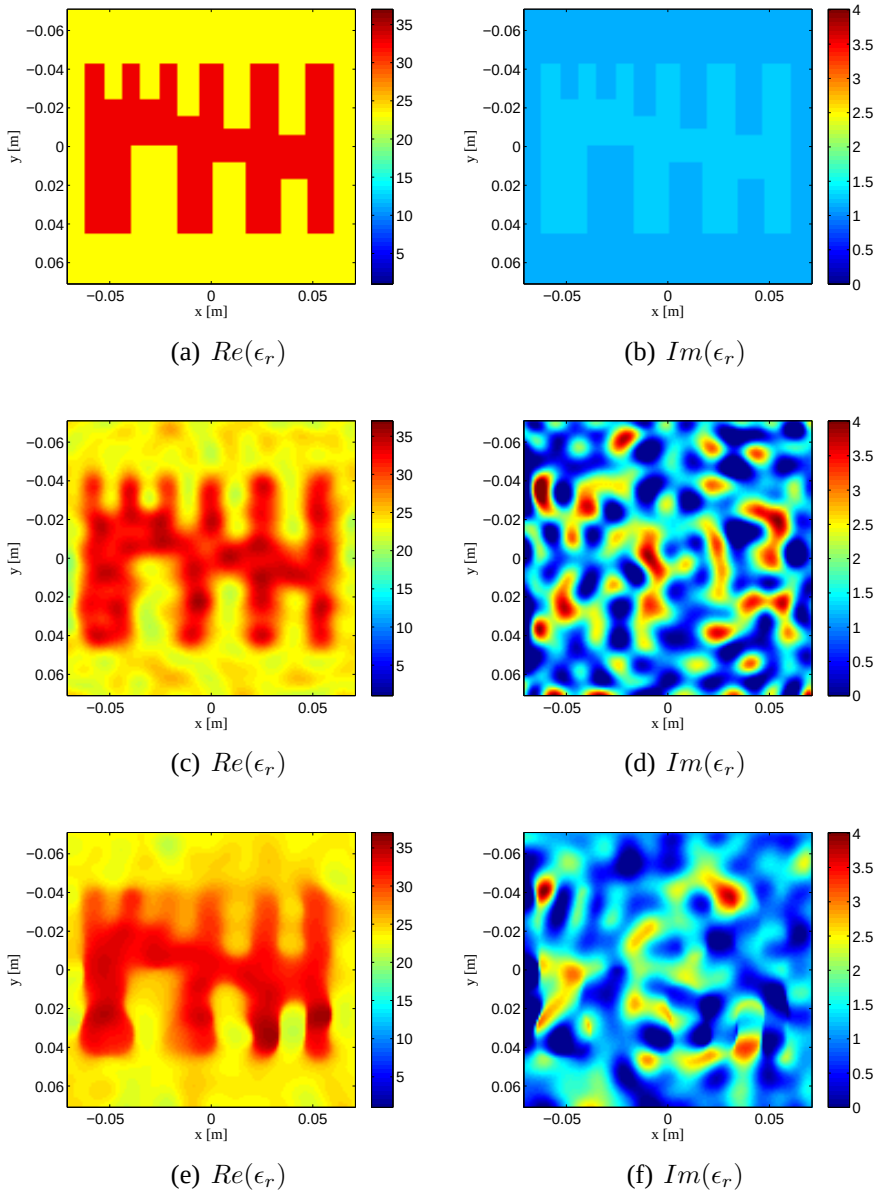

(a) $Re(\epsilon_r)$ (b) $Im(\epsilon_r)$

(c) $Re(\epsilon_r)$ (d) $Im(\epsilon_r)$

(e) $Re(\epsilon_r)$ (f) $Im(\epsilon_r)$

Fig. 8.8: Synthetic *E*-target data set (II) (a)-(b) true relative complex permittivity profile of the target (c)-(d) reconstructed relative complex permittivity when the scattering data is collected inside the rotating triangular conducting enclosure using 6 transmitters and 6 receivers and 48 rotations of the enclosure (e)-(f) reconstructed relative complex permittivity when the scattering data is collected in the open-region embedding using 16 transmitters and 16 receivers.

larized cost-functional

$$\mathcal{C}_n(\chi) = \mathcal{C}^{\text{ROT}}(\chi)\mathcal{C}_n^{\text{MR}}(\chi). \tag{8.9}$$

The positive parameter δ_n^2 in (5.15) is chosen to be $\mathcal{F}^{\text{ROT}}(\underline{\chi}_n)/\Delta A$ where $\mathcal{F}^{\text{ROT}}(\underline{\chi}_n)$ is the discrete form of $\mathcal{C}^{\text{ROT}}(\chi_n)$. The contrast vector is then updated in the form of $\underline{\chi}_{n+1} = \underline{\chi}_n + \nu_n \Delta\underline{\chi}_n$ where $\Delta\underline{\chi}_n$ is the correction and ν_n is an appropriate step length at the n^{th} iteration of the algorithm. The correction vector $\Delta\underline{\chi}_n$ is then found by solving

$$\left[\left(\sum_{l=1}^{L} \eta_{\mathcal{S},l}\, \underline{\boldsymbol{J}}_{l,n}^H\, \underline{\boldsymbol{J}}_{l,n}\right) - \beta_n \underline{\boldsymbol{\mathcal{L}}}_n\right] \Delta\underline{\chi}_n = \left(\sum_{l=1}^{L} \eta_{\mathcal{S},l}\, \underline{\boldsymbol{J}}_{l,n}^H\, \underline{d}_{l,n}\right) + \beta_n \underline{\boldsymbol{\mathcal{L}}}_n \underline{\chi}_n \tag{8.10}$$

where $\underline{\boldsymbol{\mathcal{L}}}_n$ is given in Section 5.2.2. The matrix $\underline{\boldsymbol{J}}_{l,n}$ is the Jacobian matrix corresponding to the l^{th} rotation of the enclosure and at the n^{th} iteration of the inversion algorithm. The weight β_n is equal to $L \times \mathcal{F}^{\text{ROT}}(\underline{\chi}_n)$. The discrepancy vector $\underline{d}_{l,n}$ is

$$\underline{d}_{l,n} = -\left(\underline{E}_{l,n}^{\text{scat}} - \underline{E}_{\text{meas},l}^{\text{scat}}\right). \tag{8.11}$$

To calculate the Jacobian matrices $\underline{\boldsymbol{J}}_{l,n}$ and the simulated scattered field $\underline{E}_{l,n}^{\text{scat}}$, we utilize a finite element method (FEM) [135].

Inversion results are shown for two synthetic data sets that have been created with a frequency-domain FEM forward solver. To all synthetic data sets, 3% noise was added using the formula (4.31). In both cases, we use the equilateral triangular PEC enclosure shown in figure 8.6 and assume that the radius of the circumscribing circle of the triangle is 0.24 m. The radius of the measurement circle $\mathcal{S}$, see figure 8.6 is chosen to be 0.1 m for both data sets. We assume that the relative complex permittivity of the matching fluid is $23.4 + j1.13$.

The first synthetic data set is collected from the target described in Section 7.5.2, which is also used in Section 8.1 and shown in figure 8.1 (a)-(b). Similar to the inversion results

shown in Section 8.1, the frequency of operation is chosen to be 1 GHz. We consider only 4 transmitters and 4 receivers per transmitter which are evenly spaced on $\mathcal{S}$. Therefore, for the l^{th} rotation of the PEC enclosure, we have $\underline{E}^{\text{scat}}_{\text{meas},l} \in \mathbb{C}^{16}$. The PEC enclosure is rotated 12 times ($L = 12$) with a step of 15°. Therefore, the number of measured data will be $12 \times 16 = 192$. The inversion of this scattering data, which is collected in the rotatable PEC enclosure, is shown in figure 8.7. The inversion of the scattering data collected from the same target in the open-region configuration using 16 transmitters and 16 receivers ($\underline{E}^{\text{scat}}_{\text{meas}} \in \mathbb{C}^{256}$) is shown in figure 8.4 (a)-(b). As can be seen, the reconstruction inside the rotating PEC enclosure with only 4 transceivers and the reconstruction inside the open-region configurations with 16 transceivers are very similar for this target and both provide a reasonable reconstruction for both the real and imaginary parts of the target's relative complex permittivity.

Finally, we consider the synthetic *E*-target data set (II) described in Section 5.6.2. The target is shown in figure 8.8 (a)-(b). To collect scattered field data, we consider 6 transmitters and 6 receivers per transmitter; thus, $\underline{E}^{\text{scat}}_{\text{meas},l} \in \mathbb{C}^{36}$. The PEC enclosure is then rotated 48 times with a step of 2.5°; thus, providing $48 \times 36 = 1728$ scattering measurements. The inversion of the scattering data collected inside the rotating PEC enclosure is shown in figure 8.8 (c)-(d), while the inversion of the scattering data collected in the open-region embedding using 16 transmitters and 16 receivers is shown in figure 8.8 (e)-(f). In both cases, the real part of the permittivity is reconstructed well but the imaginary part is poorly reconstructed. This is due to the fact the imaginary part of the contrast is much smaller than the real part of the contrast (the contrast of the target is about $0.40 - j0.01$). To get a better reconstruction for this target, we apply the image enhancement method, presented in Section 5.7, to the final reconstructions of both reconstructions. The enhanced reconstructions for both cases are shown in figure 8.9.

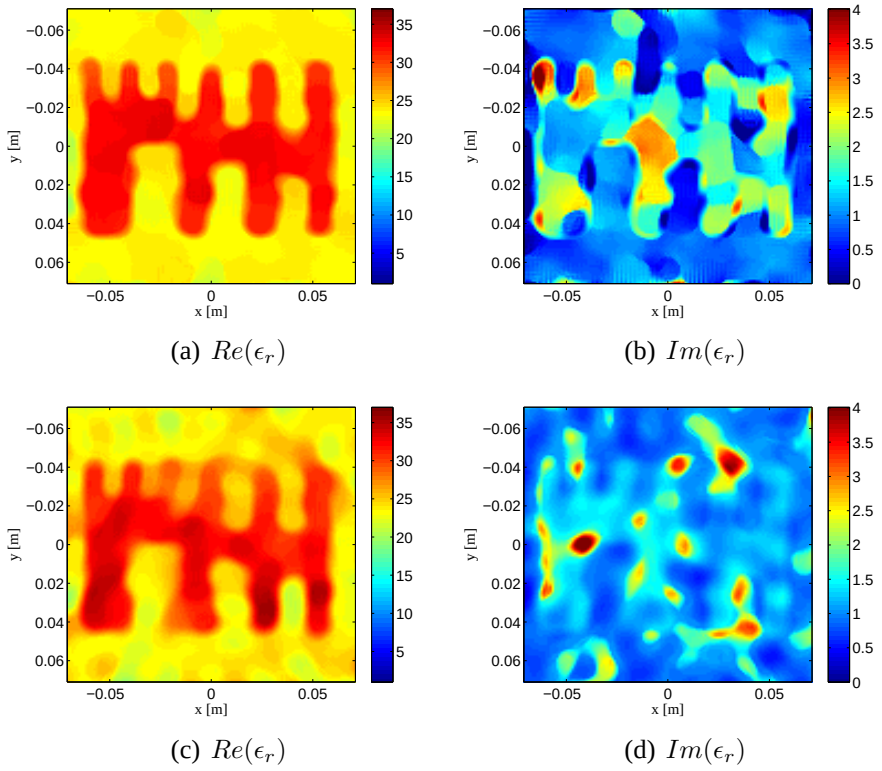

(a) $Re(\epsilon_r)$ (b) $Im(\epsilon_r)$

(c) $Re(\epsilon_r)$ (d) $Im(\epsilon_r)$

Fig. 8.9: Synthetic *E*-target data set (II); Reconstruction results after applying the enhancement algorithm inside (a)-(b) the rotatable triangular conductive enclosure with 6 transmitters and 6 receivers and 48 rotations, and (c)-(d) the open-region embedding with 16 transmitters and 16 receivers.

A better imaginary-part reconstruction can be achieved by utilizing *a priori* information about the expected ratio between the real and imaginary parts of the target's contrast as outlined in Section 5.6.2. Considering this ratio as $Q = 40$, the reconstructions of both data sets, shown in figure 8.10, become very similar and satisfactory.

Using these two data sets, the possibility of imaging inside a rotatable triangular conductive enclosure using a minimal antenna array having as few as only four or six co-resident elements has been demonstrated for the 2D TM case. This study may result in the development of MWT systems which introduce less modeling error to MWT algorithms compared to the existing MWT systems while maintaining the ability to collect sufficient scattering information about the OI. Considering that the modeling error can be thought of as part of the

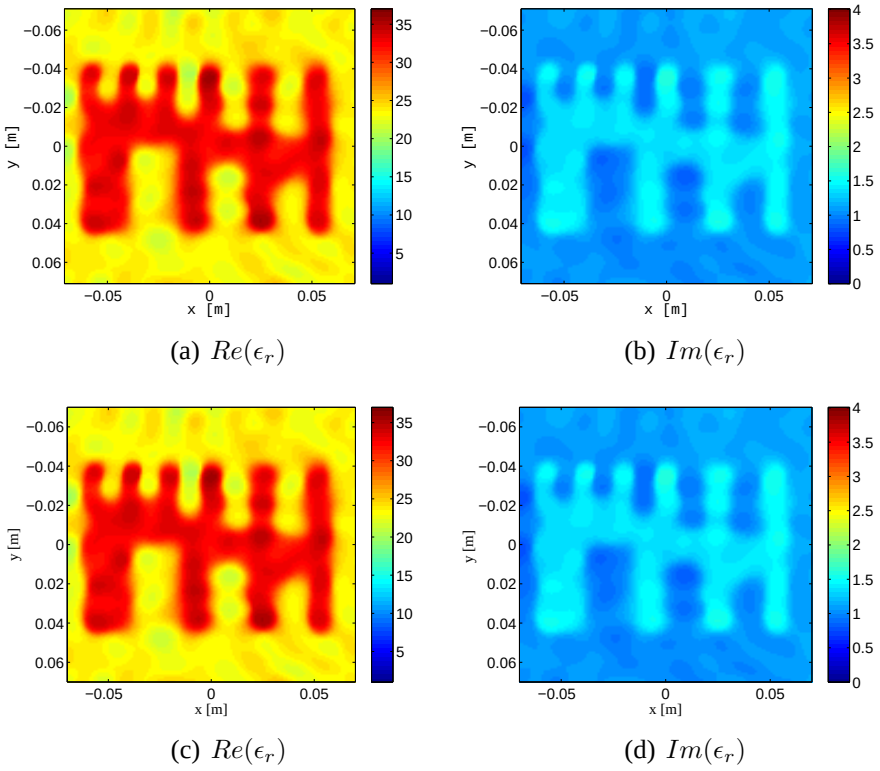

(a) $Re(\epsilon_r)$ (b) $Im(\epsilon_r)$

(c) $Re(\epsilon_r)$ (d) $Im(\epsilon_r)$

Fig. 8.10: Synthetic *E*-target data set (II): pre-scaled GNI with $Q = 40$ (a)-(b) inversion inside the rotatable triangular conductive enclosure with 6 transmitters and 6 receivers and 48 rotations of the enclosure, and (c)-(d) inversion inside the open-region embedding with 16 transmitters and 16 receivers.

manifest noise, and noting that the achievable resolution limit is affected by the signal-to-noise ratio [106, 136], the proposed MWT system may offer an enhanced spatial resolution over the existing MWT systems.

9

University of Manitoba MWT Systems

> *One day sir, you may tax it.* (Michael Faraday in reply to British Chancellor of the Exchequer when asked of the practical value of electricity in 1850) [149, pg. 56].

Our research group at the University of Manitoba has constructed a microwave tomography prototype with a plexiglass casing [145], as well as a prototype with a metallic casing [150]. At the current state of development, the background medium, in both systems, is free-space and the inversion is performed under the 2D TM assumption. Thus, we assume $\boldsymbol{E}^{\text{scat}}_{\text{meas},t} = E^{\text{scat}}_{\text{meas},t}\hat{z}$ and $\boldsymbol{E}^{\text{inc}}_{t} = E^{\text{inc}}_{t}\hat{z}$. We note that for our MWT systems, we have utilized a frequency selection procedure to determine the optimum operational frequency(ies) of the systems. This frequency selection procedure is not part of this thesis and will not be explained here but can be found in [145] for the MWT system with plexiglass casing and in [151, 152] for the MWT system with metallic casing.

9.1 MWT system with plexiglass casing

A photograph of the current prototype is shown in figure 9.1. We have employed a two-port Agilent 8363B PNA-Series Network Analyzer (NA) as our microwave source and receiver, capable of producing measurements at discrete frequencies or sweeps within the required frequencies at an approximate system dynamic range of 122 dB (an additional 15 dB of dynamic range is available using the configurable test set). The NA is connected to the antennas with a 2×24 cross-bar mechanical switch (Agilent 87050A-K24), which provides isolation of greater than 95 dB over the frequency range of interest. Twenty-four antennas are arranged at even intervals of 15° in a circular array at the midpoint height along the inside of a plexiglass cylinder. The cylinder has a radius of ≈ 22 cm, is 50.8 cm tall and is water-tight, allowing it to be filled with a matching liquid (not utilized in this work). The future use of a matching fluid may necessitate even higher isolation than 95 dB, and a re-design of the switch, but solutions to this do exist; *e.g.*, see [153]. For use with certain classes of test targets, there is also a motor assembly located underneath the cylinder support structure that consists of two precision stepper motors arranged to provide accurate positioning of the target within the chamber. The test target may be placed on a plastic platform mounted on a central nylon pillar protruding from a water-tight, sealed hole in the center of the cylinder's bottom boundary, and can be rotated 360° (at increments smaller than 1° if needed). A vertical movement range for the pillar of roughly 15 cm is also accommodated by the motor assembly to provide full 3D positioning of the target through the 2D plane of the antenna array.

Communication between the NA, switch, and the controlling computer is accomplished through the General Purpose Interface Bus (GPIB), operating via a GPIB-Ethernet hub. The data acquisition process is entirely automated. A full measurement at a single frequency, ($23 \times 24 = 552$ data points) takes less than 1 minute (this time depends highly on the sweep

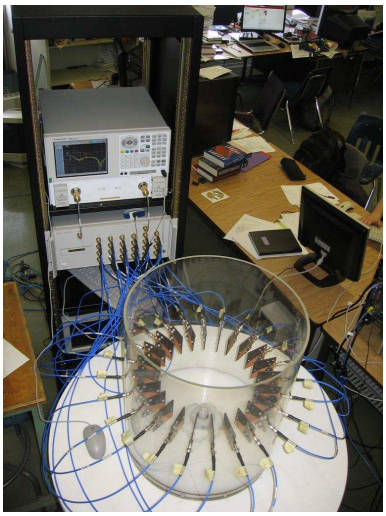

Fig. 9.1: The University of Manitoba microwave tomography prototype with plexiglass casing. The 24 Vivaldi antennas are connected to a network analyzer via a 2×24 switch. At the current state of development, the background medium is air.

time utilized for the NA). It is possible to further reduce this time, which will ultimately be limited by the stabilization time of the mechanical switch.

9.1.1 Co-resident antennas

For this system, we utilize Vivaldi antennas [154], which have been specifically designed and improved for this near-field microwave tomography system [155]. The design bandwidth of the antennas is from 3 GHz to 10 GHz, although in practice we have found them to have a usable S_{11} from 2 GHz to 10 GHz. They utilize a double-layer construction which significantly reduces the cross-polarization level of the radiation pattern [155]. This is critical to the use of the 2D TM assumption about the wave propagation in the chamber, as antennas which create and detect x and y polarized fields would seriously degrade the resulting images. A picture of one of the antennas is shown in figure 9.2.

It is further desirable that these antennas have a radiation pattern as similar as possible to an

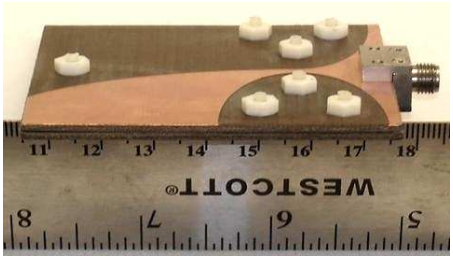

Fig. 9.2: Close-up of one of the double layered Vivaldi antennas used in the University of Manitoba's microwave tomography system with plexiglass casing. The two layers are held together with Teflon screws.

ideal 2D electric line source ideal radiator, as this is the assumed source for the inversion algorithms used throughout. A detailed description of the antenna gain pattern and beamwidth can be found in [145]. We note that the antennas are more directive than a true 2D electric line source. While this runs counter to the incident field assumption, it minimizes the coupling between the nearest non-active antennas to the active (transmitting) antenna, which is also a problem for the inversion process [145].

9.1.2 Data collection and calibration

As the utilized MWT inversion algorithms require scattered field measurements, and any physical system is only capable of detecting the total field, the raw data are first collected for the MWT system with no scatterer present. This data, labeled the 'incident' measurement, is then subtracted from all the subsequent data to produce the scattered field data.

The scattered data must then be calibrated. There are two purposes for the calibration: (*i*) to convert the S_{21} values measured by the NA into field values needed by the inversion algorithms, and (*ii*) to eliminate and compensate for as many measurement errors as possible. To perform the calibration, we first measure scattered data from a metallic cylinder with a known radius placed in the middle of the chamber. Assuming that the t^{th} transmitter is

active, we denote the measured S parameters as $S_{21,t}^{\text{scat,known}}$. Next, the scattering experiment is repeated, but with the unknown target present. These S parameters are denoted $S_{21,t}^{\text{scat,OI}}$. Assuming a 2D line source generated incident field, we further denote the analytic scattered fields from the known metallic cylinder as $E_t^{\text{scat,known}}$ which may be calculated using the formula given in [156].

Finally, the calibrated measured fields, $E_{\text{meas},t}^{\text{scat}}$, for the unknown target are calculated by

$$E_{\text{meas},t}^{\text{scat}} = \frac{E_t^{\text{scat,known}}}{S_{21,t}^{\text{scat,known}}} S_{21,t}^{\text{scat,OI}}. \tag{9.1}$$

This method of calibration will eliminate any errors which are constant over the two S_{21} measurements. Examples of these types of 'removable' errors include cable losses and phase shifts, or mis-matches at connectors. However, there are other factors in the measurement which are not constant between the two measurements, and thus not entirely removed via the above calibration object. For example, the antenna factor is not guaranteed to be the same for the known and unknown measurements (as the system is operating in the near-field). Another error which is not entirely compensated for is the antenna coupling, as the coupling will change when different scatterers are present in the chamber. For these reasons, the known object should be as similar as possible to the expected class of unknown target.

While some MWT systems utilize the 'known' object to be the empty chamber (*i.e.*, the incident measurement is utilized), *e.g.*, see [153, 130] and Section 9.3.1, we have found that the use of a metallic cylinder calibration object improves the inversion results for our system with plexiglass casing [145]. A well-characterized penetrable scatter used for calibration would eliminate more systematic errors, and provide even better imaging results, but due to the ease of characterization we have utilized a metallic cylinder [145].

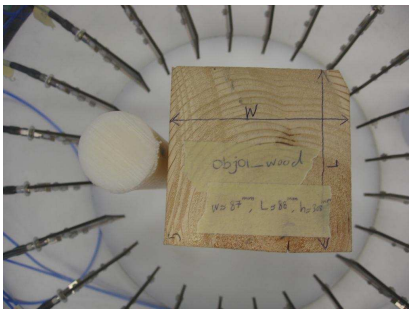

Fig. 9.3: Scatterer #1: dielectric phantom target consisting of nylon and wooden cylinders.

9.1.3 Inversion results from our MWT system with plexiglass casing

For all reconstructions presented herein, the only constraint on the minimization utilized was to keep the reconstructed relative complex permittivity within physical ranges (*i.e.*, $\text{Re}(\epsilon_r) \geq 1$ and $\text{Im}(\epsilon_r) \geq 0$). This was accomplished by over-writing the values at the end of each iteration in the inversion process if these constraints were violated. In this section, we consider two phantoms which will be explained below.

For the first phantom experiment, we utilize a circular nylon-66 cylinder with a diameter of 3.8 cm (1.5 inches) and an (approximately) square cross-section wooden block. We refer to this target as Scatterer #1. With the Agilent 85070E dielectric probe kit, we measured the wood to have a contrast of $\chi^{\text{wood}} \approx 1.0 + j0.2$ at 3 GHz. As the nylon-66 cylinder is too small for accurate bulk-material measurement, we utilize the published contrast of $\chi^{\text{nyl}} = 2.0 + j0.03$ at 3 GHz [156].

The target was placed in the chamber, as shown in figure 9.3, with an air background and 23×24 measurements were taken for the frequencies of 3 GHz and 6 GHz. The single-frequency 3 GHz reconstruction from the enhanced DBIM [55] is shown in figure 9.4 (a)-(b), and the frequency-hopping based [111] reconstruction of the two frequencies is shown in figure 9.4 (c)-(d). We note that the off-axis rotation of the wood in all reconstructions

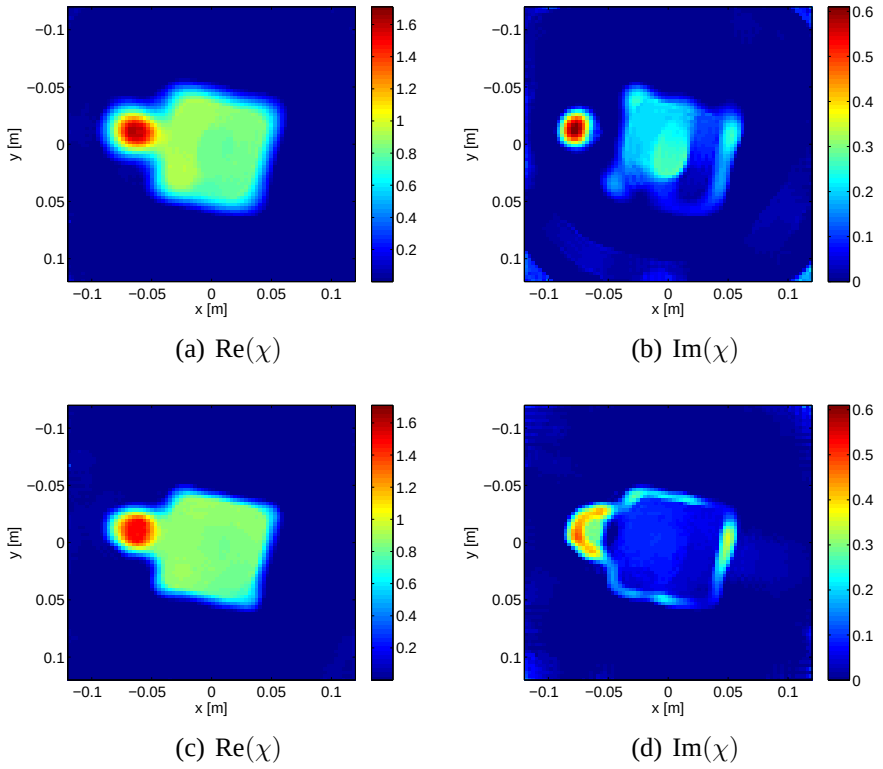

(a) Re(χ) (b) Im(χ)

(c) Re(χ) (d) Im(χ)

Fig. 9.4: Scatterer #1: (a)-(b) single-frequency reconstruction at 3 GHz, and (c)-(d) multiple-frequency reconstruction at 3 GHz and 6 GHz (using the frequency-hopping technique).

reflects the physical orientation of the wood for the measurement. We also note that the enhanced-DBIM inversion is very similar to the MR-GNI reconstruction (not shown here) of this target. The details of the enhanced DBIM can be found in [55].

For the 3 GHz reconstruction, figure 9.4 (a)-(b), we note that the real part of the contrast shows the overall structure of the targets quite well, but the reconstruction for nylon is 20% low: $Re(\chi) = 1.6$ instead of the expected value of $Re(\chi^{\text{nyl}}) = 2.0$. For the wooden object, the real part of the contrast is reconstructed as ≈ 1.1, within 10%, and the reconstruction shows a homogeneous region (which is what we expect). For the imaginary part of the reconstruction at 3 GHz, we note that the presence of the two distinct objects is clear, but the imaginary part of the nylon is overestimated (Im(χ) ≈ 0.6, when it should be Im(χ^{nyl}) $= 0.03$). Further, the imaginary part of the contrast for the wooden object is not homogeneous,

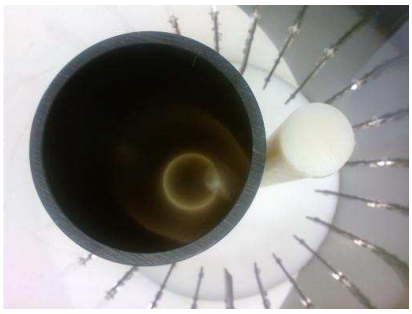

Fig. 9.5: Scatterer #2: dielectric phantom target consisting of PVC and nylon cylinders. The separation between the cylinders was 1 cm.

although the expected value of $\mathrm{Im}(\chi) = 0.2$ is achieved in the center.

For the multiple-frequency reconstruction at 3 GHz and 6 GHz, figure 9.4 (c)-(d), the contrast of the nylon is closer to the expected value than for the single-frequency case for the imaginary part ($\mathrm{Im}(\chi) \approx 0.45$). For the wood, the real part is again accurate (roughly the same as for the 3 GHz reconstruction). The edges of the objects are visible in the imaginary part of the reconstructed contrast, and the interior of the wood is more homogeneous, but the edges of the wood show some overshoot (in one particular spot, $\mathrm{Im}(\chi) \approx 0.4$ when the expected value is 0.2).

The second scatterer, to which we refer as Scatterer #2, consists of the same nylon cylinder, but this time combined with a hollow Poly-Vinyl-Chloride (PVC) cylinder. A photograph of the phantom is shown in figure 9.5. The thickness of the PVC cylinder is ≈ 0.6 cm, and it has a radius of ≈ 6.5 cm. The permittivity of the PVC cylinder was not measured, because the thin width of the cylinder wall would make the measurements invalid (the measurement would require a larger mass of PVC). However, published values [157] give the contrast of PVC at 3 GHz as $\chi^{\mathrm{PVC}} \approx 1.5 + j0.01$. For this phantom, data were collected at 3, 4.5 and 6 GHz. The reconstructions of this phantom at 3 GHz, as well as the multiple-frequency reconstructions, using the enhanced DBIM are shown in figure 9.6. The 3 GHz

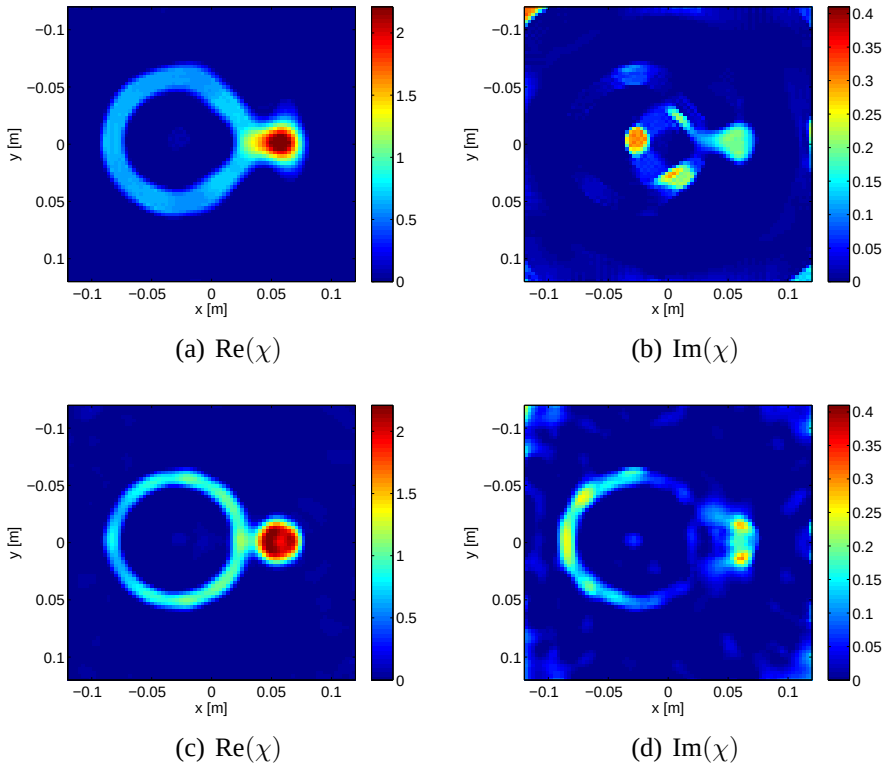

(a) Re(χ) (b) Im(χ)

(c) Re(χ) (d) Im(χ)

Fig. 9.6: Scatterer #2: (a)-(b) single-frequency reconstruction at 3 GHz, and (c)-(d) multiple-frequency reconstruction at 3 GHz, 4.5 GHz, and 6 GHz (using the frequency-hopping technique).

reconstruction (figure 9.6 (a)-(b)) overestimates the real part of the contrast for the nylon (2.2 instead of 2.0). The thickness of the PVC is estimated to be too wide ($\approx$ 1.7 cm instead of 0.6 cm). In the imaginary part of 3 GHz reconstruction, the overall structure of the phantom is not visible. This is mostly due to the large artifact in the center of the PVC pipe. The value of Im(χ) for the nylon is 0.2, but the edges are blurred. The multiple-frequency reconstruction, figure 9.6 (c)-(d), shows the object clearly in the real part of the reconstruction, but the contrast of nylon cylinder is slightly overshot. The real part of the PVC pipe reconstruction is thinner and closer to the actual size (≈ 1.2 cm). In the imaginary part of the reconstruction, the nylon's shape is not recognizable, and the value is overshot. Additionally, the imaginary part of the PVC pipe's shape does not follow the entire way around the cylinder.

In both phantoms, the multiple-frequency reconstructions were an improvement over the single-frequency case. This is particularly apparent in the imaginary part of the permittivity of Scatterer $\#2$. As expected through the use of higher-frequency data the multiple-frequency reconstructions had less blurred edges. As well, in Scatterer $\#2$, the multiple-frequency reconstruction clearly shows that two distinct objects are present, and the separation of the two objects is (arguably) visible (the physical separation was 1 cm, or $\lambda_b/5$ where λ_b is the wavelength of the background medium (air) at the highest frequency).

In general, the exact contrast values were not obtained. We suspect that these errors in the reconstructions are primarily due to the large amount of measurement noise and modeling error caused by the mutual coupling of the antennas. Other sources of error, such as the assumption of a 2D line source based incident field are probably also a factor. We expect that when the MWT system is filled with a lossy matching fluid the antenna coupling will become significantly less noticeable due to losses in the fluid.

9.2 Resolution

Perhaps the largest remaining challenge to make MWT a competitive biomedical imaging modality is to improve the achievable resolution over what has been reported for current state-of-the-art MWT systems, making it more comparable to MRI, ultrasound, and x-ray CT. The lower resolution of MWT is directly linked to the relatively larger wavelengths being used to interrogate the object of interest. There is, however, no known theoretical limit to the spatial resolution obtainable from MWT; image resolution as low as $1/6$ of a wavelength has been obtained for near-field imaging systems [158] and it has been suggested that the true resolution limit is governed by the achievable signal-to-noise ratio of the measurements [136], and not the wavelength (*c.f.*, low-frequency impedance tomography

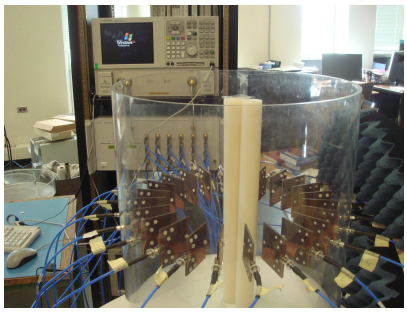

Fig. 9.7: The MWT system with 2 nylon cylinders for the resolution test.

systems [159]).

As the resolution limit for MWT technology is not currently known, and the future success of MWT depends upon improving the resolution performance of such systems, having a means of comparing the performance of different MWT systems (including the utilized data acquisition techniques, measurement calibration methods, and imaging algorithms) is important to the on-going research effort in this area. In this section, we quantify the resolution performance of our air-filled MWT system with plexiglass casing by using a series of well-defined simple experiments designed to reveal the *separation resolution* limit of the system. The concept of separation resolution, though not identified as such, has been used before by other investigators as an indicator of their systems' performance and therefore allows for a direct comparison between systems. We show that the achievable separation resolution is much smaller than a half-wavelength, the Rayleigh limit, and is much better than previously published results. Some of the deficiencies in using the separation resolution as a way of measuring systems' expected resolution performance are discussed and exemplified by examining images of more complicated targets. In the light of such examples, the scattering mechanisms responsible for the non-applicability of the concept are reviewed, but it is concluded that, lacking other well-defined indicators of resolution performance applicable to MWT, using separation resolution provides a good initial metric of system performance.

9.2.1 Separation resolution

In any imaging technology, resolution is an ambiguous concept. Classically, it refers to the ability of the imaging system to resolve two 'point' targets that produce a scattered field of equal intensity. The resolution limit can be defined using Rayleigh's criterion [160], where two targets are considered resolved if the maximum value of the scattered spatial waveform pattern due to one target is at, or farther away than, the first minimum in the scattered waveform pattern of the other target [161]. Resolution beyond this limit is referred to as super-resolution [160, 162]. In inverse scattering problems the Rayleigh (or base) resolution criterion may be generated via a linearization (*i.e.*, Born approximation) of the inverse scattering problem for idealized point targets. After the linearization of the inverse scattering problem, and using the Rayleigh criterion, the theoretically best possible resolution is $\lambda_b/2$ in the far-field and $\lambda_b/4$ in the near-field [158], where λ_b is the wavelength in the background medium, depending upon the transmitter/receiver configuration. In these linearization techniques, resolution beyond $\lambda_b/2$ is made possible by the collection and use of evanescent waves when the transmitters/receivers are located in the near-field [158].

The use of nonlinear inverse scattering algorithms, which take into account multiple scattering events and penetration into a target, can improve resolution beyond these limits and can be even further improved through the placement of the transmit/receive elements in the near-field. However, with a nonlinear inversion algorithm a 'point' target is no longer readily defined and imaged theoretically, thus some other target must be utilized. Some authors [162, 106] have resorted to the use of canonical circular targets, with maximum resolution defined as the minimum detectable separation between the two targets. We refer to this type of resolution with canonical targets as *separation resolution*. It is the nature of the nonlinear inverse scattering problem that no absolute (target-independent) resolution limit is definable; the resolution limit achieved is only applicable to those particular targets

used. However, it does provide some indication of the resolving capabilities of the system, and provides a quantitative metric to measure system improvements or make comparisons between systems.

Under this definition, and using a ground-penetrating-radar type data collection scheme, a resolution of $1/10$ of a wavelength with synthetic data [163], and a resolution of $\lambda_b/6$ with experimental data have been reported [162]. For biomedical applications, using a circular data collection configuration in a lossy background environment, a separation resolution of $\lambda_b/4$ has been reported [106]. Resolution well beyond this level is achievable, as will be shown herein.

9.2.2 Methods

We now investigate the achievable separation resolution with our MWT system with plexiglass casing based on our studies presented in [164]. The frequency of operation is chosen to be 5 GHz at which the wavelength of the background medium (air) is $\lambda_b = 0.06$ m. Similar to the work outlined in [162] and [106], we select two canonical targets each consisting of a nylon-66 cylinder 3.81 cm in diameter and 44 cm in height, see figure 9.7. At 5 GHz, the nylon has a relative complex permittivity of $\epsilon_r \approx 3.0 + j0.03$. The contrast will then be $\chi \approx 2.0 + j0.03$. Data were collected for 24 transmitters with 23 receivers operating for each transmitter (a total of 24×23 data points). The data were inverted using the MR-GNI method explained in Section 5.2.2. The only *a-priori* information used is to keep the reconstructed permittivity within physical bounds as denoted in Section 9.1.3.

The target, consisting of the two cylinders, was centered within the imaging system and the separation of the two cylinders was varied from 0 mm (*i.e.* touching) to 10 mm, in 1 mm steps. To determine the separation resolution limit, a 1D cross-section of the real part of the

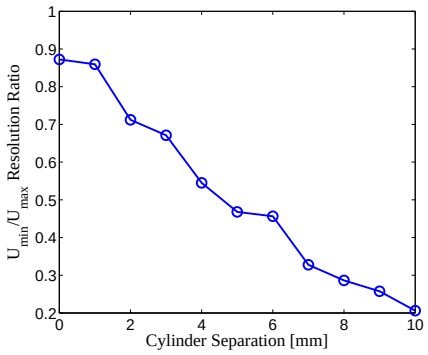

Fig. 9.8: Plot of the resolution ratio, $U_{\min}/U_{\max}$, for various separations, $0-10$ mm in 1 mm steps, of the two cylinders.

reconstructed 2D image is taken running through the center of the two cylinders. Defining $U_{\min}$ as the minimum pixel value on the 1D cross-sectional image between the two targets and $U_{\max}$ as the first maximum closest to this minimum value, the ratio of the minimum pixel value to the maximum pixel value $U_{\min}/U_{\max}$ is generated. Applying the Rayleigh criterion, if the ratio $U_{\min}/U_{\max}$ is less than 0.81 then the cylinders are deemed to be resolved.

To show that the obtained separation resolution limit will depend on the environment surrounding the two targets as well as the targets itself, we consider four more data sets (at $f = 5$ GHz). The first three data sets use the same two cylinders placed within a slightly more complicated environment: the two nylon cylinders (separated by 0 mm, 5 mm, and 10 mm) were centered within a hollow PVC cylinder described in Section 9.1.3. Finally, we consider a phantom made up of Ultra High Molecular Weight (UHMW) polyethylene. The permittivity of this phantom, at the operating frequency of 5 GHz, was measured to be $\epsilon_r = 2.54 + j0.014$. Noting that the background medium in our MWT system is air, the contrast of the phantom is $\chi = 1.54 + j0.014$. The geometry of the phantom is the same as the one shown in figure 6.5 (a)-(b) (but, of course, with a different relative complex permittivity). As can be seen, this phantom has different distances between its details ranging from 8 mm to 20 mm.

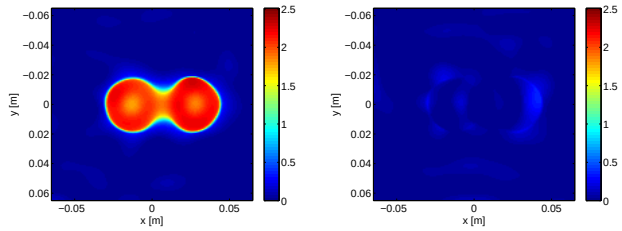

(a) 0 mm, Re(χ) (b) 0 mm, Im(χ)

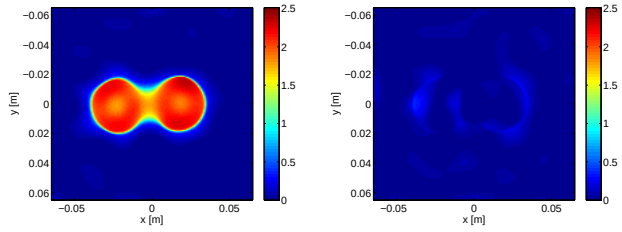

(c) 1 mm, Re(χ) (d) 1 mm, Im(χ)

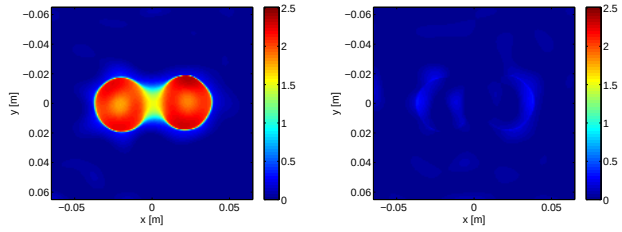

(e) 2 mm, Re(χ) (f) 2 mm, Im(χ)

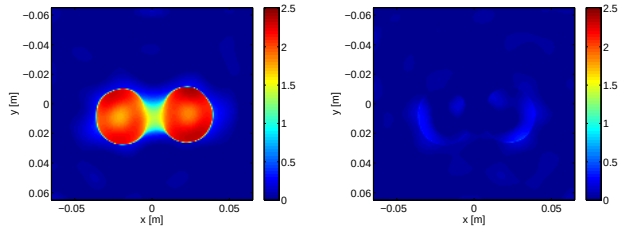

(g) 3 mm, Re(χ) (h) 3 mm, Im(χ)

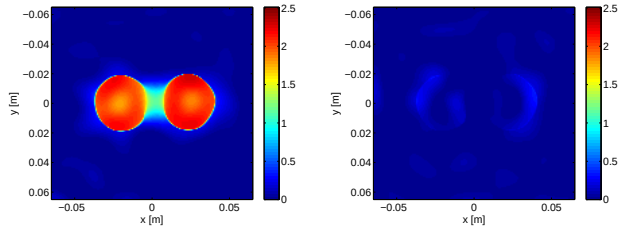

(i) 4 mm, Re(χ) (j) 4 mm, Im(χ)

Fig. 9.9: Reconstruction of the two nylon-66 cylinders for $0 - 4$ mm in 1 mm steps.

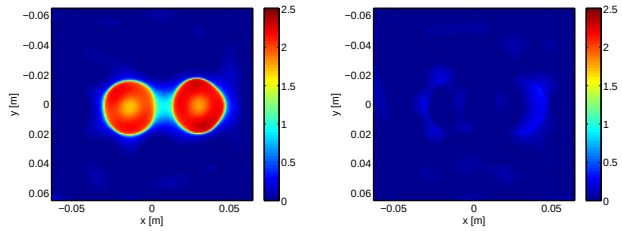

(a) 5 mm, Re(χ) (b) 5 mm, Im(χ)

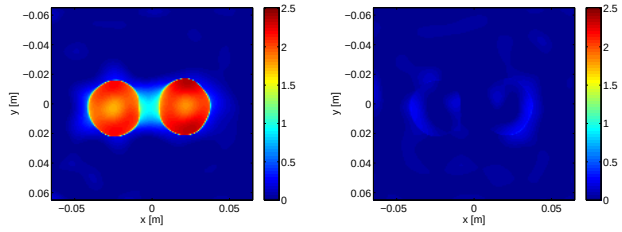

(c) 6 mm, Re(χ) (d) 6 mm, Im(χ)

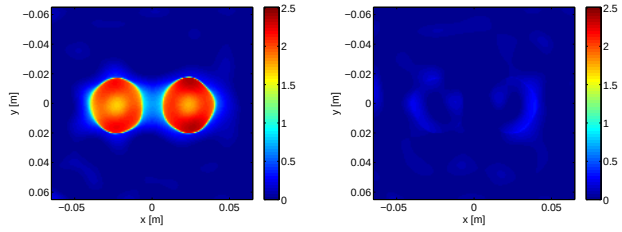

(e) 7 mm, Re(χ) (f) 7 mm, Im(χ)

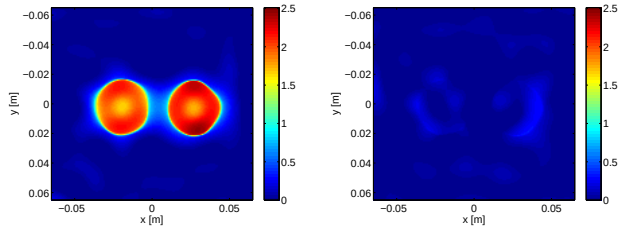

(g) 8 mm, Re(χ) (h) 8 mm, Im(χ)

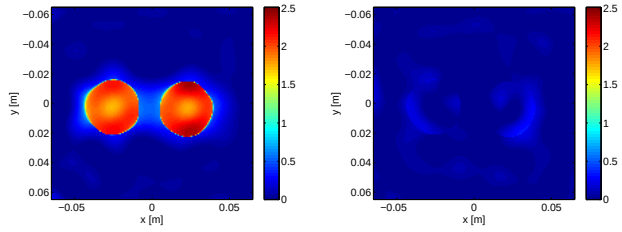

(i) 9 mm, Re(χ) (j) 9 mm, Im(χ)

Fig. 9.10: Reconstruction of the two nylon-66 cylinders for $5 - 9$ mm in 1 mm steps.

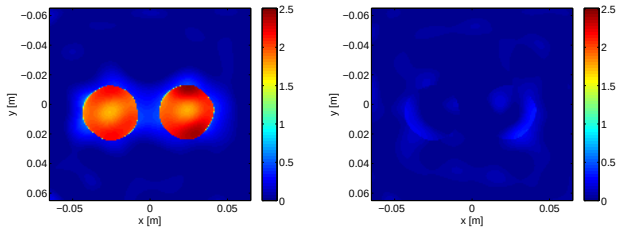

(a) 10 mm, Re(χ) (b) 10 mm, Im(χ)

Fig. 9.11: Reconstruction of the two nylon-66 cylinders with 10 mm separation.

9.2.3 Results

The resolution ratio $U_{\min}/U_{\max}$, corresponding to the two nylon targets, is plotted in figure 9.8. Reconstructed images of the contrast for 0–10 mm in 1 mm step are shown in in figures 9.9, 9.10, and 9.11. By considering the directly collected data points, the two cylinders are resolved for all separations of 2 mm. We estimate a confidence interval of ± 0.4 mm due to errors in our positioning system.

The reconstructions of the contrast when the two cylinders (with three different separations) are embedded in the PVC cylinder is shown in figure 9.12. According to the definition of the separation resolution used herein, the resolution ratios for these three data sets can be found. For example for the 5 mm separation, the resolution ratio increases to 0.52 from a ratio of 0.47 when the cylinders were not embedded, and under the definition of separation resolution limit used herein, the two cylinders are considered resolved. However, the inclusion of the PVC cylinder has clearly degraded the overall reconstruction of the nylon cylinders.

The reconstruction of the UHMW polyethylene phantom, using the MR-GNI, method is shown in figure 9.13. As can be seen in this figure, the details in the top-left of this phantom have not been resolved. We note that the top-left part of the phantom, which has not been resolved, corresponds to $8\,\text{mm} \approx \lambda_b/8$ separation. We also note that the separation of

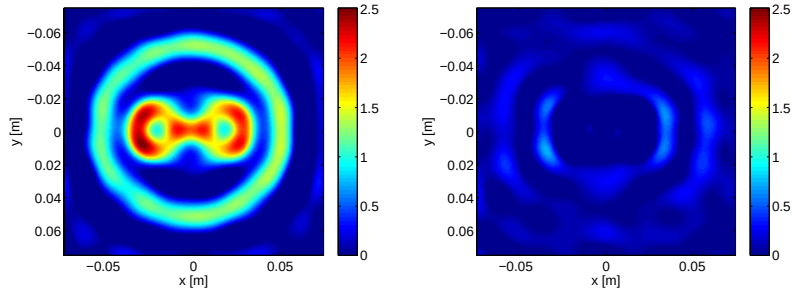

(a) 0 mm, Re(χ) (b) 0 mm, Im(χ)

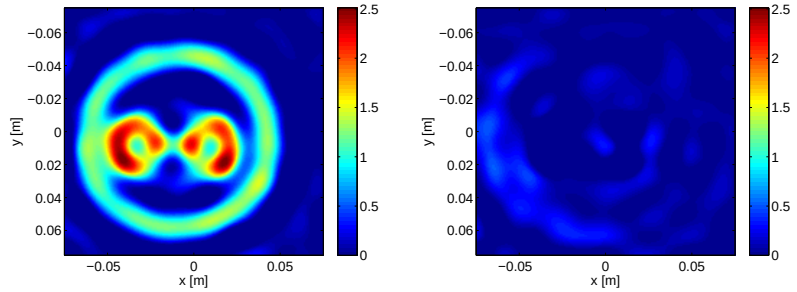

(c) 5 mm, Re(χ) (d) 5 mm, Im(χ)

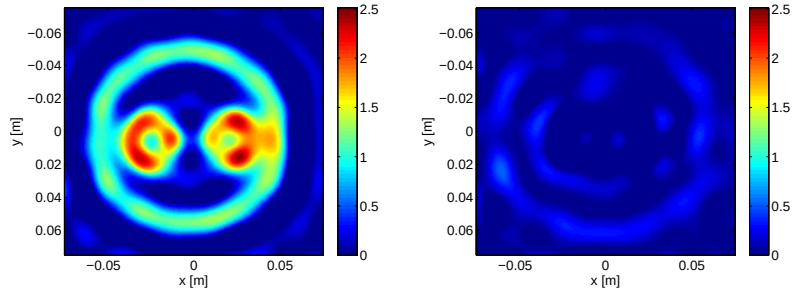

(e) 10 mm, Re(χ) (f) 10 mm, Im(χ)

Fig. 9.12: Reconstruction of two nylon-66 cylinders embedded in a larger PVC cylinder. For this reconstruction, the two cylinders were separated by (a)-(b) 0 mm, (c)-(d) 5 mm, and (e)-(f) 10 mm.

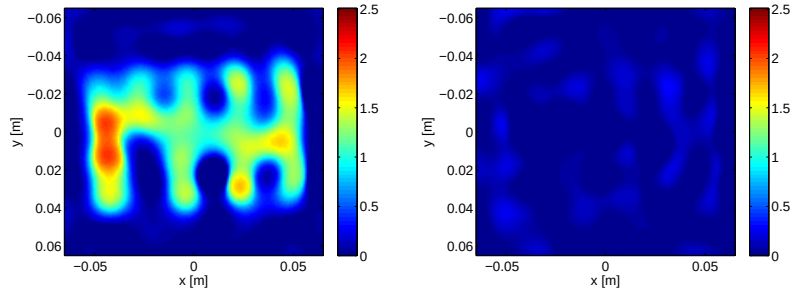

(a) Re(χ) (b) Im(χ)

Fig. 9.13: Reconstruction of the UHMW polyethylene phantom.

10 mm $= \lambda_b/6$ has been resolved.

9.2.4 Discussion

According to the results obtained with this experimental setup, a separation resolution of 2 mm has been achieved, which corresponds to a resolution of $\lambda_b/30$ at 5 GHz. This is a significant improvement over published experimental results using similar microwave tomography systems [162, 106], and highlights the potential for the technology. This high resolution is achieved through the collection and use of near-field data as well as the use of a nonlinear inversion algorithm which accounts for multiple scattering.

While we have resolved the targets at a separation of 2 mm, an inspection of figure 9.8 shows that the resolution limit should be at an even lower separation. A lower bound on the limiting separation resolution can be estimated to be 1.3 mm or $\approx \lambda_b/45$. This simple estimate assumes a linear variation in the resolution-ratio between 1 mm and 2 mm, and no errors in the positioning of the cylinders.

The use of the Rayleigh resolution criteria is qualitatively supported by observing the real-part reconstructions of 0 mm and 2 mm separation, shown in figure 9.9 (a) and (e). In the

0 mm reconstruction, the two cylinders are connected with a region of red (a pixel value of ≈ 1.9), while for the separated 2 mm reconstruction, the color switches to yellow with a pixel value of ≈ 1.5. We argue that, qualitatively, one would guess that the two cylinders are separated given the 2 mm reconstruction.

As expected, the resolution ratio shown in figure 9.8 reduces monotonically as the separation increases. However, it does not start from a value of 1.0 when the two cylinders are touching. This is due to variations in the reconstructed contrast throughout the cylinders, which raises the maximum pixel value in some regions within the cylinders (see, *e.g.*, the slight rise in the right cylinder of the 0 mm reconstruction).

The reconstructions which include the PVC cylinder (figure 9.12) shows one of the limitations in determining the separation resolution using the simplistic target environments considered herein. As expected when a PVC cylinder surrounds the target, the ratio of $U_{\min}/U_{\max}$ increases, which implies a reduction in separation resolution. The inclusion of the PVC cylinder also degrades the reconstruction of the nylon cylinders, to the point that they no longer appear as solid targets. The degradation is due to both (*i*) a loss in the amount of useful energy interrogating the target (the PVC provides a significant barrier to the wave which now must pass through the PVC wall twice before being detected by the antennas), and (*ii*) an increase in the amount of multiple scattering present because of the presence of the surrounding cylinder. The limitations in determining the separation resolution for a more complicated scatterer can be seen in the reconstruction of the UHMW polyethylene phantom (figure 9.13), where the separation of $\lambda_b/8$ was not resolved.

While not the main focus of this section, it is interesting to note that the diameter of the two nylon cylinders is also reconstructed quite accurately (at least in the simple case with no PVC cylinder surrounding the target). For example, in the 10 mm separation reconstruction (figure 9.11) the average reconstructed diameter of the nylon cylinders is 3.55 cm (calculated

using the full-width at half-maximum criteria), an error of $\approx 7\%$, from the true diameter.

9.3 MWT system with metallic casing

In this section, we consider a MWT system where the chamber surrounding the antennas and the OI is made of metallic material. One of the main potential advantages of MWT systems with metallic casing (over those with dielectric casing) is the possibility of using low-loss (or, lossless) matching fluids within them to image the OI. This is important as it is expected that imaging in a low-loss matching fluid offers an enhanced resolution compared to imaging in a lossy matching fluid due to providing a data set with a better signal-to-noise ratio [106, 136]. Very few inversions from experimentally collected data within MWT systems with metallic casing have been reported: only from the system currently under development at the Institut Fresnel [139], and from the system described herein which currently under development at the University of Manitoba [148] (both make the 2D TM assumption). The results from both of these systems are not satisfactory when compared to the results obtained from open-region MWT systems. This will be discussed in more details in Section 9.3.2. Also, a MWT system with a metallic hemisphere was built in the Technical University of Denmark for breast cancer imaging [165] where, to the best of our knowledge, no inversion of experimental data has been reported yet.

The University of Manitoba MWT system with metallic casing utilizes the same vector network analyzer, switch, and data collection process as used in our MWT system with dielectric casing, but substitutes the plexiglass chamber for a chamber made of stainless steel. Prototypes with different cylinder sizes and with a series of antenna types have been constructed, and data collected from them.

9.3.1 Inversion results from our MWT systems with metallic casing

In this section, we show some preliminary results from the University of Manitoba MWT systems with circular metallic casing which is currently under development. The experimental results are preliminary in that no well-established techniques are currently available for the calibration of data obtained from within conductive enclosure setups; we simply use the same calibration technique that was previously used by other researchers for open-region setups.

The first system is shown in figure 9.14 (a). Twenty-four monopole antennas are arranged at even intervals of 15 degrees in a circular array at the midpoint height along the inside of a stainless steel cylinder of radius 0.224 m, and of height 0.508 m. The monopole antennas, shown in figure 9.14 (b), are simple wires with right-angle bends placed into the female end of the bulk-head SMA connectors that protrude into the wall of the cylinder. These monopoles are oriented in the vertical direction, parallel to the cylindrical walls. The distance of the antennas from the wall of the chamber is only 0.01 m. Other resistively loaded antennas have been investigated for this system, but as the system design is not part of this thesis, results for only the simple monopoles are shown. Although the stainless steel enclosure is water-tight, allowing it to be filled with a matching liquid, the background medium, at the current state of development, is air. The OI is the same block of wood, described in Section 9.1.3, with $\epsilon_r \approx 2 + j0.2$ at 1 GHz. The target was placed at the center of the metallic chamber, shown in figure 9.14 (a), and 23×24 measurements were taken at this frequency (23 receivers per transmitter).

As mentioned earlier, the vector network analyzer collects scattering parameters between antenna ports. Note that the 24 antennas are co-resident during all measurements. As the imaging algorithm requires scattered field measurements, the data is first collected for the

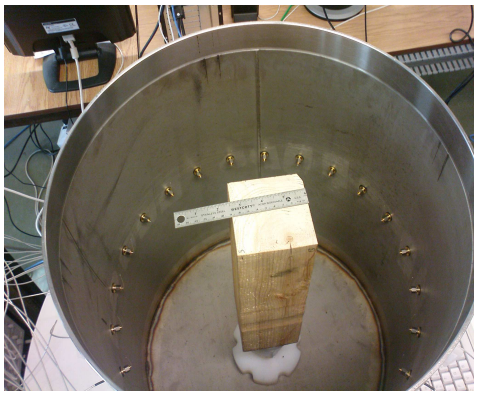

(a) Dielectric phantom target inside the MWT system

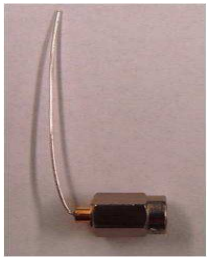

(b) Monopole antenna

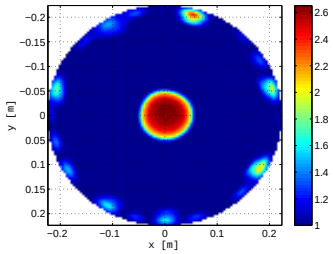

(c) $Re(\epsilon_r)$

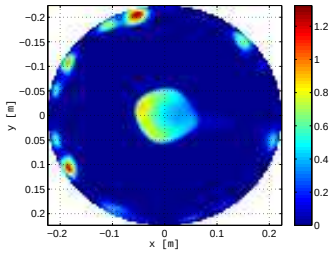

(d) $Im(\epsilon_r)$

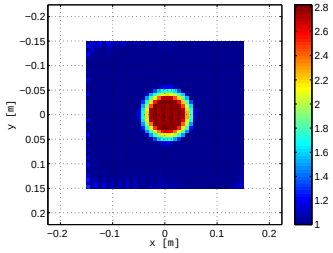

(e) $Re(\epsilon_r)$

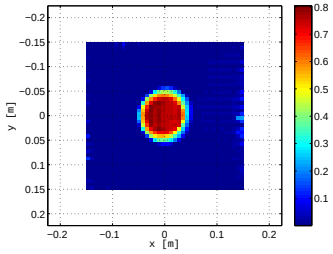

(f) $Im(\epsilon_r)$

Fig. 9.14: Experimental data set (a) the object of interest inside the circular metallic enclosure, (b) monopole antenna, (c)-(d) eigenfunction CSI reconstruction, and (e)-(f) Gauss-Newton reconstruction. For the eigenfunction CSI method, the imaging domain is the whole interior of the metallic enclosure whereas for the Gauss-Newton inversion, it is a 0.3 m $\times 0.3$ m square.

MWT system in the absence of the OI. Assuming that the t^{th} transmitter is active, this data is labeled the *incident* measurement $S^{\text{inc}}_{21,t}$, and consists of 23 measurements. We then perform the same experiment in the presence of the OI. This data set is labeled the *total* measurement $S_{21,t}$. The measured incident data is then subtracted from the measured total data and is denoted by the measured *scattered* data, $S^{\text{scat}}_{21,t} = S_{21,t} - S^{\text{inc}}_{21,t}$.

Modeling the incident field in the inversion algorithm by E^{inc}_t given in (7.17), the calibrated measured scattered fields for the unknown target corresponding to the t^{th} transmitter are calculated by

$$E^{\text{scat}}_{\text{meas},t} = \frac{E^{\text{inc}}_t}{S^{\text{inc}}_{21,t}} S^{\text{scat}}_{21,t}. \tag{9.2}$$

where E^{inc}_t is calculated at the receiver locations. The field $E^{\text{scat}}_{\text{meas},t}$ is then used in the inversion algorithm. The measured $S^{\text{inc}}_{21,t}$ and the simulated E^{inc}_t corresponding to the first transmitter, $t = 1$, are shown in figure 9.15 at the 23 receiver locations. This frequency was chosen because of the reasonable match between the raw S^{inc}_{21} and the analytic incident field assumed in the inversion model. Although this calibration technique is the one that has been successfully used to calibrate the Fresnel 2001 and 2005 data sets [118, 102] (collected in an anechoic chamber), it is not ideally suited to measurements taken inside conductive enclosures because the mutual coupling between the co-resident antennas is much greater than that in open-region systems.

The inversion result using eigenfunction contrast source inversion method, explained in Chapter 7, is shown in figure 9.14 (c)-(d). As can be seen, the shape of the square wooden cylinder is not resolved and the reconstructed permittivity is over the measured value. We note the artifacts due to the presence of the antennas. To check whether the poor inversion result is due to the use of eigenfunction CSI or the calibrated measured data itself, we have also inverted the calibrated measured data using the GNI algorithm with a FEM forward

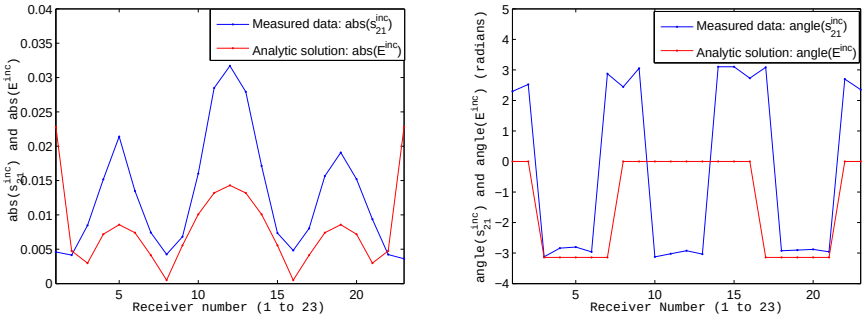

(a) Absolute value (b) Phase value

Fig. 9.15: Comparison of the simulated incident field and the measured S_{21}^{inc} for the first transmitter at the 23 receiver locations (a) absolute value, and (b) phase.

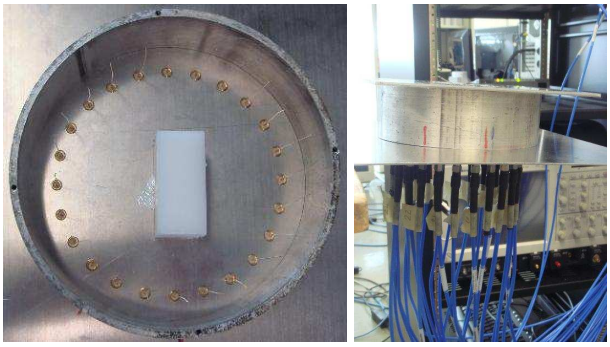

(a) Top view (b) Side view

Fig. 9.16: The second MWT system with metallic casing (a) top view (with an OI in the center of the chamber), and (b) side view.

solver [135].[1] The inversion results using the GNI method are shown in figure 9.14 (e)-(f). As can be seen the reconstruction results from the eigenfunction CSI and the GNI method are very similar.

The second MWT system with metallic casing, shown in figure 9.16, was constructed with a radius of 8.08 cm but having a height of only 5.28 cm. In addition, to better approximate 2D line sources, the antennas are fed straight up through the bottom aluminum plate of the enclosure. Twenty-four threaded holes were tapped at even intervals into the bottom plate

[1] As outlined in [135], this GNI algorithm is equipped with the additive-multiplicative regularization (see Section 5.2.3). It also uses the image enhancement algorithm (see Section 5.7).

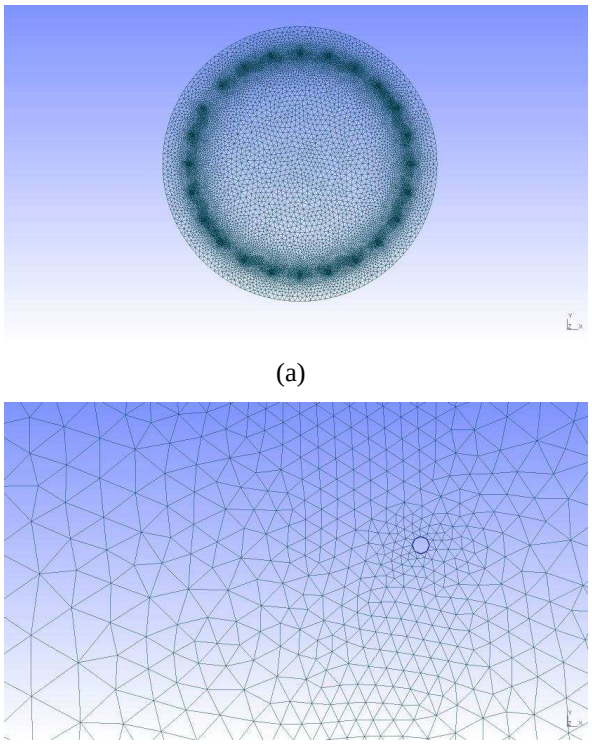

(a)

(b)

Fig. 9.17: Example of the FEM mesh for the small-sized MWT system with metallic casing: (a) the 24 antennas are modeled as small PEC cylinders, as shown in (b) the zoomed image.

at a radial offset of 1.5 cm from the circular peripheral wall of the enclosure, where SMA bulkhead adapters could be screwed in to feed a set of straight loaded antennas (consisting of the axial-lead 47 resistors). These make-shift resistor "antennas" nearly spanned the entire 5.28 cm height of the cylinder, clipped only about two or three millimeters from shorting to the metal top plate. The frequency of operation for this system is 2.7 GHz. Using this system, two different data sets were collected from a rectangular homogeneous target of dimensions 2 cm $\times$ 6 cm with a height roughly equal to that of the system's chamber. These two data sets are distinguished by the position of the target within the chamber. It should also be noted that the relative complex permittivity of this target was measured using the Agilent 85070E dielectric probe kit to be $\epsilon_r = 2.6 + j0.12$ (thus, having the contrast of $\chi = 1.6 + j0.12$) at the frequency of operation (*i.e.*, 2.7 GHz).

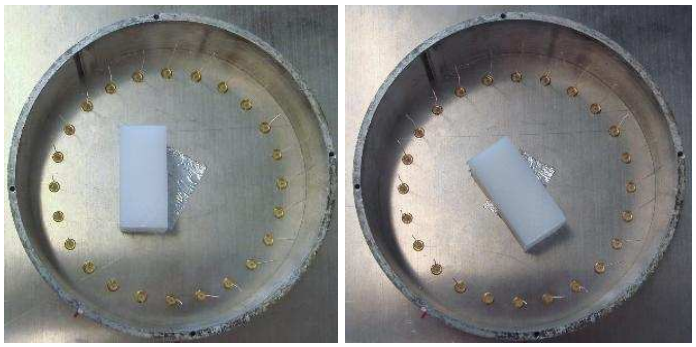

(a) (b)

Fig. 9.18: The two different positions of the homogeneous scatterer within the MWT system with metallic enclosure.

For the data sets collected in this system, we have applied both the GNI (in conjunction with a FEM forward solver) and the eigenfunction CSI methods. Both of these algorithms failed in inverting the data sets. The reasons for this failure have been studied in [151] in which it was concluded that the strong mutual coupling between co-resident antennas in this small-sized chamber is one of the main reasons for this failure. We note that the mutual coupling, which leads to modeling error, has not been modeled in the inversion algorithm.

Having this reason in mind and to somehow model the mutual coupling between the antennas within the inversion algorithm, we attempted to model the co-resident antennas by constructing an FEM mesh which consists of 24 small PEC circles of radius 0.26 mm to represent the 24 co-resident antennas[2]. This FEM mesh has been shown in figure 9.17. Due to the fact that the small circles representing the antennas are at the exact positions of the sources/receivers, and that they represent PEC boundaries (where no field may penetrate), we chose to place the transmitter/receiver points in the inversion algorithm $\lambda_b/20 \approx 5$ mm away from the edge of the small PEC circles. This leads to some errors in the inversion, and future work will focus on better ways to take the antennas into account. However, as will be seen, this method provides reasonable inversion results.

[2] The radius of these small PEC circles are chosen in *ad hoc* way.

We now show some inversion results from the small-sized MWT system with metallic casing using the GNI method in conjunction with a FEM forward solver which uses the FEM mesh with the 24 small PEC circles. The first inversion was performed on data collected with the object shifted toward the left-side of the MWT system's chamber, as shown in figure 9.18 (a). The inversion of this data set is shown in figure 9.19 (a)-(b). The inversion has reproduced the position and overall dimensions of the dielectric target reasonably well, despite the peculiar deformations near the midpoint of its length and blurred edges around its perimeter giving the reconstructed rectangular target more of an hour-glass shape. These types of blurred edges can also be seen in the inversion of experimental data from the Institut Fresnel MWT system with metallic casing [139]. Quantitatively, the real part of the reconstructed permittivity has undershot the measured value 1.6, and the object's profile appears lossless, with no imaginary part being produced by the algorithm aside from a few minor artifacts. The second inversion was performed on data collected with the object rotated approximately 45° counter-clockwise from its initial orientation shown in figure 9.16 (a). The inversion result, shown in figure 9.19 (c)-(d) confirms the algorithm's ability to track rotational motion of the object. However, the reconstruction of the object is not very good as the edges of the rectangle have not been reconstructed. Also, the reconstructed imaginary-part of the contrast has an anomaly in the center of the imaging domain.

9.3.2 Discussion

The inversion results of the experimental data sets collected inside the two MWT systems with metallic casing are not satisfactory[3]. Based on our experience, we speculate that the main difficulty with inverting the experimental data from the MWT systems with metallic casing, when the background medium is air, is due to the high mutual coupling between the

[3] We note that the inversion of the synthetic data sets collected inside a metallic chamber was quite successful as shown in Chapters 7 and 8.

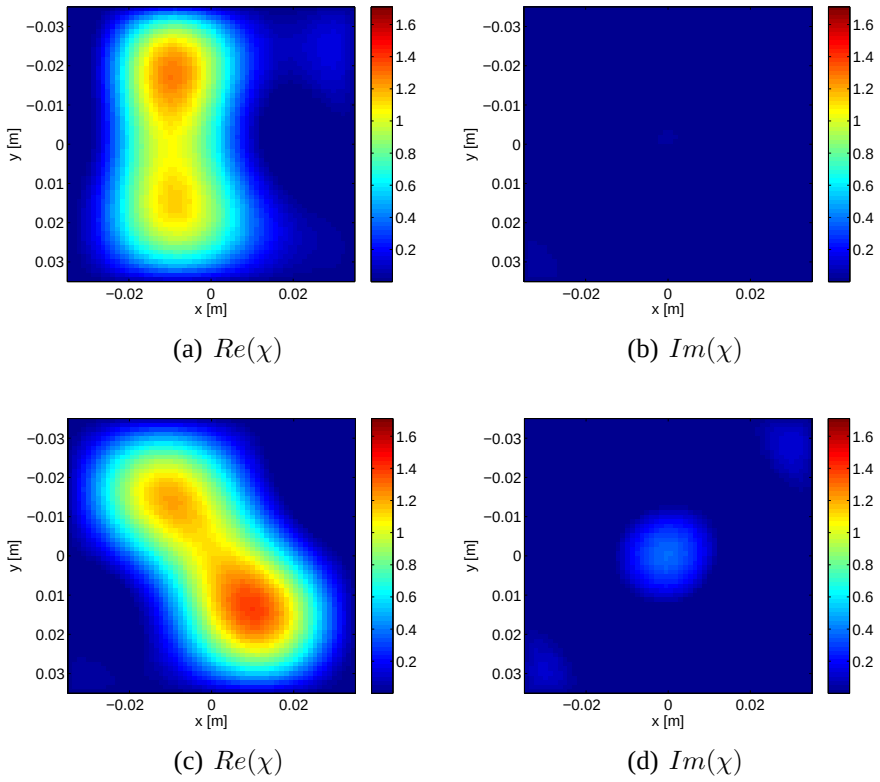

(a) $Re(\chi)$ (b) $Im(\chi)$

(c) $Re(\chi)$ (d) $Im(\chi)$

Fig. 9.19: Inversion of the homogeneous target, in two different positions, collected inside the MWT system with metallic casing.

co-resident antennas which is not entirely removable by the existing calibration techniques, like the one used in here[4]. The mutual coupling between the co-resident antennas is much greater in our PEC-enclosed system compared to that present in our plexiglass-enclosed system. This has been concluded by comparing two S_{11} measurements taken in each case: (*i*) S_{11} measurements for a single antenna when no other antennas are present in the enclosure, and (*ii*) S_{11} measurements for the same antenna when the other 23 antennas are present in the enclosure. In the metallic enclosure, the S_{11} measurements with only one antenna in the enclosure is quite different from the S_{11} measurements when all antennas are present in the chamber. This has been discussed in details in [151, 152]. Due to this, the presence of the

[4] We have successfully used the calibration technique used in Section 9.3.1, known as *incident-field calibration*, for open-region configurations [55, 57]. Other researchers have also successfully used this calibration technique for MWT systems with dielectric casing [12].

co-resident antennas substantially changes the input impedance of the transmitting antenna; thus, it is likely that the field distribution inside the chamber is quite different than that of an empty 2D metallic enclosure. This results in a large modeling error in the inversion algorithms developed for inverting the data collected inside the metallic casing, like the eigenfunction CSI method and the inversion method presented in [139]. This is due to the fact that these inversion algorithms implicitly assume that the Green's function of the actual MWT system is that of a empty 2D metallic enclosure. However, this implicit assumption is not an acceptable approximation at all as the mutual coupling between co-resident antennas changes the Green's function of the MWT system sufficiently such that it cannot be modeled with the analytic Green's function of the empty 2D metallic enclosure[5]. Although the GNI method in conjunction with the FEM mesh which consists of the small PEC circles can partially take the mutual coupling between antennas into account, it is far from being a good model.

To improve the reconstruction results, at least four methods may be fruitful. These are

1. designing a calibration technique which transforms the S_{21} measurements to field values in such a way that the mutual effects between co-resident antennas are calibrated out,

2. implementing an inversion algorithm which can take the antenna into account properly,

3. decreasing the number of elements in the antenna array (*e.g.*, having only 4 antennas), and

[5] It should be noted that in MWT systems with dielectric casing, such approximations are made in the inversion algorithms. For example, in Dartmouth College MWT system [12], the Green's function of system is approximated by the 2D Green's function of a homogeneous background where the water-glycerin matching fluid extends to infinity. Although these kinds of approximation work well in conjunction with MWT systems with dielectric casing when a relatively high loss matching fluid is used, they do not provide meaningful results in conjunction with our air-filled MWT system with metallic enclosures

4. utilizing an appropriate lossy matching fluid within the chamber.

All of these methods are now under investigation in our research group and are part of our planned future work. If the calibration technique mentioned in the first method can be developed, the eigenfunction CSI method in its current form should result in accurate reconstructions with the calibrated measured data. If the second method is successful, this will require utilizing numerical eigenvectors in the eigenfunction CSI method. Also, in this case, the GNI method with a modified FEM mesh to incorporate the antenna elements may be used. We note that the rotatable MWT system explained in Chapter 8 is one way to effect method 3. It is also expected that the fourth method, *i.e.*, utilizing a lossy matching fluid, can provide reasonable results at the expense of losing some SNR due to the presence of the lossy matching fluid. However, this may not be a good solution as our main goal is to use a very low-loss (or, lossless) matching fluid to maintain a good SNR in the collected data.

10

Conclusions and Future Work

> *... when a traveler reaches a fork in the road, the L^1-norm tells him to take either one way or the other, but the L^2-norm instructs him to head off into the bushes* (J. F. Claerbout and F. Muir [166]).

This final chapter summarizes the main results and achievements of this thesis and presents an outline of the future work which might be fruitful to perform.

10.1 Conclusion

In this thesis, we formulated the MWT problem as an optimization problem. A number of methods for solving the MWT problem were reviewed. These methods were classified into two categories distinguished by their use (or, lack of use) of a forward solver.

Treating the ill-posedness of the problem was considered using different regularization techniques in conjunction with the Gauss-Newton inversion algorithm. These regularization techniques were studied and classified into two categories. The first category consists of the penalty and projection methods whereas the second category consists of additive, multiplicative and additive-multiplicative regularization techniques. It was shown that these methods can be viewed from within a single consistent framework after applying some modifications. This framework helps to clarify the function of these regularization techniques. In addition, two regularization techniques which can incorporate *a priori* information about the object being imaged were presented. An image enhancement algorithm for the final image obtained from the Gauss-Newton inversion algorithm was introduced. While adding little computational complexity to the inversion algorithm, this image enhancement algorithm was useful in removing the spurious oscillations in the final reconstructions obtained from the inversion method.

The 2D TM and 2D TE inversions for the open-region configuration were compared. It was concluded that the TE inversion, which utilizes both rectangular components of the electric vector at each receiver position, can result in more accurate reconstruction than the TM inversion when utilizing near-field scattering data collected using only a few transmitters and receivers. This study was a preliminary study to compare the performance of the scalar and vectorial inversions and may justify the added cost and complexity of developing MWT systems capable of collecting vectorial data.

A new eigenfunction CSI method was presented for circular metallic enclosures within the 2D TM framework. This method is based on expressing the unknown contrast and contrast sources as truncated eigenfunction expansions corresponding to the Helmholtz operator in a homogeneous background medium. The expansion coefficients become the unknowns in the inverse problem which is formulated by introducing these eigenfunction expansions into the

CSI functional. The conjugate gradient technique is used to minimize the functional with respect to these expansion coefficients.

Using the 2D TM assumption, we successfully used the multiplicative regularized Gauss-Newton inversion method in conjunction with an FEM forward solver for the MWT problem inside an arbitrarily-shaped PEC enclosure. It was demonstrated that MWT systems with PEC enclosures of different shapes may provide non-redundant information about the object being imaged when the scattered field data is collected using only a few transmitters and receivers in a low-loss (or, lossless) background medium. Based on this observation, we propose a novel MWT system wherein a rotatable conductive triangular enclosure is used to generate electromagnetic scattering data that are collected at each static position of the enclosure using a minimal antenna array having as few as only four co-resident elements. The antenna array remains fixed with respect to the target being imaged and only the boundary of the conductive enclosure is rotated. The possibility of imaging in such a system was shown using some synthetic examples.

We presented our results from the University of Manitoba's MWT systems. At the current state of development, the inversion results from the MWT system with plexiglass casing are reasonable. The resolution of this MWT system was investigated using two cylindrical nylon targets. At the operating frequency of 5 GHz, a separation resolution of 2 mm, or $1/30$ of the wavelength in the background medium (air), was achieved. Although it is not a sufficiently robust indicator of the expected resolution obtainable for complex targets, the achieved separation resolution is significantly better than any of the previously published resolution limits for similar MWT systems. Also, preliminary results were presented for our MWT systems with metallic casing. These preliminary inversions showed poor results for the current system but it is our expectation that there will be much improvement in obtaining images once appropriate calibration techniques are implemented or appropriate

modifications are made in the system design; both of which are part of the future work.

10.2 Future work

We suggest future work in two main directions. The first one is concerned with the development of inversion algorithms and the second one is concerned with the development of measurement systems.

10.2.1 Inversion algorithms

In many applications, there is *a priori* information about the object being imaged. This information, if incorporated correctly into the inversion algorithms, can enhance the reconstruction significantly. Most contributions in the area of inversion algorithms lie in the development of *blind* inversion algorithms where it is assumed that there is no *a priori* information about the OI. Thus, there exists significant room for the development of inversion algorithms which are able to properly incorporate *a priori* information about the OI. Utilizing this information in the inversion algorithms can push MWT toward becoming an independent or complementary medical imaging modality. Toward this end, focusing on a particular application such as breast cancer imaging may be very fruitful. For this application, Magnetic Resonance Imaging (MRI) has achieved high spatial resolution. However, it has limited specificity in identifying tumor and benign lesions. On the other hand, MWT has a limited resolution while having the potential to improve the specificity of breast cancer imaging due to the difference between the dielectric properties of tumor and benign lesion within the microwave spectrum. This provides room for development of a hybrid imaging technique if MRI information can be incorporated within the MWT imaging algorithms. We

note that this type of imaging has already been started for near-infrared tomography and MRI [167].

10.2.2 Experimental systems

Microwave tomography systems, currently in existence, have no ability (or, very limited ability) to collect near-field vectorial data. Thus, MWT algorithms in conjunction with these systems work within the framework of the 2D TM or 3D scalar assumption. This introduces modeling error into the utilized inversion algorithm. To reduce this modeling error, effort needs to be placed on the development of MWT systems that can collect near-field vectorial data so that a 3D full-vectorial MWT algorithm can be utilized to invert the collected data set.

Current state-of-the-art MWT systems utilize lossy matching fluids so that little or no energy that reaches the boundary of the system's chamber makes it back to the antennas. This simplifies the system's calibration and makes it possible for MWT algorithms to assume that the matching fluid extends to infinity, not to the boundary of the system's casing. However, the data which are collected in a lossy matching fluid will have a poorer SNR than data collected in a low-loss (or, lossless) matching fluid. Thus, moving toward MWT systems which couple the energy into the OI through a low-loss or lossless matching fluid may result in enhanced imaging. As pointed out in Chapters 7 and 9, we think that this can be achieved by using a conductive enclosure MWT system. However, as explained in Section 9.3.2, the appropriate design and calibration of such systems have not been investigated yet and are part of future work.

APPENDIX

A

Published Papers

Herein, we provide the list of published works during this research.

A.1 Refereed journal papers

1. **Puyan Mojabi** and Joe LoVetri, "Eigenfunction Contrast Source Inversion for Circular Metallic Enclosures," *Inverse Problems*, vol. 26, (23pp), 2010.

2. Colin Gilmore, **Puyan Mojabi**, Amer Zakaria, Majid Ostadrahimi, Cam Kaye, Sima Noghanian, Lotfollah Shafai, Stephen Pistorius and Joe LoVetri, "A Wideband Microwave Tomography System with a Novel Frequency Selection Procedure," *IEEE Transactions on Biomedical Engineering*, vol. 57, no. 4, pp. 894-904, 2010.

3. **Puyan Mojabi** and Joe LoVetri, "Comparison of TE and TM Inversions in the Framework of the Gauss-Newton Method," *IEEE Transactions on Antennas and Propagation*, vol. 58, no. 4, pp. 1336-1348, 2010.

4. **Puyan Mojabi** and Joe LoVetri, "Enhancement of the Krylov Subspace Regularization for Microwave Biomedical Imaging," *IEEE Transactions on Medical Imaging*, vol. 28, no. 12, pp. 2015-2019, 2009.

5. **Puyan Mojabi** and Joe LoVetri, "Microwave Biomedical Imaging Using the Multiplicative Regularized Gauss-Newton Inversion," *IEEE Antennas and Wireless Propagation Letters*, vol. 8, pp. 645-648, 2009.

6. **Puyan Mojabi** and Joe LoVetri, "Overview and Classification of Some Regularization Techniques for the Gauss-Newton Inversion Method Applied to Inverse Scattering Problems," *IEEE Transactions on Antennas and Propagation*, vol. 57, no. 9, pp. 2658-2665, 2009.

7. Colin Gilmore, **Puyan Mojabi** and Joe LoVetri, "Comparison of an Enhanced Distorted Born Iterative Method and the Multiplicative Regularized Contrast Source Inversion
Method," *IEEE Transactions on Antennas and Propagation*, vol. 57, no. 8, pp. 2341-2351, 2009.

8. **Puyan Mojabi** and Joe LoVetri, "Adapting the Normalized Cumulative Periodogram Parameter Choice Method to the Tikhonov Regularization of 2D TM Electromagnetic Inverse Scattering Using Born Iterative Method," *Progress In Electromagnetic Research (PIER) M*, vol. 1, pp. 111-138, 2008.

9. **Puyan Mojabi** and Joe LoVetri, "Preliminary Investigation of the NCP Parameter Choice Method for Inverse Scattering Problems Using BIM: 2D TM Case," *Applied Computational Electromagnetic Society (ACES) Journal*, vol. 23, no. 3, pp. 207-214, 2008.

A.2 Refereed articles in books

1. Cameron Kaye, Colin Gilmore, **Puyan Mojabi**, Dmitry Firsov and Joe LoVetri, "Development of a Resonant Chamber Microwave Tomography System," *Ultra-Wideband Short-Pulse Electromagnetics*, Springer Science+Business Media, Editor: Frank Sabbath, vol. 9, pp. 519-526, 2010.

A.3 Refereed conference papers

1. Colin Gilmore, **Puyan Mojabi**, Amer Zakaria, Majid Ostadrahimi, Cam Kaye, Sima Noghanian, Lotfollah Shafai, Stephen Pistorius and Joe LoVetri,"An Ultra-Wideband Microwave Tomography System: Preliminary Results," *31st Annual International IEEE Engineering in Medicine and Biology Society Conference (EMBS)*, Minneapolis, Minnesota, USA, pp. 2288-2291, September 2009.

2. **Puyan Mojabi**, Colin Gilmore, Amer Zakaria, Cam Kaye, Stephen Pistorius and Joe LoVetri, "Progress in Experimental Resonant Chamber Imaging for Biomedical Applications," *USNC/URSI National Radio Science Meeting*, Charleston, South Carolina, USA, June 2009.

3. **Puyan Mojabi**, Colin Gilmore, Amer Zakaria and Joe LoVetri, "Biomedical Microwave Inversion in Conducting Cylinders of Arbitrary Shapes," *13th International Symposium on Antenna Technology and Applied Electromagnetics and the Canadian Radio Sciences Meeting*, Banff, Alberta, Canada, February 2009.

4. **Puyan Mojabi** and Joe LoVetri, "Inversion of TE Experimental Data Using the Distorted Born Iterative Method," *29th General Assembly of the International Union of Radio Science*, Chicago, Illinois, USA, August 2008.

5. Cameron Kaye, Colin Gilmore, **Puyan Mojabi**, Dmitry Firsov and Joe LoVetri, "Development of a Resonant Chamber Microwave Tomography System," *European Electromagnetics Symposium (EURO EM)*, Lausanne, Switzerland, July 2008.

6. Colin Gilmore, **Puyan Mojabi** and Joe LoVetri, "Comparison of the Distorted Born Iterative and Multiplicative Regularized Contrast Source Inversion Methods: The 2-D TM Case," *24th international review of progress in Applied Computational Electromagnetics (ACES)*, Niagara Falls, Ontario, Canada, March-April 2008.

7. **Puyan Mojabi** and Joe LoVetri, "Introduction of a New NCP-Based Parameter-Choice Method For Tikhonov Regularization of Biomedical Microwave Imaging," *The First North American Radio Science Conference (URSI)*, Ottawa, Ontario, Canada, July 2007.

8. **Puyan Mojabi** and Joe LoVetri, "Application of the NCP Parameter-Choice Method to the General- Form Tikhonov Regularization of 2-D/TM Inverse Scattering Problems," *The 23rd International Review of Progress in Applied Computational Electromagnetics (ACES)*, Verona, Italy, March 2007.

A.4 Submitted journal papers

1. Colin Gilmore, **Puyan Mojabi**, Amer Zakaria, Stephen Pistorius and Joe LoVetri, "On Super-Resolution with an Experimental Microwave Tomography System," submitted to *IEEE Antennas and Wireless Propagation Letters*.

2. **Puyan Mojabi** and Joe LoVetri, "A Novel Microwave Tomography System Using a Rotatable Conductive Enclosure," (Under preparation).

B

Forward Scattering Problem

This method will be called the conjugate gradient method or, more briefly, the cg-method, for reasons which will unfold from the theory developed in later sections ... The results indicate that the method is very suitable for high speed machines. (Hestenes and Stiefel [168]).

As explained in Section 2.3.2, the forward scattering problem, when the t^{th} transmitter is active, may be formulated by minimizing the cost–functional $\mathcal{C}^{\text{FWD}} : L^2(\mathcal{D}) \rightarrow \mathbb{R}$ over $\boldsymbol{E}_t$:

$$\mathcal{C}^{\text{FWD}}(\boldsymbol{E}_t) = \frac{1}{\left\|\boldsymbol{E}_t^{\text{inc}}\right\|_{\mathcal{D}}^2} \left\|\boldsymbol{E}_t^{\text{inc}} - \left(\mathcal{I} - \mathcal{G}_{\mathcal{D}}^{\chi}\right)(\boldsymbol{E}_t)\right\|_{\mathcal{D}}^2 . \tag{B.1}$$

This cost-functional can be minimized using numerical techniques such as the Conjugate Gradient (CG) algorithm where the total field at the m^{th} iteration is updated as

$$\boldsymbol{E}_{t,m+1} = \boldsymbol{E}_{t,m} + \beta_{t,m}\boldsymbol{d}_{t,m} \tag{B.2}$$

where $\boldsymbol{d}_{t,m}$ is the conjugate gradient direction and $\beta_{t,m} \in \mathbb{R}^+$ represents its weight. The conjugate gradient direction can be found as [109]

$$\boldsymbol{d}_{t,m} = \begin{cases} \boldsymbol{g}_{t,1} & m = 0 \\ \boldsymbol{g}_{t,m} + \frac{\left\|\boldsymbol{g}_{t,m}\right\|_{\mathcal{D}}^2}{\left\|\boldsymbol{g}_{t,m-1}\right\|_{\mathcal{D}}^2} \boldsymbol{d}_{t,m-1} & m \neq 0 \end{cases} \tag{B.3}$$

where $\boldsymbol{g}_{t,m}$ is the maximum variation of $\mathcal{C}^{\text{FWD}}$ with respect to $\boldsymbol{E}$ at $\boldsymbol{E}_t = \boldsymbol{E}_{t,m}$. To find $\boldsymbol{g}_{t,m}$, we start with finding the limit

$$\delta\mathcal{C}^{\text{FWD}}(\boldsymbol{E}_t)|_{\boldsymbol{E}_t=\boldsymbol{E}_{t,m}} = \lim_{\epsilon\to 0} \frac{\mathcal{C}^{\text{FWD}}(\boldsymbol{E}_{t,m} + \epsilon\boldsymbol{\Psi}) - \mathcal{C}^{\text{FWD}}(\boldsymbol{E}_{t,m})}{\epsilon}. \tag{B.4}$$

where $\boldsymbol{\Psi} \in L^2(\mathcal{D})$. The calculation of the above limit will result in

$$\delta\mathcal{C}^{\text{FWD}}(\boldsymbol{E}_t)|_{\boldsymbol{E}_t=\boldsymbol{E}_{t,m}} = \frac{-2\text{Re}\left\langle (\mathcal{I} - \mathcal{G}_{\mathcal{D}}^{\chi})^a (\boldsymbol{R}_{t,m}), \boldsymbol{\Psi} \right\rangle_{\mathcal{D}}}{\left\|\boldsymbol{E}_t^{\text{inc}}\right\|_{\mathcal{D}}^2} \tag{B.5}$$

where

$$\boldsymbol{R}_{t,m} = \boldsymbol{E}_t^{\text{inc}} - (\mathcal{I} - \mathcal{G}_{\mathcal{D}}^{\chi})(\boldsymbol{E}_{t,m}). \tag{B.6}$$

From (B.5), it can be seen that $\delta\mathcal{C}^{\text{FWD}}(\boldsymbol{E}_t)|_{\boldsymbol{E}_t=\boldsymbol{E}_{t,m}}$ reaches its maximum (considering functions $\boldsymbol{\Psi}$ with identical norms) for

$$\boldsymbol{\Psi} = \boldsymbol{g}_{t,m} = (\mathcal{I} - \mathcal{G}_{\mathcal{D}}^{\chi})^a (\boldsymbol{R}_{t,m}). \tag{B.7}$$

Using the definition of the adjoint operator, it can be easily shown that $(\mathcal{I} - \mathcal{G}_{\mathcal{D}}^{\chi})^a = \mathcal{I} - \chi^* \mathcal{G}_{\mathcal{D}}^a$ where $\mathcal{G}_{\mathcal{D}}^a$ is given in (2.14). Therefore,

$$\boldsymbol{g}_{t,m} = \left[\mathcal{I} - \chi^* \mathcal{G}_{\mathcal{D}}^a\right](\boldsymbol{R}_{t,m}). \tag{B.8}$$

At the m^{th} iteration of the CG algorithm, the weight $\beta_{t,m}$ is found by minimizing $\mathcal{C}^{\text{FWD}}$ over $\beta_{t,m}$ when $\boldsymbol{E}_t$ is substituted by $\boldsymbol{E}_{t,m} + \beta_{t,m}\boldsymbol{d}_{t,m}$. The derivative of $\mathcal{C}^{\text{FWD}}$ with respect to $\beta_{t,m}$ will result in

$$\frac{\partial \mathcal{C}^{\text{FWD}}}{\partial \beta_m} = \frac{\beta_m^2 \left\| \mathcal{I} - \mathcal{G}_{\mathcal{D}}^{\chi}(\boldsymbol{d}_{t,m}) \right\|_{\mathcal{D}}^2}{\left\| \boldsymbol{E}_t^{\text{inc}} \right\|_{\mathcal{D}}^2} - \frac{2\beta_{t,m} \text{Re}\left\langle \boldsymbol{R}_{t,m}, \left(\mathcal{I} - \mathcal{G}_{\mathcal{D}}^{\chi}\right)(\boldsymbol{d}_{t,m}) \right\rangle_{\mathcal{D}}}{\left\| \boldsymbol{E}^{\text{inc}} \right\|_{\mathcal{D}}^2}. \tag{B.9}$$

Therefore, the weight $\beta_{t,m}$ will be

$$\beta_{t,m} = \frac{\text{Re}\left\langle \boldsymbol{R}_{t,m}, \left(\mathcal{I} - \mathcal{G}_{\mathcal{D}}^{\chi}\right)(\boldsymbol{d}_{t,m}) \right\rangle_{\mathcal{D}}}{\left\| \mathcal{I} - \mathcal{G}_{\mathcal{D}}^{\chi}(\boldsymbol{d}_{t,m}) \right\|_{\mathcal{D}}^2}. \tag{B.10}$$

In the MWT problem, the OI is irradiated several times with a number of given incident fields, say $\boldsymbol{E}_t^{\text{inc}}$ ($t = 1, \ldots, T_x$), corresponding to different transmitters around the OI. Most MWT algorithms require that the forward scattering problem, (B.1), is solved for these different incident fields assuming a known predicted contrast χ. Therefore, having a fast forward solver is crucial. Assuming an unbounded homogeneous background for the MWT problem, the operations of $\mathcal{G}_{\mathcal{D}}^{\chi}$ and its adjoint on an arbitrary function in $L^2(\mathcal{D})$, as required for minimizing (B.1) using the CG method, can be accelerated using the Fast Fourier Transform (FFT) in the discrete domain due to the convolutional property of the associated integral equation [36, 37].

Since in practical MWT systems, two successive transmitter positions are usually close, we can further accelerate the forward solver by using the marching-on-in-source-position technique [38], [30] which provides a good initial guess for the CG-FFT algorithm. In our utilized marching-on-in-source-position technique, the initial guess of the CG-FFT algorithm for the first three transmitters, $t = 1, 2, 3$, is simply the incident field corresponding to those transmitters; that is, $\boldsymbol{E}_{t,0} = \boldsymbol{E}_t^{\text{inc}}$. Then, an appropriate initial guess for the CG-FFT algorithm with respect to the t^{th} transmitter ($t \geq 4$) is obtained via an extrapolation

of the fields corresponding to some previous transmitter positions which have been already calculated. Specifically, the initial guess for the CG-FFT algorithm corresponding to t^{th} transmitter ($t \geq 4$) is written as,

$$\boldsymbol{E}_{t,0}(\boldsymbol{q}) = \sum_{i=1}^{3} a_i \boldsymbol{E}_{t-i}(\boldsymbol{q}) \tag{B.11}$$

where $\boldsymbol{E}_{t-i}(\boldsymbol{q})$ is the converged solution of (B.1) with respect to $(t-i)^{\text{th}}$ transmitter. A closed-form expression for the coefficients a_i is available such that they minimize the following norm [30]

$$\left\| (\mathcal{I} - \mathcal{G}_{\mathcal{D}}^{\chi}) \boldsymbol{E}_{t,0} - \boldsymbol{E}_t^{\text{inc}} \right\|_{\mathcal{D}}. \tag{B.12}$$

This completes the brief description of the so-called CG-FFT forward solver and the marching-on-in-source-position acceleration technique utilized in this research.

C

Computation of Derivatives Using Wirtinger Calculus

> *Nicht einer mystischen Verwendung von $\sqrt{-1}$ hat die Analysis ihre wirklich bedeutenden Erfolge des letzen Jahrhunderts zu verdanken, sondern dem ganz natürlichen Umstande, dass man unendlich viel freier in der mathematischen Bewgung ist, wenn man die Grössen in einer Ebene statt nur in einer Limie variiren läßt.* Translation: *Analysis does not owe its really significant successes of the last century to any mysterious use of $\sqrt{-1}$, but to the quite natural circumstance that one has infinitely more freedom of mathematical movement if he lets quantities vary in a plane instead of only on a line.* (Leopold Kronecker [169]).

In many applications, one optimizes a real-valued cost-functional over a complex-valued vector quantity. The main difficulty in such situations is that any non-constant real-valued cost-functional is not analytic in the complex domain [71]; thus, it is not complex differentiable. One way to handle this problem is to optimize the cost-functional with respect to the real and imaginary parts of the complex-valued vector. Of course, within the framework of

this approach, we implicitly assume that the cost-functional is differentiable with respect to the real and imaginary parts of the complex-valued vector. This type of differentiability is sometimes referred to as real differentiability [170] (as opposed to complex differentiability), and it has been used in microwave tomography by different authors; *e.g.*, see [42, 107].

Another approach to handle this problem is to treat the complex-valued vector and its complex conjugate as two independent vectors over which to perform the optimization. This method which has been used by different authors [72, 73, 71, 30, 58] makes use of Wirtinger calculus [70] which provides a way to bypass the strict definition of complex differentiability. In this appendix, we consider the Wirtinger calculus for optimizing a real-valued cost-functional over a complex vector. We then describe the extension of this calculus for the infinite-dimensional case.

Let $\mathcal{F}$ be a real-valued cost-functional of a complex-valued N-dimensional vector $\underline{\chi}$. That is, $\mathcal{F} : \mathbb{C}^N \rightarrow \mathbb{R}$. Assuming that the cost-functional $\mathcal{F}$ is not constant, it can be easily verified that the cost-functional $\mathcal{F}$ is not analytic (holomorphic) in $\underline{\chi}$ [71, 170]. Thus, it is not complex differentiable with respect to $\underline{\chi}$. It is well-known that a non-holomorphic cost-functional can be expressed in terms of its complex argument and the complex conjugate of the argument [170][1]. Thus, we can define the cost-functional $\tilde{\mathcal{F}}(\underline{\chi}, \underline{\chi}^*)$ such that $\tilde{\mathcal{F}}(\underline{\chi}, \underline{\chi}^*) = \mathcal{F}(\underline{\chi})$. It can be shown that if $\mathcal{F}$ is real differentiable with respect to $\underline{\chi}_R = \mathrm{Re}(\underline{\chi})$ and $\underline{\chi}_I = \mathrm{Im}(\underline{\chi})$, the real and imaginary parts of $\underline{\chi}$, the cost-functional $\tilde{\mathcal{F}}$ is holomorphic in $\underline{\chi}$ for fixed $\underline{\chi}^*$ and holomorphic in $\underline{\chi}^*$ for fixed $\underline{\chi}$ [170, 171, 71]. Therefore, assuming that $\mathcal{F}$ is real differentiable, one can *formally* define two partial derivatives [170]

$$\frac{\partial \tilde{\mathcal{F}}}{\partial \underline{\chi}}\Big|_{\underline{\chi}^*=\text{const.}} \tag{C.1}$$

[1] For example, the non-holomorphic cost-functional $\mathcal{F}(\underline{\chi}) = \left\|\underline{\chi}\right\|^2$ can be written as $\tilde{\mathcal{F}}(\underline{\chi}, \underline{\chi}^*) = \mathcal{F}(\chi) = (\underline{\chi}^*)^T \underline{\chi}$.

and,

$$\frac{\partial \tilde{\mathcal{F}}}{\partial \underline{\chi}^*}|_{\underline{\chi}=\text{const.}} \tag{C.2}$$

It should be noted that these two derivatives are formal in the sense that one cannot truly vary $\underline{\chi}$ while keeping $\underline{\chi}^*$ constant or vice versa.

Using these formal derivatives and noting that $\tilde{\mathcal{F}}(\underline{\chi}, \underline{\chi}^*) = \mathcal{F}(\underline{\chi})$, the first differential of $\mathcal{F}$ can be written as

$$d\mathcal{F} = \left[\frac{\partial \tilde{\mathcal{F}}}{\partial \underline{\chi}}\right]^T d\underline{\chi} + \left[\frac{\partial \tilde{\mathcal{F}}}{\partial \underline{\chi}^*}\right]^T d\underline{\chi}^*. \tag{C.3}$$

Defining the inner product between two complex vectors of the same size as $\langle \underline{w}, \underline{v} \rangle = \underline{v}^H \underline{w}$, (C.3) may be written as

$$d\mathcal{F} = \left\langle \frac{\partial \tilde{\mathcal{F}}}{\partial \underline{\chi}}, d\underline{\chi}^* \right\rangle + \left\langle \frac{\partial \tilde{\mathcal{F}}}{\partial \underline{\chi}^*}, d\underline{\chi} \right\rangle \tag{C.4}$$

One important relation between these two formal derivatives is [72, 73, 71]

$$\left\langle \frac{\partial \tilde{\mathcal{F}}}{\partial \underline{\chi}}, d\underline{\chi}^* \right\rangle = \left\{ \left\langle \frac{\partial \tilde{\mathcal{F}}}{\partial \underline{\chi}^*}, d\underline{\chi} \right\rangle \right\}^* \tag{C.5}$$

Using (C.5) and (C.4), the first differential of $\mathcal{F}$ may be written as

$$d\mathcal{F} = 2\text{Re}\left\{ \left\langle \frac{\partial \tilde{\mathcal{F}}}{\partial \underline{\chi}}, d\underline{\chi}^* \right\rangle \right\} = 2\text{Re}\left\{ \left\langle \frac{\partial \tilde{\mathcal{F}}}{\partial \underline{\chi}^*}, d\underline{\chi} \right\rangle \right\}. \tag{C.6}$$

We note that the first differential of $\mathcal{F}$ can also be written in terms of the variations with respect to $\underline{\chi}_R$ and $\underline{\chi}_I$. That is,

$$d\mathcal{F} = \left[\frac{\partial \mathcal{F}}{\partial \underline{\chi}_R}\right]^T \text{Re}(d\underline{\chi}) + \left[\frac{\partial \mathcal{F}}{\partial \underline{\chi}_I}\right]^T \text{Im}(d\underline{\chi}) = \left\langle \frac{\partial \mathcal{F}}{\partial \underline{\chi}_R}, \text{Re}(d\underline{\chi}) \right\rangle + \left\langle \frac{\partial \mathcal{F}}{\partial \underline{\chi}_I}, \text{Im}(d\underline{\chi}) \right\rangle. \tag{C.7}$$

Considering (C.7), and noting that (C.6) can be written as

$$d\mathcal{F} = \left\langle 2\text{Re}\left\{\frac{\partial\tilde{\mathcal{F}}}{\partial\underline{\chi}^*}\right\}, \text{Re}\left\{d\underline{\chi}\right\}\right\rangle + \left\langle 2\text{Im}\left\{\frac{\partial\tilde{\mathcal{F}}}{\partial\underline{\chi}^*}\right\}, \text{Im}\left\{d\underline{\chi}\right\}\right\rangle, \tag{C.8}$$

it can be concluded that

$$2\text{Re}\left\{\frac{\partial\tilde{\mathcal{F}}}{\partial\underline{\chi}^*}\right\} = \frac{\partial\mathcal{F}}{\partial\underline{\chi}_R} \quad \text{and,} \quad 2\text{Im}\left\{\frac{\partial\tilde{\mathcal{F}}}{\partial\underline{\chi}^*}\right\} = \frac{\partial\mathcal{F}}{\partial\underline{\chi}_I}. \tag{C.9}$$

Thus,

$$\frac{\partial\tilde{\mathcal{F}}}{\partial\underline{\chi}^*} = \frac{1}{2}\left(\frac{\partial\mathcal{F}}{\partial\underline{\chi}_R} + j\frac{\partial\mathcal{F}}{\partial\underline{\chi}_I}\right). \tag{C.10}$$

Using a similar procedure, it can be shown that

$$\frac{\partial\tilde{\mathcal{F}}}{\partial\underline{\chi}} = \frac{1}{2}\left(\frac{\partial\mathcal{F}}{\partial\underline{\chi}_R} - j\frac{\partial\mathcal{F}}{\partial\underline{\chi}_I}\right). \tag{C.11}$$

Within this thesis, we apply the Wirtinger calculus to the infinite-dimensional case where the cost-functional $\mathcal{C}$ maps the complex function $\chi \in L^2(\mathcal{D})$ to $\mathbb{R}$. We, therefore, consider the cost-functional $\tilde{\mathcal{C}}(\chi, \chi^*)$ such that $\tilde{\mathcal{C}}(\chi, \chi^*) = \mathcal{C}(\chi)$. The first variation of $\mathcal{C}$ can then be written as

$$\delta\mathcal{C} = \frac{\partial\tilde{\mathcal{C}}}{\partial\chi}(\delta\chi) + \frac{\partial\tilde{\mathcal{C}}}{\partial\chi^*}(\delta\chi^*) \tag{C.12}$$

The derivative operators $\partial\tilde{\mathcal{C}}/\partial\chi$ and $\partial\tilde{\mathcal{C}}/\partial\chi^*$ are linear mappings from $L^2(\mathcal{D})$ to $\mathbb{C}$ and satisfy

$$\frac{\partial\tilde{\mathcal{C}}}{\partial\chi}(\delta\chi) = \left\{\frac{\partial\tilde{\mathcal{C}}}{\partial\chi^*}(\delta\chi^*)\right\}^*. \tag{C.13}$$

Noting (C.13) and (C.12), the first variation of $\mathcal{C}$ can also be written as

$$\delta\mathcal{C} = 2\text{Re}\left\{\frac{\partial\tilde{\mathcal{C}}}{\partial\chi}(\delta\chi)\right\} = 2\text{Re}\left\{\frac{\partial\tilde{\mathcal{C}}}{\partial\chi^*}(\delta\chi^*)\right\}. \tag{C.14}$$

Sometimes, when we are dealing with nonlinear cost-functionals, it may not be straightforward to find the cost-functional $\tilde{\mathcal{C}}(\chi, \chi^*)$. To find the formal derivative operators in these situations, we may first find the Gateaux differential [172, pg. 498] of the cost-functional $\mathcal{C}$ as

$$\delta\mathcal{C} = \lim_{\epsilon \to 0} \frac{\mathcal{C}(\chi + \epsilon\delta\chi) - \mathcal{C}(\chi)}{\epsilon}. \tag{C.15}$$

The result of the above limit will be of the form

$$2\text{Re}\,\langle f, \delta\chi \rangle_{\mathcal{D}} \tag{C.16}$$

where the inner product over $\mathcal{D}$ is defined in (2.6) and $f \in L^2(\mathcal{D})$. Thus, the Gateaux differential can be written as

$$\delta\mathcal{C} = \langle f, \delta\chi \rangle_{\mathcal{D}} + \langle f^*, \delta\chi^* \rangle_{\mathcal{D}}\,. \tag{C.17}$$

Comparing (C.17) with (C.12), the derivative operators can then be found as

$$\frac{\partial\tilde{\mathcal{C}}}{\partial\chi}(\delta\chi) = \langle f^*, \delta\chi^* \rangle_{\mathcal{D}} \tag{C.18}$$

$$\frac{\partial\tilde{\mathcal{C}}}{\partial\chi^*}(\delta\chi^*) = \langle f, \delta\chi \rangle_{\mathcal{D}} \tag{C.19}$$

Finally, we note that the validity of the Wirtinger calculus is proved in many references for the univariate and multivariate calculus [70, 71, 72, 73, 170] and is extendable to the infinite dimensional case where it is sometimes called functional Wirtinger calculus [173].

D

Required Derivative Operators

Le présent travail est une première tentative pour établir systématiquement quelques principes fondamentaux du Calcul Fonctionnel et les appliquer ensuite à certains exemples concrets. Translation: *The present work is a first attempt to systematically establish some basic principles of the Calculus of Functionals and apply them to some concrete examples.* (Maurice René Fréchet; from the Introduction of his PhD thesis [174] supervised by Jacques Hadamard and submitted in 1906).

In this Appendix, we derive the required derivative operators utilized in Chapters 4 and 5.

D.1 Derivative of the scattered field with respect to the contrast

Assuming that the t^{th} transmitter is active, the first derivative of the scattered field with respect to the contrast χ, at the n^{th} iteration of the GNI algorithm where $\chi = \chi_n$, may be

found via

$$\begin{aligned}\frac{\partial \mathcal{E}_t^{\text{scat}}}{\partial \chi}|_{\chi=\chi_n}(\psi) &= \lim_{\epsilon\to 0}\frac{\mathcal{E}_t^{\text{scat}}(\chi_n+\epsilon\psi)-\mathcal{E}_t^{\text{scat}}(\chi_n)}{\epsilon} \\ &= \lim_{\epsilon\to 0}\frac{\boldsymbol{E}_{t,\chi_n+\epsilon\psi}^{\text{scat}}(\boldsymbol{p})-\boldsymbol{E}_{t,\chi_n}^{\text{scat}}(\boldsymbol{p})}{\epsilon}\end{aligned} \tag{D.1}$$

where $\psi \in L^2(\mathcal{D})$, $\epsilon \in \mathbb{R}$, and $\boldsymbol{E}_{t,\chi_n+\epsilon\psi}^{\text{scat}}(\boldsymbol{p})$ and $\boldsymbol{E}_{t,\chi_n}^{\text{scat}}(\boldsymbol{p})$ denotes the scattered field on the measurement domain corresponding to $\chi_n+\epsilon\psi$ and χ_n respectively (when the t^{th} transmitter is active). It is well known that the scattered field $\boldsymbol{E}_{t,\chi_n}^{\text{scat}}$ satisfies the vector wave equation [35]

$$\nabla\times\nabla\times\boldsymbol{E}_{t,\chi_n}^{\text{scat}}-k_b^2\boldsymbol{E}_{t,\chi_n}^{\text{scat}}=k_b^2\chi_n\boldsymbol{E}_{t,\chi_n} \tag{D.2}$$

where $\nabla\times$ denotes the curl operator and $\boldsymbol{E}_{t,\chi_n}$ is the total field in the presence of the contrast χ_n when the t^{th} transmitter is active. Similar to the above equation, $\boldsymbol{E}_{t,\chi_n+\epsilon\psi}^{\text{scat}}$ satisfies

$$\nabla\times\nabla\times\boldsymbol{E}_{t,\chi_n+\epsilon\psi}^{\text{scat}}-k_b^2\boldsymbol{E}_{t,\chi_n+\epsilon\psi}^{\text{scat}}=k_b^2(\chi_n+\epsilon\psi)\boldsymbol{E}_{t,\chi_n+\epsilon\psi} \tag{D.3}$$

where $\boldsymbol{E}_{t,\chi_n+\epsilon\psi}$ is the total field in the presence of the contrast $\chi_n+\epsilon\psi$. Subtracting (D.2) from (D.3), it results in

$$\begin{aligned}\nabla\times\nabla\times(\boldsymbol{E}_{t,\chi_n+\epsilon\psi}^{\text{scat}}-\boldsymbol{E}_{t,\chi_n}^{\text{scat}}) &- k_b^2(\boldsymbol{E}_{t,\chi_n+\epsilon\psi}^{\text{scat}}-\boldsymbol{E}_{t,\chi_n}^{\text{scat}}) \\ &= k_b^2\chi_n(\boldsymbol{E}_{t,\chi_n+\epsilon\psi}-\boldsymbol{E}_{t,\chi_n})+\epsilon k_b^2\psi\boldsymbol{E}_{t,\chi_n+\epsilon\psi}\end{aligned} \tag{D.4}$$

Noting that $\boldsymbol{E}_{t,\chi_n+\epsilon\psi}=\boldsymbol{E}_{t,\chi_n+\epsilon\psi}^{\text{scat}}+\boldsymbol{E}_t^{\text{inc}}$ and $\boldsymbol{E}_{t,\chi_n}=\boldsymbol{E}_{t,\chi_n}^{\text{scat}}+\boldsymbol{E}_t^{\text{inc}}$, (D.4) may be re-written as

$$\nabla\times\nabla\times(\boldsymbol{E}_{t,\chi_n+\epsilon\psi}^{\text{scat}}-\boldsymbol{E}_{t,\chi_n}^{\text{scat}})-k^2(\boldsymbol{E}_{t,\chi_n+\epsilon\psi}^{\text{scat}}-\boldsymbol{E}_{t,\chi_n}^{\text{scat}})=\epsilon k_b^2\psi\boldsymbol{E}_{t,\chi_n+\epsilon\psi} \tag{D.5}$$

where $k^2=k_b^2(1+\chi_n)$ is the wavenumber squared corresponding to the contrast χ_n. We now define the inhomogeneous Green's function which corresponds to the contrast χ_n. The

inhomogeneous Green's function, $\bar{\bar{G}}^{\text{inh}}$, sometimes referred to as the distorted Green's function, satisfies

$$\nabla \times \nabla \times \bar{\bar{G}}^{\text{inh}}(\boldsymbol{r}, \boldsymbol{r}') - k^2 \bar{\bar{G}}^{\text{inh}}(\boldsymbol{r}, \boldsymbol{r}') = \bar{\bar{I}}\delta(\boldsymbol{r} - \boldsymbol{r}') \tag{D.6}$$

where $\bar{\bar{I}}$ is the identity dyad, $\delta(.)$ represents the Dirac delta function, and $\boldsymbol{r}$ and $\boldsymbol{r}'$ represent two arbitrary position vectors. Noting (D.6) and (D.5), it can be concluded that

$$\boldsymbol{E}^{\text{scat}}_{t,\chi_n+\epsilon\psi}(\boldsymbol{p}) - \boldsymbol{E}^{\text{scat}}_{t,\chi_n}(\boldsymbol{p}) = k_b^2 \int_{\mathcal{D}} \bar{\bar{G}}^{\text{inh}}(\boldsymbol{p}, \boldsymbol{q}) \cdot \epsilon\psi(\boldsymbol{q}) \boldsymbol{E}_{t,\chi_n+\epsilon\psi}(\boldsymbol{q}) d\boldsymbol{q}. \tag{D.7}$$

Using (D.7), equation (D.1) may be written as

$$\frac{\partial \mathcal{E}^{\text{scat}}_t}{\partial \chi}|_{\chi=\chi_n}(\psi) = \lim_{\epsilon \to 0} \frac{k_b^2 \int_{\mathcal{D}} \bar{\bar{G}}^{\text{inh}}(\boldsymbol{p}, \boldsymbol{q}) \cdot \epsilon\psi(\boldsymbol{q}) \boldsymbol{E}_{t,\chi_n+\epsilon\psi}(\boldsymbol{q}) d\boldsymbol{q}}{\epsilon} \tag{D.8}$$

Noting (2.19), the field $\tilde{\boldsymbol{E}}(\boldsymbol{q})$ may be written as

$$\begin{aligned} \boldsymbol{E}_{t,\chi_n+\epsilon\psi}(\boldsymbol{q}) = \mathcal{E}_t(\chi_n + \epsilon\psi) = \mathcal{E}_t(\chi_n) + \frac{\partial \mathcal{E}_t}{\partial \chi}|_{\chi=\chi_n}(\epsilon\psi) + o(\|\epsilon\psi\|_{\mathcal{D}}) = \\ \boldsymbol{E}_{t,\chi_n}(\boldsymbol{q}) + \epsilon \frac{\partial \mathcal{E}_t}{\partial \chi}|_{\chi=\chi_n}(\psi) + o(\|\epsilon\psi\|_{\mathcal{D}}) \end{aligned} \tag{D.9}$$

where the little-o notation represents

$$\lim_{\|\psi\|_{\mathcal{D}} \to 0} \frac{o(\|\psi\|_{\mathcal{D}})}{\|\psi\|_{\mathcal{D}}} = 0. \tag{D.10}$$

Noting (D.9), equation (D.8) can be simplified to

$$\frac{\partial \mathcal{E}^{\text{scat}}_t}{\partial \chi}|_{\chi=\chi_n}(\psi) = k_b^2 \int_{\mathcal{D}} \bar{\bar{G}}^{\text{inh}}(\boldsymbol{p}, \boldsymbol{q}) \cdot \psi(\boldsymbol{q}) \boldsymbol{E}_{t,\chi_n}(\boldsymbol{q}) d\boldsymbol{q}. \tag{D.11}$$

We will note that the generation of the dyadic Green's function $\bar{\bar{G}}^{\text{inh}}(\boldsymbol{p}, \boldsymbol{q})$ as it requires evaluating the field at the receiver located at $\boldsymbol{p} \in \mathcal{S}$ for the excitation located at $\boldsymbol{q} \in \mathcal{D}$.

As the number of receivers are usually much less than that of the testing points within the imaging domain, it is computationally more efficient to formulate the derivative operator in terms of $\bar{\bar{G}}^{\text{inh}}(\boldsymbol{q},\boldsymbol{p})$. To do so, we use the reciprocity relation

$$\bar{\bar{G}}^{\text{inh}}(\boldsymbol{p},\boldsymbol{q}) = \left[\bar{\bar{G}}^{\text{inh}}(\boldsymbol{q},\boldsymbol{p})\right]^T \tag{D.12}$$

Using (D.12), the derivative operator, (D.11), may be written as

$$\frac{\partial \mathcal{E}_t^{\text{scat}}}{\partial \chi}|_{\chi=\chi_n}(\psi) = k_b^2 \int_{\mathcal{D}} \left[\bar{\bar{G}}^{\text{inh}}(\boldsymbol{q},\boldsymbol{p})\right]^T \cdot \psi(\boldsymbol{q}) \boldsymbol{E}_{t,\chi_n}(\boldsymbol{q}) d\boldsymbol{q} \tag{D.13}$$

Equation (D.13), may be written as

$$\frac{\partial \mathcal{E}_t^{\text{scat}}}{\partial \chi}|_{\chi=\chi_n}(\psi) = k_b^2 \int_{\mathcal{D}} \psi(\boldsymbol{q}) \boldsymbol{E}_{t,\chi_n}(\boldsymbol{q}) \cdot \bar{\bar{G}}^{\text{inh}}(\boldsymbol{q},\boldsymbol{p}) d\boldsymbol{q} \tag{D.14}$$

For more clarity, we sometimes refer to the distorted Green's function corresponding to χ_n as $\bar{\bar{G}}^{\text{inh}}(\boldsymbol{q},\boldsymbol{p};\chi_n)$ and also write $\boldsymbol{E}_{t,\chi_n}(\boldsymbol{q})$ as $\boldsymbol{E}_t(\boldsymbol{q};\chi_n)$. This completes the derivation of the operator $\partial \mathcal{E}_t^{\text{scat}}/\partial \chi$.

As will be seen in Section D.2, the Gauss-Newton inversion method also requires the adjoint of the operator $\frac{\partial \mathcal{E}^{\text{scat}}}{\partial \chi}$. The adjoint operator, $\left(\frac{\partial \mathcal{E}^{\text{scat}}}{\partial \chi}\right)^a$ satisfies

$$\left\langle \boldsymbol{\Gamma}, \frac{\partial \mathcal{E}_t^{\text{scat}}}{\partial \chi}|_{\chi=\chi_n}(\psi) \right\rangle_{\mathcal{S}} = \left\langle \left(\frac{\partial \mathcal{E}_t^{\text{scat}}}{\partial \chi}|_{\chi=\chi_n}\right)^a (\boldsymbol{\Gamma}), \psi \right\rangle_{\mathcal{D}}, \tag{D.15}$$

where $\boldsymbol{\Gamma} \in L^2(\mathcal{S})$ and $\psi \in L^2(\mathcal{D})$. Using (D.15) and (D.14), it is straightforward to show that

$$\left(\frac{\partial \mathcal{E}_t^{\text{scat}}}{\partial \chi}|_{\chi=\chi_n}\right)^a (\boldsymbol{\Gamma}) = \left(k_b^2\right)^* \left[\boldsymbol{E}_{t,\chi_n}(\boldsymbol{q})\right]^* \cdot \int_{\mathcal{S}} \left[\bar{\bar{G}}^{\text{inh}}(\boldsymbol{q},\boldsymbol{p})\right]^* \cdot \boldsymbol{\Gamma}(\boldsymbol{p}) d\boldsymbol{p} \tag{D.16}$$

The second derivative of the scattered field with respect to the contrast is ignored to avoid its computational cost. Although the second derivative is ignored, it will be derived to show why its calculation is computationally expensive. The second derivative operator $\partial^2\mathcal{E}_t^{\text{scat}}/\partial\chi^2$ is a linear mapping from $L^2(\mathcal{D})$ to the space of linear operators which map from $L^2(\mathcal{D})$ to $L^2(\mathcal{S})$. denoting $\psi \in L^2(\mathcal{D})$ and $\varphi \in L^2(\mathcal{D})$, the second derivative operator, at the n^{th} iteration of the algorithm where $\chi = \chi_n$ may be found via

$$\left[\frac{\partial^2\mathcal{E}_t^{\text{scat}}}{\partial\chi^2}|_{\chi=\chi_n}(\varphi)\right](\psi) = \lim_{\epsilon\to 0}\frac{\frac{\partial\mathcal{E}_t^{\text{scat}}}{\partial\chi}|_{\chi=\chi_n+\epsilon\psi}(\varphi) - \frac{\partial\mathcal{E}_t^{\text{scat}}}{\partial\chi}|_{\chi=\chi_n}(\varphi)}{\epsilon}. \tag{D.17}$$

Using (D.14), equation (D.17) may be written as

$$\left[\frac{\partial^2\mathcal{E}_t^{\text{scat}}}{\partial\chi^2}|_{\chi=\chi_n}(\varphi)\right](\psi) = \lim_{\epsilon\to 0}\left[\frac{k_b^2\int_{\mathcal{D}}\varphi(\boldsymbol{q})\boldsymbol{E}_t(\boldsymbol{q};\chi_n+\epsilon\psi)\cdot\bar{\bar{G}}^{\text{inh}}(\boldsymbol{q},\boldsymbol{p};\chi_n+\epsilon\psi)d\boldsymbol{q}}{\epsilon} - \frac{k_b^2\int_{\mathcal{D}}\varphi(\boldsymbol{q})\boldsymbol{E}_t(\boldsymbol{q};\chi_n)\cdot\bar{\bar{G}}^{\text{inh}}(\boldsymbol{q},\boldsymbol{p};\chi_n)d\boldsymbol{q}}{\epsilon}\right] \tag{D.18}$$

where $\boldsymbol{E}_t(\boldsymbol{q};\chi_n+\epsilon\psi)$ and $\boldsymbol{E}_t(\boldsymbol{q};\chi_n)$ are the total fields within the imaging domain in the presence of $\chi_n+\epsilon\psi$ and χ_n respectively. Also, $\bar{\bar{G}}^{\text{inh}}(\boldsymbol{q},\boldsymbol{p};\chi_n+\epsilon\psi)$ and $\bar{\bar{G}}^{\text{inh}}(\boldsymbol{q},\boldsymbol{p};\chi_n)$ are the dyadic Green's functions for the inhomogeneous backgrounds $\chi_n+\epsilon\psi$ and χ_n respectively.

After making the mathematical calculations and simplifications, (D.18) is simplified to

$$\left[\frac{\partial^2\mathcal{E}_t^{\text{scat}}}{\partial\chi^2}|_{\chi=\chi_n}(\varphi)\right](\psi) = k_b^2\int_{\mathcal{D}}\varphi(\boldsymbol{q})\left[\frac{\partial\mathcal{E}_t}{\partial\chi}|_{\chi=\chi_n}(\psi)\cdot\bar{\bar{G}}^{\text{inh}}(\boldsymbol{q},\boldsymbol{p};\chi_n) + \boldsymbol{E}_t(\boldsymbol{q};\chi_n)\cdot\frac{\partial\bar{\bar{G}}^{\text{inh}}(\boldsymbol{q},\boldsymbol{p};\chi)}{\partial\chi}|_{\chi=\chi_n}(\psi)\right]d\boldsymbol{q} \tag{D.19}$$

As briefly explained in Chapter 4, the calculation of this second derivative is very computationally expensive. Thus, it is avoided in the GNI method.

D.2 Required derivatives for the data misfit cost-functional

Herein, we show the derivation of the required derivatives for the Gauss-Newton inversion method assuming the cost-functional to be minimized is $\mathcal{C}(\chi) \equiv \mathcal{C}^{\text{LS}}(\chi)$ where the data misfit $\mathcal{C}^{\text{LS}}$ is given in (3.1). As discussed in Appendix C, the cost-functional $\mathcal{C}^{\text{LS}}$ is not holomorphic in χ. We, therefore, consider the cost-functional $\tilde{\mathcal{C}}^{\text{LS}}(\chi, \chi^*)$ which satisfies $\tilde{\mathcal{C}}^{\text{LS}}(\chi, \chi^*) = \mathcal{C}^{\text{LS}}(\chi)$. The cost-functional $\tilde{\mathcal{C}}$ is holomorphic in χ for fixed χ^* and vice versa (see Appendix C for more discussion).

To find the derivatives of $\tilde{\mathcal{C}}^{\text{LS}}(\chi)$ with respect to χ and χ^* at $\chi = \chi_n$, we start with finding the limit

$$\lim_{\epsilon\to 0} \frac{\mathcal{C}^{\text{LS}}(\chi_n + \epsilon\psi) - \mathcal{C}^{\text{LS}}(\chi_n)}{\epsilon} = \lim_{\epsilon\to 0} \eta_{\mathcal{S}} \frac{\sum_{t=1}^{T_x} \left\| \boldsymbol{\mathcal{E}}_t^{\text{scat}}(\chi_n + \epsilon\psi) - \boldsymbol{E}_{\text{meas},t}^{\text{scat}} \right\|_{\mathcal{S}}^2 - \sum_{t=1}^{T_x} \left\| \boldsymbol{\mathcal{E}}_t^{\text{scat}}(\chi_n) - \boldsymbol{E}_{\text{meas},t}^{\text{scat}} \right\|_{\mathcal{S}}^2}{\epsilon} \tag{D.20}$$

where $\epsilon \in \mathbb{R}$, $\psi \in L^2(\mathcal{D})$, and $\eta_{\mathcal{S}} = \left[\sum_{t=1}^{T_x} \left\| \boldsymbol{E}_{\text{meas},t}^{\text{scat}} \right\|_{\mathcal{S}}^2 \right]^{-1}$. Utilizing the little-$o$ notation, (D.10), the expression (D.20) can be written as

$$\lim_{\epsilon\to 0} \eta_{\mathcal{S}} \left[\frac{\sum_{t=1}^{T_x} \left\| \boldsymbol{\mathcal{E}}_t^{\text{scat}}(\chi_n) + \epsilon \frac{\partial \boldsymbol{\mathcal{E}}_t^{\text{scat}}}{\partial \chi}|_{\chi=\chi_n}(\psi) + o(\|\epsilon\psi\|_{\mathcal{D}}) - \boldsymbol{E}_{\text{meas},t}^{\text{scat}} \right\|_{\mathcal{S}}^2}{\epsilon} - \frac{\sum_{t=1}^{T_x} \left\| \boldsymbol{\mathcal{E}}_t^{\text{scat}}(\chi_n) - \boldsymbol{E}_{\text{meas},t}^{\text{scat}} \right\|_{\mathcal{S}}^2}{\epsilon} \right] \tag{D.21}$$

The above limit may then be simplified as

$$2\eta_{\mathcal{S}} \sum_{t=1}^{T_x} \mathrm{Re} \left\langle \mathcal{E}_t^{\text{scat}}(\chi_n) - \boldsymbol{E}_{\text{meas},t}^{\text{scat}}, \frac{\partial \mathcal{E}_t^{\text{scat}}}{\partial \chi}|_{\chi=\chi_n}(\psi) \right\rangle_{\mathcal{S}}, \tag{D.22}$$

where 'Re' denotes the real-part operator. The above expression can then be written as,

$$\begin{aligned} &\left\langle \eta_{\mathcal{S}} \sum_{t=1}^{T_x} \left[\frac{\partial \mathcal{E}_t^{\text{scat}}}{\partial \chi}|_{\chi=\chi_n} \right]^a (\mathcal{E}_t^{\text{scat}}(\chi_n) - \boldsymbol{E}_{\text{meas},t}^{\text{scat}}), \psi \right\rangle_{\mathcal{D}} + \\ &\left\langle \eta_{\mathcal{S}} \sum_{t=1}^{T_x} \left\{ \left[\frac{\partial \mathcal{E}_t^{\text{scat}}}{\partial \chi}|_{\chi=\chi_n} \right]^a (\mathcal{E}_t^{\text{scat}}(\chi_n) - \boldsymbol{E}_{\text{meas},t}^{\text{scat}}) \right\}^*, \psi^* \right\rangle_{\mathcal{D}}. \end{aligned} \tag{D.23}$$

Considering the definition of the functional derivative [77], [172] and the definition of the inner product given in (2.8), it can be concluded that

$$\frac{\partial \tilde{\mathcal{C}}^{\text{LS}}}{\partial \chi}|_{\chi=\chi_n}(\psi) = \left\langle \eta_{\mathcal{S}} \sum_{t=1}^{T_x} \left\{ \left[\frac{\partial \mathcal{E}_t^{\text{scat}}}{\partial \chi}|_{\chi=\chi_n} \right]^a (\mathcal{E}^{\text{scat}}(\chi_n) - \boldsymbol{E}_{\text{meas},t}^{\text{scat}}) \right\}^*, \psi^* \right\rangle_{\mathcal{D}}, \tag{D.24}$$

and

$$\frac{\partial \tilde{\mathcal{C}}^{\text{LS}}}{\partial \chi^*}|_{\chi=\chi_n}(\psi^*) = \left\langle \eta_{\mathcal{S}} \sum_{t=1}^{T_x} \left[\frac{\partial \mathcal{E}_t^{\text{scat}}}{\partial \chi}|_{\chi=\chi_n} \right]^a (\mathcal{E}_t^{\text{scat}}(\chi_n) - \boldsymbol{E}_{\text{meas},t}^{\text{scat}}), \psi \right\rangle_{\mathcal{D}}. \tag{D.25}$$

We note that

$$\frac{\partial \tilde{\mathcal{C}}^{\text{LS}}}{\partial \chi^*}|_{\chi=\chi_n}(\psi^*) = \left\{ \frac{\partial \tilde{\mathcal{C}}^{\text{LS}}}{\partial \chi}|_{\chi=\chi_n}(\psi) \right\}^*. \tag{D.26}$$

To find $\left[\frac{\partial^2 \tilde{\mathcal{C}}^{\text{LS}}}{\partial \chi^* \partial \chi}|_{\chi=\chi_n}(\varphi) \right](\psi^*)$ and $\left[\frac{\partial^2 \tilde{\mathcal{C}}^{\text{LS}}}{\partial \chi \partial \chi}|_{\chi=\chi_n}(\varphi) \right](\psi)$, we start with finding the limit

$$\lim_{\epsilon \to 0} \frac{\frac{\partial \tilde{\mathcal{C}}^{\text{LS}}}{\partial \chi}|_{\chi=\chi_n+\epsilon\psi}(\varphi) - \frac{\partial \tilde{\mathcal{C}}^{\text{LS}}}{\partial \chi}|_{\chi=\chi_n}(\varphi)}{\epsilon}. \tag{D.27}$$

Noting (D.24), the above limit can be written as

$$\lim_{\epsilon\to 0}\eta_{\mathcal{S}}\frac{\sum_{t=1}^{T_x}\left\langle\frac{\partial\mathcal{E}_t^{\text{scat}}}{\partial\chi}|_{\chi=\chi_n+\epsilon\psi}(\varphi),\mathcal{E}_t^{\text{scat}}(\chi_n+\epsilon\psi)-\boldsymbol{E}_{\text{meas},t}^{\text{scat}}\right\rangle_{\mathcal{S}}}{\epsilon}- \frac{\eta_{\mathcal{S}}\sum_{t=1}^{T_x}\left\langle\frac{\partial\mathcal{E}_t^{\text{scat}}}{\partial\chi}|_{\chi=\chi_n}(\varphi),\mathcal{E}_t^{\text{scat}}(\chi_n)-\boldsymbol{E}_{\text{meas},t}^{\text{scat}}\right\rangle_{\mathcal{S}}}{\epsilon}. \tag{D.28}$$

Utilizing (D.10), the above limit can be simplified to

$$\lim_{\epsilon\to 0}\frac{\eta_{\mathcal{S}}\sum_{t=1}^{T_x}\left\langle\frac{\partial\mathcal{E}_t^{\text{scat}}}{\partial\chi}|_{\chi=\chi_n}(\varphi)+\epsilon\frac{\partial^2\mathcal{E}^{\text{scat}}}{\partial\chi^2}|_{\chi=\chi_n}(\varphi)(\psi),\mathcal{E}_t^{\text{scat}}(\chi_n)+\epsilon\frac{\partial\mathcal{E}_t^{\text{scat}}}{\partial\chi}(\psi)-\boldsymbol{E}_{\text{meas},t}^{\text{scat}}\right\rangle_{\mathcal{S}}}{\epsilon} - \frac{\eta_{\mathcal{S}}\sum_{t=1}^{T_x}\left\langle\frac{\partial\mathcal{E}_t^{\text{scat}}}{\partial\chi}|_{\chi=\chi_n}(\varphi),\mathcal{E}_t^{\text{scat}}(\chi_n)-\boldsymbol{E}_{\text{meas},t}^{\text{scat}}\right\rangle_{\mathcal{S}}}{\epsilon}. \tag{D.29}$$

The above limit will then be

$$\eta_{\mathcal{S}}\sum_{t=1}^{T_x}\left\langle\frac{\partial\mathcal{E}_t^{\text{scat}}}{\partial\chi}|_{\chi=\chi_n}(\varphi),\frac{\partial\mathcal{E}_t^{\text{scat}}}{\partial\chi}|_{\chi=\chi_n}(\psi)\right\rangle_{\mathcal{S}}+ \sum_{t=1}^{T_x}\eta_{\mathcal{S}}\left\langle\left[\frac{\partial^2\mathcal{E}_t^{\text{scat}}}{\partial\chi^2}|_{\chi=\chi_n}(\varphi)\right](\psi),\mathcal{E}_t^{\text{scat}}(\chi_n)-\boldsymbol{E}_{\text{meas},t}^{\text{scat}}\right\rangle_{\mathcal{S}}. \tag{D.30}$$

Using the definition of the adjoint operator, the above expression may be written as

$$\left\langle\eta_{\mathcal{S}}\sum_{t=1}^{T_x}\left[\frac{\partial\mathcal{E}_t^{\text{scat}}}{\partial\chi}|_{\chi=\chi_n}\right]^a\left[\frac{\partial\mathcal{E}_t^{\text{scat}}}{\partial\chi}|_{\chi=\chi_n}\right](\varphi),\psi\right\rangle_{\mathcal{D}}+ \left\langle\eta_{\mathcal{S}}\sum_{t=1}^{T_x}\left\{\left[\frac{\partial^2\mathcal{E}_t^{\text{scat}}}{\partial\chi^2}|_{\chi=\chi_n}(\varphi)\right]^a\left(\mathcal{E}_t^{\text{scat}}(\chi_n)-\boldsymbol{E}_{\text{meas},t}^{\text{scat}}\right)\right\}^*,\psi^*\right\rangle_{\mathcal{D}}. \tag{D.31}$$

Therefore, it can be concluded that

$$\left[\frac{\partial^2\tilde{\mathcal{C}}^{\text{LS}}}{\partial\chi^*\partial\chi}|_{\chi=\chi_n}(\varphi)\right](\psi^*) = \left\langle \eta_{\mathcal{S}} \sum_{t=1}^{T_x} \left[\frac{\partial\mathcal{E}_t^{\text{scat}}}{\partial\chi}|_{\chi=\chi_n}\right]^a \left[\frac{\partial\mathcal{E}_t^{\text{scat}}}{\partial\chi}|_{\chi=\chi_n}\right](\varphi), \psi \right\rangle_{\mathcal{D}} \tag{D.32}$$

and

$$\left[\frac{\partial^2\tilde{\mathcal{C}}^{\text{LS}}}{\partial\chi\partial\chi}|_{\chi=\chi_n}(\varphi)\right](\psi) = \left\langle \eta_{\mathcal{S}} \sum_{t=1}^{T_x} \left\{\left[\frac{\partial^2\mathcal{E}_t^{\text{scat}}}{\partial\chi^2}|_{\chi=\chi_n}(\varphi)\right]^a \left(\mathcal{E}_t^{\text{scat}}(\chi_n) - \boldsymbol{E}_{\text{meas},t}^{\text{scat}}\right)\right\}^*, \psi^* \right\rangle_{\mathcal{D}} \tag{D.33}$$

To find $\left[\frac{\partial^2\tilde{\mathcal{C}}^{\text{LS}}}{\partial\chi\partial\chi^*}|_{\chi=\chi_n}(\varphi^*)\right](\psi)$ and $\left[\frac{\partial^2\tilde{\mathcal{C}}^{\text{LS}}}{\partial\chi^*\partial\chi^*}|_{\chi=\chi_n}(\varphi^*)\right](\psi^*)$, we start with finding the limit

$$\lim_{\epsilon\to 0} \frac{\frac{\partial\tilde{\mathcal{C}}^{\text{LS}}}{\partial\chi^*}|_{\chi=\chi_n+\epsilon\psi}(\varphi^*) - \frac{\partial\tilde{\mathcal{C}}^{\text{LS}}}{\partial\chi^*}|_{\chi=\chi_n}(\varphi^*)}{\epsilon}. \tag{D.34}$$

Using the same procedure utilized to derive (D.32) and (D.33), we can derive the following

$$\left[\frac{\partial^2\tilde{\mathcal{C}}^{\text{LS}}}{\partial\chi\partial\chi^*}|_{\chi=\chi_n}(\varphi^*)\right](\psi) = \left\{\left[\frac{\partial^2\tilde{\mathcal{C}}^{\text{LS}}}{\partial\chi^*\partial\chi}|_{\chi=\chi_n}(\varphi)\right](\psi^*)\right\}^* \tag{D.35}$$

and

$$\left[\frac{\partial^2\tilde{\mathcal{C}}^{\text{LS}}}{\partial\chi^*\partial\chi^*}|_{\chi=\chi_n}(\varphi^*)\right](\psi^*) = \left\{\left[\frac{\partial^2\tilde{\mathcal{C}}^{\text{LS}}}{\partial\chi\partial\chi}|_{\chi=\chi_n}(\varphi)\right](\psi)\right\}^*. \tag{D.36}$$

D.3 Derivatives of the L^2-norm total variation regularizer

In this thesis, we have considered two forms of the L^2-norm total variation regularizer. The first one is $\mathcal{C}^{\text{AR}}(\chi)$ which is given in (5.7). The second one, $\mathcal{C}_n^{\text{MR}}(\chi)$, is the weighted L^2-norm total variation regularizer which is given in (5.15). As discussed in Appendix C, we consider the cost-functional $\tilde{\mathcal{C}}_n^{\text{MR}}(\chi,\chi^*)$ which satisfies $\tilde{\mathcal{C}}_n^{\text{MR}}(\chi,\chi^*) = \mathcal{C}_n^{\text{MR}}(\chi)$. To find the

derivatives of $\tilde{\mathcal{C}}_n^{\text{MR}}(\chi)$ with respect to χ and χ^*, at the n^{th} iteration of the Gauss-Newton inversion algorithm where $\chi = \chi_n$, we start with finding the limit

$$\lim_{\epsilon \to 0} \frac{\mathcal{C}_n^{\text{MR}}(\chi_n + \epsilon\psi) - \mathcal{C}_n^{\text{MR}}(\chi_n)}{\epsilon} \tag{D.37}$$

Noting that $\mathcal{C}_n^{\text{MR}}(\chi) = \|b_n \nabla \chi\|_{\mathcal{D}}^2 + \alpha_n^2 \|b_n\|_{\mathcal{D}}^2$, the above limit can be written as

$$\lim_{\epsilon \to 0} \frac{\|b_n \nabla(\chi_n + \epsilon\psi)\|_{\mathcal{D}}^2 + \alpha_n^2 \|b_n\|_{\mathcal{D}}^2 - \|b_n \nabla \chi_n\|_{\mathcal{D}}^2 - \alpha_n^2 \|b_n\|_{\mathcal{D}}^2}{\epsilon} \tag{D.38}$$

Utilizing (D.10) and noting that b_n is a real function, the above limit can be simplified to

$$2\text{Re}\, \langle b_n \nabla \chi_n, b_n \nabla \psi \rangle_{\mathcal{D}} = 2\text{Re} \int_{\mathcal{D}} b_n^2(\boldsymbol{q}) \nabla \chi_n(\boldsymbol{q}) \cdot \nabla \psi^*(\boldsymbol{q}) d\boldsymbol{q}. \tag{D.39}$$

Noting that

$$\nabla \cdot \Big((b_n^2 \nabla \chi_n) \psi^* \Big) = \psi^* \nabla \cdot (b_n^2 \nabla \chi_n) + b_n^2 \nabla \chi_n \cdot \nabla \psi^*, \tag{D.40}$$

where '$\nabla\cdot$' denotes the divergence operator, (D.39) may be written as

$$2\text{Re} \int_{\mathcal{D}} \Big\{ \nabla \cdot \Big(\big(b_n^2(\boldsymbol{q}) \nabla \chi_n(\boldsymbol{q}) \big) \psi^*(\boldsymbol{q}) \Big) - \psi^*(\boldsymbol{q}) \nabla \cdot \Big(b_n^2(\boldsymbol{q}) \nabla \chi_n(\boldsymbol{q}) \Big) \Big\} d\boldsymbol{q}. \tag{D.41}$$

Using the divergence theorem [175], the above expression can be written as

$$2\text{Re} \left\{ \int_{\partial \mathcal{D}} \big(b_n^2(\boldsymbol{q}) \nabla \chi_n(\boldsymbol{q}) \big) \psi^*(\boldsymbol{q}) \cdot \boldsymbol{n} d\boldsymbol{q} - \int_{\mathcal{D}} \psi^*(\boldsymbol{q}) \nabla \cdot \Big(b_n^2(\boldsymbol{q}) \nabla \chi_n(\boldsymbol{q}) \Big) d\boldsymbol{q} \right\} \tag{D.42}$$

where $\partial\mathcal{D}$ denotes the boundary of the imaging domain $\mathcal{D}$, and $\boldsymbol{n}$ is the outward pointing unit normal vector of the boundary $\partial\mathcal{D}$.

In MWT reconstruction algorithms, it is implicitly assumed that the contrast function vanishes on the boundary of the imaging domain; $\chi(\boldsymbol{q} \in \partial\mathcal{D}) = 0$. That is, the permittivity

at the boundary of the imaging domain is equal to that of the background medium; *i.e.*, $\epsilon_r(\boldsymbol{q} \in \partial\mathcal{D}) = \epsilon_b$. Noting this implicit restriction on the contrast function, the domain of the cost-functional $\mathcal{C}_n^{\text{MR}}$ can be defined more accurately as the L^2 space of complex functions defined on the imaging domain, $L^2(\mathcal{D})$, which vanish on $\partial\mathcal{D}$. Using this definition, the function ψ also needs to vanish on $\partial\mathcal{D}$. Thus,

$$\int_{\partial\mathcal{D}} \big(b_n^2(\boldsymbol{q})\nabla\chi_n(\boldsymbol{q})\big)\psi^*(\boldsymbol{q})d\boldsymbol{q} = 0. \tag{D.43}$$

Noting (D.43), equation (D.42) can be written as

$$-2\text{Re}\int_{\mathcal{D}} \psi^*(\boldsymbol{q})\nabla\cdot\Big(b_n^2(\boldsymbol{q})\nabla\chi_n(\boldsymbol{q})\Big)d\boldsymbol{q} = 2\text{Re}\left\langle -\nabla\cdot(b_n^2\nabla\chi_n), \psi\right\rangle_{\mathcal{D}}. \tag{D.44}$$

Thus,

$$\lim_{\epsilon\to 0}\frac{\mathcal{C}_n^{\text{MR}}(\chi_n+\epsilon\psi)-\mathcal{C}_n^{\text{MR}}(\chi_n)}{\epsilon} = \left\langle -\nabla\cdot(b_n^2\nabla\chi_n), \psi\right\rangle_{\mathcal{D}} + \left\langle \left[-\nabla\cdot(b_n^2\nabla\chi_n)\right]^*, \psi^*\right\rangle_{\mathcal{D}} \tag{D.45}$$

Noting (D.45), the derivative operators may be written as

$$\frac{\partial\tilde{\mathcal{C}}_n^{\text{MR}}}{\partial\chi^*}|_{\chi=\chi_n}(\psi^*) = \left\langle -\nabla\cdot(b_n^2\nabla\chi_n), \psi\right\rangle_{\mathcal{D}} \tag{D.46}$$

and

$$\frac{\partial\tilde{\mathcal{C}}_n^{\text{MR}}}{\partial\chi}|_{\chi=\chi_n}(\psi) = \left\langle \left[-\nabla\cdot(b_n^2\nabla\chi_n)\right]^*, \psi^*\right\rangle_{\mathcal{D}}. \tag{D.47}$$

We note that

$$\frac{\partial\tilde{\mathcal{C}}_n^{\text{MR}}}{\partial\chi}|_{\chi=\chi_n}(\psi) = \left\{\frac{\partial\mathcal{C}^{\text{MR}}}{\partial\chi^*}|_{\chi=\chi_n}(\psi^*)\right\}^*. \tag{D.48}$$

To find the derivatives $\left[\frac{\partial^2\tilde{\mathcal{C}}_n^{\text{MR}}}{\partial\chi^*\partial\chi}|_{\chi=\chi_n}(\varphi)\right](\psi^*)$, and $\left[\frac{\partial^2\tilde{\mathcal{C}}_n^{\text{MR}}}{\partial\chi\partial\chi}|_{\chi=\chi_n}(\varphi)\right](\psi)$, we start with finding

the limit

$$\lim_{\epsilon \to 0} \frac{\frac{\partial \tilde{\mathcal{C}}_n^{\text{MR}}}{\partial \chi}|_{\chi=\chi_n+\epsilon\psi}(\varphi) - \frac{\partial \tilde{\mathcal{C}}_n^{\text{MR}}}{\partial \chi}|_{\chi=\chi_n}(\varphi)}{\epsilon} \tag{D.49}$$

Utilizing (D.47) and noting that b_n^2 is a real function, the above limit may be written as

$$\lim_{\epsilon \to 0} \frac{\langle -\nabla \cdot (b_n^2 \nabla(\chi_n^* + \epsilon\psi^*)), \varphi^* \rangle_{\mathcal{D}} - \langle -\nabla \cdot (b_n^2 \nabla \chi_n^*), \varphi^* \rangle_{\mathcal{D}}}{\epsilon} \tag{D.50}$$

After mathematical simplifications and noting that the operator '$\mathcal{L}_n \triangleq \nabla \cdot (b_n^2 \nabla)$' is a self adjoint operator (*i.e.*, $\mathcal{L}_n = \mathcal{L}_n^a$), see Appendix E for the proof, the above limit can be simplified to

$$\lim_{\epsilon \to 0} \frac{\frac{\partial \tilde{\mathcal{C}}_n^{\text{MR}}}{\partial \chi}|_{\chi=\chi_n+\epsilon\psi}(\varphi) - \frac{\partial \tilde{\mathcal{C}}_n^{\text{MR}}}{\partial \chi}|_{\chi=\chi_n}(\varphi)}{\epsilon} = \left\langle -\nabla \cdot (b_n^2 \nabla \varphi), \psi \right\rangle_{\mathcal{D}}. \tag{D.51}$$

Therefore,

$$\left[\frac{\partial^2 \tilde{\mathcal{C}}_n^{\text{MR}}}{\partial \chi^* \partial \chi}(\varphi) \right] (\psi^*) = \left\langle -\nabla \cdot (b_n^2 \nabla \varphi), \psi \right\rangle_{\mathcal{D}} \tag{D.52}$$

and

$$\left[\frac{\partial^2 \tilde{\mathcal{C}}_n^{\text{MR}}}{\partial \chi \partial \chi}(\varphi) \right] (\psi) = 0. \tag{D.53}$$

Using the same procedure, it can be concluded that

$$\left[\frac{\partial^2 \tilde{\mathcal{C}}_n^{\text{MR}}}{\partial \chi \partial \chi^*}(\varphi^*) \right] (\psi) = \left\{ \left[\frac{\partial^2 \tilde{\mathcal{C}}_n^{\text{MR}}}{\partial \chi^* \partial \chi}(\varphi) \right] (\psi^*) \right\}^* \tag{D.54}$$

and

$$\left[\frac{\partial^2 \tilde{\mathcal{C}}_n^{\text{MR}}}{\partial \chi^* \partial \chi^*}(\varphi) \right] (\psi) = \left\{ \left[\frac{\partial^2 \tilde{\mathcal{C}}_n^{\text{MR}}}{\partial \chi \partial \chi}(\varphi) \right] (\psi) \right\}^* = 0. \tag{D.55}$$

Noting that $\mathcal{C}^{\text{AR}}$ is a special form of $\mathcal{C}_n^{\text{MR}}$, the derivatives of $\tilde{\mathcal{C}}^{\text{AR}}(\chi, \chi^*)$ can be derived in a

similar way. These are

$$\frac{\partial \tilde{\mathcal{C}}^{\text{AR}}}{\partial \chi^*}|_{\chi=\chi_n}(\psi^*) = \left\langle -\frac{1}{A}\nabla\cdot(\nabla\chi_n), \psi \right\rangle_{\mathcal{D}} = \left\langle -\frac{1}{A}\nabla^2\chi_n, \psi \right\rangle_{\mathcal{D}}, \tag{D.56}$$

$$\frac{\partial \tilde{\mathcal{C}}^{\text{AR}}}{\partial \chi}|_{\chi=\chi_n}(\psi) = \left\{ \frac{\partial \tilde{\mathcal{C}}^{\text{AR}}}{\partial \chi^*}|_{\chi=\chi_n}(\psi^*) \right\}^*, \tag{D.57}$$

$$\left[\frac{\partial^2 \tilde{\mathcal{C}}^{\text{AR}}}{\partial \chi^*\partial\chi}|_{\chi=\chi_n}(\varphi)\right](\psi^*) = \left\langle -\frac{1}{A}\nabla\cdot(\nabla\varphi), \psi \right\rangle_{\mathcal{D}} = \left\langle -\frac{1}{A}\nabla^2\varphi, \psi \right\rangle_{\mathcal{D}}, \tag{D.58}$$

$$\left[\frac{\partial^2 \tilde{\mathcal{C}}^{\text{AR}}}{\partial \chi\partial\chi^*}|_{\chi=\chi_n}(\varphi^*)\right](\psi) = \left\{ \left[\frac{\partial^2 \tilde{\mathcal{C}}^{\text{AR}}}{\partial \chi^*\partial\chi}|_{\chi=\chi_n}(\varphi)\right](\psi^*) \right\}^*, \tag{D.59}$$

and

$$\left[\frac{\partial^2 \tilde{\mathcal{C}}^{\text{AR}}}{\partial \chi\partial\chi}|_{\chi=\chi_n}(\varphi)\right](\psi) = \left\{ \left[\frac{\partial^2 \tilde{\mathcal{C}}^{\text{AR}}}{\partial \chi^*\partial\chi^*}|_{\chi=\chi_n}(\varphi^*)\right](\psi^*) \right\}^* = 0, \tag{D.60}$$

where A is the area of the imaging domain and ∇^2 denotes the Laplacian operator.

D.4 Required derivatives for the shape and location reconstruction

In this section, we derive the required derivatives for the multiplicative regularizer given in (5.34). To find the first derivatives at the n^{th} iteration of the GNI algorithm, we start with finding the limit

$$\lim_{\epsilon\to 0} \frac{\mathcal{C}_n^{\text{MR,hom}}(\chi_n + \epsilon\psi) - \mathcal{C}_n^{\text{MR,hom}}(\chi_n)}{\epsilon}. \tag{D.61}$$

The above limit can be written as

$$\lim_{\epsilon\to 0}\frac{1}{A\epsilon}\int_{\mathcal{D}}\prod_{l=1}^{L}\xi_{l,n}^2(\boldsymbol{q})\left(\left|\chi_n(\boldsymbol{q})+\epsilon\psi(\boldsymbol{q})-\chi_l^h\right|^2+\alpha_n^2\right)- \prod_{l=1}^{L}\xi_{l,n}^2(\boldsymbol{q})\left(\left|\chi_n(\boldsymbol{q})-\chi_l^h\right|^2+\alpha_n^2\right)d\boldsymbol{q} \tag{D.62}$$

where

$$\xi_{l,n}(\boldsymbol{q})\triangleq\left(\left|\chi_n(\boldsymbol{q})-\chi_l^h\right|^2+\alpha_n^2\right)^{-\frac{1}{2}}. \tag{D.63}$$

Utilizing (D.10), the above limit can be simplified to (the argument $\boldsymbol{q}$ has been dropped for simplicity)

$$\lim_{\epsilon\to 0}\frac{1}{A\epsilon}\int_{\mathcal{D}}\prod_{l=1}^{L}\xi_{l,n}^2\left(2\epsilon\text{Re}\left\{\left(\chi_n-\chi_l^h\right)\psi^*\right\}+\left|\chi_n-\chi_l^h\right|^2+\alpha_n^2\right)- \prod_{l=1}^{L}\xi_{l,n}^2\left(\left|\chi_n-\chi_l^h\right|^2+\alpha_n^2\right)d\boldsymbol{q} \tag{D.64}$$

Utilizing (D.10) and after mathematical simplifications, the above limit can be written as

$$\frac{2}{A}\int_{\mathcal{D}}\sum_{l=1}^{L}\left[\xi_{l,n}^2\text{Re}\left\{\left(\chi_n-\chi_l^h\right)\psi^*\right\}\prod_{l'=\{1,\cdots,L\}-\{l\}}\left\{\xi_{l',n}^2\left(\left|\chi_n-\chi_{l'}^h\right|^2+\alpha_n^2\right)\right\}\right]d\boldsymbol{q}. \tag{D.65}$$

Noting that

$$\xi_{l',n}^2\left(\left|\chi_n-\chi_{l'}^h\right|^2+\alpha_n^2\right)=1, \tag{D.66}$$

expression (D.65) may be written as

$$\frac{2}{A}\sum_{l=1}^{L}\xi_{l,n}^2\text{Re}\left\langle\chi_n-\chi_l^h,\psi\right\rangle_{\mathcal{D}}. \tag{D.67}$$

Writing the above limit as

$$\left\langle \frac{1}{A}\sum_{l=1}^{L}\xi_{l,n}^{2}\left(\chi_n-\chi_l^h\right),\psi\right\rangle_{\mathcal{D}}+\left\langle \frac{1}{A}\sum_{l=1}^{L}\xi_{l,n}^{2}\left(\chi_n-\chi_l^h\right)^*,\psi^*\right\rangle_{\mathcal{D}}, \tag{D.68}$$

the derivative operators may then be written as

$$\frac{\partial\tilde{\mathcal{C}}_n^{\text{MR,hom}}}{\partial\chi}|_{\chi=\chi_n}(\psi)=\left\langle \frac{1}{A}\sum_{l=1}^{L}\xi_{l,n}^{2}\left(\chi_n-\chi_l^h\right)^*,\psi^*\right\rangle_{\mathcal{D}}, \tag{D.69}$$

and

$$\frac{\partial\tilde{\mathcal{C}}_n^{\text{MR,hom}}}{\partial\chi^*}|_{\chi=\chi_n}(\psi^*)=\left\langle \frac{1}{A}\sum_{l=1}^{L}\xi_{l,n}^{2}\left(\chi_n-\chi_l^h\right),\psi\right\rangle_{\mathcal{D}}. \tag{D.70}$$

where $\tilde{\mathcal{C}}_n^{\text{MR,hom}}(\chi,\chi^*)=\mathcal{C}_n^{\text{MR,hom}}(\chi)$ (see Appendix C for more discussion).

To find the derivatives $\left[\frac{\partial^2\tilde{\mathcal{C}}_n^{\text{MR,hom}}}{\partial\chi^*\partial\chi}|_{\chi=\chi_n}(\varphi)\right](\psi^*)$, and $\left[\frac{\partial^2\tilde{\mathcal{C}}_n^{\text{MR,hom}}}{\partial\chi\partial\chi}|_{\chi=\chi_n}(\varphi)\right](\psi)$, we start with finding the limit

$$\lim_{\epsilon\to0}\frac{\frac{\partial\tilde{\mathcal{C}}_n^{\text{MR,hom}}}{\partial\chi}|_{\chi=\chi_n+\epsilon\psi}(\varphi)-\frac{\partial\tilde{\mathcal{C}}_n^{\text{MR}}}{\partial\chi}|_{\chi=\chi_n}(\varphi)}{\epsilon}. \tag{D.71}$$

Utilizing (D.69), the above limit may be written as

$$\lim_{\epsilon\to0}\frac{\left\langle \frac{1}{A}\sum_{l=1}^{L}\xi_{l,n}^{2}\left(\chi_n+\epsilon\psi-\chi_l^h\right)^*,\varphi^*\right\rangle_{\mathcal{D}}-\left\langle \frac{1}{A}\sum_{l=1}^{L}\xi_{l,n}^{2}\left(\chi_n-\chi_l^h\right)^*,\varphi^*\right\rangle_{\mathcal{D}}}{\epsilon} \tag{D.72}$$

which can be simplified as

$$\left\langle \frac{1}{A}\sum_{l=1}^{L}\xi_{l,n}^{2}\psi^*,\varphi^*\right\rangle_{\mathcal{D}}. \tag{D.73}$$

Writing the above expression as

$$\left\langle \frac{1}{A}\sum_{l=1}^{L}\xi_{l,n}^{2}\varphi,\psi\right\rangle_{\mathcal{D}}, \tag{D.74}$$

it can be concluded that

$$\left[\frac{\partial^2 \tilde{\mathcal{C}}_n^{\text{MR,hom}}}{\partial \chi^* \partial \chi}|_{\chi=\chi_n}(\varphi)\right](\psi^*) = \left\langle \frac{1}{A}\sum_{l=1}^{L} \xi_{l,n}^2 \varphi, \psi \right\rangle_{\mathcal{D}}, \tag{D.75}$$

and

$$\left[\frac{\partial^2 \tilde{\mathcal{C}}_n^{\text{MR,hom}}}{\partial \chi \partial \chi}|_{\chi=\chi_n}(\varphi)\right](\psi) = 0. \tag{D.76}$$

Using a similar procedure, we can derive

$$\left[\frac{\partial^2 \tilde{\mathcal{C}}_n^{\text{MR,hom}}}{\partial \chi \partial \chi^*}|_{\chi=\chi_n}(\varphi^*)\right](\psi) = \left\{\left[\frac{\partial^2 \tilde{\mathcal{C}}_n^{\text{MR,hom}}}{\partial \chi^* \partial \chi}|_{\chi=\chi_n}(\varphi)\right](\psi^*)\right\}^*, \tag{D.77}$$

and

$$\left[\frac{\partial^2 \tilde{\mathcal{C}}_n^{\text{MR,hom}}}{\partial \chi^* \partial \chi^*}|_{\chi=\chi_n}(\varphi^*)\right](\psi^*) = 0. \tag{D.78}$$

D.5 Required derivatives with respect to real and imaginary parts of the contrast

As mentioned in Chapter 4, the derivatives of the cost-functional may be taken with respect to real and imaginary parts of the contrast; *i.e.*, χ_R and χ_I (as opposed to χ and χ^*). To find the first derivative of the data misfit cost-functional with respect to χ_R and χ_I, we may start with (D.20) and re-write (D.22) as,

$$\text{Re}\left\langle 2\eta_{\mathcal{S}} \sum_{t=1}^{T_x} \left[\frac{\partial \mathcal{E}_t^{\text{scat}}}{\partial \chi}|_{\chi=\chi_n}\right]^a \left(\mathcal{E}_t^{\text{scat}}(\chi_n) - \boldsymbol{E}_{\text{meas},t}^{\text{scat}}\right), \psi \right\rangle_{\mathcal{D}}. \tag{D.79}$$

Noting that for two complex functions, φ and ψ, we have

$$\text{Re}\,\langle \varphi, \psi \rangle_{\mathcal{D}} = \langle \varphi_R, \psi_R \rangle_{\mathcal{D}} + \langle \varphi_I, \psi_I \rangle_{\mathcal{D}}, \tag{D.80}$$

The expression (D.79) may then be written as

$$\left\langle 2\eta_{\mathcal{S}} \sum_{t=1}^{T_x} \text{Re}\left\{ \left[\frac{\partial \mathcal{E}_t^{\text{scat}}}{\partial \chi}|_{\chi=\chi_n} \right]^a \left(\mathcal{E}_t^{\text{scat}}(\chi_n) - \boldsymbol{E}_{\text{meas},t}^{\text{scat}} \right) \right\}, \psi_R \right\rangle_{\mathcal{D}} + \left\langle 2\eta_{\mathcal{S}} \sum_{t=1}^{T_x} \text{Im}\left\{ \left[\frac{\partial \mathcal{E}_t^{\text{scat}}}{\partial \chi}|_{\chi=\chi_n} \right]^a \left(\mathcal{E}_t^{\text{scat}}(\chi_n) - \boldsymbol{E}_{\text{meas},t}^{\text{scat}} \right) \right\}, \psi_I \right\rangle_{\mathcal{D}}. \tag{D.81}$$

Therefore, it can be concluded that

$$\frac{\partial \mathcal{C}^{\text{LS}}}{\partial \chi_R}|_{\chi=\chi_n}(\psi_R) = \left\langle 2\eta_{\mathcal{S}} \sum_{t=1}^{T_x} \text{Re}\left\{ \left[\frac{\partial \mathcal{E}_t^{\text{scat}}}{\partial \chi}|_{\chi=\chi_n} \right]^a \left(\mathcal{E}_t^{\text{scat}}(\chi_n) - \boldsymbol{E}_{\text{meas},t}^{\text{scat}} \right) \right\}, \psi_R \right\rangle_{\mathcal{D}}, \tag{D.82}$$

and

$$\frac{\partial \mathcal{C}^{\text{LS}}}{\partial \chi_I}|_{\chi=\chi_n}(\psi_I) = \left\langle 2\eta_{\mathcal{S}} \sum_{t=1}^{T_x} \text{Im}\left\{ \left[\frac{\partial \mathcal{E}_t^{\text{scat}}}{\partial \chi}|_{\chi=\chi_n} \right]^a \left(\mathcal{E}_t^{\text{scat}}(\chi_n) - \boldsymbol{E}_{\text{meas},t}^{\text{scat}} \right) \right\}, \psi_I \right\rangle_{\mathcal{D}}. \tag{D.83}$$

To find the second derivatives $\left[\frac{\partial^2 \mathcal{C}^{\text{LS}}}{\partial \chi_R \partial \chi_I}|_{\chi=\chi_n}(\varphi_I)\right](\psi_R)$ and $\left[\frac{\partial^2 \mathcal{C}^{\text{LS}}}{\partial \chi_I \partial \chi_I}|_{\chi=\chi_n}(\varphi_I)\right](\psi_I)$, we start with finding the limit

$$\lim_{\epsilon \to 0} \frac{\frac{\partial \mathcal{C}^{\text{LS}}}{\partial \chi_I}|_{\chi=\chi_n+\epsilon\psi}(\varphi_I) - \frac{\partial \mathcal{C}^{\text{LS}}}{\partial \chi_I}|_{\chi=\chi_n}(\varphi_I)}{\epsilon} \tag{D.84}$$

Utilizing (D.83), and the definition of the adjoint operator as well as noting that φ_I is a real function, the above limit may be written as

$$\lim_{\epsilon \to 0} \frac{2\eta_{\mathcal{S}}}{\epsilon} \sum_{t=1}^{T_x} \left[\text{Im} \left\langle \mathcal{E}_t^{\text{scat}}(\chi_n + \epsilon\psi) - \boldsymbol{E}_{\text{meas},t}^{\text{scat}}, \frac{\partial \mathcal{E}_t^{\text{scat}}}{\partial \chi}|_{\chi=\chi_n+\epsilon\psi}(\varphi_I) \right\rangle_{\mathcal{D}} - \text{Im} \left\langle \mathcal{E}_t^{\text{scat}}(\chi_n) - \boldsymbol{E}_{\text{meas},t}^{\text{scat}}, \frac{\partial \mathcal{E}_t^{\text{scat}}}{\partial \chi}|_{\chi=\chi_n}(\varphi_I) \right\rangle_{\mathcal{D}} \right]. \tag{D.85}$$

After mathematical simplifications and utilizing (D.10), the above limit can be simplified to

$$2\eta_{\mathcal{S}} \sum_{t=1}^{T_x} \Bigg[- \operatorname{Im} \left\langle \left[\frac{\partial \mathcal{E}_t^{\text{scat}}}{\partial \chi} |_{\chi=\chi_n} \right]^a \left[\frac{\partial \mathcal{E}_t^{\text{scat}}}{\partial \chi} |_{\chi=\chi_n} \right] (\varphi_I), \psi \right\rangle_{\mathcal{D}} + \operatorname{Im} \left\langle \left[\frac{\partial^2 \mathcal{E}_t^{\text{scat}}}{\partial \chi^2} |_{\chi=\chi_n} (\varphi_I) \right]^a (\mathcal{E}_t^{\text{scat}}(\chi_n) - \boldsymbol{E}_{\text{meas},t}^{\text{scat}}), \psi \right\rangle_{\mathcal{D}} \Bigg]. \tag{D.86}$$

Noting that for two complex functions, φ and ψ, we have

$$\operatorname{Im} \langle \varphi, \psi \rangle_{\mathcal{D}} = \langle \varphi_I, \psi_R \rangle_{\mathcal{D}} - \langle \varphi_R, \psi_I \rangle_{\mathcal{D}}, \tag{D.87}$$

the expression (D.86) may be written as

$$\begin{aligned} 2\eta_{\mathcal{S}} \sum_{t=1}^{T_x} \Bigg[& \left\langle -\operatorname{Im} \left\{ \left[\frac{\partial \mathcal{E}_t^{\text{scat}}}{\partial \chi} |_{\chi=\chi_n} \right]^a \left[\frac{\partial \mathcal{E}_t^{\text{scat}}}{\partial \chi} |_{\chi=\chi_n} \right] (\varphi_I) \right\}, \psi_R \right\rangle_{\mathcal{D}} + \\ & \left\langle \operatorname{Re} \left\{ \left[\frac{\partial \mathcal{E}_t^{\text{scat}}}{\partial \chi} |_{\chi=\chi_n} \right]^a \left[\frac{\partial \mathcal{E}_t^{\text{scat}}}{\partial \chi} |_{\chi=\chi_n} \right] (\varphi_I) \right\}, \psi_I \right\rangle_{\mathcal{D}} + \\ & \left\langle \operatorname{Im} \left\{ \left[\frac{\partial^2 \mathcal{E}_t^{\text{scat}}}{\partial \chi^2} |_{\chi=\chi_n} (\varphi_I) \right]^a (\mathcal{E}_t^{\text{scat}}(\chi_n) - \boldsymbol{E}_{\text{meas},t}^{\text{scat}}) \right\}, \psi_R \right\rangle_{\mathcal{D}} + \\ & \left\langle -\operatorname{Re} \left\{ \left[\frac{\partial^2 \mathcal{E}_t^{\text{scat}}}{\partial \chi^2} |_{\chi=\chi_n} (\varphi_I) \right]^a (\mathcal{E}_t^{\text{scat}}(\chi_n) - \boldsymbol{E}_{\text{meas},t}^{\text{scat}}) \right\}, \psi_I \right\rangle_{\mathcal{D}} \Bigg]. \end{aligned} \tag{D.88}$$

Therefore,

$$\begin{aligned} \frac{\partial^2 \mathcal{C}^{\text{LS}}}{\partial \chi_R \partial \chi_I} |_{\chi=\chi_n} (\varphi_I)(\psi_R) = \Bigg\langle 2\eta_{\mathcal{S}} \sum_{t=1}^{T_x} \operatorname{Im} \Bigg\{ & - \left[\frac{\partial \mathcal{E}_t^{\text{scat}}}{\partial \chi} |_{\chi=\chi_n} \right]^a \left[\frac{\partial \mathcal{E}_t^{\text{scat}}}{\partial \chi} |_{\chi=\chi_n} \right] (\varphi_I) + \\ & \left[\frac{\partial^2 \mathcal{E}_t^{\text{scat}}}{\partial \chi^2} |_{\chi=\chi_n} (\varphi_I) \right]^a (\mathcal{E}_t^{\text{scat}}(\chi_n) - \boldsymbol{E}_{\text{meas},t}^{\text{scat}}) \Bigg\}, \psi_R \Bigg\rangle_{\mathcal{D}}, \end{aligned} \tag{D.89}$$

and

$$\begin{aligned} \frac{\partial^2 \mathcal{C}^{\text{LS}}}{\partial \chi_I \partial \chi_I} |_{\chi=\chi_n} (\varphi_I)(\psi_I) = \Bigg\langle 2\eta_{\mathcal{S}} \sum_{t=1}^{T_x} \operatorname{Re} \Bigg\{ & \left[\frac{\partial \mathcal{E}_t^{\text{scat}}}{\partial \chi} |_{\chi=\chi_n} \right]^a \left[\frac{\partial \mathcal{E}_t^{\text{scat}}}{\partial \chi} |_{\chi=\chi_n} \right] (\varphi_I) - \\ & \left[\frac{\partial^2 \mathcal{E}_t^{\text{scat}}}{\partial \chi^2} |_{\chi=\chi_n} (\varphi_I) \right]^a (\mathcal{E}_t^{\text{scat}}(\chi_n) - \boldsymbol{E}_{\text{meas},t}^{\text{scat}}) \Bigg\}, \psi_I \Bigg\rangle_{\mathcal{D}}. \end{aligned} \tag{D.90}$$

To find the derivatives $\left[\frac{\partial^2 \mathcal{C}^{\text{LS}}}{\partial \chi_I \partial \chi_R}|_{\chi=\chi_n}(\varphi_R)\right](\psi_I)$ and $\left[\frac{\partial^2 \mathcal{C}^{\text{LS}}}{\partial \chi_R \partial \chi_R}|_{\chi=\chi_n}(\varphi_R)\right](\psi_R)$, we start with finding the limit

$$\lim_{\epsilon \to 0} \frac{\frac{\partial \mathcal{C}^{\text{LS}}}{\partial \chi_R}|_{\chi=\chi_n+\epsilon\psi}(\varphi_R) - \frac{\partial \mathcal{C}^{\text{LS}}}{\partial \chi_R}|_{\chi=\chi_n}(\varphi_R)}{\epsilon} \tag{D.91}$$

After mathematical simplifications similar to the ones presented above, the limit (D.91) will be

$$\begin{aligned} 2\eta_{\mathcal{S}} \sum_{t=1}^{T_x} \Bigg[\text{Re} \Bigg\langle \left[\frac{\partial \mathcal{E}_t^{\text{scat}}}{\partial \chi}|_{\chi=\chi_n}\right]^a \left[\frac{\partial \mathcal{E}_t^{\text{scat}}}{\partial \chi}|_{\chi=\chi_n}\right](\varphi_R), \psi \Bigg\rangle_{\mathcal{D}} + \\ \text{Re} \Bigg\langle \left[\frac{\partial^2 \mathcal{E}_t^{\text{scat}}}{\partial \chi^2}|_{\chi=\chi_n}(\varphi_R)\right]^a (\mathcal{E}_t^{\text{scat}}(\chi_n) - \boldsymbol{E}_{\text{meas},t}^{\text{scat}}), \psi \Bigg\rangle_{\mathcal{D}} \Bigg]. \end{aligned} \tag{D.92}$$

Noting (D.92) and utilizing (D.80), it can be concluded that

$$\begin{aligned} \frac{\partial^2 \mathcal{C}^{\text{LS}}}{\partial \chi_I \partial \chi_R}|_{\chi=\chi_n}(\varphi_R)(\psi_I) = \Bigg\langle 2\eta_{\mathcal{S}} \sum_{t=1}^{T_x} \text{Im} \Bigg\{ \left[\frac{\partial \mathcal{E}_t^{\text{scat}}}{\partial \chi}|_{\chi=\chi_n}\right]^a \left[\frac{\partial \mathcal{E}_t^{\text{scat}}}{\partial \chi}|_{\chi=\chi_n}\right](\varphi_R) + \\ \left[\frac{\partial^2 \mathcal{E}_t^{\text{scat}}}{\partial \chi^2}|_{\chi=\chi_n}(\varphi_R)\right]^a (\mathcal{E}_t^{\text{scat}}(\chi_n) - \boldsymbol{E}_{\text{meas},t}^{\text{scat}}) \Bigg\}, \psi_I \Bigg\rangle_{\mathcal{D}}, \end{aligned} \tag{D.93}$$

and

$$\begin{aligned} \frac{\partial^2 \mathcal{C}^{\text{LS}}}{\partial \chi_R \partial \chi_R}|_{\chi=\chi_n}(\varphi_R)(\psi_R) = \Bigg\langle 2\eta_{\mathcal{S}} \sum_{t=1}^{T_x} \text{Re} \Bigg\{ \left[\frac{\partial \mathcal{E}_t^{\text{scat}}}{\partial \chi}|_{\chi=\chi_n}\right]^a \left[\frac{\partial \mathcal{E}_t^{\text{scat}}}{\partial \chi}|_{\chi=\chi_n}\right](\varphi_R) + \\ \left[\frac{\partial^2 \mathcal{E}_t^{\text{scat}}}{\partial \chi^2}|_{\chi=\chi_n}(\varphi_R)\right]^a (\mathcal{E}_t^{\text{scat}}(\chi_n) - \boldsymbol{E}_{\text{meas},t}^{\text{scat}}) \Bigg\}, \psi_R \Bigg\rangle_{\mathcal{D}}. \end{aligned} \tag{D.94}$$

It should also be noted that in the Gauss-Newton inversion method, the operator $\frac{\partial^2 \mathcal{E}_t^{\text{scat}}}{\partial \chi^2}$ is neglected; see (4.3). Thus, (D.89), (D.90), (D.93), and (D.94) can be simplified. For example, (D.94) will be approximated by

$$\frac{\partial^2 \mathcal{C}^{\text{LS}}}{\partial \chi_R \partial \chi_R}|_{\chi=\chi_n}(\varphi_R)(\psi_R) \approx \Bigg\langle 2\eta_{\mathcal{S}} \sum_{t=1}^{T_x} \text{Re} \Bigg\{ \left[\frac{\partial \mathcal{E}_t^{\text{scat}}}{\partial \chi}|_{\chi=\chi_n}\right]^a \left[\frac{\partial \mathcal{E}_t^{\text{scat}}}{\partial \chi}|_{\chi=\chi_n}\right](\varphi_R) \Bigg\}, \psi_R \Bigg\rangle_{\mathcal{D}} \tag{D.95}$$

The pre-scaled GNI method, see Section 5.6.2, also requires the derivatives of $\mathcal{C}_n^{\text{MR,scaled}}$, (5.42) with respect to χ_R and χ_I. Using the same procedure explained above, these derivatives may be derived as

$$\frac{\partial \mathcal{C}_n^{\text{MR,scaled}}}{\partial \chi_R}|_{\chi=\chi_n}(\psi_R) = \left\langle -2\nabla \cdot \left[(b_n^{\text{scaled}})^2 \, \nabla \chi_{R,n} \right], \psi_R \right\rangle_{\mathcal{D}}, \tag{D.96}$$

$$\frac{\partial \mathcal{C}_n^{\text{MR,scaled}}}{\partial \chi_I}|_{\chi=\chi_n}(\psi_I) = \left\langle -2Q^2\nabla \cdot \left[(b_n^{\text{scaled}})^2 \, \nabla \chi_{I,n} \right], \psi_I \right\rangle_{\mathcal{D}}, \tag{D.97}$$

$$\frac{\partial^2 \mathcal{C}_n^{\text{MR,scaled}}}{\partial \chi_R \chi_R}|_{\chi=\chi_n}(\varphi_R)(\psi_R) = \left\langle -2\nabla \cdot \left[(b_n^{\text{scaled}})^2 \, \nabla \varphi_R \right], \psi_R \right\rangle_{\mathcal{D}}, \tag{D.98}$$

$$\frac{\partial^2 \mathcal{C}_n^{\text{MR,scaled}}}{\partial \chi_I \chi_I}|_{\chi=\chi_n}(\varphi_I)(\psi_I) = \left\langle -2Q^2\nabla \cdot \left[(b_n^{\text{scaled}})^2 \, \nabla \varphi_I \right], \psi_I \right\rangle_{\mathcal{D}}, \tag{D.99}$$

and

$$\frac{\partial^2 \mathcal{C}_n^{\text{MR,scaled}}}{\partial \chi_R \chi_I}|_{\chi=\chi_n}(\varphi_I)(\psi_R) = \frac{\partial^2 \mathcal{C}_n^{\text{MR,scaled}}}{\partial \chi_I \chi_R}|_{\chi=\chi_n}(\varphi_R)(\psi_I) = 0, \tag{D.100}$$

where

$$b_n^{\text{scaled}}(\boldsymbol{q}) \triangleq A^{-\frac{1}{2}} (|\nabla \chi_{R,n}(\boldsymbol{q})|^2 + Q^2 \, |\nabla \chi_{I,n}(\boldsymbol{q})|^2 + \alpha_n^2)^{-\frac{1}{2}}. \tag{D.101}$$

E

Self-Adjointness and Negative Definiteness

We are servants rather than masters in mathematics. (Charles Hermite [176] in whose honor a number of mathematical entities, such as Hermitian matrix, has been named).

We here prove that the operators $\underline{\mathbf{\Sigma}}$ and $\underline{\boldsymbol{\mathcal{L}}}_n$, which are the discrete forms of $\frac{1}{A}\nabla^2$ and $\mathcal{L}_n \triangleq \nabla \cdot (b_n^2 \nabla)$ respectively, are self-adjoint and negative definite using a procedure similar to the standard approach for proving Green's first and second identities [175, pg. 36].

E.1 Self-adjointness

Assuming φ and ψ are in $L^2(\mathcal{D})$, and letting b_n^2 be a positive function in $L^2(\mathcal{D})$, we may write,

$$\nabla \cdot (\psi^* b_n^2 \nabla \varphi) = \psi^* \nabla \cdot (b_n^2 \nabla \varphi) + \nabla \psi^* \cdot b_n^2 \nabla \varphi \tag{E.1}$$

Using the divergence theorem and definition of the inner product, we obtain

$$\left\langle \nabla \cdot (b_n^2 \nabla \varphi), \psi \right\rangle_{\mathcal{D}} + \int_{\mathcal{D}} b_n^2 \nabla \psi^* \cdot \nabla \varphi d\boldsymbol{q} = \oint_{\partial \mathcal{D}} b_n^2 \psi^* \frac{\partial \varphi}{\partial n} d\boldsymbol{q} \tag{E.2}$$

where $\partial \mathcal{D}$ denotes the boundary of the imaging domain and the derivative $\partial / \partial n$ represents the outward directed normal derivative on $\partial \mathcal{D}$. Interchanging ψ^* and φ and subtracting, we have

$$\begin{aligned} \left\langle \nabla \cdot (b_n^2 \nabla \varphi), \psi \right\rangle_{\mathcal{D}} - \left\langle \varphi, \nabla \cdot (b_n^2 \nabla \psi) \right\rangle_{\mathcal{D}} = \\ \oint_{\partial \mathcal{D}} b_n^2 (\psi^* \frac{\partial \varphi}{\partial n} - \varphi \frac{\partial \psi^*}{\partial n}) d\boldsymbol{q}. \end{aligned} \tag{E.3}$$

Noting that φ and ψ vanish on $\partial \mathcal{D}$ (see the explanation provided in Section D.3), it can be concluded that

$$\left\langle \varphi, \nabla \cdot (b_n^2 \nabla \psi) \right\rangle_{\mathcal{D}} = \left\langle \nabla \cdot (b_n^2 \nabla \varphi), \psi \right\rangle_{\mathcal{D}}. \tag{E.4}$$

The equality (E.4) implies that the operator $\mathcal{L}_n \triangleq \nabla \cdot (b_n^2 \nabla)$ is self-adjoint.

E.2 Negative definiteness

Letting $\varphi = \psi$ in (E.2) and noting that ψ vanishes on $\partial \mathcal{D}$ (see the explanation provided in Section D.3), we have

$$\left\langle \nabla \cdot (b_n^2 \nabla \psi), \psi \right\rangle_{\mathcal{D}} = - \int_{\mathcal{D}} b_n^2 \left| \nabla \psi \right|^2 d\boldsymbol{q} \tag{E.5}$$

Noting that the right hand side of (E.5) is negative, it can be concluded that the operator $\mathcal{L}_n$ is negative definite.

As the operator $\frac{1}{A}\nabla^2$ is a special form of $\mathcal{L}_n$, when $b_n^2(\boldsymbol{q}) = \frac{1}{A}$, it is also self-adjoint and negative definite.

F

Discretization Procedure for the TE Forward Solver

The skeptic will say: "It may well be true that this system of equations is reasonable from a logical standpoint. But this does not prove that it corresponds to nature." You are right, dear skeptic. Experience alone can decide on truth... Pure logical thinking cannot yield us any knowledge of the empirical world: all knowledge of reality starts from experience and ends in it. (Albert Einstein [177]).

In this Appendix, we describe the discretization procedure used in the Transverse Electric (TE) forward solver. This discretization is based on what explained in [27]. As noted in Section 2.3.2, the forward scattering problem is concerned with solving the domain equation, (2.17). Before discussing the discretization procedure, we first multiply both sides of (2.17) by the electric contrast χ; thus, we have

$$\boldsymbol{W} = \chi \boldsymbol{E}^{\text{inc}} + \chi \mathcal{G}_{\mathcal{D}}(\boldsymbol{W}), \tag{F.1}$$

where the contrast sources $\boldsymbol{W}$ is defined as $\boldsymbol{W} \triangleq \chi \boldsymbol{E}$. Now, we take $\boldsymbol{W}$ as the fundamental unknown of the forward solver. We note that by having $\boldsymbol{W}$, we can then find $\boldsymbol{E}$ as

$$\boldsymbol{E} = \boldsymbol{E}^{\text{inc}} + \mathcal{G}_{\mathcal{D}}(\boldsymbol{W}). \tag{F.2}$$

Noting (2.1), (F.1) may be written as

$$W_\kappa = \chi E_\kappa^{\text{inc}} + \chi \left(k_b^2 A_\kappa + B_\kappa \right) \tag{F.3}$$

where the subscript κ denotes the components of the vector-valued functions. That is, $\kappa \in \{x, y\}$. The functions A_κ and B_κ are given as

$$A_\kappa(\boldsymbol{q}) = \int_{\mathcal{D}} g(\boldsymbol{q}, \boldsymbol{q}') W_\kappa(\boldsymbol{q}') d\boldsymbol{q}', \tag{F.4}$$

$$B_\kappa(\boldsymbol{q}) = \hat{\kappa} \cdot (\nabla_{\boldsymbol{q}} \nabla_{\boldsymbol{q}} \cdot [A_x(\boldsymbol{q}) \hat{x} + A_y(\boldsymbol{q}) \hat{y}]). \tag{F.5}$$

We assume that the imaging domain $\mathcal{D}$ is uniformly discretized into $M \times P$ rectangular subdomains along x and y directions. Each rectangular subdomain will then have an area of $\Delta x \times \Delta y$ with center points

$$(x_m, y_p) = \left(x_{\frac{1}{2}} + (m - \frac{1}{2}) \Delta x, y_{\frac{1}{2}} + (p - \frac{1}{2}) \Delta y \right), \tag{F.6}$$

where $m = 1, \cdots, M$ and $p = 1, \cdots, P$ and $x_{\frac{1}{2}}$ and $y_{\frac{1}{2}}$ denote the lower bounds in x and y directions respectively. In each rectangular subdomain, we assume that the contrast is

constant and equal to the value of the contrast function at the center point. That is,

$$\chi_{m,p} = \chi(x_m\hat{x} + y_p\hat{y}). \tag{F.7}$$

Similar discretization are also used for W_κ, E_κ^{inc}, A_κ, and B_κ. Thus, the discrete form of (F.3) may be written as

$$W_{\kappa;m,p} = \chi_{m,p}E^{\text{inc}}_{\kappa;m,p} + \chi_{m,p}\left(k_b^2 A_{\kappa;m,p} + B_{\kappa;m,p}\right) \tag{F.8}$$

The vectors B_x and B_y are computed with finite difference rules as

$$\begin{aligned} B_{x;m,p} = \frac{A_{x;m-1,p} - 2A_{x;m,p} + A_{x;m+1,p}}{\Delta x^2} + \\ \frac{A_{y;m-1,p-1} - A_{y;m-1,p+1} - A_{y;m+1,p-1} + A_{y;m+1,p+1}}{4\Delta x \Delta y} \end{aligned} \tag{F.9}$$

$$\begin{aligned} B_{y;m,p} = \frac{A_{y;m,p-1} - 2A_{y;m,p} + A_{y;m,p+1}}{\Delta y^2} + \\ \frac{A_{x;m-1,p-1} - A_{x;m-1,p+1} - A_{x;m+1,p-1} + A_{x;m+1,p+1}}{4\Delta x \Delta y} \end{aligned} \tag{F.10}$$

As can be seen in (F.9) and (F.10), calculation of the vectors B_x and B_y require the discrete form of A_x and A_y. In order to cope with the singularity of the Green's function, we use the method presented in [27, 29, 178] and then compute the integral (F.4) using a midpoint rule. That is,

$$A_{\kappa,m,p} = \Delta x \Delta y \sum_{m'=1}^{M}\sum_{p'=1}^{P} \mathscr{G}_{m-m',p-p'} W_{\kappa;m',p'} \tag{F.11}$$

where $m = 0, \cdots, M+1$, $p = 0, \cdots, P+1$ and [29]

$$\mathscr{G}_{m-m',p-p'} = \begin{cases} \frac{j}{k_b a} J_1\left(\frac{1}{2}k_b a\right) H_0^1\left[k_b\sqrt{\left(x_m - x_{m'}\right)^2 + \left(y_p - y_{p'}\right)^2}\right] & (x_m, y_p) \neq (x_{m'}, y_{p'}) \\ \frac{j}{k_b a}\left[H_1^1\left(\frac{1}{2}k_b a\right) + \frac{4j}{\pi k_b a}\right] & (x_m, y_p) = (x_{m'}, y_{p'}) \end{cases} \tag{F.12}$$

The parameter a is chosen to be $a = \min\{\Delta x, \Delta y\}$. Finally, it should be noted that (F.9), (F.10), and (F.11) can be efficiently computed using FFT routines. This completes the discretization procedure for the utilized TE forward solver.

Bibliography

[1] A. N. Tikhonov and V. Y. Arsenin, *Solutions of Ill-Posed Problems*. New York: John Wiley & Sons, 1977.

[2] M. Pastorino, S. Caorsi, and A. Massa, "A global optimization technique for microwave nondestructive evaluation," *IEEE. Trans. Instrum. and Meas.*, vol. 51, no. 4, pp. 666–673, Aug 2002.

[3] W. H. Weedon, W. C. Chew, and P. E. Mayes, "A step-frequency radar imaging system for microwave nondestructive evaluation," *Progress in Electromagnetic Research*, vol. 28, pp. 121–146, 2000.

[4] A. Abubakar, T. Habashy, V. Druskin, L. Knizhnerman, and D. Alumbaugh, "2.5D forward and inverse modeling for interpreting low-frequency electromagnetic measurements," *Geophysics*, vol. 73, no. 4, pp. F165–F177, July-Aug 2008.

[5] A. Abubakar and P. M. van den Berg, "Non-linear three-dimensional inversion of cross-well electrical measurements," *Geophysical Prospecting*, vol. 48, pp. 109–134, 2000.

[6] L. P. Song, C. Yu, and Q. H. Liu, "Through-wall imaging (TWI) by radar: 2-D tomographic results and analyses," *IEEE Trans. Geosci. Remote Sensing*, vol. 43, no. 12, pp. 2793–2798, Dec 2005.

[7] P. M. Meaney, M. W. Fanning, T. Raynolds, C. J. Fox., Q. Fang, C. A. Kogel, S. P. Poplack, and K. D. Paulsen, "Initial clinical experience with microwave breast imaging in women with normal mammography," *Acad Radiol.*, March 2007.

[8] S. Poplack, T. Tosteson, W. Wells, B. Pogue, P. Meaney, A. Hartov, C. Kogel, S. Soho, J. Gibson, and K. Paulsen, "Electromagnetic breast imaging results of a pilot study in women with abnormal mammograms," *Radiology*, vol. 243, no. 2, pp. 350–359, 2007.

[9] A. Abubakar, "Three-dimensional nonlinear inversion of electrical conductivity," Ph.D. dissertation, Delft University, Delft, Netherlands, 2000.

[10] M. Oristaglio and H. Blok, *Wavefield imaging and inversion in electromagnetics and acoustics*. Course Notes TU Delft, 1995.

[11] A. Abubakar, P. M. van den Berg, and J. J. Mallorqui, "Imaging of biomedical data using a multiplicative regularized contrast source inversion method," *IEEE Trans. Microwave Theory Tech.*, vol. 50, no. 7, pp. 1761–1777, July 2002.

[12] T. Rubæk, P. M. Meaney, P. Meincke, and K. D. Paulsen, "Nonlinear microwave imaging for breast-cancer screening using Gauss-Newton's method and the CGLS inversion algorithm," *IEEE Trans. Antennas Propag.*, vol. 55, no. 8, pp. 2320–2331, Aug 2007.

[13] E. C. Fear, X. Li, S. C. Hagness, and M. Stuchly, "Confocal microwave imaging for breast cancer detection: localization of tumors in three dimensions," *IEEE Trans. Biomed Eng.*, vol. 49, no. 8, pp. 812–822, Aug 2002.

[14] S. Y. Semenov and D. R. Corfield, "Microwave tomography for brain imaging: Feasibility assessment for stroke detection," *International Journal of Antennas and Propagation*, 2008.

[15] P. M. Meaney, T. Zhou, M. W. Fanning, S. A. Geimer, and K. D. Paulsen, "Microwave imaging for bone fracture risk assessment," in *Proc. 2008 Applied Computational Electromagnetics Symp.*, Niagra Falls, Canada, March 31-April 4, pp. 462–466.

[16] S. Y. Semenov, R. H. Svenson, V. G. Posukh, A. G. Nazarov, Y. E. Sizov, A. E. Bulyshev, A. E. Souvorov, W. Chen, J. Kasell, and G. P. Tastis, "Dielectrical spectroscopy of canine myocardium during acute ischemia and hypoxia at frequency spectrum from 100 KHz to 6 GHz," *IEEE Trans. Med. Imag*, vol. 21, no. 6, pp. 703–707, June 2002.

[17] S. Semenov, "Microwave tomography: review of the progress towards clinical applications," *Phil. Trans. R. Soc. A*, vol. 367, pp. 3021–3042, July 2009.

[18] M. Lazebnik and *et. al.*, "A large-scale study of the ultrawideband microwave dielectric properties of normal, benign, and malignant breast tissues obtained from cancer surgeries," *Physics in Medicine and Biology*, vol. 52, pp. 6093–6115, 2007.

[19] J. M. Sill and E. C. Fear, "Tissue sensing adaptive radar for breast cancer detection–experimental investigation of simple tumor models," *IEEE Trans. Microwave Theory Tech.*, vol. 53, no. 11, pp. 3312–3319, November 2005.

[20] X. Li and S. C. Hagness, "A confocal microwave imaging algorithm for breast cancer detection," *IEEE Microwave Wireless Comp. Letters*, vol. 11, no. 3, pp. 130–132, March 2001.

[21] E. Bond, X. Li, S. C. Hagness, and B. D. van Veen, "Microwave imaging via space-time beamforming for early detection of breast cancer," *IEEE Trans. Antennas Propag.*, vol. 51, no. 8, pp. 1690–1705, August 2003.

[22] P. Kosmas and C. M. Rappaport, "FDTD-based time reversal for microwave breast cancer detection–localization in three dimensions," *IEEE Trans. Microwave Theory Tech.*, vol. 54, no. 4, pp. 1921–1927, June 2006.

[23] P. C. Hansen, "Numerical tools for analysis and solution of fredholm integral equations of the first kind," *Inverse Problems*, vol. 8, pp. 849–872, 1992.

[24] A. J. Devaney, "Nonuniqueness in the inverse scattering problem," *J. Math. Phys.*, vol. 19, no. 7, pp. 1526–1531, 1978.

[25] A. J. Devaney and G. C. Sherman, "Nonuniqueness in inverse source and scattering problems," *IEEE Trans. Antennas Propag.*, vol. 30, no. 5, pp. 1034–1042, Sep 1982.

[26] A. Kirsch, *An introduction to the mathematical theory of inverse problems*. New York: Springer-Verlag, 1996.

[27] A. Abubakar and P. M. van den Berg, "Iterative forward and inverse algorithms based on domain integral equations for three-dimensional electric and magnetic objects," *J. Comput. Phys.*, vol. 195, pp. 236–262, 2004.

[28] I. Rekanos and A. Raisanen, "Microwave imaging in the time domain of buried multiple scatterers by using an FDTD-based optimization technique," *IEEE Transactions on Magnetics*, vol. 39, no. 3, pp. 1381–1384, May 2003.

[29] B. J. Kooij and P. M. van den Berg, "Nonlinear inversion in TE scattering," *IEEE Trans. Microwave Theory Tech.*, vol. 46, no. 11, pp. 1704–1712, Nov. 1998.

[30] J. D. Zaeytijd, A. Franchois, C. Eyraud, and J.-M. Geffrin, "Full-wave three-dimensional microwave imaging with a regularized Gauss-Newton method–theory and experiment," *IEEE Trans. Antennas Propag.*, vol. 55, no. 11, pp. 3279–3292, Nov 2007.

[31] A. E. Bulyshev, A. E. Souvorov, S. Y. Semenov, V. G. Posukh, and Y. E. Sizov, "Three dimensional vector microwave tomography: Theory and computational experiments," *Inverse Probl.*, vol. 20, pp. 1239–1259, 2004.

[32] P. Meaney, K. Paulsen, S. Geimer, S. Haider, and M. Fanning, "Quantification of 3-D field effects during 2-D microwave imaging," *IEEE Trans. Biomed. Eng.*, vol. 49, no. 7, pp. 708–720, July 2002.

[33] C. Balanis, *Advanced Engineering Electromagnetics*. New York: John Wiley and Sons, 1989.

[34] J. Ma, W. C. Chew, C. C. Lu, and J. Song, "Image reconstruction from TE scattering data using equation of strong permittivity fluctuation," *IEEE Trans. Antennas Propag.*, vol. 48, no. 6, pp. 860–867, June 2000.

[35] W. Chew, *Waves and Fields in Inhomogenous Media*. New York: Van Nostrand Reinhold, 1990.

[36] T. Sarkar, E. Arvas, and S. Rao, "Application of FFT and the conjugate gradient method for the solution of electromagnetic radiation from electrically large and small conducting bodies," *IEEE Trans. Antennas Propag.*, vol. 34, no. 5, pp. 635–640, May 1986.

[37] P. Zwamborn and P. van den Berg, "The three dimensional weak form of the conjugate gradient FFT method for solving scattering problems," *IEEE Trans. Microwave Theory Tech.*, vol. 40, no. 9, pp. 1757–1766, Sep 1992.

[38] A. G. Tijhuis, K. Belkebir, and A. C. S. Litman, "Theoretical and computational aspects of 2-D inverse profiling," *IEEE Trans. Geosci. Remote Sensing*, vol. 39, no. 6, pp. 1316–1330, 2001.

[39] M. Kac, "Can one hear the shape of a drum," *American Mathematical Monthly*, vol. 73, pp. 1–23, 1966.

[40] W. C. Chew and Y. M. Wang, "Reconstruction of two-dimensional permittivity distribution using the distorted Born iterative method," *IEEE Trans. Med. Imaging*, vol. 9, no. 2, pp. 218–225, 1990.

[41] N. Joachimowicz, C. Pichot, and J. P. Hugonin, "Inverse scattering: An iterative numerical method for electromagnetic imaging," *IEEE Trans. Antennas Propag.*, vol. 39, no. 12, pp. 1742–1752, Dec 1991.

[42] A. Franchois and A. G. Tijhuis, "A quasi-Newton reconstruction algorithm for a complex microwave imaging scanner environment," *Radio Sci.*, vol. 38, no. 2, 2003.

[43] S. Caorsi, A. Massa, and M. A. Pastorino, "A computational technique based on a real-coded genetic algorithm for microwave imaging purposes," *IEEE Trans. Geosci. Remote Sensing*, vol. 38, no. 4, pp. 1697–1708, 2000.

[44] A. E. Souvorov, A. E. Bulyshev, S. Y. Semenov, R. H. Svenson, A. G. Nazarov, Y. E. Sizov, and G. P. Tastis, "Microwave tomography: A two dimensional Newton iterative scheme," *IEEE Trans. Microw. Theory Tech.*, vol. 46, no. 11, pp. 1654–1659, Nov 1998.

[45] T. M. Habashy and A. Abubakar, "A general framework for constraint minimization for the inversion of electromagnetic measurements," *Progress in Electromagnetics Research*, vol. 46, pp. 265–312, 2004.

[46] A. Franchois and C. Pichot, "Microwave imaging–complex permittivity reconstruction with a Levenberg-Marquardt method," *IEEE Trans. Antennas Propag.*, vol. 45, no. 2, pp. 203–215, Feb 1997.

[47] R. E. Kleinman and P. M. van den Berg, "A modified gradient method for two-dimensional problem in tomography," *J. Comput. Appl. Math.*, vol. 42, no. 1, pp. 17–35, 1992.

[48] P. M. van den Berg and R. E. Kleinman, "A contrast source inversion method," *Inverse Probl.*, vol. 13, pp. 1607–1620, 1997.

[49] M. Oristaglio, "Accuracy of the Born and Rytov approximations for reflection and refraction at a plane interface," *J. Opt. Soc. Am. A*, vol. 2, pp. 1987–1993, 1985.

[50] T. M. Habashy, R. Groom, and B. Spies, "Beyond the Born and Rytov approximations: a nonlinear approach to electromagnetic scattering," *J. Geophys. Res.*, vol. 98, pp. 1759–1775, 1993.

[51] Y. M. Wang and W. C. Chew, "An iterative solution of the two-dimensional electromagnetic inverse scattering problem," *Int. J. Imag. Syst. Technol.*, vol. 1, pp. 100–108, 1989.

[52] P. Mojabi and J. LoVetri, "Preliminary investigation of the NCP parameter–choice method for inverse scattering problems using BIM: 2D TM case," *Applied Computational Electromagnetic Society (ACES) Journal*, vol. 23, no. 3, pp. 207–214, 2008.

[53] ——, "Adapting the normalized cumulative periodogram parameter–choice method to the Tikhonov regularization of 2D TM electromagnetic inverse scattering using Born iterative method," *Progress In Electromagnetic Research (PIER) M*, vol. 1, pp. 111–138, 2008.

[54] N. Joachimowicz, J. J. Mallorqui, J. C. Bolomey, and A. Broquetas, "Convergence and stability assessment of Newton-Kantorovich reconstruction algorithms for microwave tomography," *IEEE Trans. Med. Imag.*, vol. 17, pp. 562–569, Aug 1998.

[55] C. Gilmore, P. Mojabi, and J. LoVetri, "Comparison of an enhanced distorted Born iterative method and the multiplicative-regularized contrast source inversion method," *IEEE Trans. Antennas Propag.*, vol. 57, no. 8, pp. 2341–2351, Aug. 2009.

[56] P. Mojabi and J. LoVetri, "Microwave biomedical imaging using the multiplicative regularized Gauss–Newton inversion," *IEEE Antennas and Wireless Propagation Letters*, vol. 8, pp. 645–648, 2009.

[57] ——, "Enhancement of the Krylov subspace regularization for microwave biomedical imaging," *IEEE Trans. Med. Imag.*, vol. 28, no. 12, pp. 2015–2019, Dec. 2009.

[58] ——, "Overview and classification of some regularization techniques for the Gauss-Newton inversion method applied to inverse scattering problems," *IEEE Trans. Antennas Propag.*, vol. 57, no. 9, pp. 2658–2665, Sept. 2009.

[59] ——, "Comparison of TE and TM inversions in the framework of the Gauss–Newton method," *IEEE Trans. Antennas Propag.*, vol. 58, no. 4, pp. 1336–1348, April 2010.

[60] R. F. Remis and P. M. van den Berg, "On the equivalence of the Newton-Kantorovich and distorted Born methods," *Inverse Problems*, vol. 16, pp. L1–L4, 2000.

[61] L. Garnero, A. Franchois, J. P. Hugonin, C. Pichot, and N. Joachimowicz, "Microwave imaging–complex permittivity reconstruction by simulated annealing," *IEEE Trans. Microw. Theory Tech.*, vol. 39, no. 11, pp. 1801–1807, Nov 1991.

[62] M. Pastorino, "Stochastic optimization methods applied to microwave imaging: A review," *IEEE Trans. Antennas Propag.*, vol. 55, no. 3, pp. 538–548, March 2007.

[63] S. Barkeshli and R. G. Lautzenheiser, "An iterative method for inverse scattering problems based on an exact gradient search," *Radio Science*, vol. 29, pp. 1119–1130, 1994.

[64] P. van den Berg, "Nonlinear scalar inverse scattering: Algorithms and applications," *Scattering and Inverse Scattering in Pure and Applied Sciences, Editors: E. R. Pike and P. C. Sabatier (London: Academic)*, vol. 1, pp. 121–141, 2001.

[65] A. Abubakar, P. M. van den Berg, and S. Y. Semenov, "A robust iterative method for Born inversion," *IEEE Trans. Geosci. Remote Sensing*, vol. 42, no. 2, pp. 342–354, Feb 2004.

[66] A. Abubakar, T. M. Habashy, P. M. van den Berg, and D. Gisolf, "The diagonalized contrast source approach: an inversion method beyond the Born approximation," *Inverse Problems*, vol. 21, no. 2, pp. 685–702.

[67] S. G. C. Gabriel and E. Corthout, "The dielectric properties of biological tissues: III. parametric models for the dielectric spectrum of tissues," *Physics in Medicine and Biology*, vol. 41, no. 11, pp. 2271–2294, 1996.

[68] J. Kaipio and E. Somersalo, *Statistical and Computational Inverse Problems*. New York: Springer Science and Business Media, 2004.

[69] E. Chong and S. Zak, *An Introduction to Optimization*. New York: Wiley Interscience, 2001.

[70] W. Wirtinger, "Zur formalen theorie der funktionen von mehr komplexen veränderlichen," *Mathematische Annalen*, vol. 97, no. 1, pp. 357–375, 1927.

[71] H. Li and T. Adali, "Complex-valued adaptive signal processing using nonlinear functions," *EURASIP Journal on Advances in Signal Processing*, 2008.

[72] D. H. Brandwood, "A complex gradient operator and its application in adaptive array theory," *IEE Proc. F and H*, vol. 130, no. 1, pp. 11–16, 1983.

[73] A. van den Bos, "Complex gradient and Hessian," *IEE Proc. Vision, Image Signal Process.*, vol. 141, no. 6, pp. 380–383, 1994.

[74] P. C. Hansen, *Rank-deficient and discrete ill-posed problems: Numerical aspects of linear inversion*. Philadelphia, PA: SIAM, 1998.

[75] G. L. Wang, W. C. Chew, T. J. Cui, A. A. Aydiner, D. L. Wright, and D. V. Smith, "3D near-to-surface conductivity reconstruction by inversion of VETEM data using the distorted Born iterative method," *Inverse Problems*, vol. 20, pp. S195–S216, 2004.

[76] A. E. Bulyshev, A. E. Souvorov, S. Y. Semenov, R. H. Svenson, A. G. Nazarov, Y. E. Sizov, and G. P. Tastis, "Three dimensional microwave tomography. theory and computer experiments in scalar approximation," *Inverse Probl.*, vol. 16, pp. 863–875, 2000.

[77] M. S. Zhdanov, *Geophysical Inverse Theory and Regularization*. Amsterdam: Elsevier, 2002.

[78] P. C. Hasen and D. P. O'leary, "The use of the L-curve in the regularization of discrete ill-posed problems," *SIAM J. Sci. Comput.*, vol. 14, no. 6, pp. 1487–1503, Nov 1993.

[79] P. R. Johnston and R. M. Gulrajani, "Selecting the corner in the L-curve approach to Tikhonov regularization," *IEEE Trans. Biomed. Eng.*, vol. 47, no. 9, pp. 1293–1296, Sep 2000.

[80] G. H. Golub, M. Heath, and G. Wahba, "Generalized cross validation as a method for choosing a good ridge parameter," *Technometrics*, vol. 21, pp. 215–224, 1979.

[81] B. W. Rust and D. P. O'Leary, "Residual periodograms for choosing regularization parameters for ill-posed problems," *Inverse Probl.*, vol. 24, 2008.

[82] P. C. Hansen, M. E. Kilmer, and R. H. Kjeldsen, "Exploiting residual information in the parameter choice for discrete ill-posed problems," *BIT Numerical Mathematics*, vol. 46, pp. 41–59, 2006.

[83] P. C. Hansen, "Analysis of discrete ill-posed problems by means of the L-curve," *SIAM Review*, vol. 34, no. 4, pp. 561–580, Dec 1992.

[84] ——, "The discrete Picard condition for discrete ill-posed problems," *BIT*, vol. 30, pp. 658–672, 1990.

[85] A. Franchois, A. Joisel, C. Pichot, and J.-C. Bolomey, "Quantitative microwave imaging with a 2.45-GHz planar microwave camera," *IEEE Trans. Med. Imag.*, vol. 17, no. 4, pp. 550–561, Aug 1998.

[86] A. Bjork, *Numerical methods for least squares problems*. Philadelphia, PA: SIAM, 1996.

[87] J. D. Shea, P. Kosmas, S. C. Hagness, and B. D. van Veen, "Three-dimensional microwave breast imaging: a bounded, multi-frequency inverse scattering solution on a uniform voxel mesh," in *Proc. XXIX General Assembly of International Union of Radio Science*, Chicago, USA, August 2008.

[88] J. Chung, J. G. Nagy, and D. P. O'leary, "A weighted-GCV method for Lanczos-hybrid regularization," *Electronic Transactions on Numerical Analysis*, vol. 28, pp. 149–167, 2008.

[89] M. Roggemann and B. Welsh, *Imaging Through Turbulence*. Boca Raton, Florida: CRC Press, 1996.

[90] M. E. Kilmer and D. P. O'leary, "Choosing regularization parameters in iterative methods for ill-posed problems," *SIAM J. Matrix Anal. Appl.*, vol. 22, no. 4, pp. 1204–1221, 2001.

[91] D. Colton and R. Kress, *Inverse Acoustic and Electromagnetic Scattering Theory*. New York: Springer-Verlag, 1992.

[92] R. Pierri, A. Liseno, and F. Soldovieri, "Shape reconstruction from PO multifrequency scattered fields via the singular value decomposition approach," *IEEE Trans. Antennas Propag.*, vol. 49, no. 9, pp. 1333–1343, Sep 2001.

[93] M. Ng, R. Chan, and W.-C. Tang, "A fast algorithm for deblurring models with Neumann boundary conditions," *SIAM J. Sci. Comput.*, vol. 21, 1999.

[94] T. K. Jensen, "Stabilization algorithms for large-scale problems," Ph.D. dissertation, Technical University of Denmark, Kongens Lyngby, Denmark, 2006.

[95] P. Charbonnier, L. Blanc-Féraud, G. Aubert, and M. Barlaud, "Deterministic edge-preserving regularization in computed imaging," *IEEE Trans. Image Processing*, vol. 6, no. 2, pp. 298–311, Feb 1997.

[96] J. Pedersen, "Modular algorithms for large scale total variation image deblurring," M.Sc. Thesis, Technical University of Denmark, Kongens Lyngby, Denmark, 2005.

[97] C. Vogel and M. Oman, "Fast, robust total variation-based reconstruction of noisy, blurred images," *IEEE Trans. Image Processing*, vol. 7, no. 6, pp. 813–824, Jun 1998.

[98] G. H. Golub and C. F. V. Loan, *Matrix Computations*. Baltimore, Maryland: Johns Hopkins University Press, 1996.

[99] A. Broquetas, J. Romeu, J. Rius, A. Elias-Fuste, A. Cardama, and L. Jofre, "Cylindrical geometry: a further step in active microwave tomography," *IEEE Trans. Microw. Theory Tech.*, vol. 39, no. 5, pp. 836–844, May 1991.

[100] C. Gabriel, S. Gabriel, and E. Corthout, "The dielectric properties of biological tissues: III. Parametric models for the dielectric spectrum of tissues," *Physics in Medicine and Biology*, vol. 41, no. 11, pp. 2271–2294, Nov 2000.

[101] J. Mallorqui, N. Joachimowicz, A. Broquetas, and J. C. Boloiney, "Quantitative images of large biological bodies in microwave tomography by using numerical and real data," *Electronics Letters*, vol. 32, no. 23, pp. 2138–2140, Nov 1996.

[102] J.-M. Geffrin, P. Sabouroux, and C. Eyraud, "Free space experimental scattering database continuation: experimental set-up and measurement precision," *Inverse Probl.*, vol. 21, pp. S117–S130, 2005.

[103] R. F. Bloemenkamp, A. Abubakar, and P. M. van den Berg, "Inversion of experimental multi-frequency data using the contrast source inversion method," *Inverse Probl.*, vol. 17, pp. 1611–1622, 2001.

[104] L. Crocco and T. Isernia, "Inverse scattering with real data: detecting and imaging homogeneous dielectric objects," *Inverse Probl.*, vol. 17, pp. 1573–1583, 2001.

[105] A. Abubakar and P. M. van den Berg, "The contrast source inversion method for location and shape reconstructions," *Inverse Probl.*, vol. 18, pp. 495–510, 2002.

[106] S. Semenov, R. Svenson, A. Bulyshev, A. Souvorov, A. Nazarov, Y. Sizov, V. Posukh, A. Pavlovsky, P. Repin, and G. Tatsis, "Spatial resolution of microwave tomography for detection of myocardial ischemia and infarction-experimental study on two-dimensional models," *IEEE Trans. Microwave Theory Tech.*, vol. 48, no. 4, pp. 538–544, Apr 2000.

[107] P. Meaney, N. Yagnamurthy, and K. D. Paulsen, "Pre-scaled two-parameter Gauss-Newton image reconstruction to reduce property recovery imbalance," *Phys. Med. Biol.*, vol. 47, pp. 1101–1119, 2002.

[108] A. Abubakar, P. M. van den Berg, T. M. Habashy, and H. Braunisch, "A multiplicative regularization approach for deblurring problems," *IEEE Trans. Image Processing*, vol. 13, no. 11, pp. 1524–1532, Nov 2004.

[109] R. Fletcher and C. M. Reeves, "Function minimization by conjugate gradients," *Comput. J.*, vol. 7, pp. 149–154, 1964.

[110] C. Morozov, "On the solution of functional equations by the method of regularization," *Soviet Math. Dokl.*, vol. 7, pp. 414–417, 1966.

[111] W. C. Chew and J. H. Lin, "A frequency–hopping approach for microwave imaging of large inhomogeneous bodies," *IEEE Microwave and Guided Wave Letters*, vol. 5, no. 12, pp. 439–441, Dec. 1995.

[112] A. Abubakar, P. M. van den Berg, and T. M. Habashy, "Application of the multiplicative regularized contrast source inversion method on TM- and TE-polarized experimental fresnel data," *Inverse Probl.*, vol. 21, pp. S5–S13, 2005.

[113] T. Sarkar, R. Mailloux, A. Oliner, M. Salazar-Palma, and D. Sengupta, *History of Wireless*. New Jersey: John Wiley and Sons, 2006.

[114] G. P. Otto and W. C. Chew, "Inverse scattering of H_z waves using local-shape function imaging: a T-matrix formulation," *Int. J. Imag. Syst. Technol.*, vol. 5, pp. 22–27, 1994.

[115] A. Abubakar and T. M. Habashy, "Nonlinear inversion of multi–frequency microwave Fresnel data using the multiplicative regularized contrast source inversion," *Progress in Electromagnetics Research*, vol. 62, pp. 193–201, 2006.

[116] C. P. Cho and Y. W. Kiang, "Inverse scattering of dielectric cylinders by a cascaded TE–TM method," *IEEE Trans. Microw. Theory Tech.*, vol. 47, no. 10, pp. 1923–1930, Oct 1999.

[117] C. Pichot, J. Y. Dauvignac, I. Aliferis, E. L. Brusq, R. Ferrayé, and V. Chatelée, "Recent nonlinear inversion methods and measurement system for microwave imaging," in *IEEE Int. Workshop on Imaging Systems and Techniques*, Stresa, Italy, May 2004.

[118] K. Belkebir and M. Saillard, "Special section: testing inversion algorithm against experimental data," *Inverse Probl.*, vol. 17, pp. 1565–1571, 2001.

[119] C. Ramananjoana, M. Lambert, and D. Lesselier, "Shape inversion from TM and TE real data by controlled evolution of level sets," *Inverse Probl.*, vol. 17, pp. 1585–1595, 2001.

[120] K. Belkebir and M. Saillard, "Testing inversion algorithms against experimental data: inhomogeneous targets," *Inverse Probl.*, vol. 21, pp. S1–S3, 2005.

[121] C. Yu, L. P. Song, and Q. H. Liu, "Inversion of multi-frequency experimental data for imaging complex objects by a DTA-CSI method," *Inverse Probl.*, vol. 21, pp. S167–S178, 2005.

[122] D. Franceschini, M. Donell, G. Franceschini, and A. Massa, "Iterative image reconstruction of two-dimensional scatterers illuminated by TE waves," *IEEE Trans. Microw. Theory Tech.*, vol. 54, no. 4, pp. 1484–1494, Apr. 2006.

[123] O. Féron, B. Duchêne, and A. Mohammad-Djafari, "Microwave imaging of piecewise constant objects in a 2D-TE configuration," *International Journal of Applied Electromagnetics and Mechanics*, vol. 26, pp. 167–174, 2007.

[124] K. Paulsen and P. Meaney, "Nonactive antenna compensation for fixed-array microwave imaging. I. model development," *IEEE Trans. Med. Imag.*, vol. 18, no. 6, pp. 496–507, June 1999.

[125] P. M. van den Berg, A. L. van Broekhoven, and A. Abubakar, "Extended contrast source inversion," *Inverse Probl.*, vol. 15, pp. 1325–1344, 1999.

[126] J. Lagarias, J. A. Reeds, M. H. Wright, and P. E. Wright, "Convergence properties of the Nelder-Mead simplex method in low dimensions," *SIAM Journal of Optimization*, vol. 9, no. 1, pp. 112–147, 1998.

[127] O. M. Bucci, N. Cardace, L. Crocco, and T. Isernia, "2D inverse scattering: degree of nonlinearity, solution strategies and polarization effects," *Proc. SPIE*, vol. 4123, pp. 185–193, 2000.

[128] C. Reid, *Hilbert*. New York: Springer-Verlag, 1996.

[129] P. Meaney, M. Fanning, D. Li, S. Poplack, and K. Paulsen, "A clinical prototype for active microwave imaging of the breast," *IEEE Trans. Microwave Theory Tech.*, vol. 48, no. 11, pp. 1841–1853, Nov 2000.

[130] C. Yu, M. Yuan, J. Stang, E. Bresslour, R. George, G. Ybarra, W. Joines, and Q. H. Liu, "Active microwave imaging II: 3-D system prototype and image reconstruction from experimental data," *IEEE Trans. Microwave Theory Tech.*, vol. 56, no. 4, pp. 991–1000, April 2008.

[131] A. Fhager, P. Hashemzadeh, and M. Persson, "Reconstruction quality and spectral content of an electromagnetic time-domain inversion algorithm," *IEEE Trans. Biomed. Eng.*, vol. 53, no. 8, pp. 1594–1604, Aug. 2006.

[132] T. Rubæk and V. Zhurbenko, "Prototype of microwave imaging system for breast-cancer screening," in *Proc. 13th International Symposium on Antenna Technology and Applied Electromagnetics and the Canadian Radio Science Meeting (ANTEM/URSI)*, Banff, Canada, Feb. 2009.

[133] L. Crocco and A. Litman, "On embedded microwave imaging systems: retrievable information and design guidelines," *Inverse Problems*, vol. 25, p. 065001 (17pp), 2009.

[134] C. Gilmore and J. LoVetri, "Enhancement of microwave tomography through the use of electrically conducting enclosures," *Inverse Problems*, vol. 24, p. 035008 (21pp), 2008.

[135] P. Mojabi, C. Gilmore, A. Zakaria, and J. LoVetri, "Biomedical microwave inversion in conducting cylinders of arbitrary shapes," in *13th International Symposium on Antenna Technology and Applied Electromagnetics and the Canadian Radio Science Meeting (ANTEM/URSI)*, Feb. 2009, pp. 1–4.

[136] P. Meaney, K. Paulsen, A. Hartov, and R. Crane, "Microwave imaging for tissue assessment: initial evaluation in multitarget tissue-equivalent phantoms," *IEEE Trans. Biomed. Eng.*, vol. 43, no. 9, pp. 878–890, Sept. 1996.

[137] P. van den Berg and J. Fokkema, "Removal of undesired wavefields related to the casing of a microwave scanner," *IEEE Trans. Microwave Theory Tech.*, vol. 51, no. 1, pp. 187–192, Jan 2003.

[138] R. Lencrerot, A. Litman, H. Tortel, and J.-M. Geffrin, "Measurement strategies for a confined microwave circular scanner," *Inverse Problems in Science and Engineering*, pp. 1–16, Jan 2009.

[139] ——, "Imposing Zernike representation for imaging two-dimensional targets," *Inverse Problems*, vol. 25, p. 035012 (21pp), 2009.

[140] A. Abubakar, W. Hu, P. van den Berg, and T. Habashy, "A finite-difference contrast source inversion method," *Inverse Problems*, vol. 24, p. 065004 (17pp), 2008.

[141] R. E. Collin, *Field Theory of Guided Waves*. New York: IEEE Press, 1991.

[142] J. Maxwell, "A dynamical theory of the electromagnetic field," *Philosophical Transactions of the Royal Society of London*, vol. 155, pp. 459–512, 1864.

[143] S. Y. Semenov, R. H. Svenson, A. E. Bulyshev, A. E. Souvorov, A. G. Nazarov, Y. E. Sizov, V. G. Posukh, A. Pavlovsky, P. N. Repin, A. N. Starostin, B. A. Voinov, M. Taran, G. P. Tastis, and V. Y. Baranov, "Three-dimensional microwave tomography: Initial experimental imaging of animals," *IEEE Trans. Biomed. Eng.*, vol. 49, no. 1, pp. 55–63, Jan 2002.

[144] T. Rubaek, O. Kim, and P. Meincke, "Computational validation of a 3-D microwave imaging system for breast-cancer screening," *IEEE Trans. Antennas Propag.*, vol. 57, no. 7, pp. 2105–2115, July 2009.

[145] C. Gilmore, P. Mojabi, A. Zakaria, M. Ostadrahimi, C. Kaye, S. Noghanian, L. Shafai, S. Pistorius, and J. LoVetri, "A wideband microwave tomography system with a novel frequency selection procedure," *IEEE Trans. Biomed. Eng.*, vol. 57, no. 4, pp. 894–904, April 2010.

[146] E. Wadbro and M. Berggren, "Microwave tomography using topology optimization techniques," *SIAM J. Sci. Comput.*, vol. 30, no. 3, pp. 1613–1633, 2008.

[147] C. Gilmore and J. LoVetri, "Corrections to the 'enhancement of microwave tomography through the use of electrically conducting enclosures'," *Inverse Problems*, vol. 26, no. 1, p. 019801 (7pp), Jan. 2010.

[148] P. Mojabi and J. LoVetri, "Eigenfunction contrast source inversion for circular metallic enclosures," *Inverse Problems*, vol. 26, no. 2, p. 025010 (23pp), Feb. 2010.

[149] Mackay, *The Harvest of a Quiet Eye: A Selection of Scientific Quotations*. Taylor & Francis, 1977.

[150] C. Kaye, C. Gilmore, P. Mojabi, D. Firsov, and J. LoVetri, "Development of a resonant chamber microwave tomography system," *Ultra-Wideband Short-Pulse Electromagnetics, Springer Science+Business Media, Editor: Frank Sabbath*, vol. 9, pp. 519–526, 2010.

[151] C. Kaye, "Development and calibration of microwave tomography imaging systems for biomedical applications using computational electromagnetics," M.Sc. Thesis, University of Manitoba, Winnipeg, Manitoba, Canada, 2009.

[152] C. Gilmore, "Towards an improved microwave tomography systems," Ph.D. dissertation, University of Manitoba, Winnipeg, Manitoba, Canada, 2009.

[153] D. Li, P. Meaney, T. Raynolds, S. Pendergrass, M. Fanning, and K. D. Paulsen, "Parallel-detection microwave spectroscopy system for breast imaging," *Review of Scientific Instruments*, vol. 75, no. 7, pp. 2305–2313, 2004.

[154] A. Abbosh, H. Kan, and M. Bialkowski, "Compact ultra-wideband planar tapered slot antenna for use in a microwave imaging system," *Microwave Opt Technol Lett*, vol. 48, 2006.

[155] M. Ostadrahimi, S. Noghanian, and L. Shafai, "A modified double layer tapered slot antenna with improved cross polarization," in *Antenna Technology and Applied Electromagnetics and the Canadian Radio Science Meeting, 2009. ANTEM/URSI 2009. 13th International Symposium on*, Feb. 2009, pp. 1–4.

[156] R. Harrington, *Time-Harmonic Electromagnetic Fields*. New York: IEEE Press, 2001.

[157] K. Murata, A. Hanawa, and R. Nozaki, "Broadband complex permittivity measurement techniques of materials with thin configuration at microwave frequencies," *J. Appl. Phys.*, vol. 98, 2005.

[158] T. J. Cui, W. C. Chew, X. X. Yin, and W. Hong, "Study of resolution and super resolution in electromagnetic imaging for half-space problems," *IEEE Trans. Antennas Propag.*, vol. 52, no. 6, pp. 1398–1411, June 2004.

[159] R. Halter, A. Hartov, and K. Paulsen, "A broadband high-frequency electrical impedance tomography system for breast imaging," *Biomedical Engineering, IEEE Transactions on*, vol. 55, no. 2, pp. 650–659, Feb. 2008.

[160] A. den Dekker and A. van den Bos, "Resolution: a survey," *Journal of the Optical Society of America A*, vol. 14, no. 3, pp. 547–557, 1997.

[161] M. Born and E. Wolf, *Principles of Optics, 7th edition*.

[162] F. Chen and W. Chew, "Experimental verification of super resolution in nonlinear inverse scattering," *Applied Physics Letters*, vol. 72, no. 23, pp. 3080–3082, 1998.

[163] M. Moghaddam and W. Chew, "Nonlinear two-dimensional velocity profile inversion using time domain data," *IEEE Trans. Geosci. Remote Sensing*, vol. 30, no. 1, pp. 147–156, 1992.

[164] C. Gilmore, P. Mojabi, A. Zakaria, S. Pistorius, and J. LoVetri, "On super-resolution with an experimental microwave tomography system," *(submitted to) IEEE Antennas and Wireless Propagation Letters*, 2010.

[165] T. Rubaek and P. Meincke, "Including antenna models in microwave imaging for breast cancer screening," in *Antennas and Propagation, 2006. EuCAP 2006. First European Conference on*, Nov. 2006, pp. 1–6.

[166] J. F. Claerbout and F. Muir, "Robust modeling with erratic data," *Geophysics*, vol. 38, pp. 826–844, 1973.

[167] B. Brooksby, H. Dehghani, B. Pogue, and K. Paulsen, "Near-infrared (NIR) tomography breast image reconstruction with a priori structural information from MRI: algorithm development for reconstructing heterogeneities," *IEEE Journal of Selected Topics in Quantum Electronics*, vol. 9, no. 2, pp. 199–209, March-April 2003.

[168] M. R. Hestenes and E. Stiefel, "Methods of conjugate gradients for solving linear systems," *Journal of Research of the National Bureau of Standards*, vol. 49, pp. 409–436, 1952.

[169] L. Kronecker, "Theorie der einfachen und der vielfachen integrale," *Editor: B.G. Teubner*, 1894.

[170] R. Remmert, *Theory of Complex Functions*. New York: Springer-Verlag, 1991.

[171] K. Kreutz-Delgado, "The complex gradient operator and the $\mathbb{CR}$-calculus," *Lecture Notes Supplement [online], University of California, San Diego*, 2006.

[172] L. V. Kantorovich and G. P. Akilov, *Functional Analysis*. Pergamon Press, 1982.

[173] H.-P. Breuer and F. Petruccione, "Stochastic dynamics of open quantum systems: Derivation of the differential Chapman-Kolmogorov equation," *Physical Review E*, vol. 51, no. 5, pp. 4041 – 4054, May 1995.

[174] M. R. Fréchet, "Sur quelques points du calcul fonctionnel," Ph.D. dissertation, École Normale Supérieure, Paris, France, 1906.

[175] J. D. Jackson, *Classical Electrodynamics, 3rd edition*. New York: John Wiley and Sons, 1998.

[176] H. Eves, *Mathematical Circles Squared*. Boston: Prindle, Weber and Schmidt, 1972.

[177] A. Einstein, *Ideas and Opinions*. New York: Wings Books, 1954.

[178] J. Richmond, "Scattering by a dielectric cylinder of arbitrary cross section shape," *IEEE Trans. Antennas Propag.*, vol. 13, no. 3, pp. 334 – 341, May 1965.